Hydrothermal alteration and rare earth element mineralisation in the French Creek Granite, Westland, New Zealand

---

A THESIS SUBMITTED IN PARTIAL FULFILMENT

OF THE REQUIREMENTS FOR THE DEGREE OF

Master of Science in Geology

AT THE

UNIVERSITY OF CANTERBURY

DEPARTMENT OF GEOLOGICAL SCIENCES

BY

Regine Morgenstern

UNIVERSITY OF CANTERBURY

DECEMBER 2016

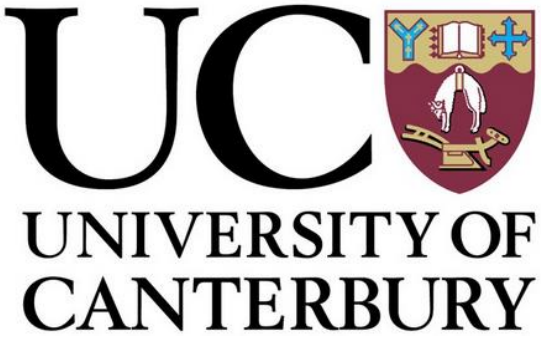

Abstract

Alkaline igneous complexes are one of two primary sources of rare earth elements (REEs), which are unique metals crucial for the economic growth of a country. Understanding REE metallogenesis in these systems is often complicated, with evidence of both magmatic and hydrothermal processes present. The A-type French Creek Granite (FCG), located on the West Coast of New Zealand, is a poorly-studied example of such a complex system in which anomalous REEs have previously been reported. The purpose of this thesis was to undertake a comprehensive field, petrological and geochemical study of the FCG, its hydrothermal alteration and, to a lesser extent, the cogenetic Hohonu Dyke Swarm (HDS), in order to better understand the type, style and location of REE mineralisation. Whole rock geochemical analyses of 54 samples using XRF and ICP-MS/AES established that the ca. 82 Ma FCG is a composite granitoid dominated by a ferroan, peraluminous biotite granite that was emplaced into a high-level (ca. 3 km) syn-tectonic setting. A syenite shell and genetically related basaltic–rhyolitic dykes are present, and trace element content, and disequilibrium textures in phenocrysts in dykes, are evidence of magma mixing. Maximum ΣREE+Y content are higher in the felsic FCG (847 ppm) relative to the mafic HDS (431 ppm). Primary REE-Zr-Y enrichment in the FCG is a function of partial melting of an enriched mantle source and subsequent extensive differentiation. Primary REE mineralisation was identified via SEM-EDS and is defined by modal allanite, zircon, apatite, fergusonite, monazite, perrierite and loparite, which typically occur with interstitial biotite. This association, and LA-ICP-MS analyses of REE-bearing giant (500 μm) zircon, indicate REE enrichment in the residual melt was likely due to high magmatic fluorine and late-stage water saturation, in addition to differentiation. Extensive sericitisation, chloritisation, hematisation, carbonate alteration and kaolinisation were identified in the altered FCG using field observations, microscopy and XRD. A zone of propylitic alteration in the Little Hohonu River and a smaller, phyllic alteration assemblage in the Eastern Hohonu River are defined, both of which generally correlate with higher REE anomalies than fresh FCG. Quartz protuberances, microscopic fractures and dyke emplacement indicate the phyllic alteration is structurally controlled, and REEs are hosted in bastnäsite group minerals, zircon, monazite and xenotime. This zone is consistently enriched (607 ppm average ΣREE+Y), indicating remobilisation and secondary REE-Zr-Y enrichment by hydrothermal fluids. Stable ^{13}C and ^{18}O isotopes from secondary carbonates indicate low temperature (~250°C) magmatic-hydrothermal fluids sourced from the cooling FCG, which were likely part of a late-stage porphyry-type system operating during the same mantle degassing and extension episode that was associated with initial Tasman Sea spreading.

Acknowledgements

Firstly, I would like to thank my supervisors Rose Turnbull, Paul Ashwell and Christopher Oze for all of their time, advice and ideas that they contributed towards this project, I am truly grateful, especially to Rose! I also could not have done this project without the help of my trusty field assistants Stefan Cook, Anders Lenskjold and Marie Eugène, who followed me into the thickest jungle, and shed sweat, and even some blood, for me. You are all troopers! I would like to thank Miriam Brabant for the use of her awesome little bach in Moana; it saved us a lot of driving and had the perfect view across the lake to our field area! I would like to thank the technicians at the University of Canterbury – Matt Cockcroft, Rob Spiers, Sacha Baldwin-Cunningham, Anekant Wandres, Chris Grimshaw, Stephen Brown and Mike Flaws – for their help with organisation of field equipment and transport, laboratory training, thin section production, geochemical analyses, and/or software support!

Secondly, I would like to say a huge thank you to Geoff Price for all of his information, ideas and knowledge on the French Creek Granite and surrounding area, and for sharing his samples with me. I am also hugely grateful to David Shelley who spent many hours helping me with my microscopic analyses and interpretation, your knowledge was invaluable! Thank you to Roger Townend for all of his help with the identification of rare earth mineral phases, I am truly grateful for all of his expert knowledge and advice on rare earth minerals and their analytical techniques. I would like to thank Todd Waight and Quinten van der Meer for also providing data and knowledge on the field site, and Ben Kennedy, Alex Nichols, Jarg Pettinga and James Pope for helpful discussion on specific aspects of the project. I would like to thank Jacqueline Dohaney who also helped with microscopic analysis, Henry Dillon from Golder Associates for his help with statistical analyses, Mark Rattenbury for providing digital geophysical data files on the study area, and ALS in Brisbane for conducting geochemical analyses.

Finally, a huge thank you to the following organisations that provided me with financial assistance to conduct my research: the Todd Foundation; the NZ Federation of Graduate Women Canterbury Branch; the Freemasons NZ; the Brian Mason Scientific and Technical Trust; the University of Canterbury; and the Geoscience Society of New Zealand! I would also like to thank the following organisations for awarding me with travel grants so that I may share my research with the wider scientific community: the Brian Mason Scientific and Technical Trust; the Royal Society of New Zealand Canterbury Branch; the American Geophysical Union; and the Australasian Institute of Mining and Metallurgy.

Table of Contents

List of Figures

Explanation of Acronyms

ASI: Alumina saturation index

CL: Cathodoluminescence

EHR: Eastern Hohonu River

FCG: French Creek Granite

HDS: Hohonu Dyke Swarm

HFSE(s): High-field-strength element(s)

HREE(s): Heavy rare earth element(s)

ICP-AES: Inductively coupled plasma atomic emission spectroscopy

ICP-MS: Inductively coupled plasma mass spectrometry

LHR: Little Hohonu River

LOI: Loss on ignition

LREE(s): Light rare earth element(s)

MSWD: Mean square weighted deviates

***p*XRF**: Portable x-ray fluorescence

QAF syenite: Quartz alkali-feldspar syenite

REE(s): Rare earth element(s)

RE mineral: Rare earth mineral

REO(s): Rare earth oxide(s)

WPG: Within-plate granite

XRD: X-ray diffraction

XRF: X-ray fluorescence

ΣREE(s): Total rare earth element(s)

Chapter 1: Introduction

1.1 Overview

Modern western society places great emphasis on the need for green energy, such as wind turbines and hybrid cars, and relies heavily on the advanced technology market where, for example, life without a smart phone is unimaginable for many. Both of these sectors fundamentally require the use of rare earth elements (REEs), and the growth of renewable energy and high-tech products have led to exponentially increasing demand for these metals (Alonso et al. 2012; Massachusetts Institute of Technology 2012; Massari & Ruberti 2013) that are vital for economic growth. In 2012, China controlled 98% of the global REE supply (Alonso et al. 2012), which leads to import dependence and predisposes other countries, such as New Zealand, to price increases if the supply is disrupted, which is what happened in 2010–2011 (Hatch 2012; Massari & Ruberti 2013).

Rare earth element mineralisation is often not a simple process; instead, it can involve multiple stages and a complex combination of processes. The primary sources of REEs on Earth are from alkaline igneous complexes and carbonatites, where REEs are concentrated by fractional crystallisation or by fluids released during cooling and crystallisation of these rocks (Christie et al. 1998). Furthermore, secondary enrichment of REEs in alkalic igneous rocks during hydrothermal circulation is now widely accepted (Kempe 1999; Lottermoser 1992; McConnell & Batterson 1987). This can result in the remobilisation and accumulation of REEs into economic deposits, which often correlate with the zones that have undergone the most intense hydrothermal alteration (Salvi & Williams-Jones 1990, 1996).

Consistent REE and other high-field-strength element (HFSE) anomalies have been documented in the ca. 82 Ma A-type French Creek Granite (FCG) and cogenetic Hohonu Dyke Swarm (HDS; Waight et al. 1998a) in Westland, New Zealand (Price 2013; Price and Ryland 2011; White and Price 2006), which is the focus of this study. This HFSE enrichment has led to interest from exploration companies that have identified the FCG as "highly prospective" for REE-Nb mineralisation (Strategic Elements Ltd 2011) based on limited reconnaissance. The alkalic FCG has undergone

variable hydrothermal alteration (Bradley et al. 1979; Waight 1995), and its geochemistry and alteration have been speculated as similar to the economic Strange Lake Zr-REE-Y-Nb deposit in Canada (Price 2013; Price & Ryland 2011; Strategic Elements 2011). This makes it an attractive prospecting target for possible economic REE mineralisation and to examine the processes involved in this mineralisation. Two notable zones of hydrothermal alteration have previously been identified: a zone of weak propylitic alteration in the lower Little Hohonu River (LHR; Brathwaite 2013) and a zone of intense 'calcitic' alteration in the Eastern Hohonu River (EHR; Waight 1995). This previous research lays the foundations of this M.Sc. thesis and these zones of hydrothermal alteration are the primary targets for REE mineralisation in the FCG. Although previous studies of the Hohonu Batholith have incorporated mineralogical and geochemical investigation of the FCG (Hamill 1972; Tulloch et al. 1994; Waight 1995; Waight et al. 1997, 1998a), no detailed studies have been conducted on the FCG to date that allows the nature of the REE enrichment to be assessed and categorised.

1.2 Research Purpose and Objectives

The purpose of this thesis is to undertake a detailed field, petrological and geochemical study of the French Creek Granite in order to better understand the type, style and location of potential REE mineralisation. This includes: 1) determining field relationships; 2) analysing the mineralogy of the French Creek Granite and dykes, and describing and assessing hydrothermal alteration; 3) analysing the REE geochemistry, quantifying the REE mineralisation, and evaluating the relationship of REE enrichment to these units; 4) determining the REE petrogenesis and the relationship between magmatism, hydrothermal activity and REE mineralisation; and 5) identifying zones of REE enrichment.

1.3 Questions to be addressed in this thesis

The following table has key questions that this thesis will address, which reflect the aims and objectives set out above:

Table 1. Questions addressed by this thesis and the methods used to solve them.

1. Determine the field relationships
What are the field relationships between the French Creek Granite, the Hohonu Dyke Swarm and the hydrothermal alteration?
Solve by: field mapping and sample collection
2. Analyse the mineralogy
What is the primary mineralogy of the French Creek Granite and the cross-cutting Hohonu Dyke Swarm? How does this relate to the secondary mineralogy observed in hydrothermally altered samples? Which primary and secondary minerals have the REEs partitioned into?
Solve with: optical microscopy, XRF, ICP-MS/AES, XRD and the SEM
3. Analyse the geochemistry and evaluate REE enrichment
What is the geochemistry of the rare earth minerals? What other minerals have the REEs partitioned into? Which REEs are present and what differences in REE content are observed between the French Creek Granite, its hydrothermal alteration and the Hohonu Dyke Swarm?
Solve with: the SEM, LA-ICP-MS, XRF and ICP-MS/AES
4. Determine petrogenetic processes involved in the REE mineralisation
What primary and secondary petrogenetic processes were involved in the REE mineralisation? What was the source of the hydrothermal fluid and how important was the hydrothermal circulation for the remobilisation of REEs? Were fluoride and chloride important components of the fluid?
Solve with: optical microscopy, stable isotopes, ICP-MS/AES, XRF, LA-ICP-MS, CL and literature review
5. Identify zones of REE enrichment
Where has the REE mineralisation occurred, if at all? Are there localities with consistent REE anomalies?
Solve by: collating XRF and ICP-MS/AES with GIS

Chapter 2: Background

2.1 Rare Earth Elements

Rare earth elements (REEs) are a series of 15 inner transition metals on the periodic table, known as the lanthanides. In order of increasing atomic number and decreasing atomic size, they are comprised of lanthanum (La), cerium (Ce), praseodymium (Pr), neodymium (Nd), promethium (Pm), samarium (Sm), europium (Eu), gadolinium (Gd), terbium (Tb), dysprosium (Dy), holmium (Ho), erbium (Er), thulium (Tm), ytterbium (Yb) and lutetium (Lu). They are commonly separated into light REEs (LREEs), from La to Sm, and heavy REEs (HREEs), from Eu to Lu. Because yttrium (Y) behaves like a HREE, it is often included as a REE. Promethium is a product of radioactive decay and is therefore negligible in natural minerals. The abundance of REEs in the crust, especially Ce, La and Nd (Fig. 1), is higher than for gold, mercury or the platinum group metals, and LREEs are up to 200 times more abundant than HREEs (Henderson 1996; Wall 2014).

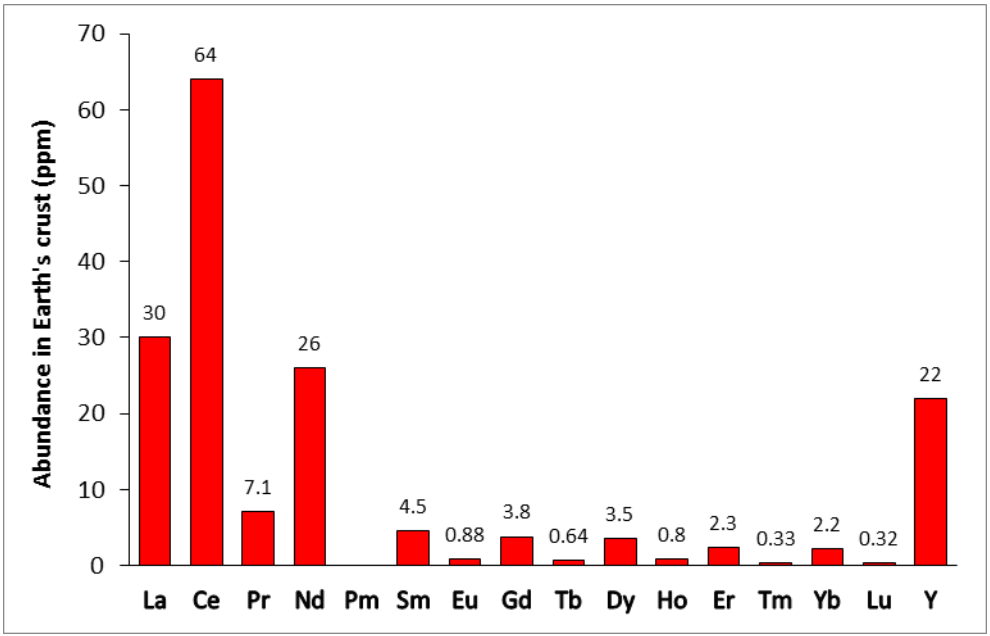

Figure 1. The abundance of rare earth elements in the crust (in ppm). Reproduced from Wall (2014).

Rare earth elements are generally only stable as oxides, not metals, and are normally trivalent, except for Ce^{4+}, which forms in oxidising aqueous systems, and Eu^{2+}, Sm^{2+} and Yb^{2+}, which occur only under reducing conditions (Henderson 1996;

Wood 1990a). Fractionation can also occur within the series (Winer 2011); for example, in reducing environments, Eu^{2+} fractionates from the other REEs and substitutes for Ca^{2+} in feldspar, producing the common negative Eu anomaly in silicate melts after plagioclase removal (Henderson 1996; Wall 2014; Winter 2011). The similarities in ionic size and coordination numbers between light RE^{3+} ions and Ca^{2+}, Na^{+} or Th^{4+} ions commonly leads to substitution between them. The same substitution can occur between U^{4+} and heavy RE^{3+} or Y^{3+} ions (Miyawaki & Nakai 1996), which are smaller due to the lanthanide contraction. Because of their large atomic size and charge, all REEs (except Eu) cannot easily substitute as cations into common silicate minerals, making them incompatible elements that concentrate in the residual melt during fractional crystallisation. However, minerals with larger cation sites such as zircon, apatite, garnet, epidote, titanite, rutile and fluorite allow minor substitution (Bea 1996; Henderson 1996). Amphiboles and clinopyroxenes can sometime contain significant REE+Y, while feldspars can contain low quantities of LREEs (Bea 1996). Partitioning of REEs into minerals depends not only on their size and charge, but also on the pressure, temperature and composition of the system (Henderson 1996).

2.1.1 Rare Earth (RE) Minerals

There are >200 RE minerals in which REE+Y form essential constituents (Bayliss & Levinson 1988; Levinson 1966), including silicates, oxides, phosphates, carbonates, fluorcarbonates and halides (Miyawaki & Nakai 1996). However, many of these, as the name suggests, are rare (Henderson 1996; Wall 2014). The majority of the world's REE supply comes from a minority of RE minerals (Table 2), of which the most abundant are bastnäsite, parisite, monazite, xenotime, loparite and Al-clays (i.e. kaolinite and halloysite; Chakhmouradian & Wall 2012). They can also be complex; with a single crystal containing >1 RE mineral. Light RE minerals commonly end with the suffix-(Ce), but will usually also contain considerable La, Nd and Pr, while heavy RE minerals are more scarce and usually end with the suffix-(Y), due to the higher relative abundance of these REEs when compared to the others (Fig. 1). The most widespread light RE minerals are the phosphate monazite-(Ce) and the economically important fluorcarbonate bastnäsite group minerals, which include

bastnäsite-(Ce), parisite-(Ce) and synchysite-(Ce). The most common heavy RE mineral is the phosphate xenotime-(Y) (Bea 1996; Christie et al. 1998; Wall 2014). Minerals with the perovskite structure, which are very diverse and abundant in the Earth, are important as a primary host of LREEs in alkalic rocks. Loparite is the REE-rich variety and commonly occurs in complex solid solution with other REE-free endmembers (Mitchell 1996).

Table 2. Some common rare earth minerals that occur in REE deposits, altered from Castor & Hedrick (2006). REO: rare earth oxide.

Mineral	Chemical formula	REO (wt. %)
Aeschynite	$(REE,Ca,Fe,Th)(Ti,Nb)_2(O,OH)_6$	36
Allanite	$(Ca,REE)_2(Al,Fe)_3(SiO_4)_3(OH)$	30
Anatase/Rutile/Brookite	TiO_2	3
Ancylite	$SrREE(CO_3)_2(OH)\cdot H_2O$	46
Bastnäsite	$REECO_3F$	76
Britholite	$(REE,Ca)_5(SiO_4,PO_4)_3(OH,F)$	62
Cerianite	$(Ce,Th)O_2$	81
Churchite	$YPO_4\cdot 2H_2O$	44
Euxenite	$(REE,Ca,U,Th)(Nb,Ta,Ti)_2O_6$	<40
Fergusonite	$(Y,REE)(Nb,Ti)O_4$	47
Florencite	$REEAl_3(PO_4)_2(OH)_6$	32
Gadolinite	$REEFeBe_2Si_2O_{10}$	52
Huanghoite	$BaREE(CO_3)_2F$	38
Kainosite	$Ca_2(Y,REE)_2Si_4O_{12}CO_3\cdot H_2O$	38
Loparite	$(REE,Na,Ca,Sr)(Ti,Nb)O_3$	36
Monazite	$(REE,Th)PO_4$	71
Mosandrite	$(Ca,Na,REE)_{12}(Ti,Zr)_2Si_7O_{31}H_6F_4$	<65
Parisite	$CaREE_2(CO_3)_3F_2$	64
Samarskite	$(REE,U,Fe)_3(Nb,Ta,Ti)_5O_{16}$	12
Synchysite	$CaREE(CO_3)_2F_2$	51
Xenotime	YPO_4	61

2.1.2 Rare Earth Element Deposits and Uses

The main hosts of REE deposits are alkaline igneous complexes (often peralkaline types) and carbonatites, which are typically also enriched further by hydrothermal processes (Chakhmouradian & Zaitsev 2012). Deposits from alkaline igneous complexes tend to have higher HREE mineralisation and tonnage, but have a lower grade, than deposits from carbonatites (Wall 2014). Secondary REE deposits, such as placer, laterite or ion-adsorption deposits also exist, in which more resistant rare

earth minerals (often xenotime and monazite) can be concentrated as the more soluble minerals (often carbonates) are altered, leached, weathered-out or adsorbed onto clay minerals (Chakhmouradian & Wall 2012; Henderson 1996; Wall 2014).

Rare earth element deposits occur in a wide variety of tectonic settings (Fig. 2). The world's largest REE supply (almost 50%) comes from the Bayan Obo altered carbonatite-hosted deposit in Inner Mongolia, China, where the main ore minerals are bastnäsite and monazite. The other major REE reserves in the world are in Russia, Greenland, Canada, Australia and California (USA) as well as numerous smaller deposits scattered around the world (Wall 2014).

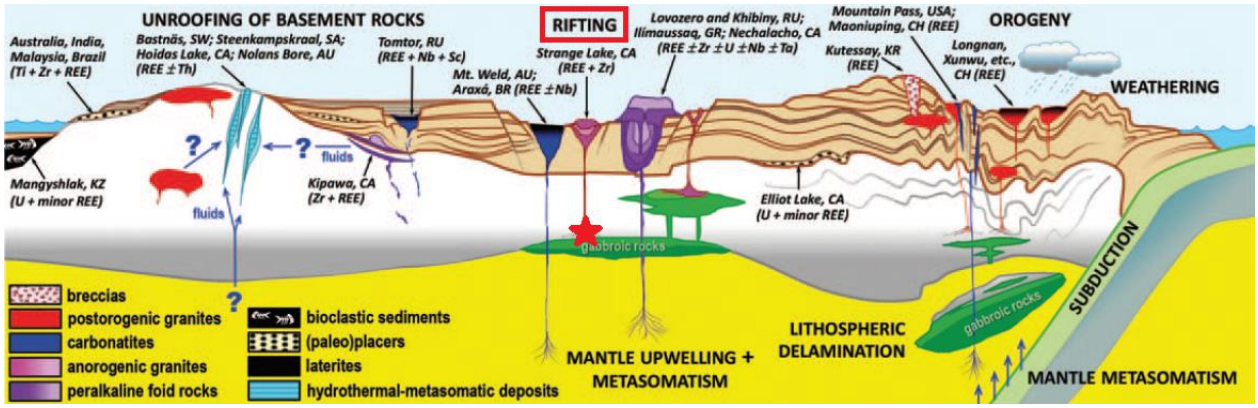

Figure 2. The tectonic setting of major REE deposits, altered from Chakhmouradian & Wall (2012). The French Creek Granite fits into the rift setting shown in the centre of the image (red box), where the Strange Lake Zr-REE-Y-Nb deposit is also located (red star).

The REEs have high melting points and useful electromagnetic properties. This makes them valuable in many technological and clean energy applications, particularly for enhancing energy efficiency in high-tech equipment. Examples include the use of Nd in wind turbine magnets, Ce in catalytic converters, and La in batteries for hybrid cars and for cracking hydrocarbons. Other applications of REEs are in low-energy light bulbs, magnets, cell phones, TVs, computers, high-temperature super conductors, specialist alloys and ceramics (Wall 2014). These useful applications led to the U.S. Department of Energy (2011) classifying Nd, Eu, Dy, Tb and Y as critical elements for energy technologies in the short- to medium-term (Wall 2014).

2.1.3 Rare Earth Elements in Carbonatites

Carbonatites are a primary source of REEs (see Section 2.1.2) and are frequently found in close spatial and temporal association with alkaline igneous complexes.

Carbonatites are igneous rocks composed of >50% primary carbonate minerals (generally calcite, dolomite or ankerite) with <20% SiO_2, and carbonatite intrusions are typically associated with fenitisation of the host rock, leading to an assemblage of sodic amphiboles, scapolite, Fe-Ti oxides and phosphate minerals. The REEs found in carbonatites are initially derived from partial melting of the upper mantle (Pecora 1956), where REEs are incorporated primarily within Ti-oxides, such as loparite. A carbonatite melt then separates from silicate magma through liquid immiscibility, and fractional crystallisation of this melt in the crust concentrates the REEs, in particular the LREEs. The most common rare earth minerals in carbonatites are carbonates (bastnäsite group minerals), phosphates (monazite and apatite) and oxides (perovskite and pyrochlore). However, the major rock-forming minerals of carbonatites, such as calcite, dolomite, amphibole and apatite, can also contain significant REEs (Chakhmouradian & Zaitsev 2012; Wyllie et al. 1996).

There is much controversy around what is, or is not, a carbonatite (Turner 2015) and it can be very difficult to distinguish between magmatic carbonatite intrusions and carbonate veins (Wyllie et al. 1996). Carbonatites derived from low-temperature hydrothermal fluids associated with high CO_2-H_2O magmas are typically those enriched in REEs (Turner 2015; Wyllie et al. 1996). Carbon and oxygen stable isotopes can help distinguish carbonatites from carbonate veins, with typical $\delta^{13}C$ values ranging from -2 to -8‰ and $\delta^{18}O$ values between 5 and 25‰. These ranges can, however, be affected by near-surface processes, such as hydrothermal circulation, and by the carbonate mineralogy (Turner 2015).

There are two occurrences of carbonatites currently documented in New Zealand, both associated with lamprophyre dykes, and the local HDS also contains lamprophyric varieties. The first are related to Jurassic–Early Cretaceous dykes of the alkaline Tapuaenuku Igneous Complex (mentioned further in Section 2.3.1) in the Inland Kaikoura Range, North Canterbury (Turner 2015), and the second are associated with Late Oligocene–Early Miocene intrusions of the Alpine Dyke Swarm in the Haast-Otago region (Christie et al. 1998; Cooper 1971; Cooper & Paterson 2008). The latter has already been identified as a prospective carbonatite-hosted REE resource for New Zealand (Christie et al. 2010).

2.1.4 Aqueous Geochemistry in Hydrothermal Systems

Hydrothermal REE-mineralising fluids are sourced from carbonatite, granitic or mantle melts (Gieré 1996). For example, the high heat flow associated with the emplacement of an alkaline intrusion can result in a convective hydrothermal system forming above the intrusion, leading to a zoned alteration assemblage that reflects the chemical- and temperature-gradients of the fluids. Hydrothermal systems are especially common in the extensive fracture systems that form in the brittle crust above relatively shallow plutons and, based on stable isotope compositions of the fluids, are commonly dominated by meteoric water rather than magmatic fluids (Winter 2011). There are a number of rare earth minerals that have frequently been reported in hydrothermally altered rocks, and REE-bearing apatite, fluorite or even calcite commonly form important gangue minerals (Gieré 1996).

In the past, REEs were considered immobile elements; however, more recent studies have demonstrated that they can be highly mobile under certain conditions, and therefore, can concentrate to exploitable levels during hydrothermal processes (Williams-Jones et al. 2012). The larger ionic radii of the LREEs means they are less compatible than HREEs (Hanchar & van Westrenen 2007) and thus they are particularly mobile (Bowden 1985). They are commonly preferentially enriched in the first melt fraction during low degrees of partial melting, or during water-rock reactions, in which the LREEs (+ Eu) will always favour the liquid component (Bowden & Kinnaird 1984; Winter 2011).

Fluid-rock interaction can lead to leaching, transport and redeposition of the REEs. The behaviour of the REEs, Ti, Zr, Th and U are similar during transportation and redeposition processes, therefore they frequently occur together in such deposits. The occurrence and concentration of REEs in hydrothermal fluids are primarily controlled by the pH, redox conditions (Eh), temperature, pressure and composition of the fluids. In acidic hydrothermal fluids, free rare earth ions are stable and are also complexed by sulphates or reduced sulphur species (H_2S, HS^- or S^{2-}), while in slightly acidic to slightly basic conditions fluoride, and to lesser extents hydroxide, complexes become more important. Above near-neutral pH (>5-6), carbonate complexes predominate under a wide range of conditions, especially at

lower temperature (Bau 1991; Gieré 1996; Wood 1990a, 1990b). Fractionation of REEs can also occur under all pH conditions, because LREEs and HREEs can be complexed by different ligands in the same fluid (Bau 1991; Gieré 1996). High-temperature saline solutions from ancient magmatic-hydrothermal systems have been found to contain the highest total REEs (up to 1290 ppm), indicating their importance in the transportation of large quantities of REEs (Gieré 1996).

Rare earth elements become more stable at higher temperatures and lower pressures, and they strongly favour participation in aqueous complexes with ligands such as F^-, Cl^-, CO_3^{2-}, OH^-, SO_4^{2-} and PO_4^{3-}. In hydrothermal systems, fluorides and carbonates are likely to be the main agents involved in the mobility of REEs (Gieré 1996; Wood 1990a, 1990b). One of the more important complexing groups in residual magmas and aqueous systems are the halides, especially fluorine because it forms strong bonds with trivalent REEs, while bonds with chloride complexes are weaker. This is especially important within all A-type granitoids, which are typically already enriched in these components (Bowden 1985; Henderson 1996). Speciation of REEs in hydrothermal fluids is therefore strongly controlled not only by the pH and concentration of REEs in the fluid, but also by the relative abundance of these ligands (Gieré 1996; Wood 1990a). Other important controls include the fluid/rock ratio, sorption processes, partition coefficients, reaction kinetics and residence time (Bau 1991; Henderson 1996; Lottermoser 1992).

The precipitation of base metal sulphides can have a direct effect on the deposition of rare earth minerals. In acidic hydrothermal systems under reduced conditions, the crystallisation of sulphide minerals can decrease the sulphide activity in the fluid, and breakdown and transport neutral REE-sulphide complexes, which recrystallise into new REE-bearing phases. Alternatively, chloride-rich hydrothermal fluids carrying ore-forming elements (e.g., Fe, Zn, Pb or Cu) as metal-chloride solutes can react with H_2S-rich fluids to precipitate sulphide minerals such as pyrite, chalcopyrite, galena and sphalerite. This liberates H^+ (or HCl), decreases the pH of the fluid and leads to REE transportation and redeposition. Similarly, this induced breakdown, transportation and redeposition of REEs also occurs in fluoride- or carbonate-rich fluids, for example, during crystallisation of fluorapatite or calcite/dolomite, respectively (Gieré 1993, 1996).

The major processes that can trigger precipitation of rare earth minerals in hydrothermal systems are summarised by Gieré (1996) and include:

1. A temperature decrease as the fluid migrates away from its source.
2. A decrease in confining pressure, such as when the fluid enters cavities or fractures (McLennan & Taylor 1979).
3. Volatile loss (e.g., CO_2 or H_2S), as a result of boiling or a pressure decrease.
4. Mixing and/or dilution between a REE-rich fluid and another fluid.
5. Fluid-wall rock reactions leading to changes in the pH, Eh or salinity of the fluid (Gieré 1990).
6. Precipitation of gangue minerals which reduce the activities of strong ligands and break down aqueous REE complexes (Gieré 1990).

2.2 A-Type Granitoids

Anorogenic (A)-type granites incorporate a wide variety of compositions, and as such, there is some ambiguity in their classification. The general consensus is that A-type granites are emplaced into either within-plate anorogenic settings (Fig. 3a) or in the final stages of an orogenic event (i.e. post-orogenic; Fig. 3b). In both instances, the tectonic setting is extensional and commonly results in anhydrous, alkaline magmas (Bowden 1985; Collins et al. 1982; Eby 1990; Whalen et al. 1987). Magma generation in these settings results from decompression melting and high heat flow associated with asthenospheric upwelling. Initial magmas are mafic in composition, derived from partial melting of the mantle, and are emplaced into the lower crust. Alkaline magmas typically ascend along localised vertical conduits to form small plugs in the upper crust (Winter 2011) and their location is generally controlled by pre-existing weaknesses in the lithosphere (Black et al. 1985; Bonin 1990). The A-type granites can be further subdivided according to their source: the A_1 group have an OIB-type signature, are generated in active continental rifts or within-plate settings, and tapped an enriched-mantle reservoir, while the A_2 group have element ratios characteristic of continental crust to island-arc basalts (Eby 1992; Winter 2011). There are a number of petrogenetic models for melt generation that ultimately lead to A-type granite magmatism: 1) fractional crystallisation from a mantle-derived magma (Bonin & Giret 1990; Turner et al. 1992); 2) partial melting of lower crustal

rocks (Collins et al. 1992; Creaser et al. 1991; Martin 2006); and 3) a mixture of these where the magmas have both a mantle and crustal origin (Eby 1990, 1992).

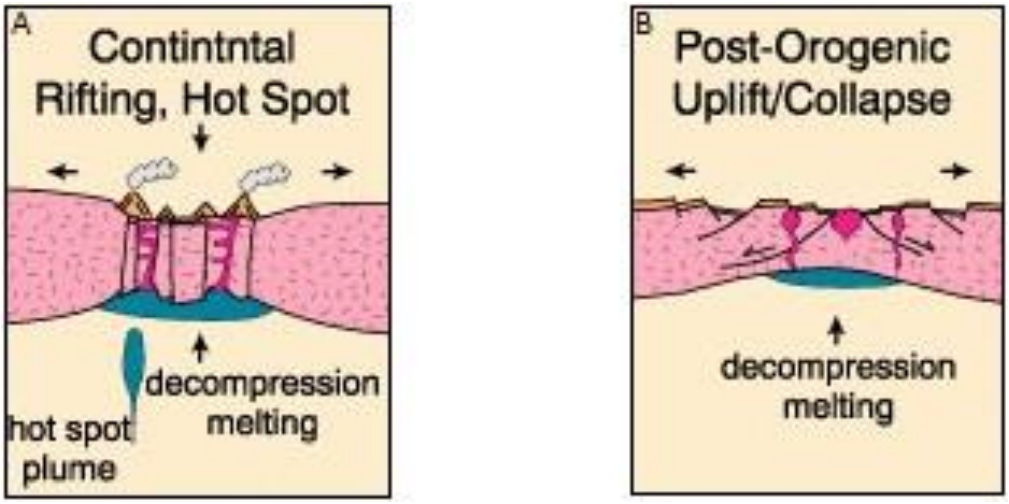

Figure 3. The tectonic settings of A-type granites, taken from Winter (2011), illustrating (A) emplacement into an anorogenic setting where melting is associated with a hot spot and/or the adiabatic ascent of the mantle; and (B) emplacement into a transitional tectonic setting with melting as a result of both crustal and mantle heat.

Alumina saturation, expressed as the alumina saturation index (ASI), the ratio of molar Al_2O_3 to molar K_2O, Na_2O and CaO, determines whether an alkaline A-type granite is peraluminous, metaluminous or peralkaline, and which minerals and REE-rich accessory phases will be present (Bea 1996; Bowden 1985). Alkaline rocks normally have excess alkalis, which are taken up by other alkali-rich phases such as feldspathoids, alkali amphiboles and/or sodic pyroxenes (Winter 2011). If the residual fluid phase is retained, the rock can evolve to give a peralkaline geochemistry with arfvedsonite and aegirine present. In contrast, if the residual fluids are exsolved, peraluminous biotite granites develop instead (Bowden 1985). Additionally, the degree of alkalinity and silica saturation is mainly controlled by the age and thickness of the lithosphere they intrude. Because A-type suites often coincide with the end of an orogenic cycle, Whalen et al. (1987) suggest that the source of A-type granites is likely to be the product of partial melting of an anhydrous, granulitic residue enriched in F and/or Cl that remained in the lower crust after orogenic magmas were removed.

A-type granitoids are chemically characterised by enrichment in SiO_2, K_2O, Na_2O and high-field-strength elements (HFSEs) – such as REEs, Y, Zr, Nb, Ta, U, and Th – and depletion in CaO and Sr. They also have high Fe/Mg, Rb/Sr and Ga/Al,

higher F and Cl content, and lower H_2O content (i.e. they are anhydrous magmas). The mafic minerals usually crystallise late and show evidence of the Fe-rich nature, with the common appearance of Fe-rich amphibole (ferrohastingsite), biotite (annite), pyroxene (ferrohedenbergite) and/or olivine (fayalite). In peralkaline A-types, sodic amphiboles (arfvedsonite and riebeckite) and/or pyroxenes (aegirine) are common (Anderson & Thomas 1985; Collins et al. 1982; Eby 1990; Frost et al. 2001; Whalen et al. 1987). Silica-oversaturated A-type granites tend to form quartz syenites and granites with abundant euhedral quartz, perthitic K-feldspar and graphic and/or granophyric intergrowths (Bonin 1990; Eby 1990; Whalen et al. 1987).

The reason A-type granitoids are typically enriched in REEs is a function of both the geochemistry of the magma and the processes by which the magma was generated. The high heat flow associated with the generation of A-type magmas increases the solubility of REE-Zr-rich accessory minerals such as apatite and zircon, which partition into the melt fraction during partial melting. High alkalinity and the presence of F and Cl increase these effects further (Creaser et al. 1991). The REEs are then concentrated by fractional crystallisation or by juvenile fluids, especially those rich in F^-, Cl^- or CO_3^{2-}, released during cooling and crystallisation of the alkaline rocks (Bowden 1985; Christie et al. 1998). Peralkaline granites commonly have the highest LREE (>230 ppm), HREEs (>35 ppm), Zr (>500 ppm), Y (>60 ppm), Nb (>25 ppm), Zn (>100 ppm) and Th (>20 ppm) anomalies, combined with high Rb/Sr (>5), however, some peraluminous biotite granites can also contain substantial LREEs, Y, Th and Zn (Bea 1996; Bowden 1985).

Hypabyssal alkaline igneous suites are common in the shallow crust, especially at subvolcanic depths (1–4 km) where they occur as ring complexes forming the root systems of calderas and domes (Bonin 1990, 2007). An alkaline ring complex is comprised of numerous layers of different composition: the interior biotite granite is surrounded by arfvedsonite granite and fayalite granite, which is in turn surrounded by a shell of syenite (Fig. 4). Shallow intrusives include ring dykes, cone sheets, zoned hydrothermal facies, and granite and quartz porphyries, with volcanic and cataclastic rocks formed at the surface (Bowden 1985; Pirajno 2009). The silica-undersaturated version can also have associated carbonatites, and the abundance of REEs and other HFSEs are features that carbonatites, and granites and syenites from

alkaline ring complexes, have in common. Whether economic mineralisation occurs within an alkaline ring complex is dictated by the source of the magma reservoir, the composition and involvement of the crust, and the involvement of hydrothermal fluids (Bowden 1985).

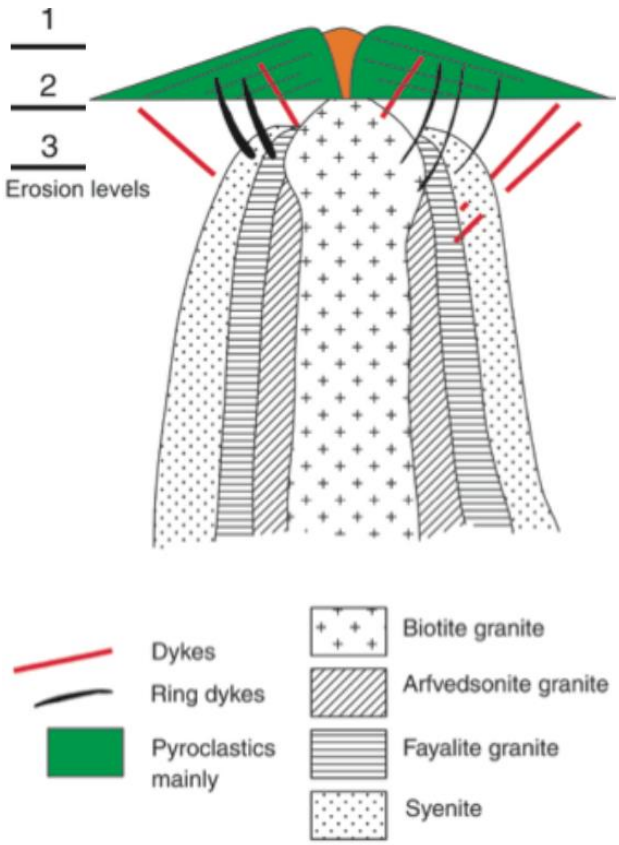

Figure 4. An idealised schematic cross-section of a silica-oversaturated alkaline ring complex, taken from Pirajno (2009).

2.3 Geological Setting

2.3.1 Regional Geological Background

New Zealand straddles the boundary between the Australian and Pacific plates and consists of various basement terranes (Fig. 5), offset by movement along the plate margin (Fig. 6a). These basement terranes are broadly divided into the Eastern and Western provinces and are separated by the Median Batholith: a series of intrusives that represent an active subduction zone that operated alongside the Gondwana supercontinent between 375–110 Ma (Bradshaw 1993; Mortimer 2004). The basement underlying the Greymouth area is the Buller Terrane (Fig. 5), which is characterised by a sequence of turbidites and shallow marine sediments of Ordovician–Early Devonian age and forms part of the Western Province (Cooper 1989; Cooper & Tulloch 1992). The tightly-folded Ordovician Greenland Group within

this terrane was metamorphosed to lower greenschist facies (Adams et al. 1975; Cooper 1989; Roser & Nathan 1997), forms the local country rock that the French Creek Granite (FCG) intrudes, and is also host to nearby gold lode mineralisation (Christie et al. 2006; Cooper 1989; Price & Ryland 2011). To the east of the Alpine Fault (Fig. 6b) is the Rakaia Subterrane; part of the Torlesse Terrane of the Eastern Province. These are younger, accreted turbidite sequences Permian–Triassic in age and increase in metamorphic grade towards the Alpine Fault, where they have been uplifted from depth (Nathan et al. 2002; Suggate & Waight 1999).

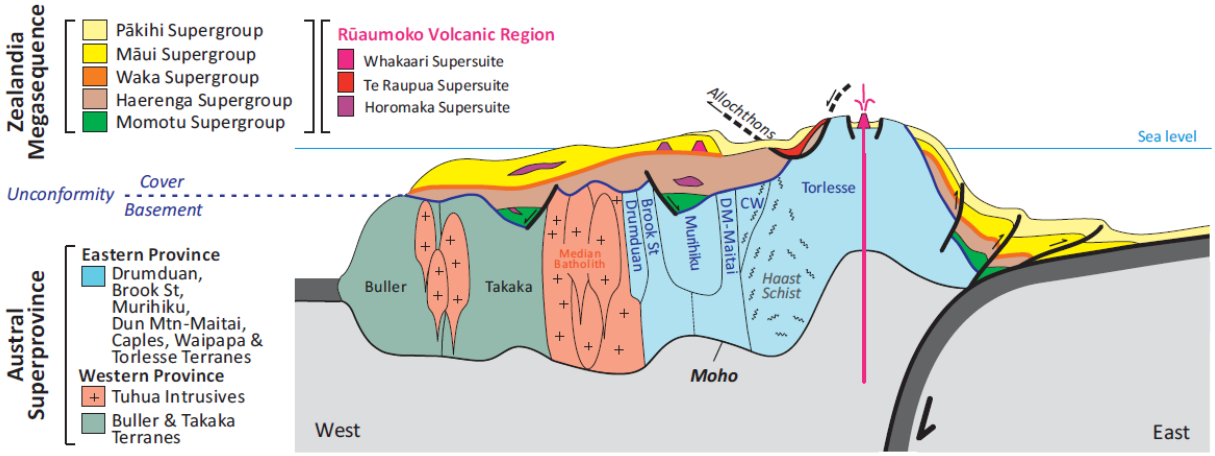

Figure 5. An idealised schematic cross-section (not to scale) illustrating the high-level stratigraphic framework across the plate boundary of New Zealand, taken from Mortimer et al. (2014).

The Buller Terrane originated alongside the palaeo-Pacific margin of Gondwana and has a complex history. Subduction along the palaeo-Pacific Gondwana margin during the Late Devonian–Early Carboniferous generated calc-alkaline S-type and I-type granitoids, of which the S-type Karamea Suite is volumetrically dominant (Cooper 1989; Cooper & Tulloch 1992; Muir et al. 1994; Tulloch 1983; Turnbull et al. 2016; Waight et al. 1997). Early Cretaceous subduction-related magmatism in response to thrusting of the Median Batholith beneath western New Zealand during terrane accretion resulted in the emplacement of the adakitic I-type Separation Point Suite (Muir et al. 1994). This magmatic pulse overlaps with, and was followed by, the higher-level intrusive, calc-alkaline, I- and S-type Rahu Suite at ca. 110 Ma (Cooper 1989; Muir et al. 1997; Tulloch 1983; Waight et al. 1997, 1998b). It locally incorporates the Hohonu Batholith (Fig. 6b; Tulloch 1988): a variety of silica-rich, I-type granitoids ranging in composition from granites and monzogranites to granodiorites and tonalites, which were emplaced 114–109 Ma and

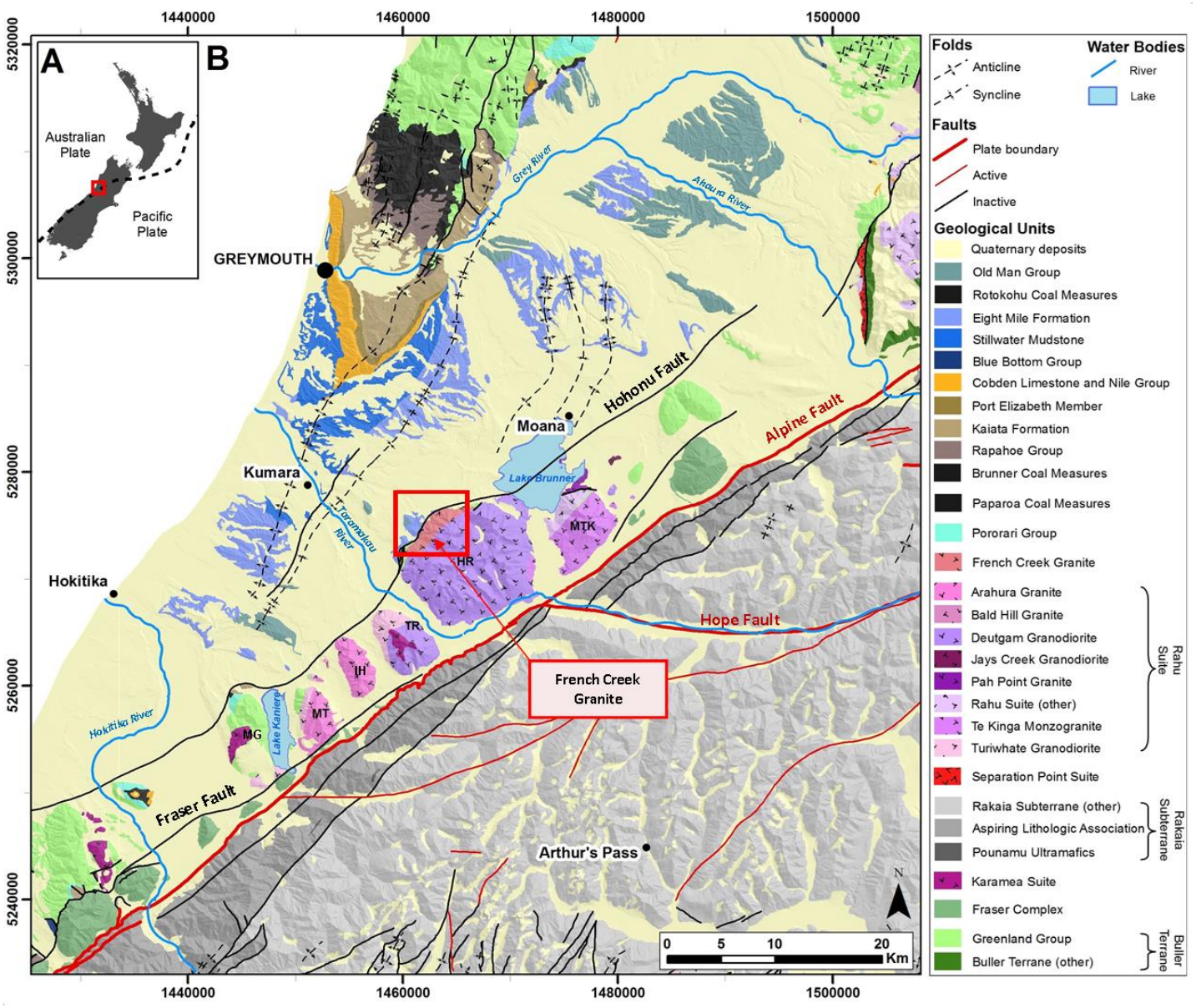

Figure 6. (A) Location of study area within the tectonic framework of New Zealand; and (B) regional geological units and structures surrounding the Hohonu Ranges (HR). These ranges are part of the Hohonu Batholith, the pink and purple units in between the Hohonu and Alpine faults. HR: Hohonu Ranges; MTK: Mt Te Kinga; TR: Turiwhate Ranges; IH: Island Hill; MT: Mt Tuhua; MG: Mt Graham. Spatial data are from Nathan et al. (2002).

record a transitional tectonic regime from subduction to extension (Mortimer 2004; Waight et al. 1997, 1998b, 1998c). Correlative Late Devonian–Early Cretaceous Rahu Suite granitoids occur further south in Fiordland and Stewart Island, and are separated 480 km dextrally by the Alpine Fault (Tulloch 1983).

Subduction along the Pacific margin of Gondwana ceased around 105 ± 5 Ma; the product of either partial subduction of a spreading ridge (Bradshaw 1989) or welding of the ridge to the Pacific Plate (Luyendyk 1995). This marked a transition from major crustal thickening to the initial phase of Gondwana breakup (Laird & Bradshaw 2004). Movement was facilitated along major low-angle detachment faults, leading to rapid unroofing and uplift of deep crustal rocks of the Paparoa Metamorphic Core Complex (Spell et al. 2000), as well as the widespread development of extensional half-graben basins. These basins were oriented WNW-ESE and were infilled with terrestrial syn-rift breccias and conglomerates of the Pororari Group (Fig. 6b; Bishop 1992; Laird 1994; Laird & Bradshaw 2004; Muir et al. 1997; Tulloch & Kimbrough 1989).

By 101 Ma, large-scale crustal extension was well underway, and rapid uplift and exhumation of buoyant Early Cretaceous granitoids had occurred. Alkaline-dominated intraplate magmatism marks the second phase of extension and the breakup between Antarctica and Australia-New Zealand (Laird 1994; Waight et al. 1998a); its source widespread throughout the region after 100 Ma (van der Meer et al. 2016). This phase of magmatism is expressed in the Eastern Province by the ca. 97 Ma Mandamus Igneous Complex (Tappenden 2003; Tulloch 1991; Weaver & Pankhurst 1991) and the 100–85 Ma Mt Somers Volcanics Group (Mortimer 2004; Tappenden 2003) in Canterbury; by the 100–96 Ma Tapuaenuku Igneous Complex (Baker et al. 1994; Laird & Bradshaw 2004) and the Blue Mountain Complex (Grapes 1975) near Kaikoura; by metamorphism and anorogenic magmatism between 102–95 Ma in Marie Byrd Land, West Antarctica (Storey et al. 1999; Weaver et al. 1994); and by large-scale uplift in southeast Australia (O'Sullivan et al. 1995).

The third phase of extension (Laird 1993; Waight et al. 1998a), and the separation of Zealandia from Australia (Fig. 7), is characterised by the alkaline ca. 88 Ma Whataroa Granite in south Westland (Tulloch et al. 2009) and the French Creek

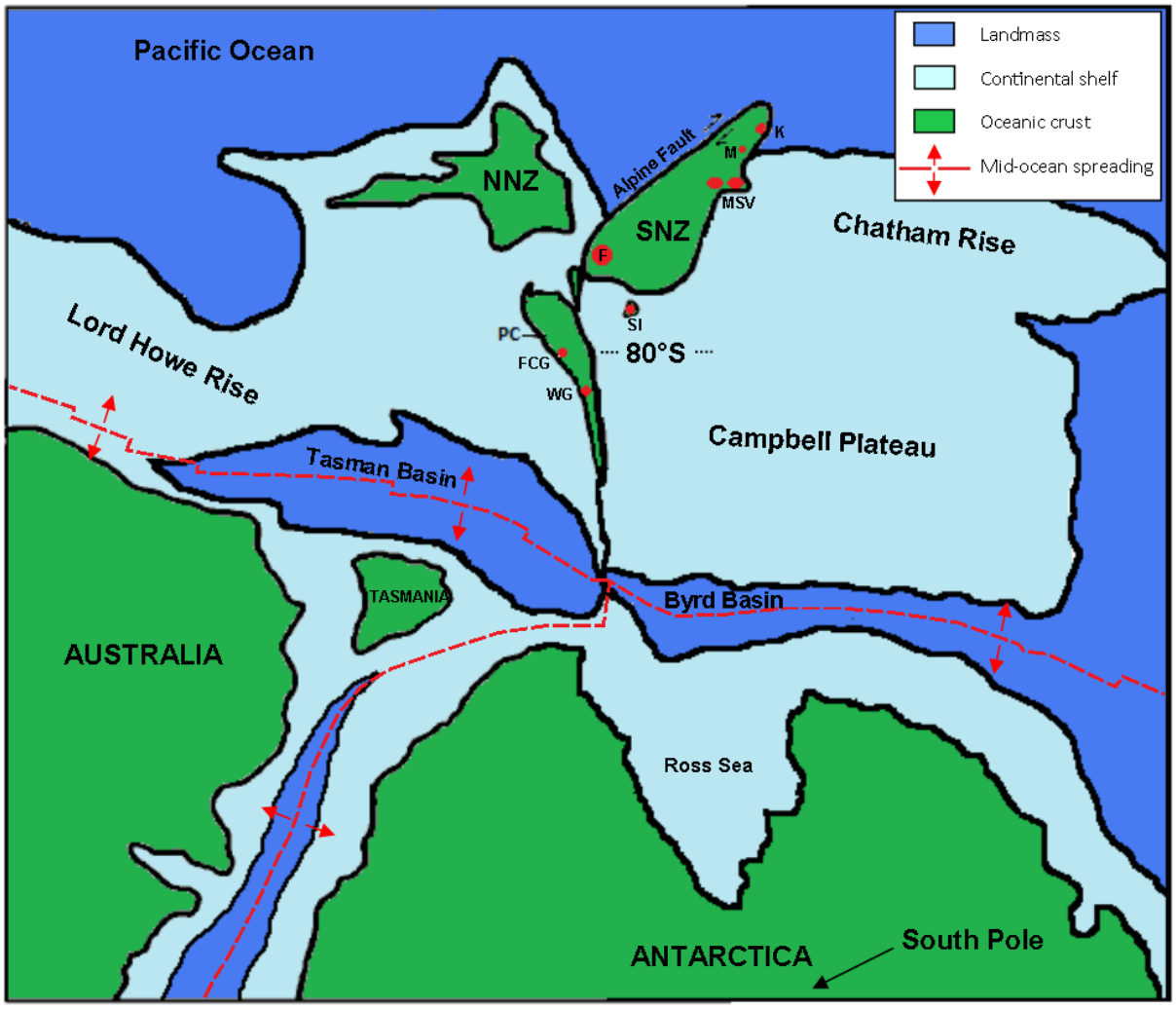

Figure 7. Gondwana reconstruction at ca. 82 Ma, adapted from Lawver et al. (1992), Tosolini & Pole (2010) and Tulloch & Kimbrough (1989). Rifting along the Tasman Basin eventually became the Tasman Sea, and the Byrd Basin became the Southern Ocean. NNZ: north New Zealand; SNZ: south New Zealand; F: Fiordland granitoids; FCG: French Creek Granite; K: Kaikoura granitoids (Tapuaenuku Igneous Complex and Blue Mountain Complex); M: Mandamus Igneous Complex; MSV: Mt Somers Volcanics Group; PC: Paparoa Metamorphic Core Complex; SI: Steward Island granitoids; and WG: Whataroa Granite.

Granite (81.7 ± 1.8 Ma U-Pb zircon ages; Waight et al. 1997) in the Hohonu Ranges. This indicates convective asthenospheric upwelling immediately prior to the formation of new oceanic crust and the onset of seafloor spreading in the Tasman Sea at ca. 84 Ma (Laird 1994; Laird & Bradshaw 2004; Waight et al. 1997; Weissel & Hayes 1977) and in the Southern Ocean at 83–79 Ma (Cande & Stock 2004; Larter et al. 2002). The emplacement of the shallow (ca. 3 km depth; Waight et al. 1997) ca. 82 Ma FCG into the mid-crustal (20–22 km depth) ca. 110 Ma Deutgam Granodiorite implies rapid uplift between ca. 114–82 Ma (Tulloch & Challis 2000; Waight et al. 1997). Additionally, an increase in A-type character between 112–82

Ma has been accredited by Tulloch et al. (2009) to decreasing crustal contamination as a result of progressive thinning of the lithosphere.

Common features in these extensional environments are alkalic dyke swarms, which have been documented in the Hohonu Ranges (Hamill 1972; Tulloch 1983; van der Meer et al. 2013, 2016; Wellman & Cooper 1971). The mafic Hohonu Dyke Swarm (HDS), cogenetic and contemporaneous with the FCG, is concentrated in the Hohonu Ranges and on nearby Mt Te Kinga (Fig. 6b; Waight 1995), and these form the youngest part of the Hohonu Batholith (Waight et al. 1998a). The dykes have a strong WNW-ESE structural trend, parallel with the opening direction of the Tasman Sea. Recent dating of these dyke swarms indicates three distinct magmatic pulses at about 102–100 Ma, 92–84 Ma and 72–68 Ma, respectively (van der Meer et al. 2016). The oldest swarm has a calc-alkaline composition related to the convergent margin of Gondwana, while the younger swarms have distinctly different chemistry that records the change to intraplate alkaline magmatism occurring prior to and during Tasman Sea spreading (van der Meer et al. 2016).

As New Zealand drifted away from Antarctica and Australia, the extensively thinned continental margin thermally subsided. By 80 Ma the landmass had been eroded to widespread lowlands where the Late Cretaceous non-marine Paparoa Coal Measures accumulated. At ca. 70 Ma, another pulse of alkalic basaltic volcanism occurred as part of the development of the New Zealand margin (Laird 1994). Tasman Sea spreading ended ca. 60 Ma (Laird 1994) and was followed by a period of relative tectonic quiescence and subsidence (Suggate & Waight 1999). The Waipounamu Erosion Surface, representing slow erosion and peneplanation during the Eocene (Nathan et al. 2002), marks the beginning of a widespread marine transgression and deposition of a passive margin sequence (Bradshaw 1989; Coates & Cox 2002; Laird & Bradshaw 2004). This is observed in the Greymouth region (Fig. 6b) with the Brunner Coal Measures infilling extensional sedimentary basins (Bishop 1992), followed by Eocene–Oligocene sandstones (Rapahoe Group), mudstones (Kaiata Formation and Port Elizabeth Member) and limestones (Cobden Limestone and Nile Group) (Nathan et al. 2002). The Oligocene limestones represent the maximum inundation and near-drowning of Zealandia, which abruptly ended with

the onset of the Kaikoura Orogeny ca. 25 Ma (Coates & Cox 2002). This was the birth of a new plate boundary, which today is represented in the South Island by the transpressive Alpine Fault and its northern splays. The products of this orogeny in the Greymouth area include folding (Suggate & Waight 1999); faulting (Nathan et al. 1986) and uplifted NE-SW trending blocks comprising Paleozoic and Mesozoic granitoids, Fraser Complex gneisses (Kimbrough et al. 1994) and Buller Terrane metasediments; and uplift of the metamorphosed Torlesse Terrane to form the Southern Alps in the east of the map area.

The renewed compressional regime led to uplift and erosion: the source of the siliciclastic sediments that were transported down fluvial systems and progressively infilled shallowing basins during the Miocene–earliest Pleistocene with mudstones (Stillwater Mudstone), sandstones (Blue Bottom Group, Eight Mile Formation and Rotokohu Coal Measures) and recent gravels (Old Man Group). Early Pleistocene deformation of these units occurred during a period of regional tectonic compression (Suggate & Waight 1999). Throughout the Quaternary, climatic fluctuations resulted in extensive glaciation of the Southern Alps and modification of the landscape. The plains surrounding the Hohonu Batholith progressively built up with glacial till (Suggate 1985), fluvial gravels, colluvial deposits and coastal interglacial marine sediments (Nathan et al. 2002; Suggate & Waight 1999).

2.3.2 Local Geology

The French Creek Granite, first mapped by Bell & Fraser (1906) and originally named the Brunner Granite by Hamill (1972), outcrops on the northwest side of the Hohonu Ranges (Fig. 8), a steep and densely vegetated pluton. Here, the FCG forms a 2 x 7 km outcrop sliver on the hanging wall between the Deutgam Granodiorite and the Cenozoic Hohonu Fault (Suggate & Waight 1999). It intrudes Greenland Group metasediments to the northeast and southwest of its mapped extent and is juxtaposed to the Eight Mile Formation on the west by the southeast-dipping, reverse Hohonu Fault (Nathan et al. 2002). The contact relationship between the FCG with the Deutgam Granodiorite is intrusive, with reactivation caused by recent faulting (Suggate & Waight 1999; Waight 1995); however, much of this contact relationship, and the eastern extent of the FCG, which is further east than QMAP

places it (Geoff Price pers. Comm.), remains unmapped owing to dense vegetation cover, treacherous terrain or burial beneath recent gravels. The HDS locally intrudes the Greenland Group basement, Deutgam Granodiorite and to a lesser extent the FCG. Hypabyssal felsic dykes related to the FCG also exist and some of these aplitic and composite dykes cut the HDS, indicating complex contemporaneous mafic and felsic magmatism (Hamill 1972; Waight 1995). The mafic dykes, which are lamprophyric-doleritic to rare phonolitic-trachytic in composition, commonly have narrow chilled margins and contain granitic xenoliths; however, Waight (1995) observed no evidence of magma mingling. Dyke swarms were often emplacement along pre-existing joints in host rocks, are between 0.1–15 m wide and are often preferentially eroded out of the slopes (Waight 1995).

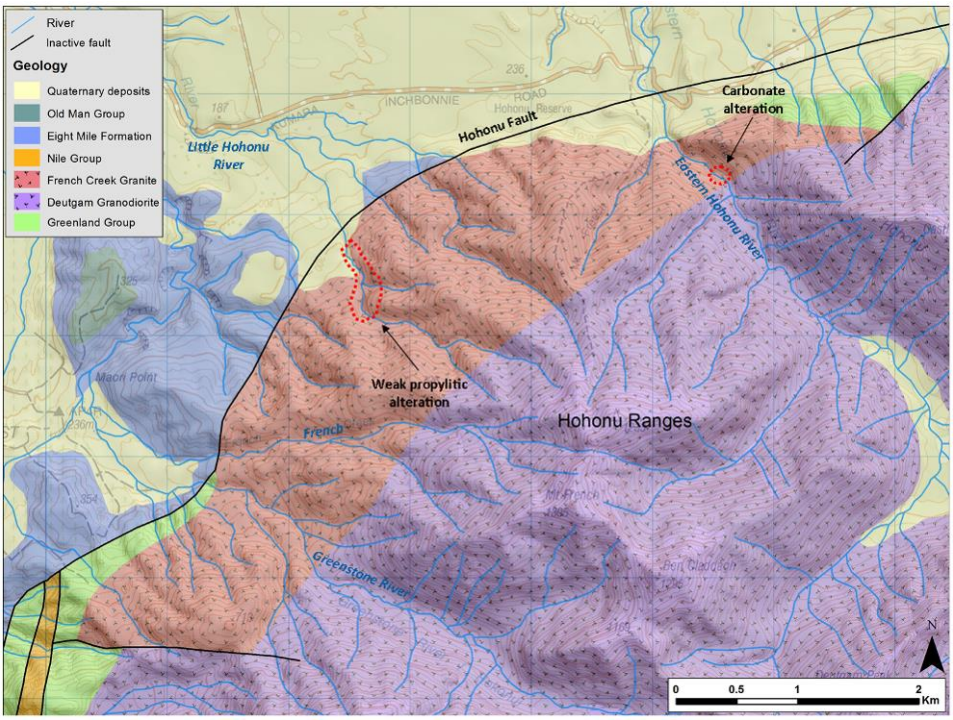

Figure 8. Map showing geological units, structures, hydrothermal alteration, local rivers, and the outcrop geometry of the French Creek Granite on the northwest margin of the Hohonu Ranges. Underlying spatial data are from Nathan et al. (2002).

The source of the FCG is inferred to be dominated by an asthenospheric component (isotopically primitive $^{87}Sr/^{86}Sr$ ratios of 0.707; Waight 1995) that tapped the enriched mantle, ponded in the previously-thinned crust at relatively high-levels, and underwent extensive fractionation of feldspar and mafic phases. It also contains a minor component of assimilated Greenland Group crust. The mafic HDS, although

from the same source, appears to have been emplaced directly to higher-levels, while the composite dykes represent continued mantle-activity in the magma chamber (Tulloch et al. 1994; Waight 1995).

The French Creek Granite is compositionally complex and is dominated by a red subsolvus biotite syenogranite, with subordinate varieties of hypersolvus amphibole monzogranite and quartz alkali-feldspar (QAF) syenite (Waight 1995). The subordinate varieties have only previously been found in the Eastern Hohonu River (Hamill 1972; Waight 1995) and possibly represent marginal phases associated with the crystallisation of distinct magma batches and/or fractionates (Waight 1995). Typical FCG has undergone hydrothermal alteration to minor kaolinite, hematite (resulting in its brick-red colour, Bradley 1977; Bradley et al. 1979) and sericite, and sub-millimetre to metre scale quartz and carbonate veins also cross-cut it. Two zones of more intense alteration have been documented in the past. The first is a zone of weak propylitic alteration (Brathwaite 2013) that extends for at least 500 m in the southern branch of the Little Hohonu River (LHR; Fig. 8). This alteration has previously been identified as the source of the panned concentrate samples with some of the most elevated REEs (Price 2013). A report by Brathwaite (2013) suggested this propylitic alteration lies on the periphery of a hydrothermal system; however, number and spacing of the five samples analysed were too small to indicate a vector towards a potential zone of higher rank mineralisation (Brathwaite 2013). The second is a 30 m wide zone of what has previously been termed 'calcitic' alteration in the Eastern Hohonu River (EHR) ~100 m before the contact with the Deutgam Granodiorite (Fig. 8). Numerous carbonate veins and an altered mafic dyke had been observed within this zone; it appeared alteration post-dated dyke emplacement and utilised the pre-existing weakness as a fluid conduit (Waight 1995). Similar carbonate alteration was found by Waight (1995) to cut other rocks proximal to the northwest margin of the Hohonu Batholith, and therefore is possibly related to fluids utilising the NE-SW trending Hohonu Fault.

2.4 Previous Exploration

A number of commercial mineral prospectors have held permits for the Hohonu Batholith, which includes intrusives of the Karamea Suite, Rahu Suite, FCG and HDS,

during the past few decades (Price & Ryland 2011). However, there has been no hard rock mining in the FCG area, only mining for alluvial gold. Mineral Report MR1303 produced by Carpentaria Exploration analysed 77 unpanned stream sediment samples for mesothermal greisen-hosted W, Mo, Sn and Bi (White & Price 2006), as well as other base metals. However, these returned no significant results and Carpentaria relinquished their permit (Painter 1972).

CanAlaska Ventures held the next permit (MR4376), following-up on Carpentaria's results, and precious, high-temperature and base metal mineralisation was found in quartz veins, pegmatites, and zones of faulting and alteration throughout the batholith. Their primary target was intrusion-related gold due to the common presence of quartz and disseminated sulphide minerals (pyrite ± chalcopyrite ± galena) in the Hohonu Ranges. They obtained 182 rock samples and 93 panned concentrate samples (White & Price 2006); those located on the northwest margin of the Hohonu Ranges are given in Fig. 9 for reference, as are samples from Waight (1995). Samples were analysed for 40 elements including Ce, La, Nb, Y and Zr (White & Price 2006). Their results have been incorporated into this study in order to spatially expand the interpretation of the FCG, especially in the hard-to-reach upper catchments.

Panned concentrate samples were generally much more enriched in Ce, La, Nb, Y and Zr than rock chip samples (Price & Ryland 2011), likely due to the accumulation of REE-bearing heavy minerals such as zircon and monazite. Some of the most elevated panned concentrate samples of gold and other metals were gathered on the flats just northeast of the FCG (Fig. 9); however, these anomalies were related to contamination within transported fluvioglacial gravels (White & Price 2006). Anomalous Ce, La, Nb, Y and Zr were discovered in all sampled streams draining the FCG (Little Hohonu River, Eastern Hohonu River, Greenstone River and French Creek), but also in streams draining the Deutgam Granodiorite and on other ranges of the Hohonu Batholith draining Rahu and Karamea suite intrusives and Greenland Group metasediments (Mt Te Kinga, Mt Graham, Mt Tuhua, Turiwhate Ranges and Island Hill; Fig. 6b). The report concluded complex differentiation and late-stage activity within the batholith, and that younger intrusions, such as the FCG

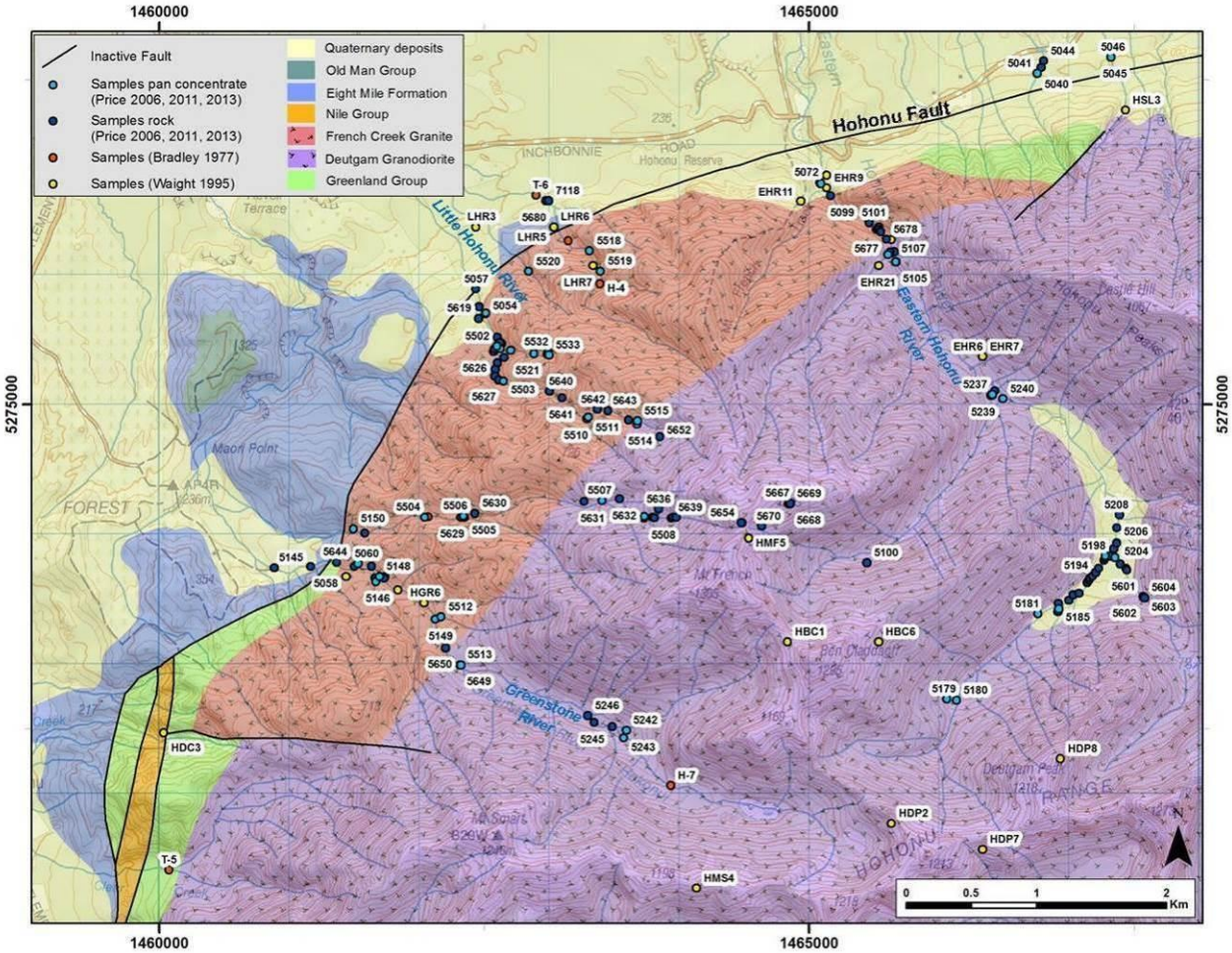

Figure 9. A compilation of previous samples in the area surrounding the French Creek Granite from Bradley (1977), Price (2013), Price & Ryland (2011), Waight (1995) and White & Price (2006). Underlying spatial data are from Nathan et al. (2002).

and HDS, are therefore more likely to contain metals in higher concentrations (White & Price 2006). Anomalous REEs have also been documented in hydrothermally altered rocks of the Paparoa Metamorphic Core Complex further north in the Paparoa Ranges, where fluids utilised fault systems to ascend (Christie et al. 1998), and the Hohonu Fault might have acted as a similar structure.

Price (2008) followed-up on the gold exploration reported in MR4376. In this report the Hohonu Batholith (Fig. 6b) was interpreted as an elongate dome: the central region, the Hohonu Ranges, has the highest elevation and therefore has likely also undergone the most erosion (Price 2008). Greenland Group country rock is still visible around some of the margins of the dome, where less erosion has taken place. The silicification and disseminated sulphides found throughout the Hohonu Ranges were inferred as central roots of a mineralised zone within the dome. The

report concluded that if there had been gold mineralisation in the Hohonu Ranges, it would have been at a higher level within the pluton and Greenland Group metasediments, and has since been eroded during Pleistocene glaciations: the likely source of the extensive alluvial gold within the surrounding Quaternary deposits. Recommendations for exploration around the margins of the batholith were made, especially toward the northeast of Lake Brunner (Price 2008).

Strategic Materials continued the previous exploration for gold, and were the first commercial operator to prospect for REEs in the area, which is summarised in report MR4886. Following anomalous samples of Ce, La, Nb and Y previously obtained by CanAlaska Ventures, Strategic Materials' priority targets for REE exploration were the alkaline FCG and HDS, due to the strong association between alkaline igneous complexes and enrichment in REEs and other precious metals (Price & Ryland 2011). They took an additional 16 panned concentrate samples and 72 rock samples (Fig. 9) and reanalysed CanAlaska Ventures' panned concentrate and rock samples, analysing for the complete suite of REEs, as well as Hf, Sn, Ta and Zr by ICP-MS/OES, while gold was analysed by fire assay. This provided confirmation of previously recognised anomalous REE targets, and led to the identification of new targets.

The FCG exhibited encouraging characteristics of REE mineralisation (i.e. elevated REEs, Nb, Y and Zr) and Strategic Elements Ltd (2011) subsequently classified the FCG as being "highly prospective" for REE-Nb mineralisation (Price 2013). The highest La+Ce+Y in panned concentrate samples was 4633 ppm (0.46%), while four rock samples contained >500 ppm total (Σ) REEs with a maximum of 957 ppm in a trachyte dyke (Strategic Elements Ltd 2011). The maximum values obtained for REEs-Nb-Y-Zr from FCG and HDS rock samples is given in Table 3. Anomalous REEs, F, Nb, P, U and Y have also been reported for the Deutgam Granodiorite (Price & Ryland 2011).

Table 3. Maximum values of REEs, Nb, Y and Zr obtained from FCG and HDS rock samples. Sample 5056 (quartz float with disseminated pyrite), 5642 (dolerite dyke), 5643 (pegmatitic quartz in FCG), 5674 (sheared FCG outcrop) and 5677 (FCG outcrop) from White & Price (2006), Price & Ryland (2011) and Price (2013)

Element	ppm	Sample
Ce	*260*	5677
La	*130*	5677
Nb	*165*	5643
Zr	*205*	5056
Y	*85*	5643
Dy	*15*	5643
Er	*10*	5643
Eu	*1.9*	5642
Gd	*14.5*	5674/5677

Element	ppm	Sample
Ho	*3.5*	5643
Lu	*2.1*	5643
Nd	*90*	5674/5677
Pr	*26*	5677
Sm	*17*	5677
Tb	*1.95*	5643
Tm	*1.75*	5643
Yb	*12*	5643

Work outlined in the next report (MR4955) by Strategic Materials lists the collection of an additional 30 panned concentrate samples and 69 rock samples. They were analysed by ICP-MS/AES, which highlighted additional REE anomalies in other branches of the LHR (Price 2013). This report focused on the results of a petrographic analysis undertaken by Brathwaite (2013) on five FCG samples taken from within the first 400 m of the FCG in the southern branch of the LHR (up to sample 5627, Fig. 9) where strongly anomalous REE-Zr-Nb-Hf-Th-Y panned concentrate samples (around sample 5502, Fig. 9) had been recovered [La (1055 ppm), Ce (1770 ppm), Nd (760 ppm), Zr (4465 ppm), Nb (1120 ppm), Hf (200 ppm), Th (1365 ppm) and Y (485 ppm); Price (2013)]. The petrographic analysis indicated varying degrees of hydrothermal alteration within the FCG, and depicted a zone of weak propylitic alteration near to where Bradley (1977) had previously located a zone of kaolinisation. The alteration assemblage was characterised by illite + chlorite ± calcite ± pyrite ± chalcopyrite, comparable to the extensive alteration surrounding the economic Strange Lake deposit in Canada (Brathwaite 2013). The primary target was the LHR, as well as the EHR (both described in Section 2.3.2), Greenstone River and French Creek (Price 2013).

Based on the geochemical assays, Strategic Materials identified 32 potential REE mineralisation targets within the permit area, the top three were in rivers draining the FCG and the fourth targeted the HDS. These were to be assessed in

more detail using results from the regional airborne geophysical survey (Price 2013). Initial evaluation of this geophysical data (MR5124) led to Strategic Materials reluctantly relinquishing their permit for the Hohonu area in 2014. This was based on: the 200 m spacing of geophysical data failing to define a high priority REE target; the potential contamination from fluvioglacial gravels in the panned concentrate samples; failing to locate consistent REE anomalies in rock samples; and the difficult terrain, which makes ground based prospecting very challenging (Murphy 2014).

Aeromagnetic and radiometric data for the northwest Hohonu Ranges are given in Fig. 10 and 11 (Vidanovich & Thomson Aviation Pty Ltd 2013). It was suggested that the stronger magnetic signatures might correspond to the alkaline rocks, within which REEs are expected to be more enriched. One such anomaly within the FCG was evaluated and downgraded based on Strategic Materials' geochemical assay results. It was advised that the radiometric signatures dominantly define secondary processes (i.e. alluvial, colluvial and regolith), and that no clear, high-priority anomalies of the kind anticipated for REE mineralisation were distinguishable during initial review of the dataset (Murphy 2014).

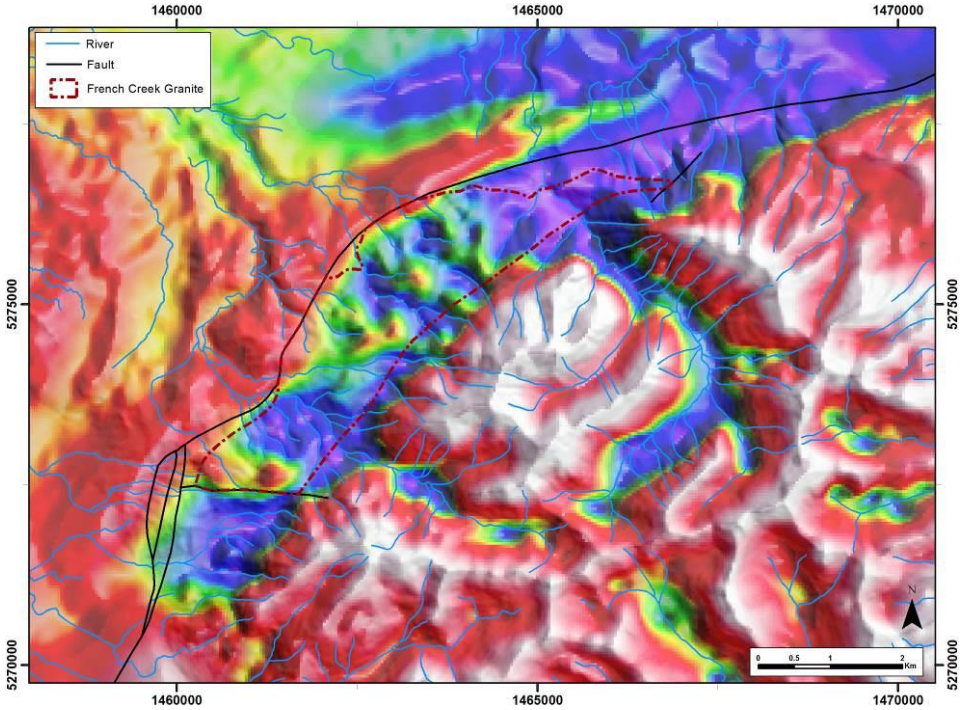

Figure 10. RGB image of the total magnetic intensity (nT) with reduced to the pole correction applied. Geophysical data are from Vidanovich & Thomson Aviation Pty Ltd (2013) and spatial data are from Nathan et al. (2002). The mapped extent of the FCG is outlined by the red dashed line. Note the eastern contact of the FCG appears further east than where QMAP places it.

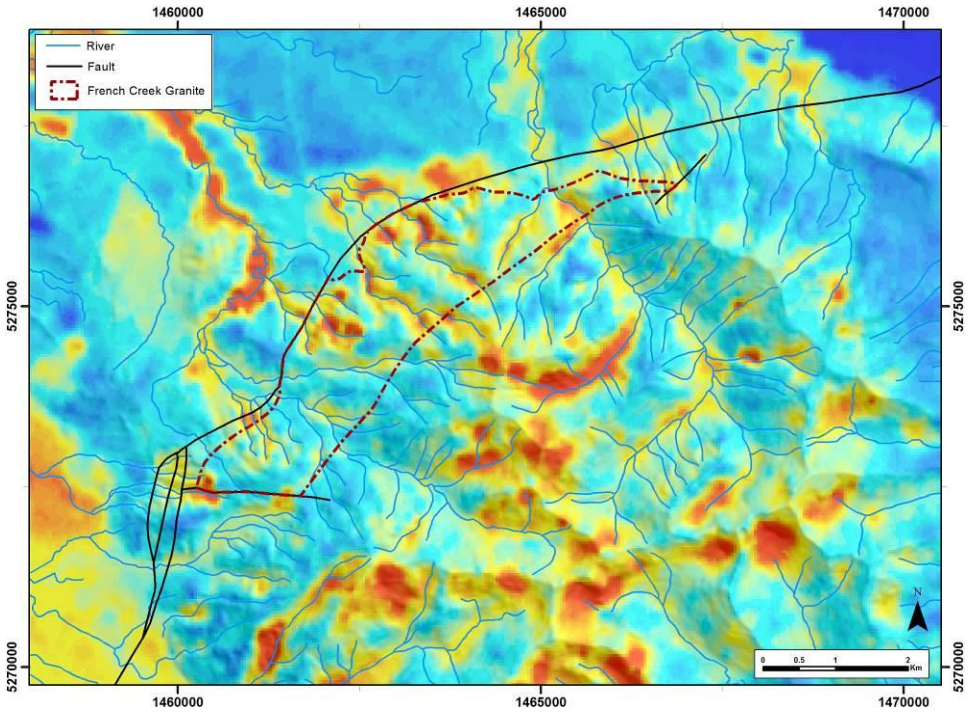

Figure 11. RGB image of the total radiometric flux (nGy/h). Geophysical data are from Vidanovich & Thomson Aviation Pty Ltd (2013) and spatial data are from Nathan et al. (2002). The mapped extent of the French Creek Granite is outlined by the red dashed line.

In the larger West Coast region, Christie et al. (2010) have identified a number of igneous and metamorphic rocks prospective for hosting REEs within monazite. These rocks include granitoids of the Karamea, Rahu and Separation Point suites, as well as the FCG and Paparoa Metamorphic Core Complex. Towards the north, major REE beach and alluvial placer deposits exist in the Westport, Barrytown and Grey River areas, with monazite, xenotime, thorite and uranothorite being the minerals of interest (Christie et al. 2010). Towards the south, a prospective carbonatite-hosted REE resource exists in Haast (Christie et al. 2010), which has been discussed in Section 2.1.3. To the east of the Alpine Fault, the Mandamus Igneous Complex has been the subject of interest as an alkaline intrusion similar to the FCG with the potential to host REE mineralisation (Strategic Elements Ltd 2011).

The above background information has been given in order to better understand REEs, common minerals they partition into, enrichment processes, the nature of REEs in A-type granites, the regional geological setting, and the exploration history of the FCG. This is vital background knowledge in order to begin to address the aims and objectives set out in Section 1.2 and important for understanding the methodology used to address the questions posed in Section 1.3.

Chapter 3: Methods

3.1 Sample Collection

Field work was conducted over two summer field seasons: one trip during December 2014 and two trips during December 2015. Samples were obtained from streams draining the FCG; both in situ samples and float samples from the river bed were collected. The three main branches of the LHR were explored until access became impossible on foot (i.e. impassable waterfalls and gorges). The entire FCG in the EHR was traversed when river flow rates were at their base level, which was when the nearby Arnold River at Moana had a flow rate of 50m^3/sec (The West Coast Regional Council 2011).

At each sample site, photographs, brief notes and the location were recorded. All sample locations were logged with a Trimble GeoExplorer 6000 Series GeoXH handheld unit that included a 2 m high antenna to increase satellite range. The Trimble GeoXH is equipped with a GNSS receiver, thereby having a positioning accuracy of 10 cm, and uses a minimum of five satellites. However, due to the dense vegetation and steep gorges it was difficult to obtain sufficient satellites for the Trimble GeoXH to locate itself at some sites. In these places, locations were recorded within ~20 m of the sample either by finding higher ground where a signal could be acquired, finding a less vegetated part of the river, or by using a Garmin GPSMAP 60CSx receiver instead, which has improved satellite reception in more difficult locations, although with lower accuracy. In a few locations no signal was obtained at all, and the distance was therefore estimated from the last known location. At these more difficult sites, field notes were taken and the sample re-located using ArcGIS.

3.2 Geographic Information System (GIS)

Spatial coordinate data from the Trimble GeoXH were uploaded into Pathfinder software for post-processing. This applied a differential correction by comparing data files against nearby public base stations. The one used, and the closest to the study area, was the Hokitika Airport base station. Once the Trimble GeoXH sample locations were corrected, and the Garmin GPSMAP 60CSx coordinates were

converted into New Zealand Geodetic Datum 2000 (NZGD2000) using the LINZ coordinate converter (Land Information New Zealand 2015), they were all exported into MS Excel and loaded into ArcGIS 10.2. In ArcMap, the XY coordinates were plotted as points on a map and overlain with a 1:50,000 topographic map sheet, rivers and place names (all from Land Information New Zealand 2016) and QMAP geological boundaries and structural data.

Petrological and geochemical information was later added to each point in order to discern spatial variability between sample locations and look for larger patterns and trends. When plotting maps of alteration intensity, float samples were omitted because they do not represent in situ rocks and are therefore useless in identifying trends. Eleven different rock varieties were identified based on colour, mineralogy, grain size, textures and alteration intensity.

Sample locations from earlier studies in the area (Bradley 1977; Price 2013; Price & Ryland 2011; Waight 1995; White & Price 2006) were also integrated (Fig. 9) in order to relate previous research to the current study. Sample locations from Waight (1995) were converted from Map Grid to NZGD2000 using the LINZ online conversion tool (Land Information New Zealand 2015); however, the Map Grid coordinates only have an accuracy of 100 m. Locations from Bradley (1977) were estimated from his base map. The spatial data from mineral exploration undertaken by Price (2013), Price & Ryland (2011) and White & Price (2006) in particular, were very beneficial in supplementing the current research by adding geochemical and petrological data in locations that were inaccessible during the course of this project.

Whole rock geochemical data of in situ rock chip samples from the current study and from the reports produced by Price (2013), Price & Ryland (2011) and White & Price (2006), were used to plot colour coded anomaly thresholds of nine different elements (Ce, Hf, La, Nb, Ta, Th, U, Y and Zr), which include the most abundant REEs (see Section 2.1) and their indicator elements, in order to show spatial distribution of the possible mineralisation. The anomaly thresholds are based on the mean and standard deviation of each of these nine elements:

1^{st} order: ≥ mean + 2 SD (pink)

2^{nd} order: ≥ mean + 1.5 SD to < mean + 2 SD (red)

3rd order: ≥ mean + 1 SD to < mean + 1.5 SD (yellow)

4th order: ≥ mean + 0.5 SD to < mean + 1 SD (green)

5th order: ≥ mean to < mean + 0.5 SD (blue)

Below mean (black)

3.3 Sample Preparation

Once samples were recovered from the field, each one was laid out, washed, cut, photographed and analysed using portable x-ray fluorescence (*p*XRF). After detailed descriptions were made, key samples were chosen based on mineralogy, textures and REE content, and were cut and/or powdered for further petrological and geochemical analyses. Please refer to Appx. A1 for a detailed description of these.

The whole rock powders in sample bags were given to the Geochemistry Lab at the University of Canterbury for XRF analysis, while the samples in the plastic vials were sent to ALS Geochemistry in Brisbane for analysis. A small amount of inherent contamination can be introduced from the ring mill hardware (Table A1), as part of the pulverising process (Rocklabs 2016). The majority of this contamination was considered to be insignificant, and those elements with high contamination were either not analysed (C and Co), or disregarded (W).

3.4 Petrology

3.4.1 Hand Sample Petrology

In addition to brief field descriptions of each sample at the macro- and mesoscopic scales, detailed hand sample descriptions were taken once each specimen had been prepared with a clean-cut surface. These included rock type; grain size; colour and colour index; identification of structures, textures (Taylor 2009; Thompson et al. 1996), and primary and secondary mineralogy; fluid pathways; alteration intensity; and basic chemical changes. Tools used to aid identification of minerals were a hand lens, dilute HCl acid, magnet, metal hardness pick and comparison chart for estimating percentage composition.

3.4.2 Optical Petrology

Forty six samples were prepared into petrographic and/or polished thin sections in the Petrology Lab at the University of Canterbury to a thickness of 35–40 µm. They were then examined using a James Swift MP3500 monocular polarising microscope for transmitted light microscopy. In addition, a selection of four polished thin sections were also examined using reflected light to identify the oxide and sulphide minerals using a Meiji MT9420/9430 binocular polarising microscope. In order to classify the rocks using the IUGS system, 300 points were counted on 12 thin sections using a Pelcon Automated Point Counter, the minimum points needed for statistical accuracy (Howarth 1998). The system used to take digital photomicrographs was the Leica DM 2500P petrological microscope with a Leica DFC295 camera and LAS software package. Additionally, four key samples were sent to Townend Mineralogy Laboratory in Western Australia for detailed reflected light microscopy.

All samples were documented in both the UC Collections database and the regional PETLAB database (GNS Science 2016), which includes information about the location, rock type and name, age, and geochemistry of each sample.

3.5 Whole Rock Geochemistry

3.5.1 Portable X-Ray Fluorescence (*fp*XRF)

After the samples were cut for detailed hand sample descriptions, an Olympus Innov-X *p*XRF Delta 50 keV handheld analyser gun was used in soil mode to scan the clean-cut surface of each specimen for 90 seconds in order to obtain an initial indication of elemental concentrations, especially the detection of low level trace elements such as REEs. This was used to acquire immediate results that could help identify which samples might be of high priority to get lab-quality geochemical analyses done on. The detection limits were in the ppm range, except for Si, Mg and Al which were at <1% and P at <0.5%. Geochemical results from a *p*XRF have been shown to be accurate, except for elements with an atomic number lighter than 17.304 (Mauriohooho et al. 2016). Before commencing the analysis on the samples, a calibration check was performed and three standards were analysed (silica blank, NIST 2710a and 2711a). These standards were re-analysed every 20–40 samples in

order to check for variability between samples. Normally multiple analyses would be performed on each sample, or the sample pulverised before analysis, in order to obtain more accurate results. However, because only a basic indication of the geochemistry was needed in order to choose which samples to send off for more detailed lab analyses, one spot analysis per sample gave satisfactory results within the given time constraints.

3.5.2 X-Ray Fluorescence (XRF)

Conventional XRF analyses were conducted in the Geochemistry Lab at the University of Canterbury, using a Phillips PW2400 Sequential Wavelength Dispersive X-ray Fluorescence Spectrometer (XRF). Ten major oxides (SiO_2, TiO_2, Al_2O_3, Fe_2O_3, MnO, MgO, CaO, Na_2O, K_2O and P_2O_5) were analysed by fused disc, whereas 16 trace elements (V, Cr, Ni, Zn, Zr, Nb, Ba, La, Ce, Nd, Ga, Pb, Rb, Sr, Th and Y) were analysed by pressed powder pellet. For major oxide analysis, glass fusion beads were prepared by fusing together approximately 1.3 g of rock powder with 6.98 g of flux ($Li_2B_4O_7$, Li2O and La_2O_3 mixture) and a few grains of oxidant (NH_4NO_3) at 1030°C for at least 15 minutes in Pt/Au crucibles. Loss on ignition (LOI) was calculated after fusion. Glass beads were formed by pouring the molten material into Pt/Au moulds and cooled rapidly. For trace element analysis, 32 mm diameter pressed powder pellets were prepared using approximately 8 g of rock powder and polyvinyl alcohol solution as a binder. Pellets were then pressed in a hardened steel die at 3000 psi for 10 seconds. These methods of analysis are based on methods by Lee (1976), Norrish & Chappell (1977), Norrish & Hutton (1969) and the Philips software/hardware manuals. Additional modifications have been made by the Department of Geological Sciences, University of Canterbury, to optimise analytical conditions.

3.5.3 Inductively Coupled Plasma Mass Spectrometry / Atomic Emission Spectroscopy (ICP-MS / AES)

Whole rock geochemistry of major oxides was analysed at ALS in Brisbane using lithium borate fusion with an inductively coupled plasma atomic emission spectroscopy (ICP-AES) finish, while trace elements were analysed by lithium borate fusion with an inductively coupled plasma mass spectrometry (ICP-MS) finish. These analyses cover 13 major oxides (Al_2O_3, BaO, CaO, Cr_2O_3, Fe_2O_3, K_2O, MgO, MnO,

Na_2O, P_2O_5, SiO_2, SrO and TiO_2) as well as 30 trace elements (Ba, Ce, Cr, Cs, Dy, Er, Eu, Ga, Gd, Hf, Ho, La, Lu, Nb, Nd, Pr, Rb, Sm, Sn, Sr, Ta, Tb, Th, Tm, U, V, W, Y, Yb and Zr). The analyses involved adding a 200 mg powder sample to 90 mg lithium metaborate flux. This was then mixed well and fused in a furnace at 1000°C. The melt was cooled and dissolved in a 100 mL solution of 4% HNO_3/2% HCl_3, which was subsequently analysed by ICP-MS/AES (ALS Global 2016). Three samples (one of the FCG, one of a silica vein and one mafic dyke) were analysed twice in order to test for variability. The lab also included certified reference standards, blanks and duplicates for quality control purposes. From the Fe_2O_3 results, FeO* could be calculated using the following equation from Winter (2010):

$$FeO^* = 0.8998 \cdot Fe_2O_3 \quad (1)$$

3.6 X-Ray Diffraction (XRD)

One unconsolidated sample (EHR81c2) that contained clay was sieved to 63 µm using deionised water. This was then funnelled into a 1 L settling column and stirred for one minute using a brass stirring rod in order to suspend all remaining particles. A watch glass was placed on top to reduce contamination, and the sample was allowed to settle for two hours in order to collect the suspended clay-sized particles (Lewis & McConchie 1994). The deionised water with suspended clay was oven dried at 50°C for ~48 hours, after which the solids were collected in a vial and sent to the Geochemistry Lab at the University of Canterbury. A Philips PW1710 X-Ray Diffractometer was used to identify the crystalline components present in the sample. Detailed analytical methods are presented in Appx. A2.

3.7 Zircon Trace Element Analysis and Dating

Zircon from within the zone of hydrothermal alteration in the Eastern Hohonu River (sample EHR81c) and from the contact of an ankerite vein with the FCG (sample EHR80c) were analysed at the Centre for Trace Element Analysis at the University of Otago, Dunedin, using laser ablation inductively coupled plasma mass spectrometry (LA-ICP-MS). In situ zircon were analysed from polished thin sections using a spot diameter of 10 µm, and the machine used was a Resonetics RESOlution M-50-LR laser ablation system. Please refer to Appx. A3 for more detailed specifications and

techniques used. Forty six spot analyses were measured, and data for 18 mass peaks (29Si, 31P, 49Ti, 89Y, 91Zr, 139La, 140Ce, 147Sm, 151Eu, 163Dy 175Lu, 177Hf, 206Pb, 207Pb, 208Pb, 232Th, 235U and 238U) were collected. Titanium was also used to calculate the temperature of zircon formation (Ferry & Watson 2007). The reference zircon standards TEMORA-2 and R33 (Black et al. 2003, 2004), and the silicate glass standard NIST 610 (Pearce et al. 1997) were measured at the beginning and end of each analytical session, as well as once every 10 unknown analyses, in order to calculate correction factors. Iolite software (Paton et al. 2011) was used for data reduction. Reported ages are $^{206}Pb/^{238}U$ ages and analyses that were >10% discordant were excluded from age calculations. Probability density plots and weighted means were produced using Isoplot (Ludwig 2003).

3.8 Bastnäsite Trace Element Analysis

Bastnäsite from within the zone of hydrothermal alteration in the Eastern Hohonu River (sample EHR81c) were analysed at the Centre for Trace Element Analysis at the University of Otago, Dunedin, using LA-ICP-MS. In situ bastnäsite were analysed from polished thin sections using a spot diameter of 10 µm, and the same machine and procedures as was used for the zircon analysis (Section 3.7). Ten spot analyses were measured, and data for 18 mass peaks (29Si, 31P, 49Ti, 89Y, 91Zr, 139La, 140Ce, 147Sm, 151Eu, 163Dy 175Lu, 177Hf, 206Pb, 207Pb, 208Pb, 232Th, 235U and 238U) were collected. Raw mass peak count rates were background subtracted, corrected for mass bias drift and converted to concentrations (in ppm) by reference standard glass NIST 610 (Pearce et al. 1997). Trace element concentrations for bastnäsite were obtained by normalising count rates for each element to those for Ca (50%) in the sample and the standard, using known CaO and trace element concentrations in NIST 610 and the estimated CaO in the bastnäsite obtained by summing the major element oxides to 100% on a weight basis.

3.9 Scanning Electron Microscope (SEM)

A JEOL JSM 6100 scanning electron microscope (SEM) was used for energy-dispersive x-ray spectroscopy (EDS) in the Mechanical Engineering Department, University of Canterbury. The EDS detector used was an Aztec 50 mm^2 SDD, and the

backscatter electron detector was used for qualitative point analysis, which is particularly useful for detecting heavy elements such as REEs. The elements were analysed as oxide percent, because REEs are generally unstable as metals in nature (see Section 2.1). Unfortunately, this instrument was replaced halfway through the SEM analyses, so the second half of the work was conducted using a JEOL JSM 7000F field emission, high resolution SEM, although it was only slightly less accurate than the JEOL JSM 6100. This second machine was also used for cathodoluminescence (CL) imaging of zircon in sample EHR81c. Both instruments were used with standard operating protocols and an accelerating voltage of 15 kV. Because of complexities within the rare earth minerals (i.e. alteration and intergrown phases), four key samples were also sent to Townend Mineralogy Laboratory in Western Australia for SEM identification using their MINIDENT database.

Cover slips were left off the thin sections, and key samples were cleaned with ethanol and coated with approximately 20 nm of carbon before SEM analysis in order to disperse the electron build-up. The carbon coat made it difficult to quantify carbon; however, the element maps were useful for determining differences in carbon distribution, and therefore, determining its presence in a certain mineral.

3.10 Stable Isotopes

Thirty samples of carbonates were analysed for $\delta^{13}C$ and $\delta^{18}O$ in the stable isotope analytical facility at the University of Canterbury. Nine hand specimens were spot drilled using a diamond-coated Dremel with a 1 mm drill head. The powder was collected using filter paper, funnelled into a sterile glass vial, and the $\delta^{13}C$ and $\delta^{18}O$ isotopic composition were analysed using 103% phosphoric acid and a ThermoFinnigan GasBench II coupled to a ThermoFinnigan Delta V^+ gas isotope ratio mass spectrometer operating at ultra-high purity He flow conditions. All equipment used during sample preparation was cleaned with compressed air between samples, and the powders were tested with dilute HCl acid to make certain they were carbonates before isotopic analyses. To convert from $\delta^{18}O$ (‰ V-PDB) values to $\delta^{18}O$ (V-SMOW) values, the following equation was used:

$$\delta^{18}O_{V\text{-}SMOW} = 1.03091 \cdot \delta^{18}O_{V\text{-}PDB} + 30.91 \text{ ‰} \quad (2)$$

Chapter 4: Results

4.1 Field Sampling and Observations

A total of 112 samples were gathered from the Eastern Hohonu River (EHR), three tributaries of the Little Hohonu River (LHR), the Greenstone River, Eel Creek, and the Mt French Track (Fig. 12 and Appx. B). The eleven different rock varieties that were identified were: relatively unaltered FCG; altered FCG; sheared FCG; microgranite; mafic-rich FCG; veins; mafic dykes; intermediate dykes; felsic (or red) dykes; QAF syenite; and pegmatites. The dense vegetation in the field area made rock-chip sampling difficult, and outcrops were only exposed within streams and walking tracks that cross-cut the FCG.

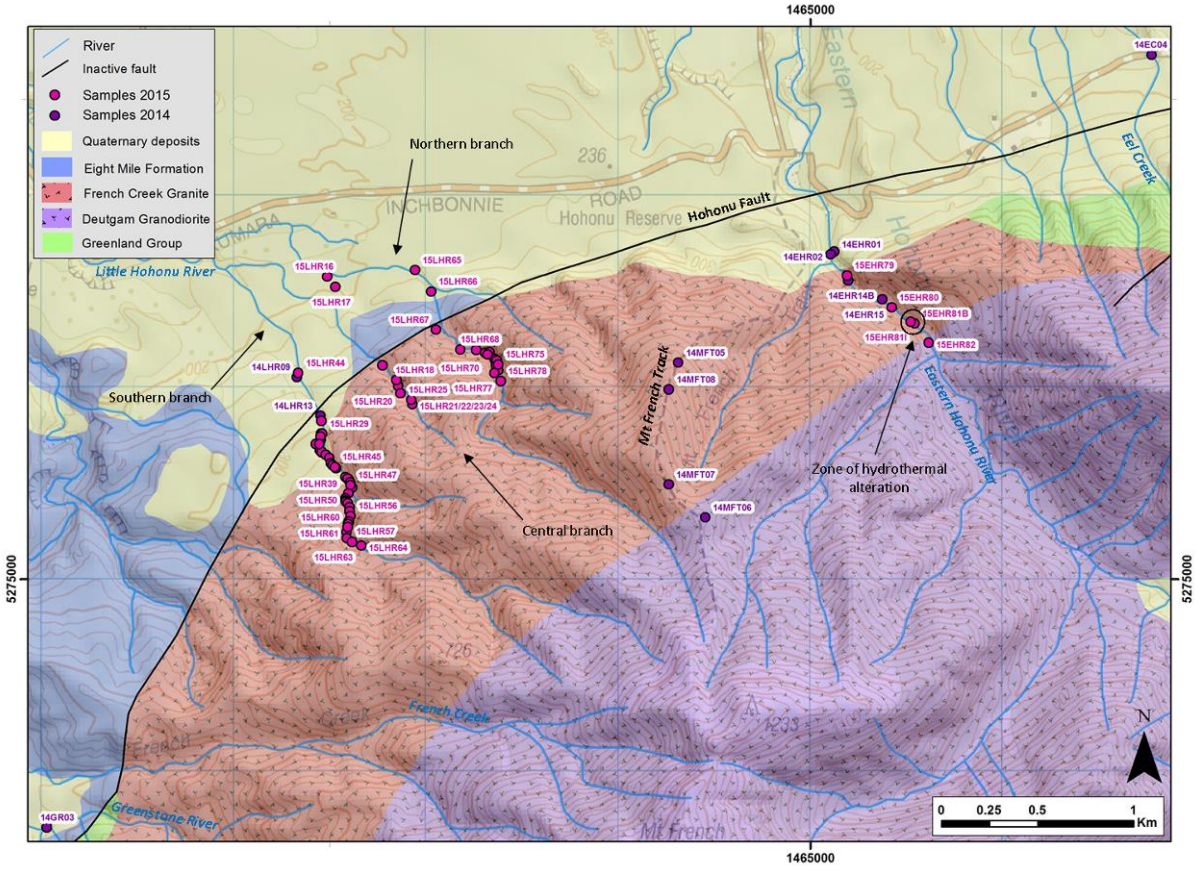

Figure 12. The locations of samples collected during the 2014–2015 field seasons. Underlying spatial data are from Nathan et al. (2002).

The FCG has typically undergone ubiquitous alteration to minor sericite and limonite, and completely fresh samples were scarce. Relatively unaltered FCG was jointed (Fig. 13a) and very hard, and often led to the presence of steep gorges (Fig.

Figure 13. (A) Resistant, jointed French Creek Granite forming a waterfall, joints are indicated by arrows and waterfall height is ~5 m; (B) relatively unaltered French Creek Granite forms steep gorges, person for scale; (C) weak, altered French Creek Granite causing landslides on the river banks, the large boulder is ~1.5 m wide; (D) quartz and ankerite veins intrude sub-parallel to a mafic dyke, adjacent French Creek Granite is highly altered, hammer for scale; and (E) pegmatite pods in the French Creek Granite, as indicated by arrows, with hammer for scale. A, B and C were taken in the southern tributary of the Little Hohonu River, D was taken in the Eastern Hohonu River, and E was taken in the northern tributary of the Little Hohonu River.

13b) and resistant topographic knickpoints that formed waterfalls (Fig. 13a), especially in the steeper upper catchments. Throughout the northwest Hohonu Ranges, the more hydrothermally altered FCG formed distinct geomorphological differences within streams, where these weaker rocks commonly led to landslides and slips in the hillside (Fig. 13c). Much of the FCG outcropping in the EHR was relatively unaltered, except for the ~30 m wide zone of hydrothermal alteration and immediately adjacent to vein intrusions (Fig. 13d), and formed an extensive gorge up to the contact with the Deutgam Granodiorite. In contrast, the FCG in the lower tributaries of the LHR contained patchy alteration zones dominated by sericite and clays, and also had small pegmatite pods (Fig. 13e) and zones of microgranite present. The pegmatite pods were relatively more abundant as float in the northern-most branch of the LHR (Fig. 12) and the adjacent FCG commonly contained very pink feldspars and less mafic minerals. The rocks from the more altered zones were too altered to obtain samples from, and sometimes white plastic clays were associated with weathered outcrops in the rivers. The FCG outcropping on the Mt French Track (Fig. 12) had a white bleached appearance, while only one float sample was gathered from each of the Greenstone River and Eel Creek (Fig. 12), both downstream of the FCG contact.

The ~30 m wide alteration zone in the EHR (Fig. 14) grades from relatively resistant and unaltered FCG upstream into a granular, veined FCG, and into a highly altered greenish granite with brown fizzing veinlets, disseminated sulphides and orange clay alteration (Fig. 15a). It then grades back into greenish granite, this time with white fizzing veins orientated sub-parallel to the strike (112/50° ESE) of the overall structure, and grades back into a granular granite, into a sheared green and pink granite and then into relatively unaltered FCG. This alteration was not observed on the other side of the river, where the hillside was covered by vegetation.

Cross-cutting veins of quartz and carbonates between 2 to >30 cm wide were present in the LHR, where fluids had permeated the granite. They rarely had sharp contacts; instead, they were often defined by diffuse silicification and alteration of the granite to sericite and/or carbonates and graded outward to less-altered FCG. Millimetre-scale quartz and carbonate veinlets, as well as stylolitic dissolution planes were also sometimes present within the FCG. Despite the abundant quartz in these

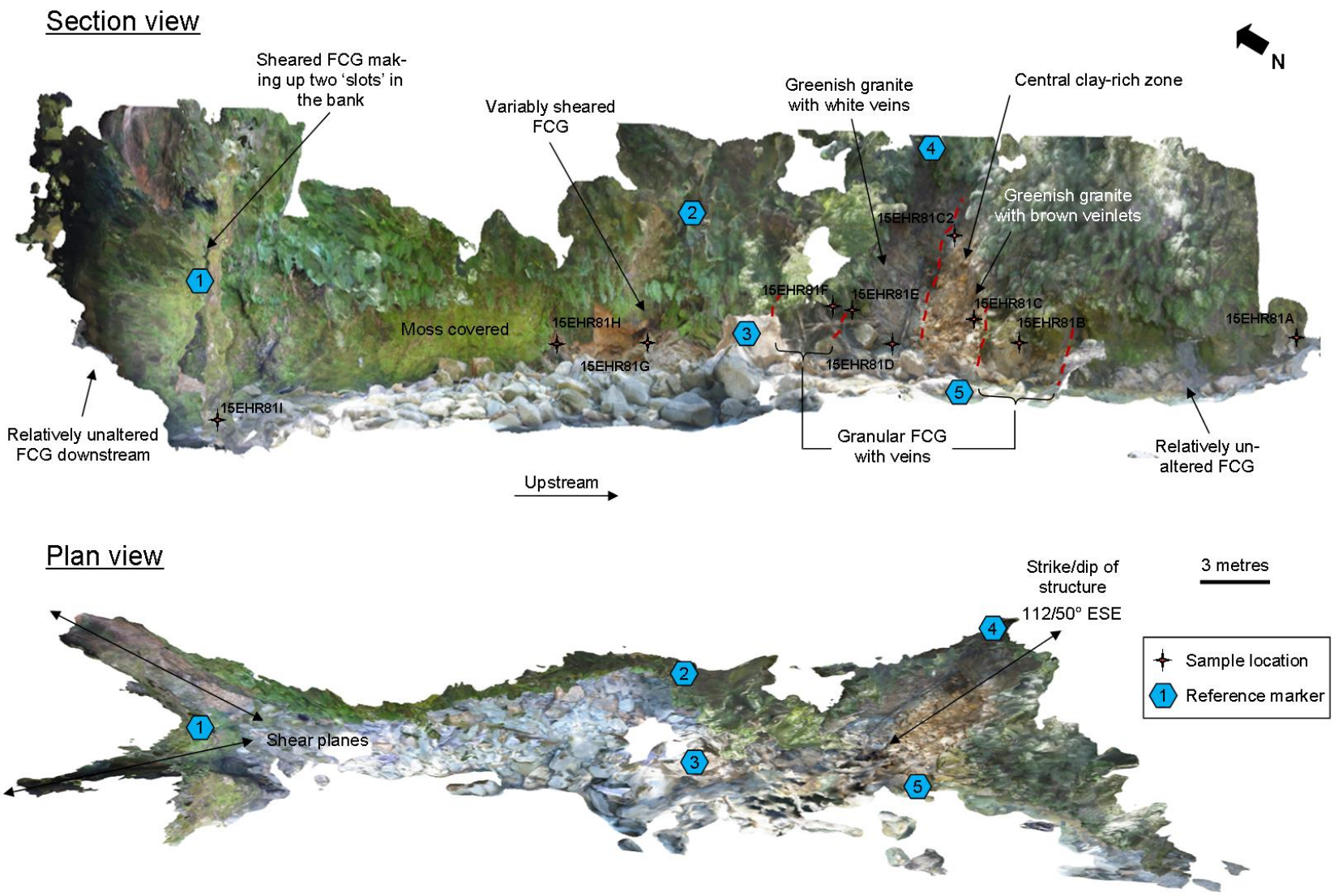

Figure 14. The ~30 m wide zone of hydrothermal alteration in the Eastern Hohonu River in both section view (above) and plan view (below). Note the location of samples, changes in lithology and orientation of structures. Model created using Agisoft PhotoScan.

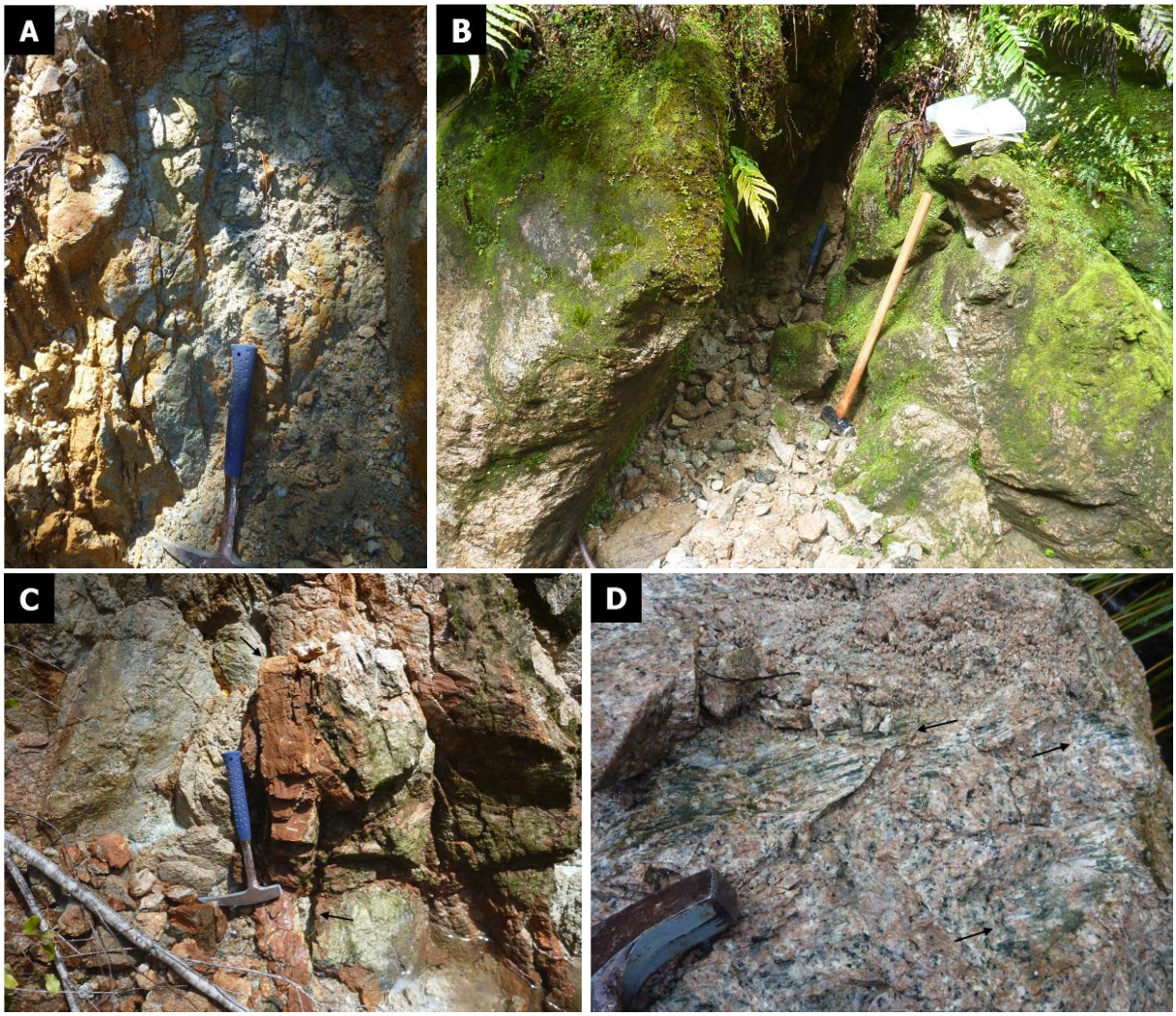

Figure 15. (A) Central zone of clay and disseminated pyrite within the zone of hydrothermal alteration in the Eastern Hohonu River; (B) 'slot' or embayment in the Little Hohonu River created by the preferential erosion of hydrothermal veins; (C) hard, brown coating on carbonate veins; and (D) shear planes in the French Creek Granite defined by streaky dark minerals. Hammer for scale.

veins, these areas were often zones of weakness and preferentially eroded out of the river banks, leaving active slips and small embayments or 'slots' (Fig. 15b). The carbonate veins commonly had a hard brown coating (Fig. 15c) with a pale white interior, and multiple generations of veining were often present. This was usually represented by later carbonate veinlets cross cutting earlier quartz veins and/or areas of silicification and sericitisation in the FCG. Much of the FCG in the lower tributaries of the LHR was sheared, with shear planes defined by dark streaky minerals (Fig. 15d), and the rock broke easily on these planes during sampling.

Centimetre- to metre-scale mafic to felsic dykes were also observed and usually had cross-cutting relationships with the FCG, except for a minority that had

gradational contacts. Rare composite dykes with more mafic interiors were also found. Felsic dykes were reddish-pink in colour and mafic dykes grey, while intermediate dykes were either of those colours or more typically a mixture of both (i.e. pink phenocrysts set in a grey groundmass). The dykes were typically relatively weak and broke into small pieces during sampling efforts. In some circumstances in the EHR, veins had taken advantage of dykes, intruding the contact between them and the FCG (Fig. 13d).

The Hohonu Fault (Fig. 12) was observed in the northern-most branch of the LHR. Here, blocks of slightly altered FCG, intermediate dykes and friable Blue Bottom Group sandstone were incorporated in an unconsolidated matrix of sand, clay, and crystals of quartz and feldspar. The fault zone was at least 3 m wide next to the Blue Bottom Group sandstone, but the upstream extent was concealed beneath Quaternary boulders. The contact of the FCG with the Deutgam Granodiorite was not observed during this study; the only time it was crossed was in the EHR, but there it was also concealed beneath river boulders.

4.2 Spatial Analysis

Figures 16 and 17 show the distribution of rock chip samples from this study as well as rock chip samples from Price (2013), Price & Ryland (2011) and White & Price (2006), and they illustrate the internal complexities within this composite granitoid. Alteration of the FCG appears relatively patchy; however, in general more alteration is present near the lower contact (i.e. near the Hohonu Fault), while samples from the upper contact with the Deutgam Granodiorite are dominantly relatively unaltered. However, this observation is difficult to justify due to the limited number of samples from the upper catchments. Note the occurrence of a syenite phase between the FCG and Deutgam Granodiorite, both in the EHR (EHR82) and on the Mt French Track (MFT06). Geoff Price's samples from other locations near this contact (French Creek, Greenstone River and the southern branch of the LHR) also indicate a higher proportion of feldspar in hand sample (5631, 5649 and 5652). Four samples of French Creek microgranite were also found, three near the lower contact and one near the upper contact (Fig 16), which is typically further east than the contact on the QMAP (as discussed in Section 2.3.2). Veins and dykes were present in all

streams that were sampled during this study, while pegmatites were only found in the northern and southern tributaries of the LHR (Fig. 17).

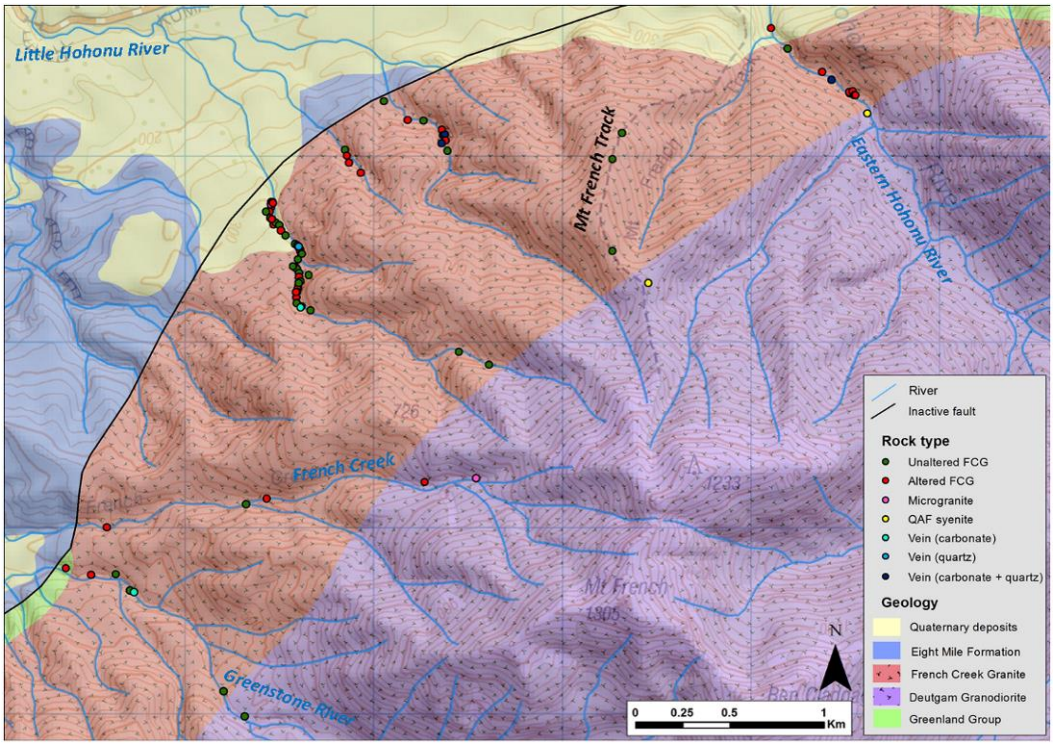

Figure 16. The different lithologies sampled in the French Creek Granite and its hydrothermal alteration. Data are from this study and from Price (2013), Price & Ryland (2011) and White & Price (2006). Underlying spatial data are from Nathan et al. (2002).

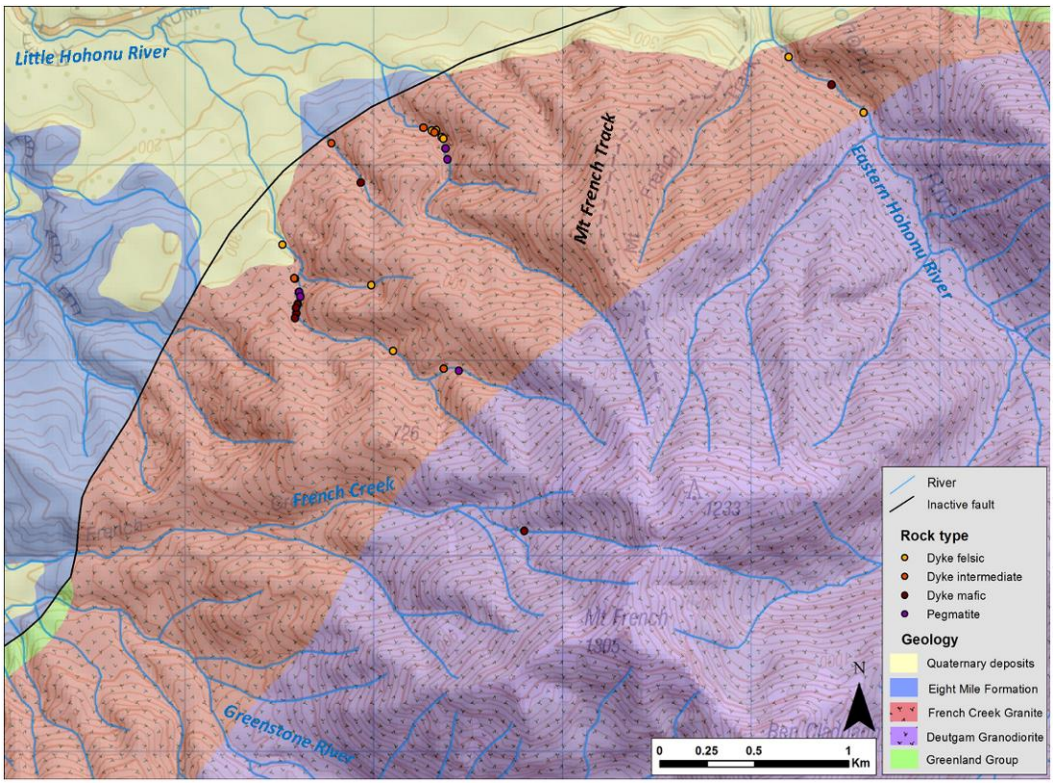

Figure 17. The different lithologies sampled in the dykes and pegmatites. Data are from this study as well as from Price (2013), Price & Ryland (2011) and White & Price (2006). Underlying spatial data are from Nathan et al. (2002).

Figure 18 shows a collection of colour coded anomaly thresholds for different elements based on the methods outlined in Section 3.2. Rare earth element (Ce, La

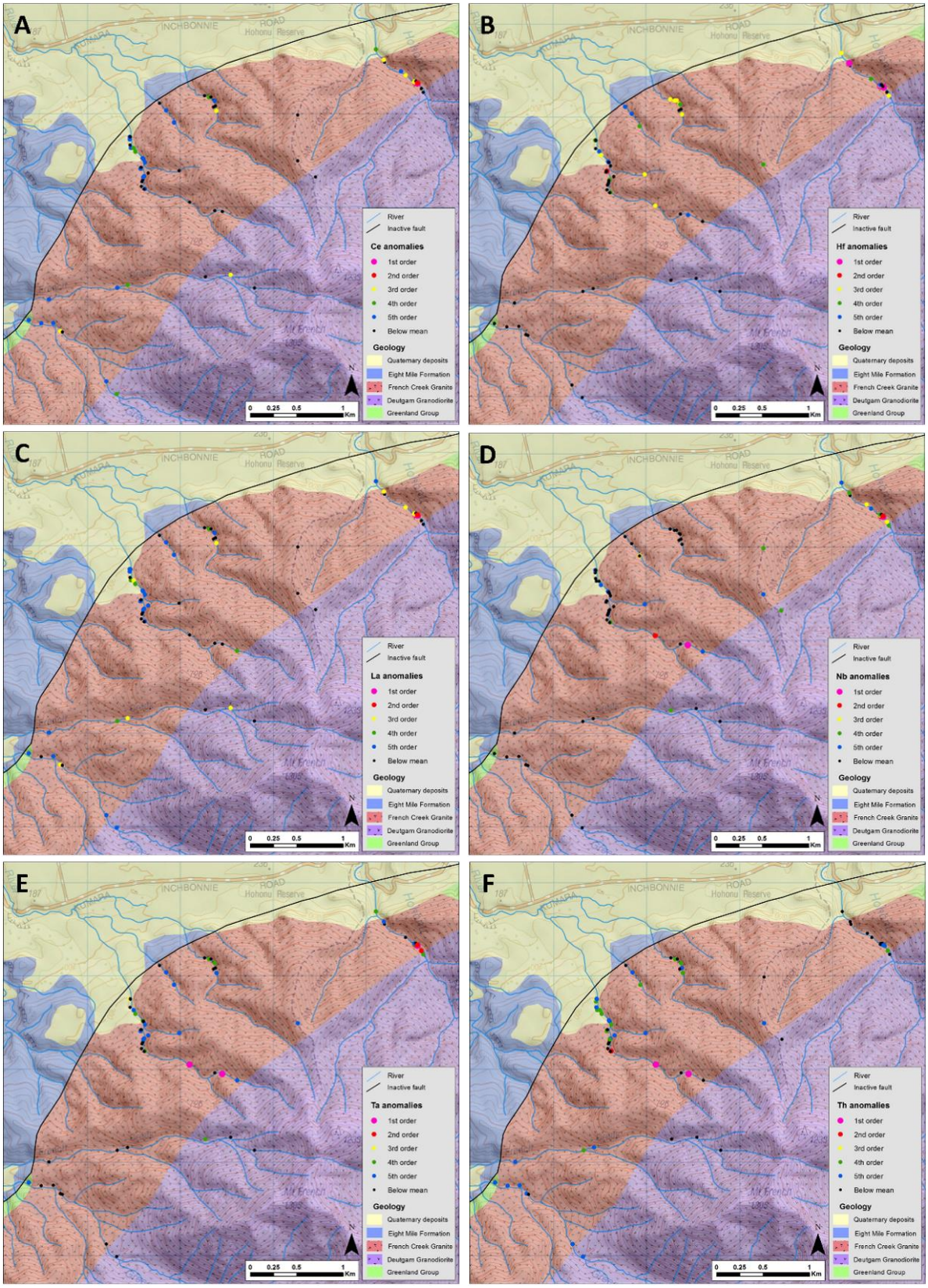

Figure 18. The distribution of anomaly thresholds for: (A) cerium; (B) hafnium; (C) lanthanum; (D) niobium; (E) tantalum; (F) thorium; (G) uranium; (H) yttrium; and (I) zirconium. Underlying spatial data are from Nathan et al. (2002).

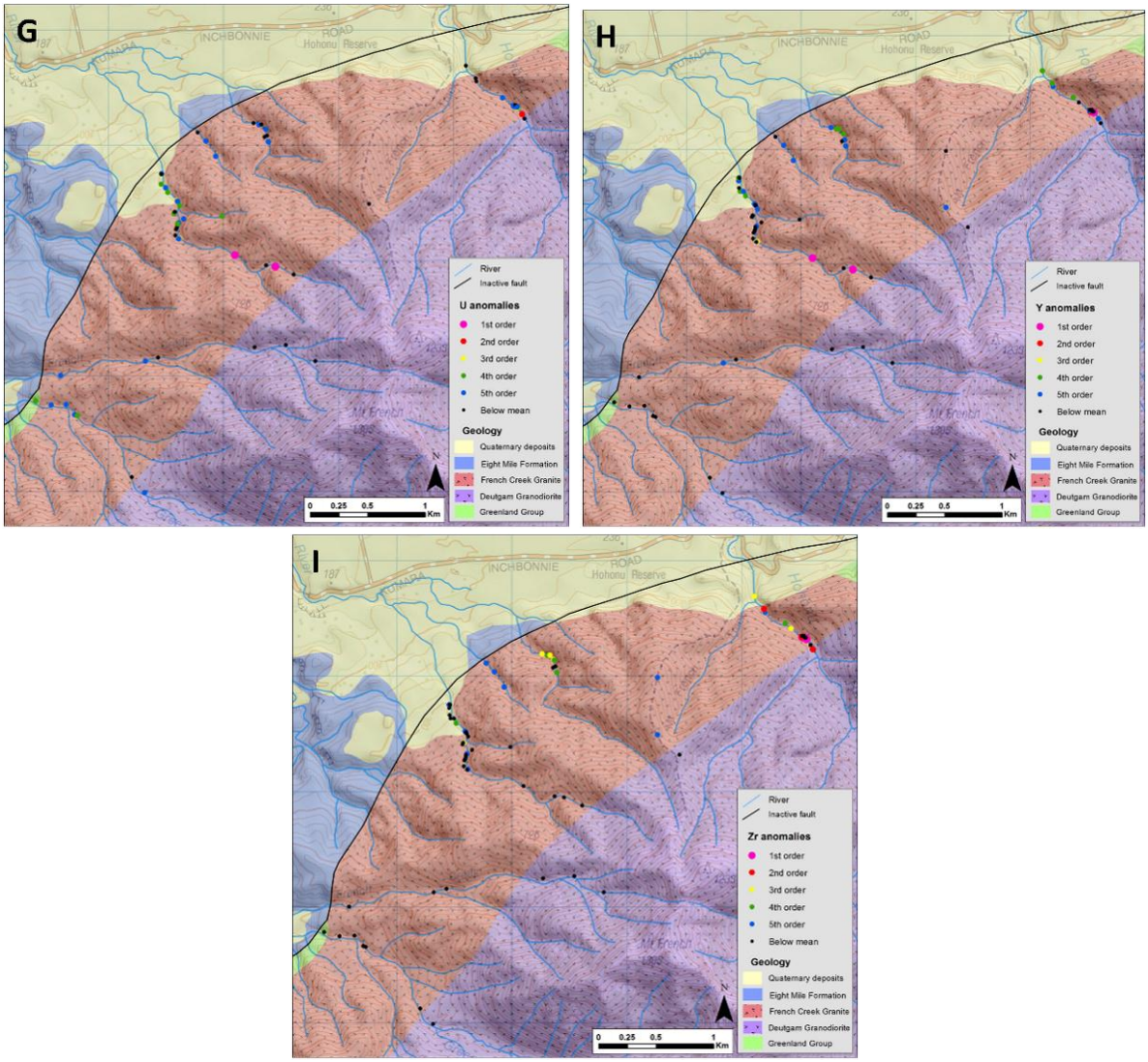

Figure 18. continued.

and Y) anomalies (Fig. 18a, c and h, respectively) are highest (i.e. 1st – 2nd order) in FCG samples from the hydrothermal alteration zone in the EHR. Additionally, Y contains 1st order anomalies in a sample of unaltered FCG and a felsic dyke in the upper southern tributary of the LHR (Fig. 18h). The associated elements Hf, Nb, Ta, Th, U and Zr (Fig. 18b, d–g and i, respectively) are also highest in the zone of hydrothermal alteration in the EHR as well as in other FCG samples in the EHR, which includes the syenite phase for some of these elements. A sample of unaltered FCG and a felsic dyke, both in the southern tributary of the LHR, contain 2nd order Th and Hf anomalies, respectively. Several intermediate to felsic dykes in the LHR contain 3rd order Hf anomalies. In addition, a few 1st – 2nd order Nb, Ta, Th and U anomalies occur in the same two samples that contain 1st order anomalous Y in the upper southern LHR tributary (Fig. 18d–g).

Basic statistical analyses using histograms, box plots and cumulative probability plots depicted two, possibly three, populations of Ce and La present within FCG samples. A small lower Ce peak centred on ~65 ppm (Fig. 19a) is inferred to represent background concentrations in the FCG; the main peak is at 165 ppm, possibly representing primary REE mineralisation. A small upper peak at ~220 ppm is also present, and might be related to hydrothermal REE enrichment. Lanthanum shows a similar distribution with peaks corresponding to 50 ppm, 90 ppm and 120 ppm, respectively. Zirconium has a different distribution with relatively high variance, a low peak at ca. 90 ppm and a long upper tail. Yttrium and Nb (Fig. 19b) are different again with only one population present, representing primary mineralisation, and higher tails that are likely associated with hydrothermal enrichment. Variograms indicate vague N-S and NE-SW patterns; the latter matches the trend of the Hohonu Fault and outcrop geometry of the FCG. However, this distribution might reflect sampling locations, and caution must be exercised with this interpretation.

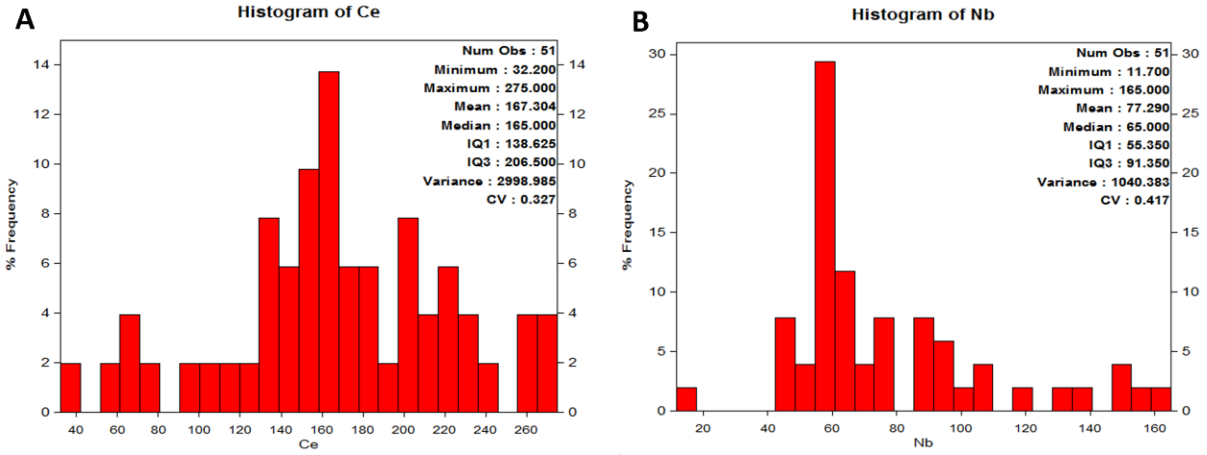

Figure 19. Histograms showing the frequency of (A) cerium and (B) niobium in the French Creek Granite.

4.3 Optical Petrology

A total of 46 samples were analysed using a petrographic microscope, and a detailed description of each can be found in Appx. C. The descriptions are divided into the following four sections: 1) the French Creek Granite; 2) its hydrothermal alteration; 3) the various cross-cutting veins; and 4) the dykes.

4.3.1 French Creek Granite (FCG)

The FCG is dominated by a biotite alkali-feldspar granite to syenogranite. K-feldspar constitutes between 40–60 modal % and these are commonly large and euhedral. They are typically hypersolvus, as indicated by abundant mesoperthites (Fig. 20a), and have often separated into two distinct feldspars. Microprobe analysis by Waight (1995) indicates Or ~60-80%. They occasionally contain small quartz and plagioclase inclusions, and frequently form both graphic and granophyric intergrowths with quartz (Fig. 20b & Appx. D1a). Quartz constitutes between 25–42 modal % of this rock type and range from skeletal to euhedral to interstitial habits. They have slight undulose extinction, and also sometimes occur as small interstitial crystals bounding larger crystals of euhedral K-feldspar, indicative of the last remaining melt fraction. Within the subordinate microgranite variety, both quartz and K-feldspar form a groundmass of smaller crystals with intense graphic and granophyric intergrowths in places, surrounding rare embayed quartz and K-feldspar phenocrysts. Plagioclase normally constitutes <10 modal % of these rocks, but can comprise up to 15 modal %. They are predominantly albite with An ~9% (Waight 1995). They are typically relatively small when compared to the quartz and K-feldspar and often have polysynthetic twins. They have semi-euhedral habits, seldom contain quartz inclusions, and have undergone more sericite alteration than the K-feldspar.

The mafic component is comprised of 1–5 modal % Fe-rich biotite (annite), and sometimes of green-brown amphibole (1–2 modal %). Biotite is yellow-brown to green, with embayments and alteration to chlorite and Fe-oxides common. The biotite generally occurs in interstitial clusters with Fe-oxides and contains zircon and apatite inclusions (Fig. 20c). Some inclusions of lensoidal quartz parallel to the biotite cleavage were also observed. Some of the amphibole has been identified as hornblende and is commonly altered to biotite, magnetite and/or limonite and rare syntaxial bastnäsite-parisite.

Common accessory minerals include zircon, apatite and magnetite, while ilmenite, fergusonite and allanite, and secondary minerals such as muscovite, bastnäsite-parisite and carbonates (siderite, ankerite and calcite), also occur. Poikiolitic zircon are almost always associated with mafic clusters of biotite-chlorite

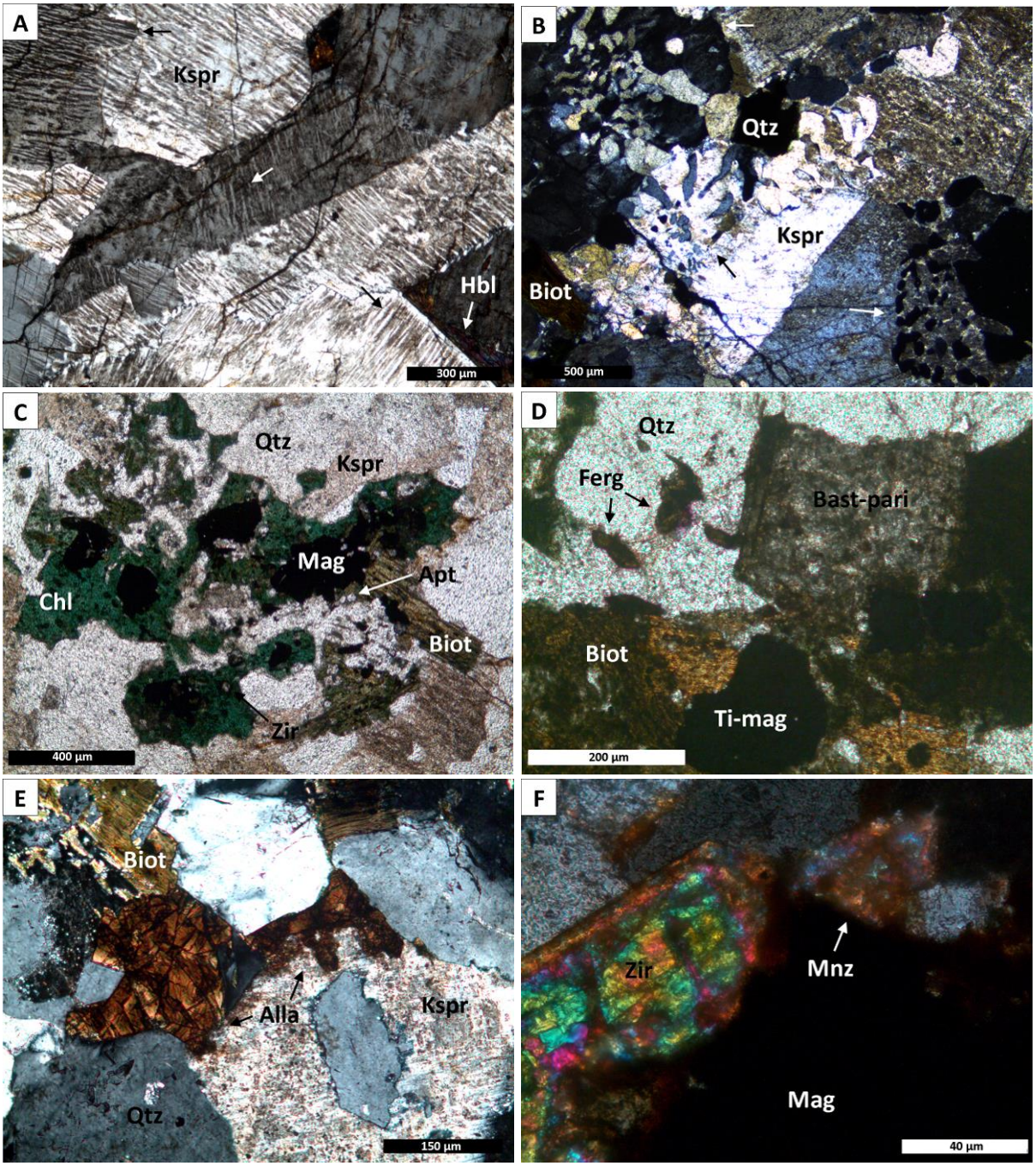

Figure 20. Photomicrographs of (A) MFT06, mesoperthites in K-feldspar with interstitial hornblende (in CPL); (B) LHR78, graphic intergrowths between quartz and K-feldspar (in CPL); (C) LHR18, a mafic cluster comprised of biotite, chlorite, magnetite, other Fe-oxides, apatite and zircon (in PPL); (D) LHR78, primary fergusonite occurring with quartz, biotite, apatite and Ti-rich magnetite, with bastnäsite-parisite pseudomorphing hornblende (in PPL); (E) GR03, primary allanite, K-feldspar, quartz and biotite (in CPL); and (F) LHR28, a crystal of monazite in association with zircon and magnetite (in CPL).

and Fe-oxides (Fig. 20c), and they can be relatively large in size (up to 0.5 mm). Apatite are hexagonal to acicular in habit and are also commonly found with these mafic clusters (Fig. 20c). Fe-oxide minerals within typical FCG are most commonly magnetite, with minor ilmenite also occurring, and contain zircon and/or apatite

inclusions. Rare titaniferous magnetite and titanomagnetite are also present, which occur alongside rare ilmenorutile and leucoxene within mafic clusters. Primary fergusonite (Fig. 20d & Appx. D1b) and allanite (Fig. 20e & Appx. D1c) occur in some FCG samples. Allanite also occurs as an alteration product of hornblende (Appx. D1d), and separate and syntaxial bastnäsite-parisite occur as an alteration product of both hornblende and allanite (Fig 20d & Appx. D1c–d). Rare primary monazite is also sometimes present, and usually occurs with zircon and magnetite (Fig. 20f & Appx. D1e). All of these rare earth minerals are typically associated with the mafic clusters. Limonite is fairly common around altered mafic components and within the K-feldspar, and small aggregates of carbonates are observed infilling cracks and miarolitic cavities. No aenigmatite, which Waight (1995) identified in typical FCG, was found during the current study.

A subordinate quartz alkali-feldspar (QAF) syenite phase contains between 70–73 modal % K-feldspar, 10–15 modal % quartz and ~1 modal % plagioclase. Amphibole (likely hornblende) was the only identified mafic phase, comprising between 5–10 modal percent. Accessory minerals include magnetite, ilmenite, zircon, carbonates, apatite and rare pyrite. The only notable textural difference when compared with the typical FCG, other than the mineralogy, is the grain boundary deformation that the K-feldspar has undergone. This is observed from perthites that appear to interfere with the neighbouring crystals (Fig. 21a) to totally irregular crystal boundaries (Fig. 21b).

The other subordinate phase found in three samples, is a mafic-rich variety of FCG that contain up to 20 modal % biotite, 15 modal % hornblende, 5 modal % each of apatite and Fe-Ti oxides (mostly magnetite), and 3 modal % zircon. Some of these samples also contain minor primary REE-bearing phases such as titanite, monazite, allanite, loparite and perrierite. Sample GR03 contains a central zone with intense granophyric texture (Appx. D1f) surrounded by abundant scattered biotite, which shows signs of confined growth (books), resorption (embayments and sieve texture), alteration to chlorite and Fe-Ti oxides and some deformation. Rare sulphides, such as pyrite, marcasite (Appx. D4a) and molybdenite are present (Townend & Townend 2016a). In addition to biotite, altered hornblende, abundant

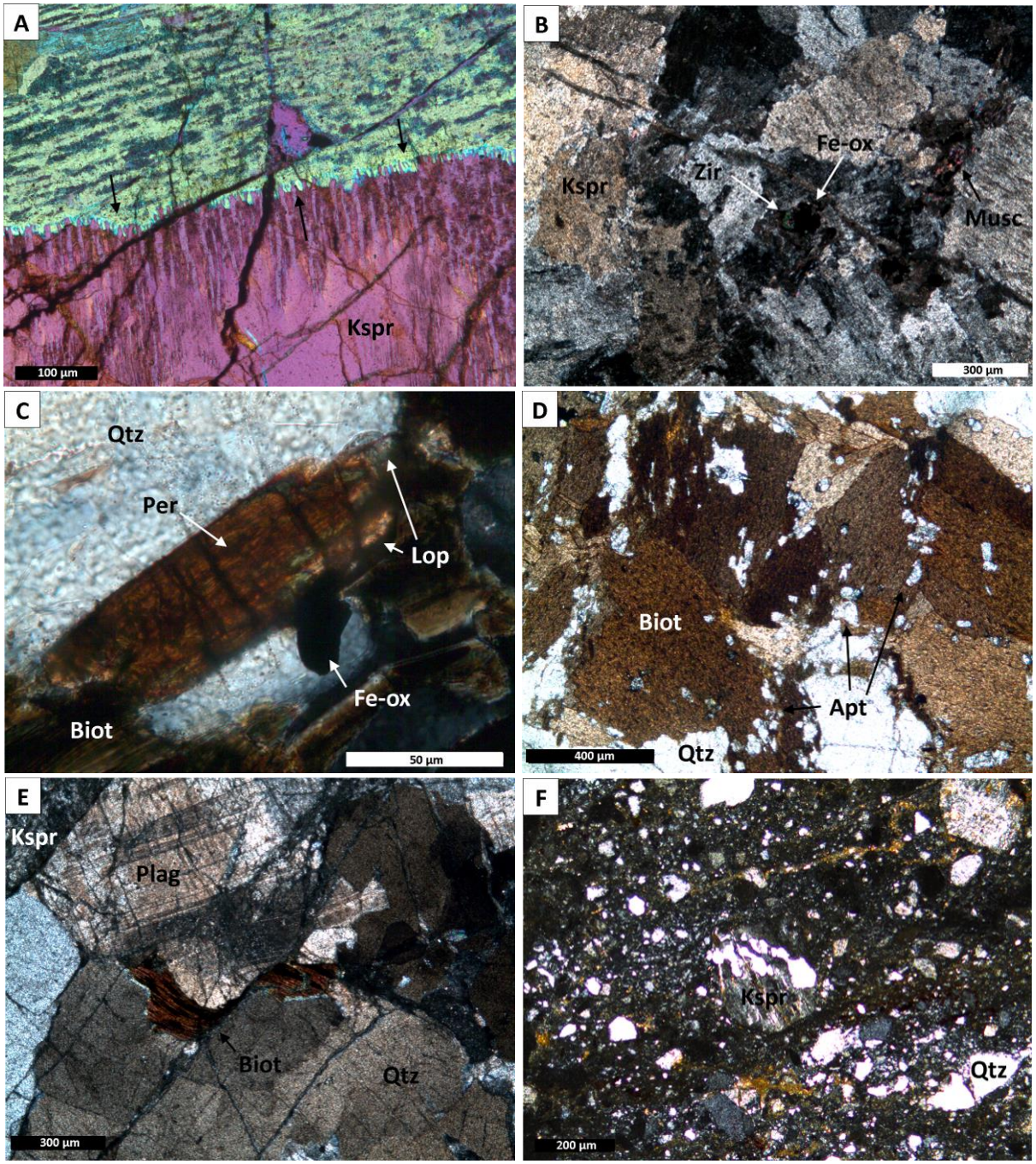

Figure 21. Photomicrographs of (A) MFT06, grain boundary migration in two adjacent K-feldspar crystals (in CPL with the sensitive tint plate in); (B) EHR82, highly irregular crystal boundaries within K-feldspar (in CPL); (C) GR03, a crystal of intergrown loparite and perrierite surrounded by quartz, biotite and Fe-oxides (in CPL); (D) LHR65, abundant apatite inclusions within biotite clusters (in PPL); (E) LHR46, bent and offset biotite surrounded by quartz, plagioclase and K-feldspar (in CPL); and (F) LHR41, granulated quartz and feldspar set in a matrix of mica, clay and pulverised quartz (in CPL).

Fe-Ti oxides and acicular apatite (Appx. D2a), broken and slightly rounded loparite and perrierite, and broken allanite, also occur. The loparite and perrierite are sometimes intergrown (Fig. 21c) and also sometimes occur as inclusions within the biotite (Appx. D2b). A second mafic-rich sample of FCG (LHR44) contains small

stubby biotite-rich lenses surrounded by microgranitic quartz and K-feldspar. It contains euhedral embayed hornblende, abundant elongate prisms to equidimensional ilmenite crystals, and broken titanite. The third mafic-rich sample (LHR65) contains abundant apatite and clusters of biotite (Fig. 21d), as well as monazite and anti-rapakivi textured feldspar with iridescence. All of the mafic-rich varieties of the FCG contain abundant zircon, which are associated with biotite.

The FCG displays variable brittle deformation that ranges from discrete cracks with slightly offset minerals to highly sheared cataclasite. Cracked minerals are very common, and the cracks are typically oxidised. Some biotite has been bent and offset (Fig. 21e), and muscovite and chlorite have grown within pressure shadows. Other mica has grown perpendicular and parallel to, or is smeared out in millimetre-scale shear planes, which are obvious at hand sample scale. One example of a semi-igneous–metamorphic crystal of biotite-chlorite (David Shelley pers. Comm.) was observed growing elongate along such a shear zone, although it had undergone no shearing itself (Appx. D2c). Advanced shearing results in angular to sub-rounded clasts of granulated quartz and K-feldspar set in a fine grained pulverised matrix of quartz, biotite, chlorite, clay ± carbonates (Fig. 21f). However, within these shear zones quartz is only slightly deformed and does not exhibit any recrystallisation. In a limited number of samples from the FCG, very irregular twins occur within K-feldspar and plagioclase, and some perthites are curved and deformed, indicating that mild ductile deformation has occurred as well as brittle deformation.

4.3.2 Hydrothermal Alteration

Modification of the FCG by hydrothermal fluids has resulted in patchy zones of sericitisation, chloritisation, silicification, kaolinisation, carbonates (siderite, ankerite and calcite), muscovite, Fe-oxides and rare sulphides (typically pyrite). This modification of the original granite ranges from mild ubiquitous alteration through to almost complete destruction of primary minerals and textures. Sericite is the most common secondary mineral; its occurrence ranges from small specks within plagioclase to pervasive sericitisation of all feldspars (Appx. D2d). Proximal to structures where fluid movement was concentrated, feldspars are often completely replaced by sericite and quartz: only pseudomorphs of streaky perthites and crystal

boundaries remain (Fig. 22a). Carbonates are another commonly occurring secondary mineral. Small aggregates of siderite and ankerite are observed altering feldspar, typically along perthites and cracks (Fig. 22a), and sometimes occur as a secondary alteration of sericite. Calcite sometimes infills miarolitic cavities and occurs in small cracks as veinlets.

The mafic minerals in the FCG (i.e. biotite and amphibole) are typically the first component to undergo alteration, leaving embayed and corroded brown to green pseudomorphs of chlorite, Fe-oxides, limonite, carbonates and/or syntaxial bastnäsite-parisite. Muscovite and streaky Fe-Ti oxides are another alteration product of biotite, while limonite is a common secondary product within K-feldspar and during oxidation of siderite. Proximal to structures where hydrothermal fluids were concentrated, zircons sometimes occur in trails or clusters.

In the zone of hydrothermal alteration in the Eastern Hohonu River (EHR), interstitial clusters of mafic components are progressively altered from hornblende, biotite, ilmenite, magnetite and/or ilmenorutile (Fig. 20c) to muscovite, hematite, Fe-oxides, bastnäsite group minerals, chlorite, siderite and/or ankerite pseudomorphs (Fig. 22b), until completely replaced by siderite, ankerite, acicular rutile/brookite needles, leucoxene (Appx. D4b), patchy bastnäsite-parisite-synchysite, pyrite, chalcopyrite (Appx. D4c), sphalerite and/or galena (Fig. 22c and Appx. D4d; Townend & Townend 2016a, 2016b). This final alteration assemblage occurs in small clusters along with halloysite and giant zircon surrounded by quartz and sericite, with a texture indicative of a granitic palimpsest. Feldspars have become completely replaced by sericite, quartz, siderite and halloysite (Fig. 22d). Apatite becomes rounded before disappearing completely towards the inner zone of alteration, while pyrochlore (to plumbopyrochlore) only occurs in some of the outer alteration zone rocks and has altered to Fe-oxides. Quartz becomes irregular, although some discontinuous euhedral vein quartz is also present, and has moderately strong elongate undulose extinction (Appx. D2e). Within the inner zone of hydrothermal alteration in the EHR, some quartz crystals have directional protuberances where they continued to grow outward along their boundaries (Fig. 22e & Appx. D2f). Such protuberances were also noted in a highly altered sample of FCG in the EHR located

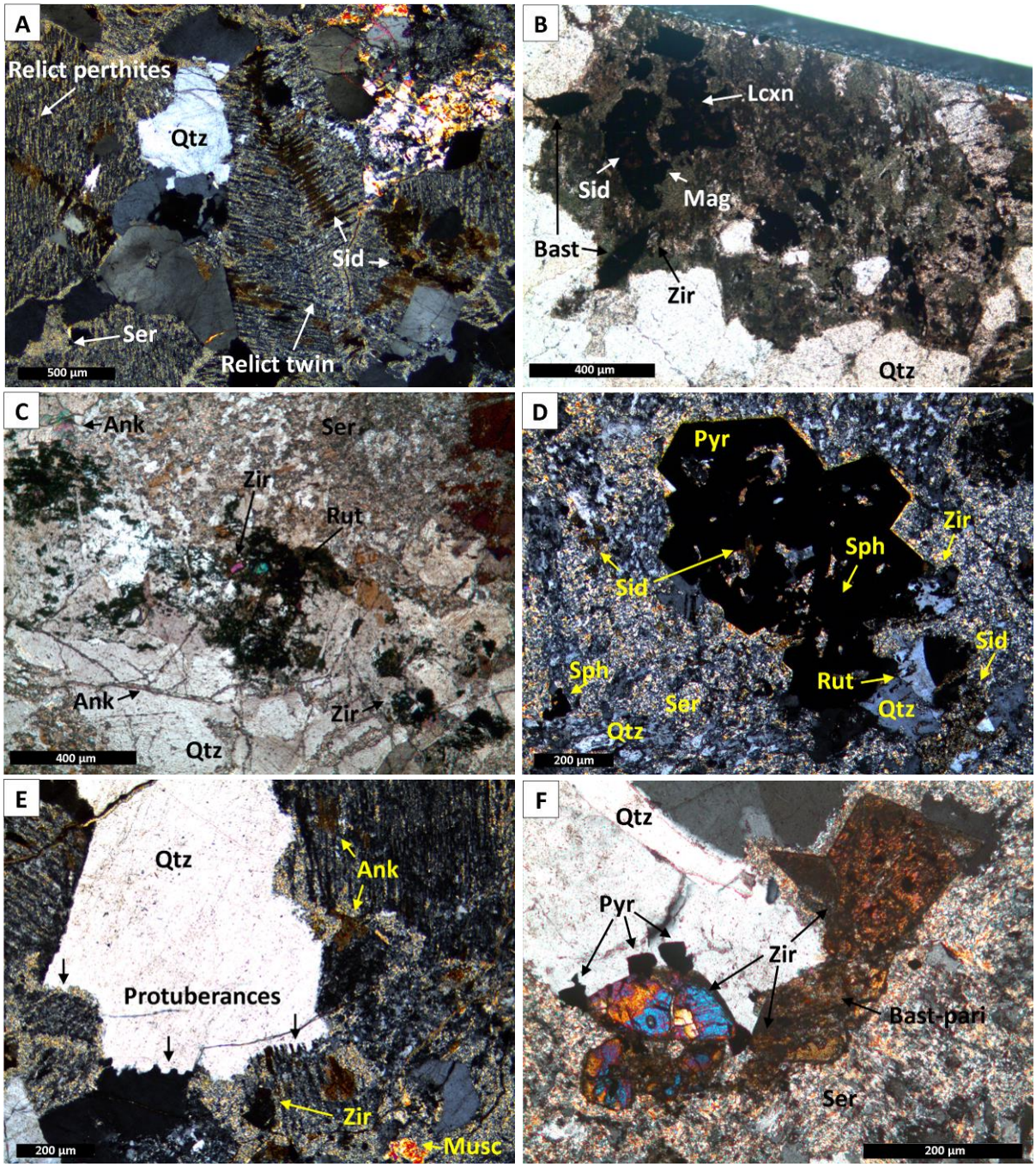

Figure 22. Photomicrographs of (A) EHR80C, sericite and quartz pseudomorphing K-feldspar with relict perthites, simple twin and crystal boundaries still observable, irregular quartz is also present (in CPL); (B) EHR81H, an altered mafic cluster which was once likely biotite or hornblende, now a mixture of magnetite, leucoxene, siderite, bastnäsite-TiO_2, Fe-Ti oxides and possibly chlorite (in PPL); (C) EHR81D, what remains of the mafic component in the inner zone of hydrothermal alteration in the Eastern Hohonu River, now a mixture of rutile, ankerite, Fe-Ti oxides and zircon, as well as ankerite veinlets, sericite and quartz (in PPL); (D) EHR81C, a cluster of pyrite, sphalerite and zircon surrounded by siderite, rutile, sericite and quartz, the euhedral pyrite has been altered to sericite, quartz and siderite, and the original feldspars are also completely replaced by these three minerals (in CPL); (E) EHR80C, protuberances growing outwards from quartz, also present are zircon, ankerite and muscovite, and relict feldspar textures defined by sericite and fine grained quartz (in CPL); and (F) EHR81C, giant zircon crystals in association with bastnäsite-parisite, pyrite and quartz, and surrounded by sericite and fine grained quartz (in CPL).

alongside a vein that had intruded a dyke. Pyrite is the dominant sulphide mineral and is commonly clustered alongside altered mafic components as well as quartz. It is disseminated and euhedral, but typically shows signs of disequilibrium (sieve texture and embayments; Fig. 22d). Sphalerite, galena and chalcopyrite are associated with pyrite and generally only form minor sulphide phases as grains or small veinlets (Appx. D4e-f; Townend & Townend 2016a).

Giant (up to 500 μm) interstitial zircon are fairly abundant within the inner zone of hydrothermal alteration in the EHR (Fig. 22f and Appx. D3a), and often exhibit odd, anhedral and broken shapes. They are often associated with the clusters of altered mafic components and quartz, and are commonly partially altered to xenotime and thorite. Zircon grains are also markedly porous and contain parisite, xenotime, galena, ilmenorutile-ferrocolumbite and thorite inclusions, as seen in SEM images later. A dirty, black, patchy coating is also characteristic of the zircon in these hydrothermally altered granites, which may be a result of metamictisation. Within some of the less altered samples in this alteration zone in the EHR, the zircon also contains quartz inclusions (Fig. 23a). Bastnäsite group minerals form as alteration products of perovskite, ilmenite and/or ilmenorutile in less altered samples (Fig. 23b & Appx. D3b), while they form anhedral fine-grained masses associated with rutile/brookite, leucoxene and zircon in the most altered samples (Fig. 23c), and are altering to titanium oxide and sericite.

Towards the outer zone of this hydrothermal alteration, the granite has been offset along fractures and has also been sheared along discrete planes. Some of these fractures have undergone dilatation before becoming offset (i.e. transtensional stresses), and crystals of quartz have continued to grow and recrystallise in these cavities (Fig. 23d). A combination of dendritic/spherulitic muscovite and Ti-oxides have also crystallised in these cracks and drusy cavities (Fig. 23e & Appx. D3c). Rare chlorite veinlets are observed within this outer zone of hydrothermal alteration, while quartz, siderite, and ankerite veins occur in the inner zone. Some of the carbonate veinlets in the inner zone display non-systematic vein arrays and en echelon-type geometry (Fig. 23f), and tend to cross-cut the quartz veins.

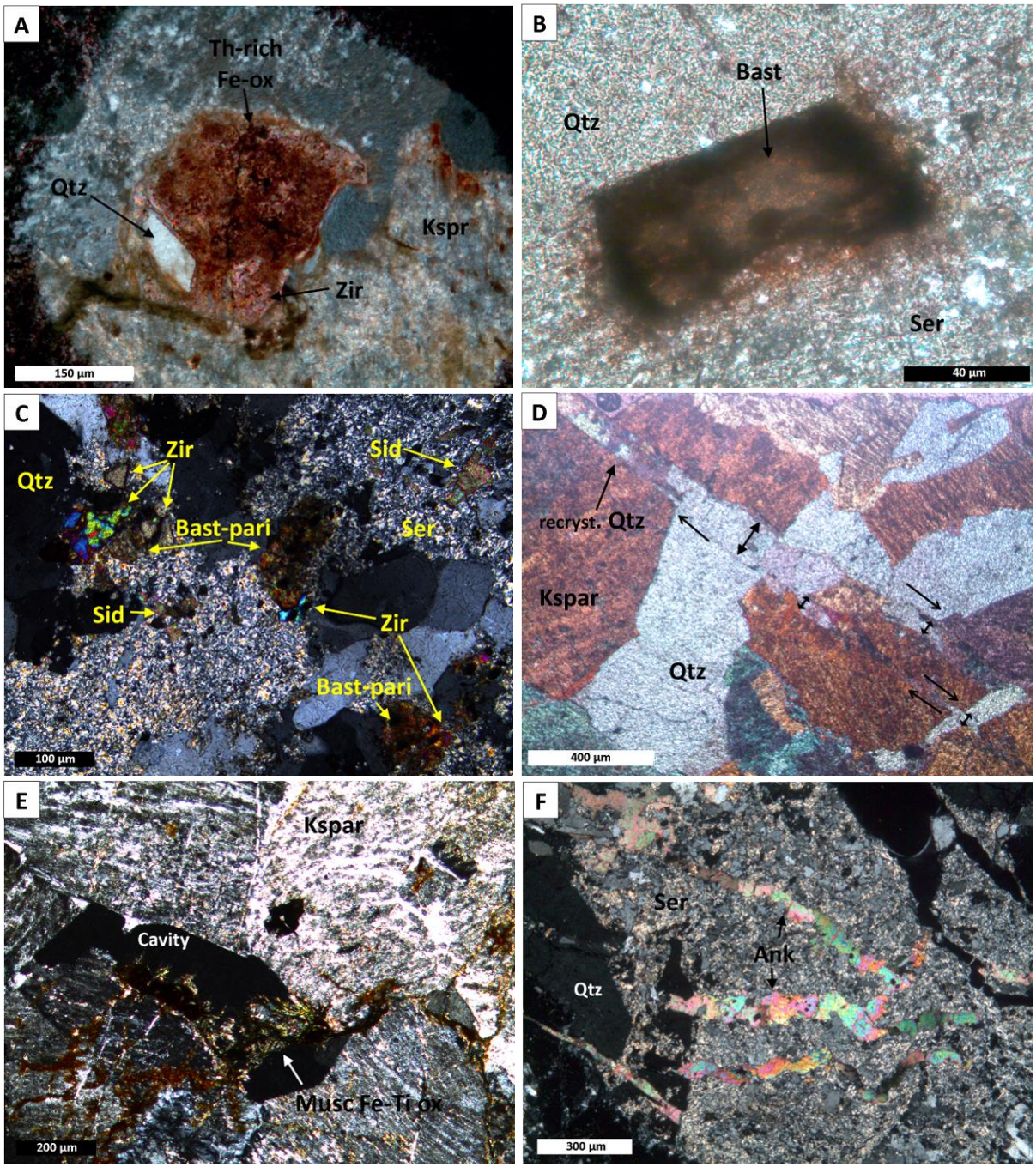

Figure 23. Photomicrographs of (A) EHR81I, metamict zircon with Th-rich Fe-oxide alteration product and quartz inclusion, surrounded by quartz as well as K-feldspar, which is altering to sericite and ankerite (in CPL); (B) EHR81A, a crystal composed of a mix of bastnäsite-TiO_2 surrounded by sericite and quartz (in PPL); (C) EHR81C, fine grained masses of bastnäsite-parisite associated with zircon and quartz, and surrounded by siderite, sericite and fine grained quartz (in CPL); (D) EHR81A, quartz offset along transtensional fractures, note quartz continued to crystallise as well as recrystallise (in CPL with the sensitive tint plate in); (E) EHR81A, intergrown muscovite and Fe-Ti oxides growing within a drusy cavity amongst perthitic K-feldspar that have undergone sericite and siderite alteration (in CPL); and (F) EHR81D, a non-systematic vein array of ankerite cross-cutting quartz and sericite in a granitic palimpsest (in CPL).

4.3.3 Cross-Cutting Veins

Quartz and carbonate veins up to ~15 cm wide cross-cut the FCG and have both sharp and gradational contacts; the latter is primarily defined by diffuse silicification and alteration of the granite to sericite and/or carbonates. For the purpose of simplicity, only veins with >50% vein quartz/carbonates and sharp contacts are described in this section. Please refer to Section 4.3.2 for a description of the diffuse hydrothermal replacement bodies in the FCG that are related to fluid conduits.

Vein quartz formed as either mosaic comb structures or as a crystal mesh of prisms elongated in the direction of the *c*-axis (Fig. 24a). One sample of a prismatic quartz vein is cross-cut by a comb quartz veinlet, and both are brecciated towards one end of the vein. The matrix of the breccia is filled with pulverised quartz; some has undergone dynamic recrystallisation, and ankerite occurs further away from the prismatic vein. Another brecciated vein (LHR25) contains highly altered clasts of granite in an ankerite matrix. The granite clasts have been altered to contain feathery sericite, quartz, zircon, muscovite and Ti-oxides, which were once likely feldspars, quartz and biotite. Some of these granite clasts are surrounded by columnar vein quartz (Fig. 24b), with evidence of some deformation indicated by elongate undulose extinction (Appx. D3d) and subgrains. The surrounding matrix has crystallised to coarse equidimensional ankerite, with microcrystalline ankerite sometimes at the boundary of the quartz (Fig. 24b) or scattered throughout it, replacing some of the larger ankerite crystals. This sample contains anomalous HREEs when compared to all other samples analysed, and euhedral synchysite and florencite were found scattered within the sericite in the altered granite clasts. Synchysite was also found scattered amongst the microcrystalline ankerite, with some synchysite crystals replaced by the ankerite, better seen in SEM images later. Florencite occurs as small zoned rosettes only within the sericite.

Carbonate veins are composed of coarsely crystalline rhombs and masses of ankerite, except for the small millimetre-scale fractures that are typically infilled by calcite. Lamellar twins are rare, but compositional zoning is relatively common. Sometimes microcrystalline ankerite is found scattered amongst coarser ankerite crystals (Fig. 24c) or containing 'phenocrysts' of the coarser ankerite (Fig. 24d).

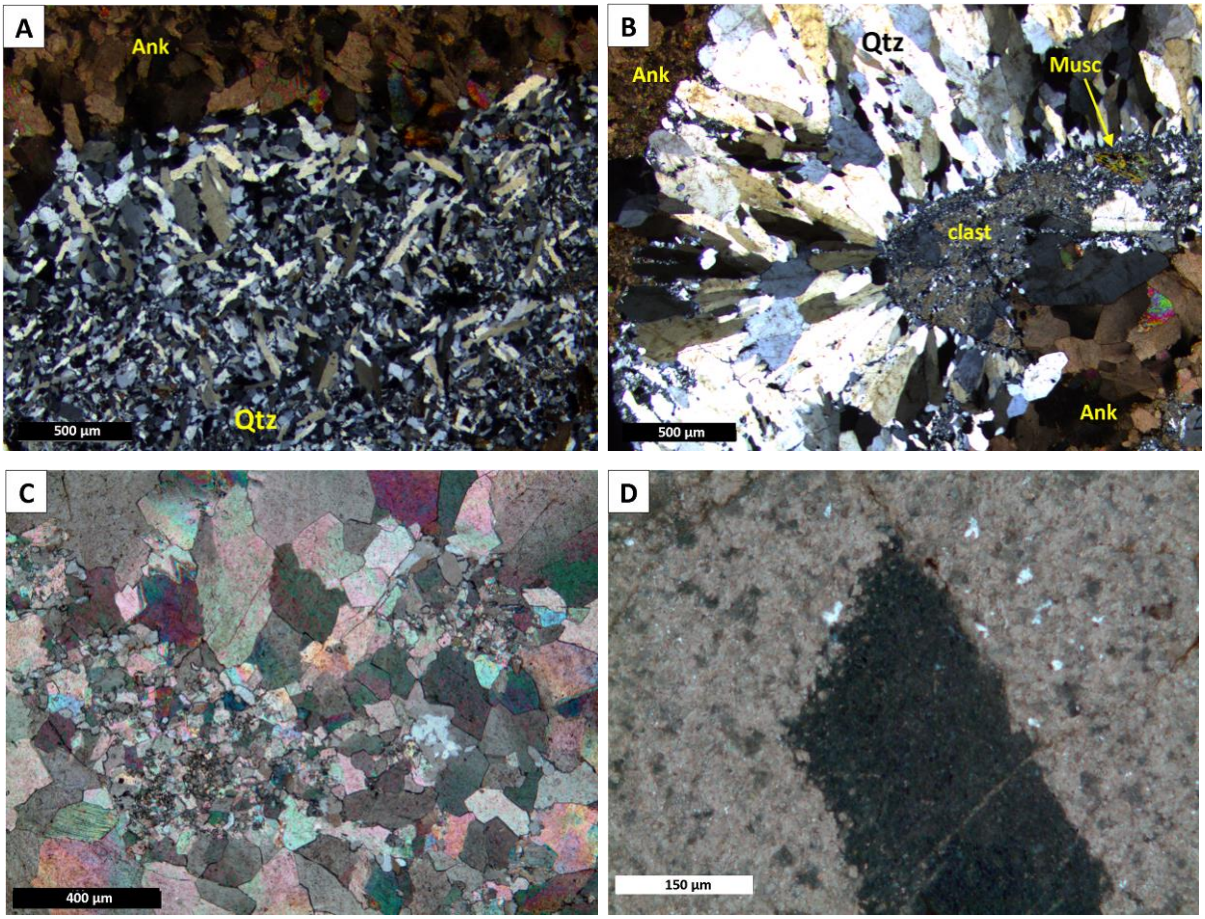

Figure 24. Photomicrographs of (A) EHR80C, a vein of prismatic quartz elongated in the direction of the *c*-axis, with small patches of microcrystalline quartz and a change to ankerite further up (in CPL); (B) LHR25, a clast of highly altered granite containing sericite, quartz and muscovite is surrounded by columnar vein quartz and coarse and microcrystalline ankerite (in CPL); (C) LHR25, patches of microcrystalline ankerite amongst coarser ankerite crystals (in CPL); and (D) LHR57, a coarse ankerite 'xenocryst' set within microcrystalline ankerite (in CPL).

Sometimes multiple stages of fluids are evident from cross-cutting relationships between veins of different composition, and the carbonates commonly formed at a later stage to an earlier silica-rich fluid. One sample contains altered granite clasts near the vein contact which are surrounded by columnar vein quartz followed by a change to ankerite with comb textures and then euhedral rhombs of ankerite grading outwards to microcrystalline ankerite. Prismatic vein quartz (elongated in the *c*-axis direction), comb quartz and microcrystalline patches of quartz also occur in this sample, often in contact with the FCG. Sometimes clasts of this quartz are included within an adjoining ankerite veinlet, or the quartz cross-cuts an ankerite veinlet, and sometimes it occurs the other way around. This suggests at least four generations of fluids that alternated in composition between silica-carbonate-silica-carbonate.

4.3.4 Hohonu Dyke Swarm (HDS) and Other Dykes

The following descriptions of the cross-cutting dykes are separated into mafic, intermediate and felsic compositions. The mafic dykes form part of the HDS, while the felsic dykes are chemically similar to the FCG. Rock names are based on chemical classification, and not the composition of phenocrysts. General textures of all dykes include porphyritic, cumulophyric clusters of phenocrysts, and generally low (<2 modal %) to non-existent vesicularity. Small anastomosing quartz and/or calcite veinlets are relatively common features cross-cutting all compositions.

Within the mafic dykes, phenocrysts form 5–39 modal % of the rock, and are commonly moderately affected by deuteric fluid, which has resulted in chlorite, calcite, sericite and/or iddingsite alteration. Plagioclase constitutes between 1–20 modal % of the phenocrysts and is generally euhedral with polysynthetic twins. Some contain glassy quartz inclusions, while others are embayed. In addition, many plagioclase crystals have been affected by sericite and carbonate alteration. Nepheline is present in the two tephrites, comprising between 2–15 modal %, and is generally completely replaced by carbonates. One of these tephrites contains amygdales of calcite, zeolites, plagioclase lathes and juvenile amphibole, while the other tephrite has a coarse groundmass of feldspar and feldspathoid lathes (Fig. 25a). Quartz (1 modal %) was only observed in one sample, where it formed rare xenocrysts with embayments and reaction rims. Olivine constitutes between 1–5 modal % of the basalts, and has been highly altered to carbonates ± iddingsite. Other mafic phases, such as augite (5–10 modal %) and amphibole (8 modal %) are common and relatively unaltered. Augite is sometimes broken and forms both small and large populations, while amphibole generally forms a juvenile phase. The groundmass is composed of plagioclase lathes, secondary chlorite, calcite, juvenile amphibole and pyroxene, biotite, nepheline, Fe-oxides and rare apatite and zircon. Cross-cutting calcite veinlets have comb textures, columnar, fibrous and/or equant habits. Fe-oxides sometimes form envelopes to these veinlets (Fig. 25a) as well as forming small solution seams sub-parallel to them.

Intermediate dykes contain 6–35 modal % phenocrysts. Of these, plagioclase constitutes 1–30 modal %, has rare compositional zoning and is commonly

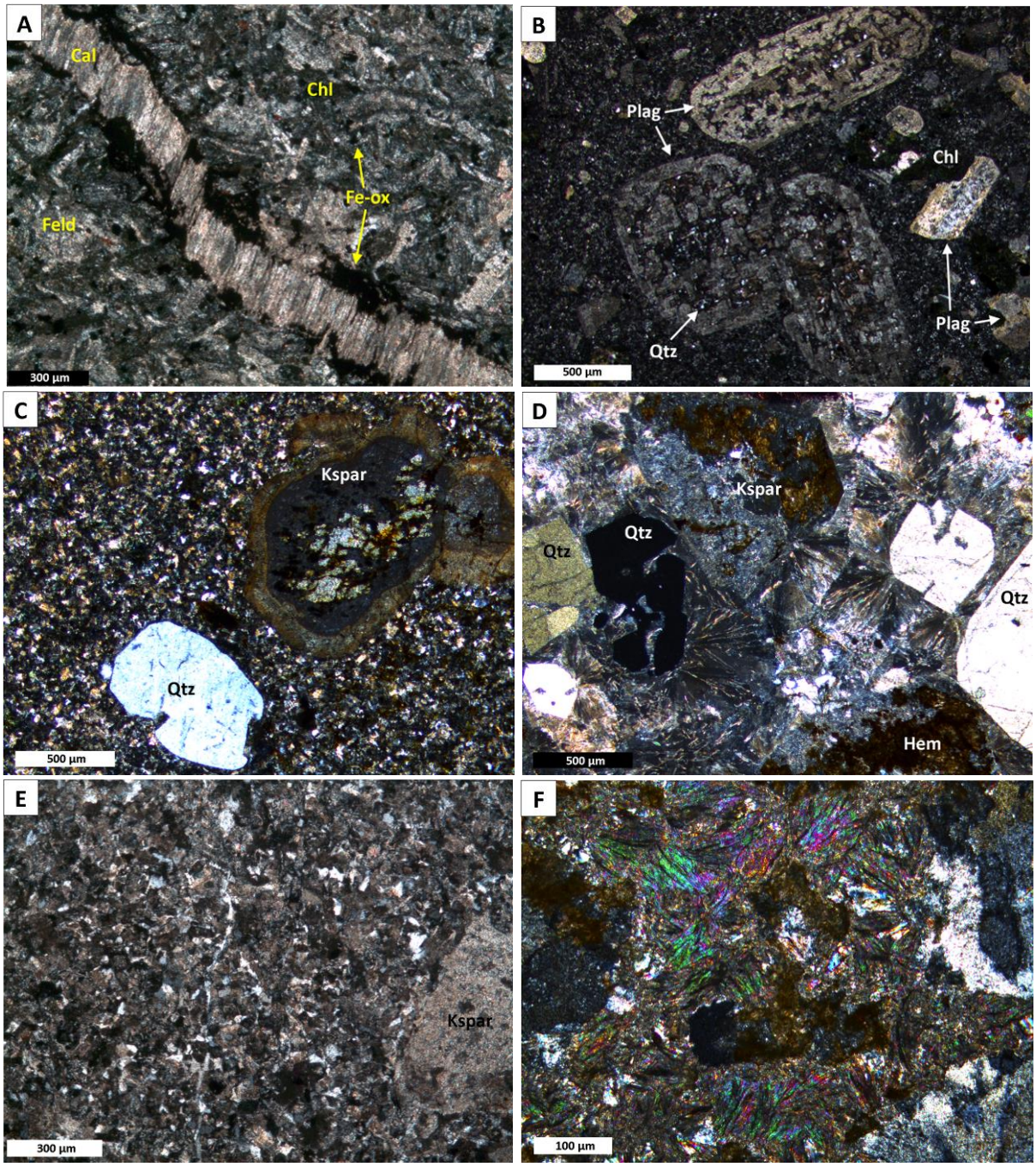

Figure 25. Photomicrographs of (A) LHR59, a veinlet of fibrous calcite with Fe-oxide envelopes cross-cuts the groundmass of a tephrite, which is dominantly composed of feldspars, feldspathoids, chlorite and Fe-oxides (in CPL); (B) LHR69, large, euhedral, skeletal plagioclase phenocrysts with glassy quartz inclusions surrounded by smaller plagioclase phenocrysts, chlorite and a groundmass of plagioclase, chlorite, Fe-oxides, calcite and rare quartz (in CPL); (C) LHR66, euhedral skeletal quartz and altered K-feldspar phenocrysts surrounded by a groundmass of feldspar lathes, carbonates, devitrified volcanic glass and Fe-oxides (in CPL); (D) LHR38, phenocrysts of skeletal quartz and altered K-feldspar surrounded by spherulitic K-feldspar altering to sericite, carbonates and hematite along fronds (in CPL); (E) LHR50, devitrified groundmass of a felsic dyke consisting of K-feldspar, quartz and minor biotite, Fe-oxides and plagioclase (in CPL); and (F) LHR38, bunches of spherulitic muscovite that crystallised within a miarolitic cavity (in CPL).

xenocrystic. They form large, skeletal, embayed crystals and are surrounded by brown reaction rims. They also contain glassy quartz inclusions that are more felsic

than the groundmass (Fig. 25b) and are relatively altered to sericite and/or carbonates, and some have become broken and/or rounded. A few samples also contain a smaller, non-skeletal plagioclase population (Fig. 25b) without glassy inclusions. K-feldspar constitutes 1–10 modal % of phenocrysts in these rocks and contain some quartz inclusions. They are also frequently surrounded by reaction rims and have mild sericitisation (Fig. 25c). Quartz constitutes 1–8 modal % and is often skeletal and rounded (Fig. 25c), with some nucleation rims. The mafic component is, at most, represented by pseudomorphs of chlorite (Fig. 25b), carbonates, limonite and other Fe-oxides, which suggest they might have originally been pyroxene, amphibole and/or biotite. Oxidation of the Fe-oxides is common in the red samples, and is likely the reason for their red colouration. The groundmass is composed of feldspar lathes altered by different extents to sericite and/or carbonates, quartz, chlorite, Fe-oxides, and rare apatite, zircon and spherulitic muscovite. It sometimes contains devitrified volcanic glass and is occasionally slightly trachytic.

The felsic dykes contain 25–30 modal % phenocrysts, unless they are completely devitrified, which is common in the most felsic rocks. K-feldspars constitute 11–12 modal %, are often large and perthitic, and sometimes form granophyric intergrowths with surrounding quartz phenocrysts. They are variably altered to sericite, carbonates and/or limonite, which sometimes just occur as euhedral pseudomorphs, and sometimes form xenocrysts. Quartz constitutes 6–8 modal % and usually has slight undulose extinction. The quartz is commonly euhedral and skeletal (Fig. 25d), but has undergone later rounding. Plagioclase is a minor phase at ~1 modal %, and is commonly anhedral and xenocrystic. Biotite is the only mafic phase observed, constituting up to 5 modal % of these rocks, and contain small zircon inclusions. Rare accessory allanite is sometimes present. The groundmass is dominantly composed of K-feldspar and quartz, which is often devitrified (Fig. 25e), with minor biotite, chlorite, plagioclase, Fe-oxides and zircon present. Two rhyolitic samples have become highly devitrified. In these samples, coarse spherulitic K-feldspar has altered to sericite along granophyric fronds and forms radial and segmented shapes surrounding the euhedral phenocrysts (Fig. 25d). Also present in these samples are bunches of spherulitic muscovite that have formed

within miarolitic cavities (Fig. 25f); the edges of the cavities are defined by the extent of the devitrified groundmass.

4.4 Whole Rock Geochemistry

Where both ICP-MS/AES and XRF results were available, the ICP-MS/AES results were used in favour of the XRF results; however, a quick scatter plot of each element indicated a very good correlation between the two different methods (r=0.999 for major elements and r=0.992 for trace elements). Therefore, data from one method could be used when data from the other was unavailable. Summary tables of the full whole rock geochemical results for each method can be found in Appx. E.

4.4.1 Major Elements

Whole rock geochemical classification of 54 samples using Igpet software separates the dominant granitic phase from the quartz alkali-feldspar (QAF) syenite, and illustrates the compositional diversity of the dykes (Fig. 26a). The pegmatite sample is off the plot to the right with 87 wt. % silica. The more mafic dykes range from tephrites and basalts to potassic trachybasalts, while intermediate dykes include shoshonites, trachyandesites and trachytes. The more felsic dykes are trachydacite and rhyolite in composition.

Shand's alumina saturation index (Fig. 26b) indicates that the majority of the FCG is weakly peraluminous (ASI <1.1), indicative of crustal melting (Frost et al. 2001). The exceptions to this are hydrothermally altered samples of FCG that are more strongly peraluminous, one syenite that plots on the boundary of metaluminous and peralkaline geochemistry, and some of the mafic-rich FCG varieties that show variation similar to the other two aforementioned exceptions. Felsic dykes range from strongly peraluminous to weakly metaluminous, intermediate dykes range from weakly to moderately metaluminous, and mafic dykes are predominantly strongly metaluminous (with one exception that has strongly peraluminous geochemistry).

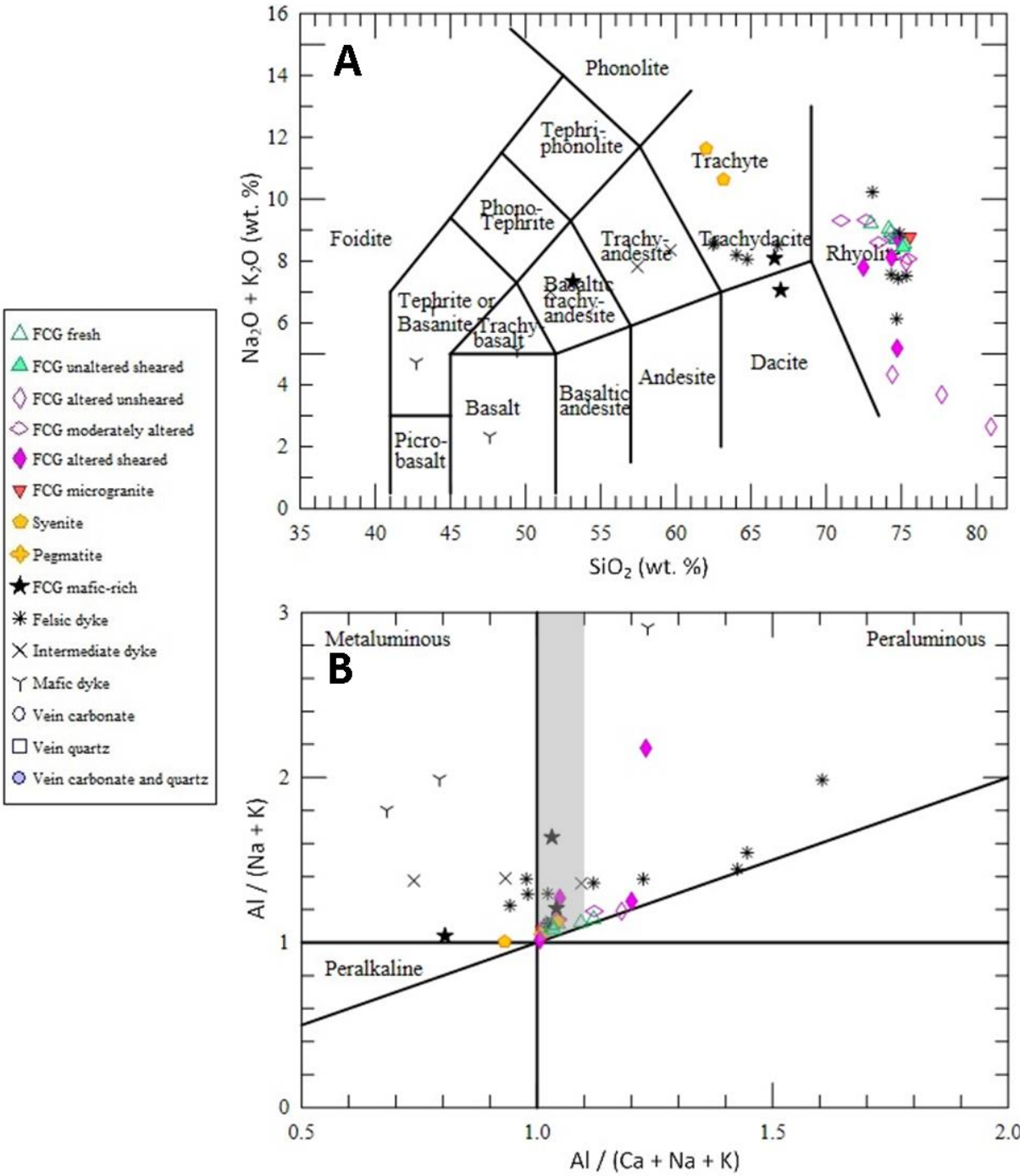

Figure 26. Geochemical plots for 48 samples of the French Creek Granite and Hohonu Dyke Swarm showing (A) TAS chemical classification diagram after Le Bas et al. (1986); and (B) classification of alumina saturation after Shand (1927), the grey field indicates weakly peraluminous types.

The major oxides were plotted on Harker variation diagrams (Fig. 27). Firstly, the relatively smooth trends (with the exception of K_2O and Na_2O) strongly indicate that the magmas are genetically related and that the magma which formed the FCG has been highly differentiated from the parental magma, which is more closely represented by the mafic HDS. There is, however, some scatter which can be

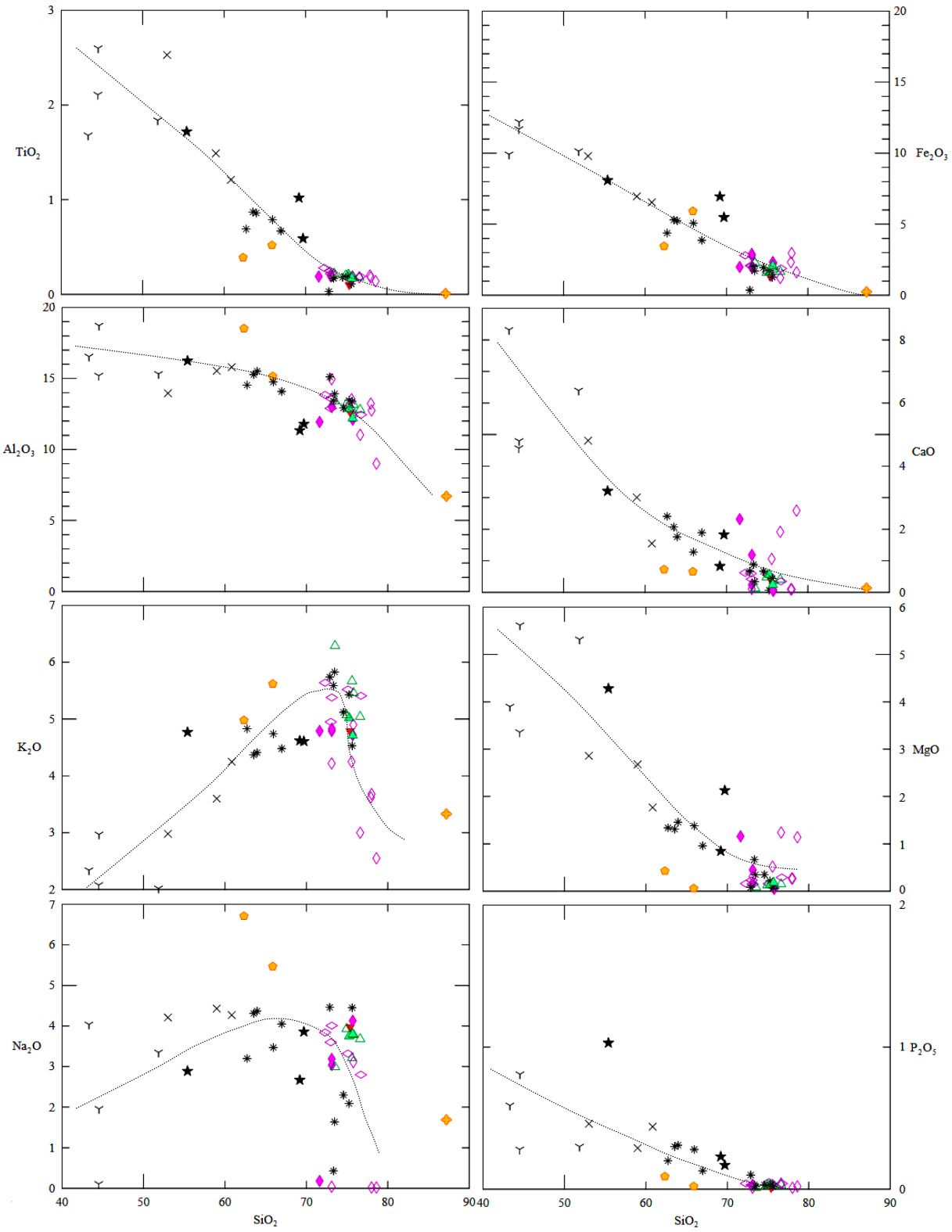

Figure 27. Harker variation diagrams for 48 analysed samples showing wt. % major oxides vs. wt. % silica. Please refer to Figure 26 for the legend.

expected in nature and from analytical error (Winter 2011). Typical FCG has very low CaO (0.1–1.2 wt. %) and MgO (0.1–0.5 wt. %) content, while Al_2O_3 (12.2–13.9 wt.

%) and SiO_2 (72.3–76.7 wt. %) are high, Fe_2O_3 (1.3–2.8 wt. %) is also relatively high, and K_2O (4.7–6.3 wt. %) is > Na_2O (2.8–4.0 wt. %). Compatible elements, such as Ti, Fe, Ca, P and even Al, show a continuous decrease with increasing silica content from the mafic, intermediate and felsic dykes through to the mafic-rich FCG, syenite, typical FCG and finally, the pegmatite. Potassium generally displays an incompatible trend from the mafic dykes through to the unaltered, slightly altered and/or sheared FCG, which then decreases again in the most altered FCG and the pegmatite. The trend in the Na_2O content is difficult to decipher; with some imagination it may be interpreted to increase slightly before decreasing again in the more altered units, in some felsic dykes and in the pegmatite. Other than these, and the two syenite samples which display a different trend, there is generally little change in Na_2O concentration with increasing silica content. The scattered K_2O and Na_2O concentrations in the most altered FCG samples highlights the difficulty in interpreting these elements in rocks that have undergone hydrothermal alteration, owing to their high mobility during water-rock interactions.

4.4.2 Trace Elements

A suite of trace elements were obtained in order to better understand the origin and petrogenesis of the FCG. The FCG falls in the A-type granite field on an S-I-A granitoid classification diagram (Fig. 28a), and into the A_1 sub-classification of Eby (1990, 1992), with Y/Nb of <1.2. Its geochemistry also places it in the within-plate granite (WPG) field on a tectonic discrimination diagram (Fig. 28b). The pegmatite is the only exception, which lies just inside the volcanic arc granite (VAG) field; however, it is disregarded because it is not representative of the granitoid. In addition, the FCG can be classified as an alkali-calcic ferroan granitoid (Fig. 28c), which signifies strong iron enrichment in the magma and is a common characteristic of A-type granitoids (Frost et al. 2001). There are a few exceptions to this, which are samples that have undergone intense hydrothermal alteration, and which, for the purposes of this geochemical classification, are disregarded. On an AFM diagram (Fig. 28d), the FCG and HDS classify as tholeiitic (except for those same altered samples of FCG that plotted in the magnesian field in Fig. 28c, which will be disregarded here also); part of the silica-oversaturated subalkaline magma series

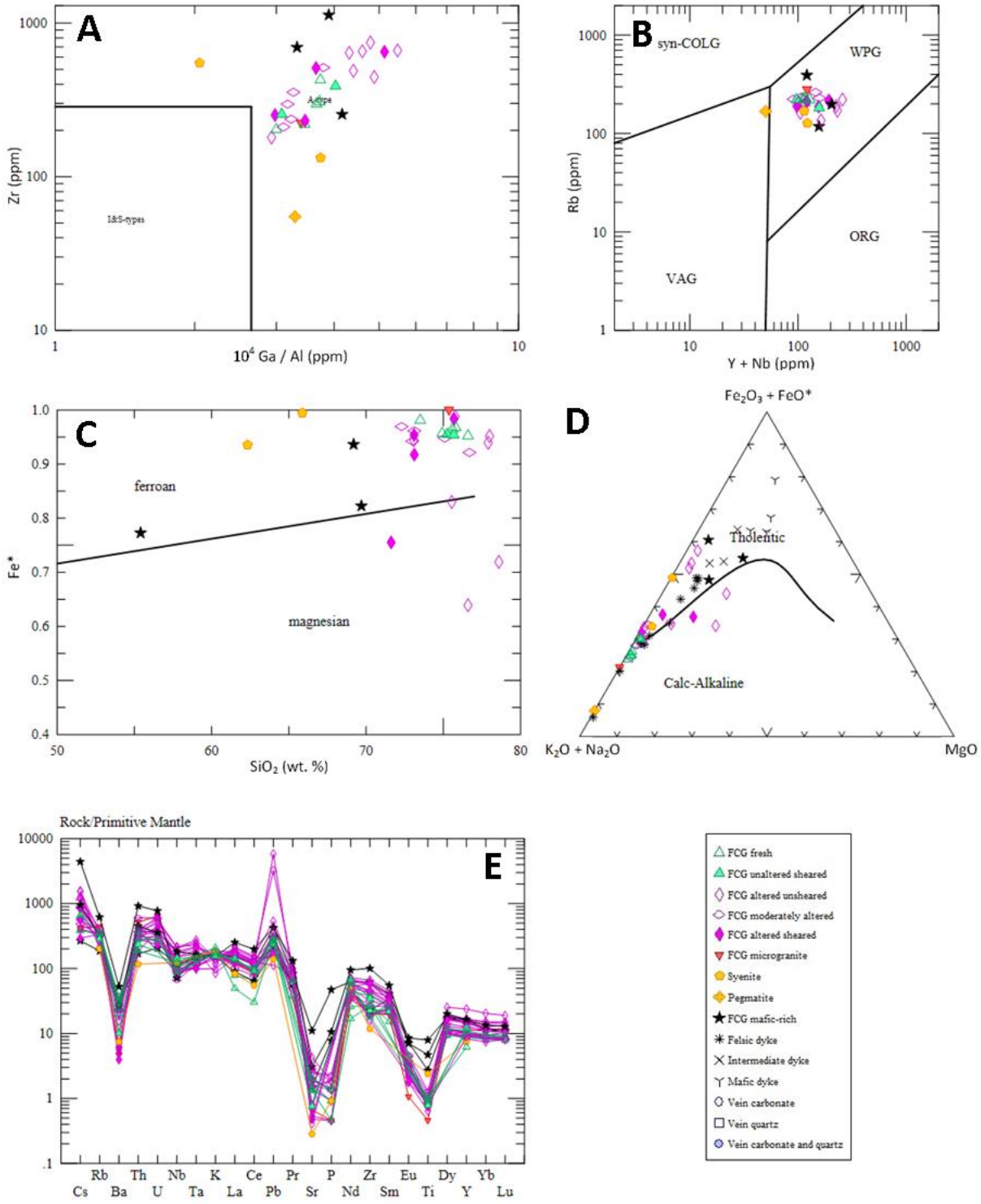

Figure 28. Geochemical plots for 48 samples of the French Creek Granite and Hohonu Dyke Swarm showing (A) S-I-A granitoid classification diagram of Whalen et al. (1987); (B) tectonic discrimination diagram after Pearce et al. (1984); (C) diagram showing the boundary between ferroan and magnesian plutons from Frost et al. (2001); (D) AFM diagram of Irvine & Baragar (1971) showing the tholeiitic composition of the French Creek Granite and Hohonu Dyke Swarm; and (E) mantle-normalised spider diagram after Sun & McDonough (1989).

typical of divergent plate settings. The AFM diagram also illustrates the depletion of iron and enrichment of alkalis as the melt evolved from the mafic HDS towards the

more felsic FCG. A more magnesium-rich primitive magma appears to be missing from the sampled dataset.

Typical FCG is characterised by high Zr (203–514 ppm), Ga (21–28 ppm), Nb (47–102 ppm), Y (28–65 ppm) and Rb (183–282 ppm), and low Cr (≤10 ppm), Ni (≤4 ppm), Sr (14–60 ppm) and V (5–15 ppm). Thorium ranges between 16–52 ppm and U between 5–14 ppm. Additionally, there are Pb and Zn anomalies in the inner zone of hydrothermal alteration in the EHR, with concentrations up to 415 ppm and 1000 ppm, respectively. These anomalies coincide with the occurrence of galena and sphalerite. On a mantle-normalised spider diagram (Fig. 28e), the different rock types share similar peaks and troughs, for example they all have a trough at Ba, Sr, P, Eu and Ti and a peak at Pb and Th, which strongly suggests they are petrologically related (Winter 2011), and is indicative of the removal of plagioclase, apatite and a Ti-rich phase, such as ilmenite, amphibole or biotite (Waight 1995).

It is evident in Fig. 29a that the concentration of total (Σ) REEs varies considerably for the different lithologies. The quartz and carbonate veins have some of the lowest ΣREEs, as do the syenite and pegmatite. The mafic dykes also have generally low ΣREEs, except for one tephrite that has almost 400 ppm ΣREEs. Total REEs increase almost linearly with an increase in K_2O through the intermediate dykes to the felsic dykes. The majority of the FCG, which includes the microgranite, unaltered, sheared, moderately altered, and rare strongly altered samples, plot roughly in the same area as the felsic dykes. The samples from the zone of hydrothermal alteration in the EHR plot separate to all other FCG and are consistently enriched in REEs; one other highly altered sample of FCG from the EHR (ca. 120 m downstream of the alteration zone) also plots in this area. The mafic-rich varieties of the FCG are highly variable; one sample contains the highest amount of ΣREEs (almost 800 ppm), one sample has ΣREEs similar to the EHR alteration zone, and the other has ΣREEs similar to the felsic dykes. The red dashed line indicates the average ΣREE content in the upper crust, which is ~150 ppm (Taylor & McLennan 1985).

The difference in REE content between the altered, unaltered and mafic-rich varieties of the FCG can also be observed on a chondrite-normalised spider diagram

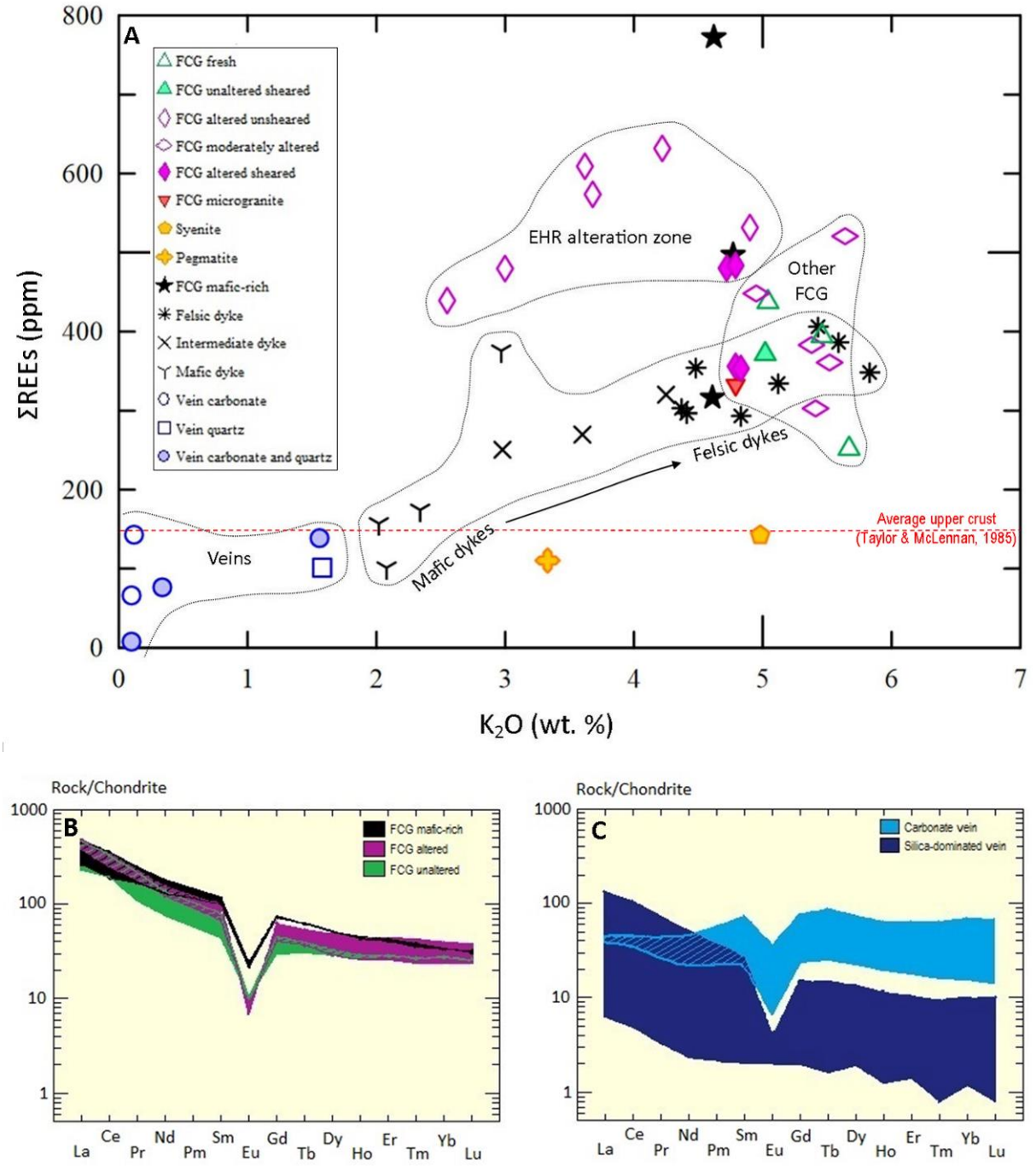

Figure 29. Geochemical plots of 54 samples of the French Creek Granite and Hohonu Dyke Swarm showing (A) total (Σ) REEs vs. changing K_2O content; (B) chondrite-normalised spider diagram showing the difference in REE content between altered and unaltered French Creek Granite and the mafic-rich variety; and (C) chondrite-normalised spider diagram showing the difference in REE content between carbonate and silica-dominated veins.

(Fig. 29b), although all are enriched in LREEs relative to the HREEs, which have a flatter trend. In this figure, the altered FCG has consistently higher concentrations of REEs, especially HREEs, than the unaltered FCG, except for the stronger negative Eu anomaly, which likely reflects the higher mobility of Eu during alteration (Bowden 1985; Bowden & Kinnaird 1984). The mafic-rich variety of the FCG also typically

contains more REEs than unaltered FCG, especially HREEs (Fig. 29b). The negative Eu anomaly is also less pronounced in this lithology, probably because it contains more plagioclase. The pegmatite and syenite, which are not shown on these spider diagrams, contain less REEs than the typical FCG, and display a very strong negative and very slight positive Eu anomaly, respectively. The silica-dominated veins (Fig. 29c) also exhibit LREE enrichment relative to the HREEs, contain lower amounts of REEs in general, and some contain a negative Eu anomaly as well. The carbonate veins have a different trend when compared to all of the other lithologies, with a flat HREE trend and depletion in LREEs. They also contain a small negative Eu anomaly.

There is some positive correlation between ΣREEs and Zr, U, Nb and Y, which can be seen in Fig. 30. There are a few outliers and the uranium data are generally more scattered, but overall, there is a reasonable relationship between the presence of these elements and the presence of ΣREEs.

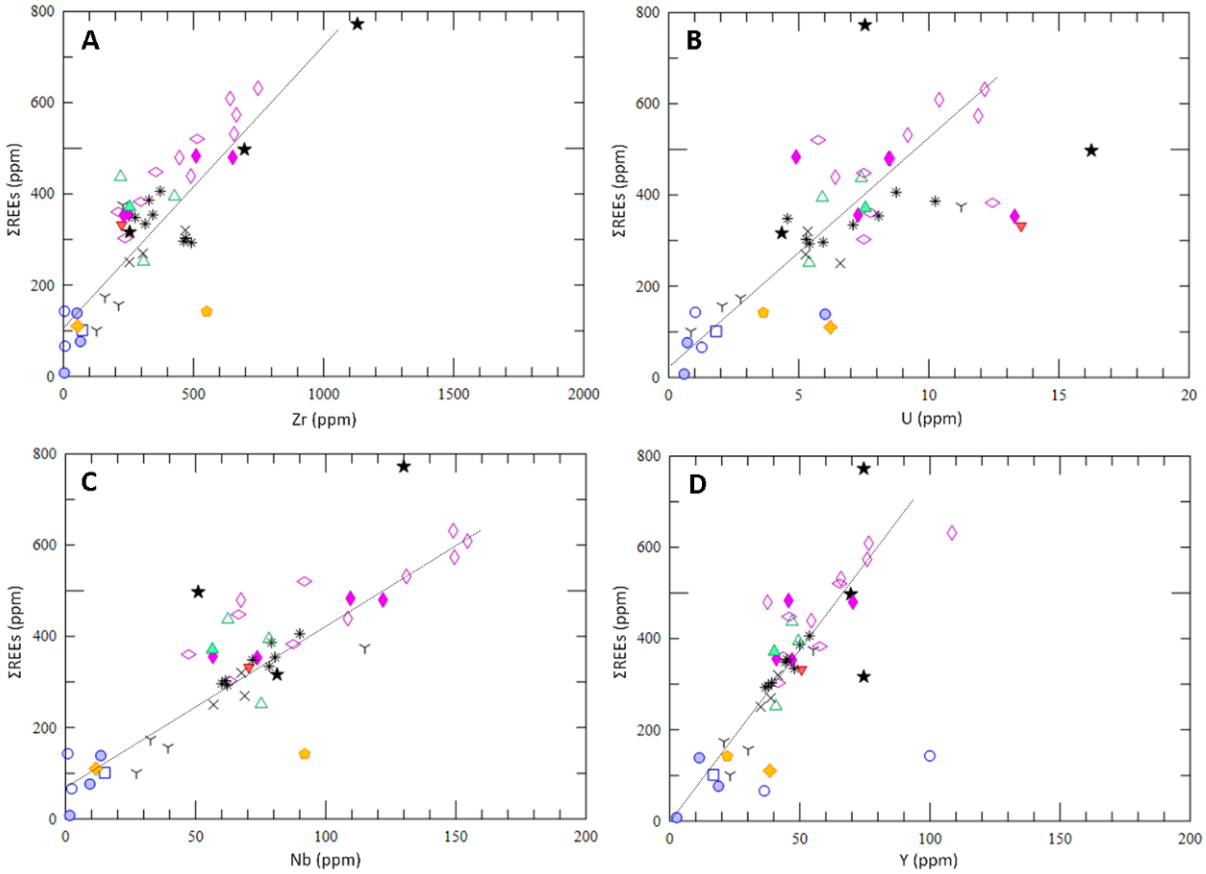

Figure 30. Bivariate plots of total (Σ) REEs vs. (A) zirconium content; (B) uranium content; (C) niobium content; and (D) yttrium content. Please refer to Fig. 29a for the legend.

4.5 XRD Analysis

One clay sample (EHR81c) from the inner zone of hydrothermal alteration in the EHR (Fig. 14) was analysed by XRD and contains 20% halloysite (part of the kaolin group) and 80% muscovite/sericite. The peak positions for halloysite are slightly offset; therefore, the halloysite might be interstratified with the muscovite/sericite. Additionally, it is likely that the estimated quantities of both of these minerals are also skewed due to the strong reflections of muscovite/sericite and the presence of quartz. The software for reducing this effect was not available.

4.6 Zircon Trace Element Analysis

From a total of 25 zircon grains analysed, 14 analyses from sample EHR80c were <10% discordant and were used in U-Pb age calculations (Appx. F1a). Zircon from sample EHR81c produced highly discordant results (Appx. F1b), which made calculation of a meaningful $^{206}Pb/^{238}U$ age problematic for that sample. The concordia age of sample EHR80c is 82.78 ± 0.83 Ma (Appx. F1a) and the weighted mean age, using the 14 analyses that were <10% discordant, is 82.55 ± 0.85 Ma (Appx. F1c), which is considered the best estimate of the magmatic age of crystallisation for this granite. The weighted mean has a mean square weighted deviate (MSWD) of 0.73, indicating the presence of only one age population. This age basically overlaps with both the previous ages of 81.7 ± 1.8 Ma and 84.11 ± 0.44 Ma for the FCG determined by Waight et al. (1997) and van der Meer (pers. Comm.), respectively. The average Ti-in-zircon temperature (Ferry & Watson 2007) of formation for sample EHR80c is 773°C and for EHR81c is 805°C. The full analytical results for these two samples can be found in Appx. F1.

Of the reference standards analysed, the R33 secondary standard produced an age of 416.3 ± 3.3 Ma, which overlaps the accepted age of 419.26 ± 0.39 Ma, while the TEMORA-2 standard produced an age of 416.2 ± 1.6 Ma, well within the accepted age of 416.78 ± 0.33 Ma (Black et al. 2003, 2004).

The chondrite-normalised spider diagram in Figure 31 illustrates distinct enrichment of all analysed REEs in zircon from sample EHR81c, which is from the zone of hydrothermal alteration in the EHR, when compared to those in sample

EHR80c. Two exceptions with higher anomalies have been removed from EHR80c and one from EHR81c. Both of these samples are also enriched in HREEs relative to the LREEs, due to the similarity in atomic radii between $HREE^{3+}$ and Zr^{4+} (Hanchar & van Westrenen 2007), and have a slight negative Eu anomaly. A distinct difference in trace element abundance between the two rock types can also be observed in Fig. 32. Figures 32a–b illustrate that Ce and Y are enriched in sample EHR81c when compared with EHR80c, while Lu is only slightly enriched (Fig. 32c) and Zr and Hf show relative depletion in comparison to EHR80c (Fig. 32d–e). Figure 32f shows that the Ti-in-zircon temperatures tend to be higher for the zircon in EHR81c when compared with zircon in EHR80c.

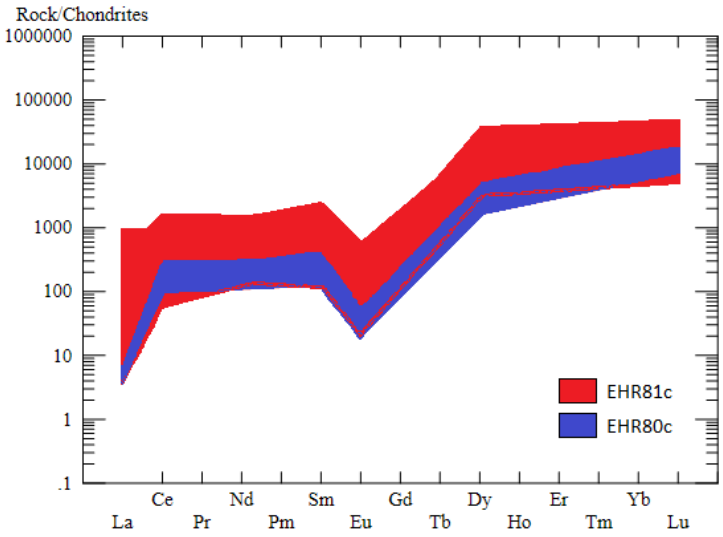

Figure 31. Chondrite-normalised spider diagram showing REE content in zircon from EHR81c (red) and EHR80c (blue).

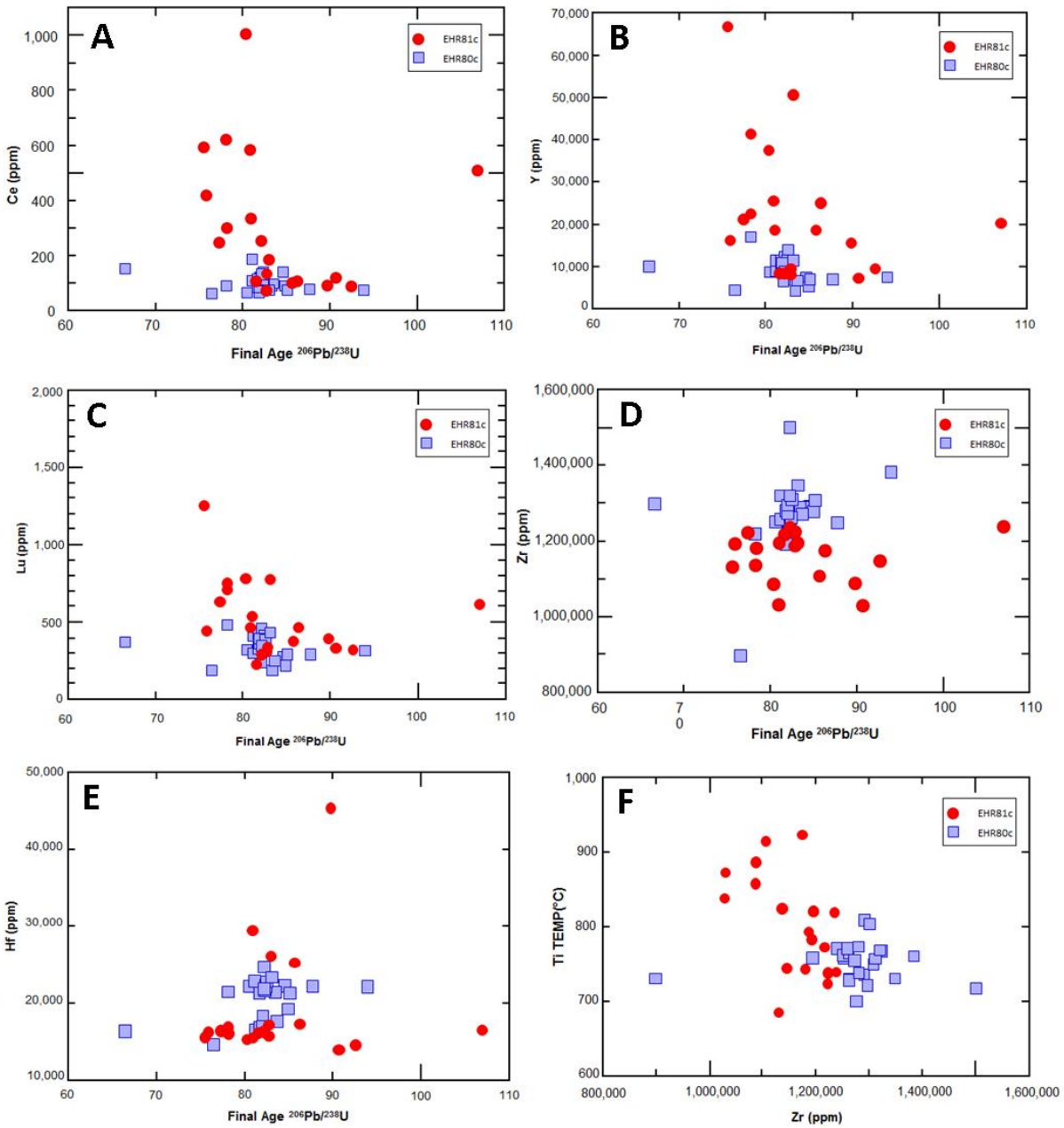

Figure 32. Trace element abundances in sample EHR81c (red circles) vs. EHR80c (blue squares) showing (A) cerium vs. age; (B) yttrium vs. age; (C) lutetium vs. age; (D) zirconium vs. age; (E) hafnium vs. age; and (F) Ti-in-zircon temperature vs. zirconium.

A more detailed analysis of sample EHR81c using cathodoluminescence (CL) imaging revealed that four of the nine zircon displayed some type of zoning, which included thin laminations (Fig. 33a), irregular patches (Fig. 33b) and a distinct inherited core. The other five zircon were un-zoned and were partially covered in semi-transparent grime (Fig. 33c–d). Furthermore, the majority of the zircon, especially the very large ones, had odd shapes with sharp corners, indicative of interstitial habits.

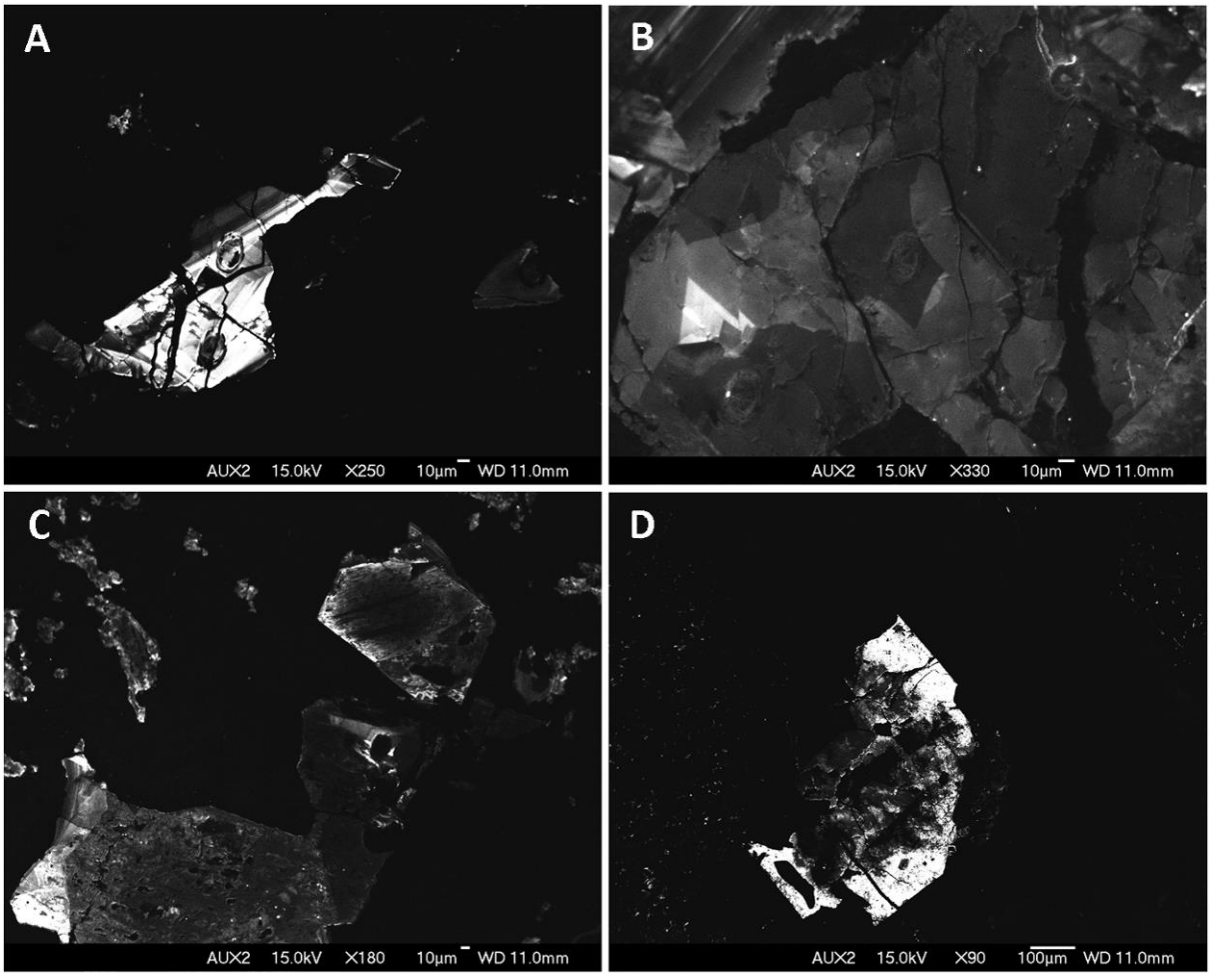

Figure 33. Cathodoluminescence imaging of zircon in sample EHR81c revealed (A) thinly laminated and (B) irregular zonation, with most of the zircon displaying very little to no zoning, and a coat of semi-transparent grime coating them (C and D). Bright areas indicate high lead, while dark areas indicate high uranium. The oval-shaped holes in the minerals are from previous laser ablation analysis.

4.7 Bastnäsite Trace Element Analysis

A semi-quantitative analysis by LA-ICP-MS of nine bastnäsite grains in sample EHR81c yielded an average composition of 31 wt. % Ce_2O_3, 18 wt. % La_2O_3, 11 wt. % Nd_2O_3, 3 wt. % Pr_2O_3, 2 wt. % each of CaO and Sm_2O_3, 1 wt. % ThO_2, and <1 wt. % Gd_2O_3, Y_2O_3, FeO, SrO and MgO (Table 4). Loss on ignition (LOI) was relatively high at 29 wt. % and likely represents the fluorine and carbonate content of the mineral. The total rare earth oxide concentration for the analysed bastnäsite in the FCG is between 61.3 and 72.5 wt. %. A tenth grain has been left out of the calculations in Table 4 and Figure 34, because it had much higher contamination by other elements, suggesting it was either intergrown with another mineral or only the edge of the grain was analysed. In Figure 34 it can be seen that LREEs are enriched

within bastnäsite, and a negative Eu anomaly is also present. The full elemental concentrations can be found in Appx. F2.

Table 4. The abundance of REOs and other oxides in nine analysed bastnäsite grains.

	Wt% oxide		
	Average	Maximum	Minimum
Ce_2O_3	31.44	32.09	30.32
La_2O_3	17.81	20.40	15.67
Nd_2O_3	10.54	11.44	9.78
Pr_2O_3	3.24	3.37	3.04
CaO	2.04	2.62	1.71
Sm_2O_3	1.63	2.10	1.24
ThO_2	1.38	2.31	0.93
Gd_2O_3	0.97	1.36	0.67
Y_2O_3	0.85	1.74	0.57
FeO	0.65	1.82	0.15
SrO	0.12	0.21	0.06
MgO	0.09	0.20	0.02

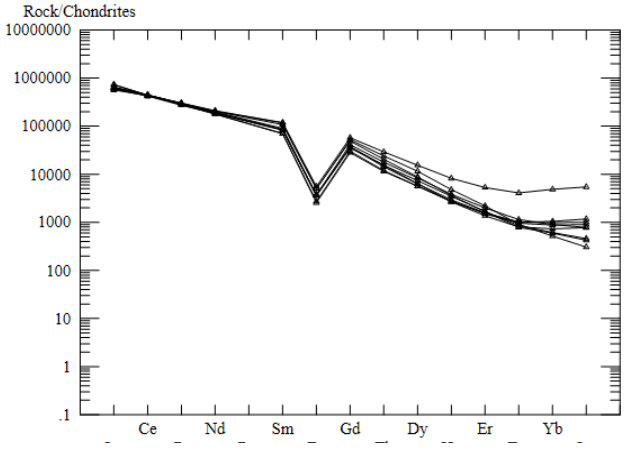

Figure 34. Chondrite-normalised spider diagram showing REE content in bastnäsite from EHR81c.

4.8 SEM-EDS Analysis

A brief description of the chemical and, in some cases, textural analyses of each of the rare earth (RE) minerals follows. The chemical formula of each RE mineral is given in Table 5. Please refer to Table G1 for the average, maximum and minimum values for each element that was found in each RE mineral.

Table 5. The chemical formula of the rare earth minerals present within the French Creek Granite.

RE mineral	Chemical formula
Fluocarbonates	
Bastnäsite-(Ce)	$(Ce,La)(CO_3)F$
Parisite-(Ce)	$Ca(Ce,La)_2(CO_3)_3F_2$
Synchysite-(Ce)	$Ca(Ce,La)(CO_3)_2F$
Oxides	
Loparite-(Ce)	$(Ce,La,Na,Ca)(Ti,Nb)O_3$
Fergusonite-(Y)	$YNbO_4$
Silicates	
Allanite-(Ce)	$(Ce,Ca)_2(Al,Fe^{3+})_3(SiO_4)_3OH$
Perrierite-(Ce)	$(Ce,Ca,Th)_4(Mg,Fe^{2+})_2(Ti,Fe^{3+})_3Si_4O_{22}$
Phosphates	
Monazite-(Ce)	$(Ce,La,Nd,Th)PO_4$
Xenotime-(Y)	YPO_4
Florencite-(Ce)	$CeAl_3(PO_4)_2(OH)_6$

Allanite-(Ce)

Total rare earth oxides (REOs) contribute 26.1 wt. % on average to the 12 grains of allanite that were analysed (samples GR03, LHR36 and EHR79). Cerium was the dominant REE (14.8 ox. %) in all but one grain, with lesser La (8.9 ox. %) and Nd (2.4 ox. %) substitution also occurring. No Y was measured in any of the grains. Calcium comprised ~10 ox. % of the grains and minor Ti (2.4 ox. %) was also present. The other elements present, and essential constituents of the mineral, were Al (10.9 ox. %), Fe (19.9 ox. %) and Si (30.5 ox. %). A representative analysis of allanite can be found in Appx. G1. Texturally, some crystals have altered to parisite-bastnäsite, Fe-oxides and amorphous aluminium silicate (Fig. 35a), while others form euhedral to subhedral primary crystals (Fig. 35b). Allanite, bastnäsite, Fe-oxides and aluminium silicate is also an alteration product from hornblende in some samples.

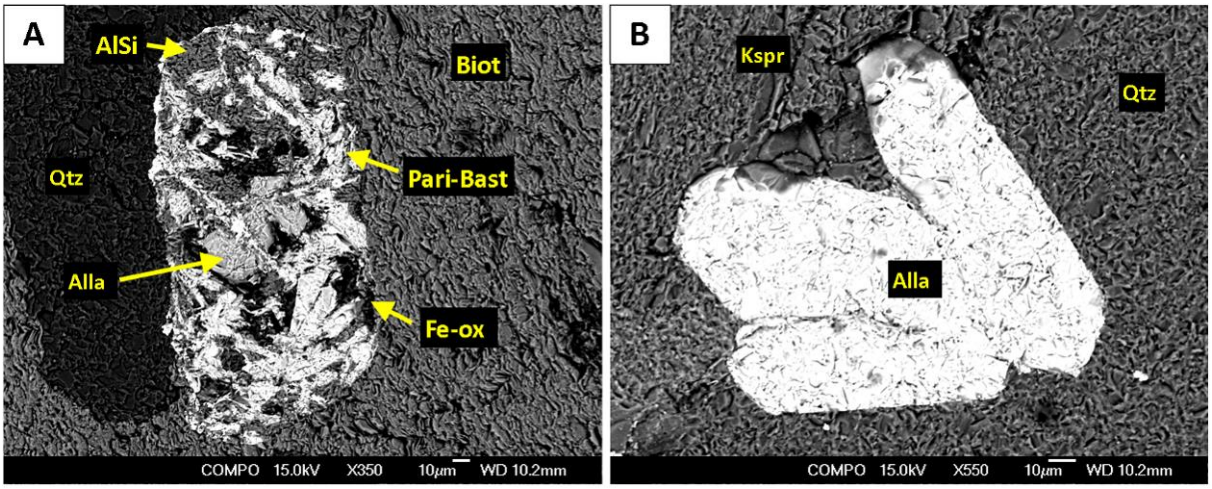

Figure 35. SEM images of (A) EHR79, a primary crystal of allanite set within quartz and biotite is altered to parisite-bastnäsite, Fe-oxides and amorphous aluminium silicate; and (B) EHR79, primary allanite set within quartz and K-feldspar.

Bastnäsite Group Minerals

Most of the analyses for this mineral group indicate complexly intergrown phases (Fig. 36a–b) which often border between low-calcium parisite and high-calcium bastnäsite; they have therefore been called syntaxial bastnäsite-parisite in this study. These two phases also occur separately, as does synchysite. Synchysite is observed to form intergrowths with parisite within the inner zone of hydrothermal alteration in the EHR (Fig. 36c; Townend & Townend 2016b). In total, 85 different analyses of

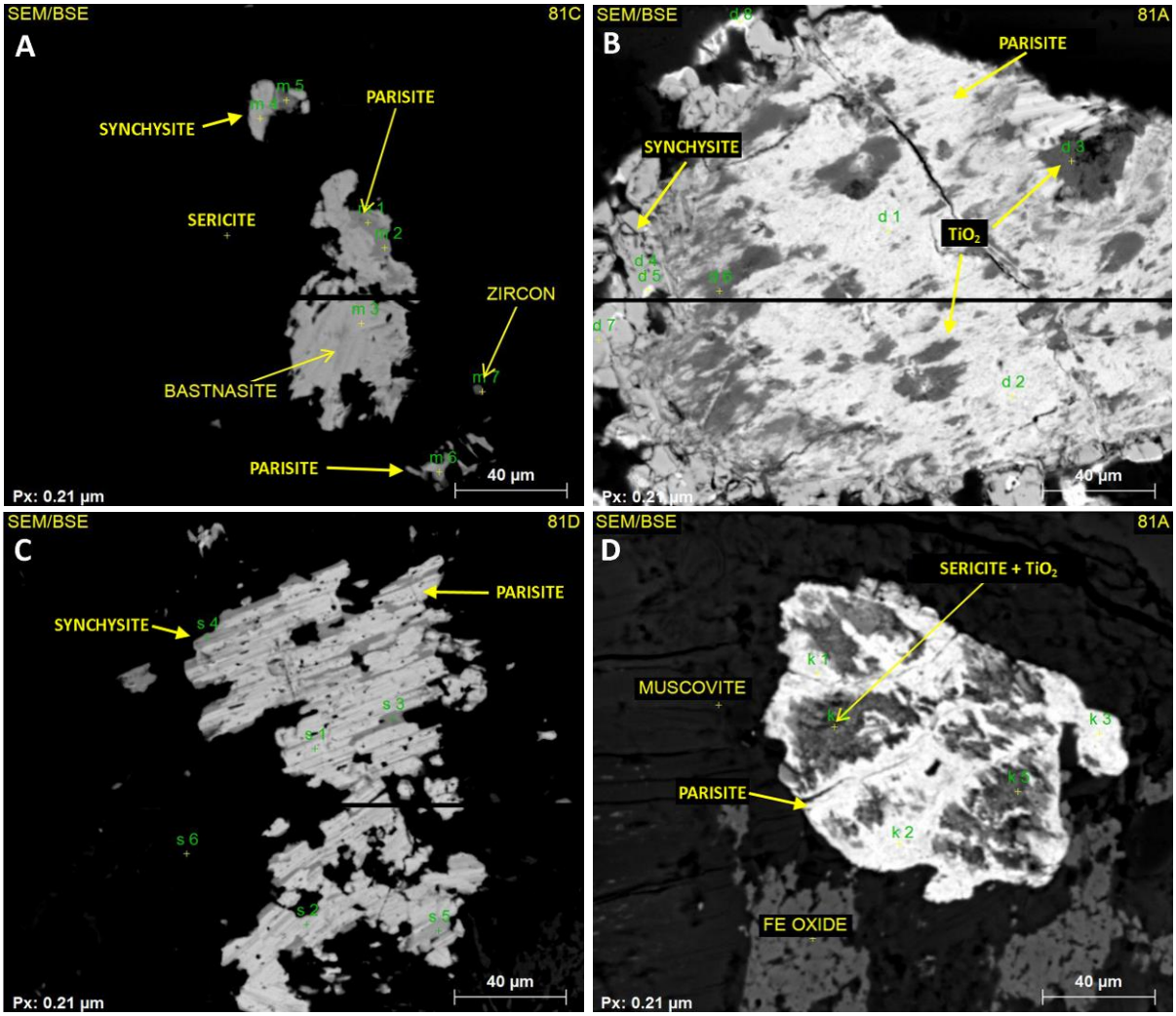

Figure 36. SEM images of bastnäsite group minerals from the inner zone of hydrothermal alteration in the Eastern Hohonu River. (A) EHR81C, complexly intergrown bastnäsite, parisite and synchysite surrounded by sericite; (B) EHR81A, synchysite on the boundary of low-calcium parisite, the latter also contains patches that are TiO_2-rich with minor Fe, Nb, Si and Al present; (C) EHR81D, a parisite grain (lighter) with lamellae of synchysite (darker); and (D) EHR81A, parisite altering to sericite and TiO_2. Images from Townend & Townend (2016b).

bastnäsite, parisite and/or synchysite were made in samples LHR25, LHR28, LHR36, LHR78, EHR79 and EHR81a–i. Pure bastnäsite had the highest total average REO content at 94 wt. %, while synchysite and the mixtures of bastnäsite-parisite ± TiO_2 (an alteration product) contained ~62.5 wt. % total REO on average. In all cases, Ce was the most abundant REE (14–55 ox. %), followed by La (11–29 ox. %) in bastnäsite and parisite, and by Nd (8–17 ox. %) in synchysite. Most grains also contained Y, which was generally <1 ox. %, except for in synchysite, where it occurred in anomalous concentrations of up to 17 ox. % with Gd (up to 7 ox. %). The chemical analyses of this synchysite suggest a mixture of synchysite-(Ce) and

synchysite-(Nd) [$Ca(Nd,Y,Gd)(CO_3)_2F$] . Other REEs that have substituted into these minerals in low quantities are Pr, Sm and Eu, as well as Th.

Calcium concentrations were highly variable, between 1 and 40 ox. %, and helped determine whether the phase was likely bastnäsite, parisite or synchysite (please refer to Table 5 for their chemical formulas). Fluorine was almost always present (up to 8 wt. %), and occasionally Cl was present too (up to 1 wt. %). Variable amounts of Ti, Nb, Fe, Mg, Na, K, Al and Si were commonly found as impure smears within the bastnäsite group minerals (Fig. 36b), and are likely a product of alteration (Fig. 36d). Two grains from the inner zone of hydrothermal alteration have a B-rich alteration product (Townend & Townend 2016b). A representative analysis of bastnäsite, parisite and synchysite are given in Appx. G2.

In general, the bastnäsite group minerals form anhedral masses, in particular in the zone of hydrothermal alteration in the EHR. In this zone, they are commonly observed in association with zircon (Fig. 37a) and TiO_2. Bastnäsite also forms euhedral pseudomorphs with TiO_2 (Fig. 37b), as a euhedral primary phase in a carbonate vein (Fig. 37c), and as an alteration product of hornblende (Fig. 37d).

Fergusonite-(Y)

Five grains of fergusonite were analysed in samples LHR28 and LHR78, which contained average total REOs of 33 wt. %. Of this, 29 ox. % was Y and 57 ox. % Nb, while minor Dy (4 ox. %), Si (5 ox. %), Ca (3 ox. %), Ti (2 ox. %), Fe (1 ox. %) and Th were also present. Texturally, they form euhedral (Fig. 37d & Appx. D1b) to subhedral (Fig. 20d) primary constituents of the rock. A representative analysis of fergusonite is given in Appx. G3.

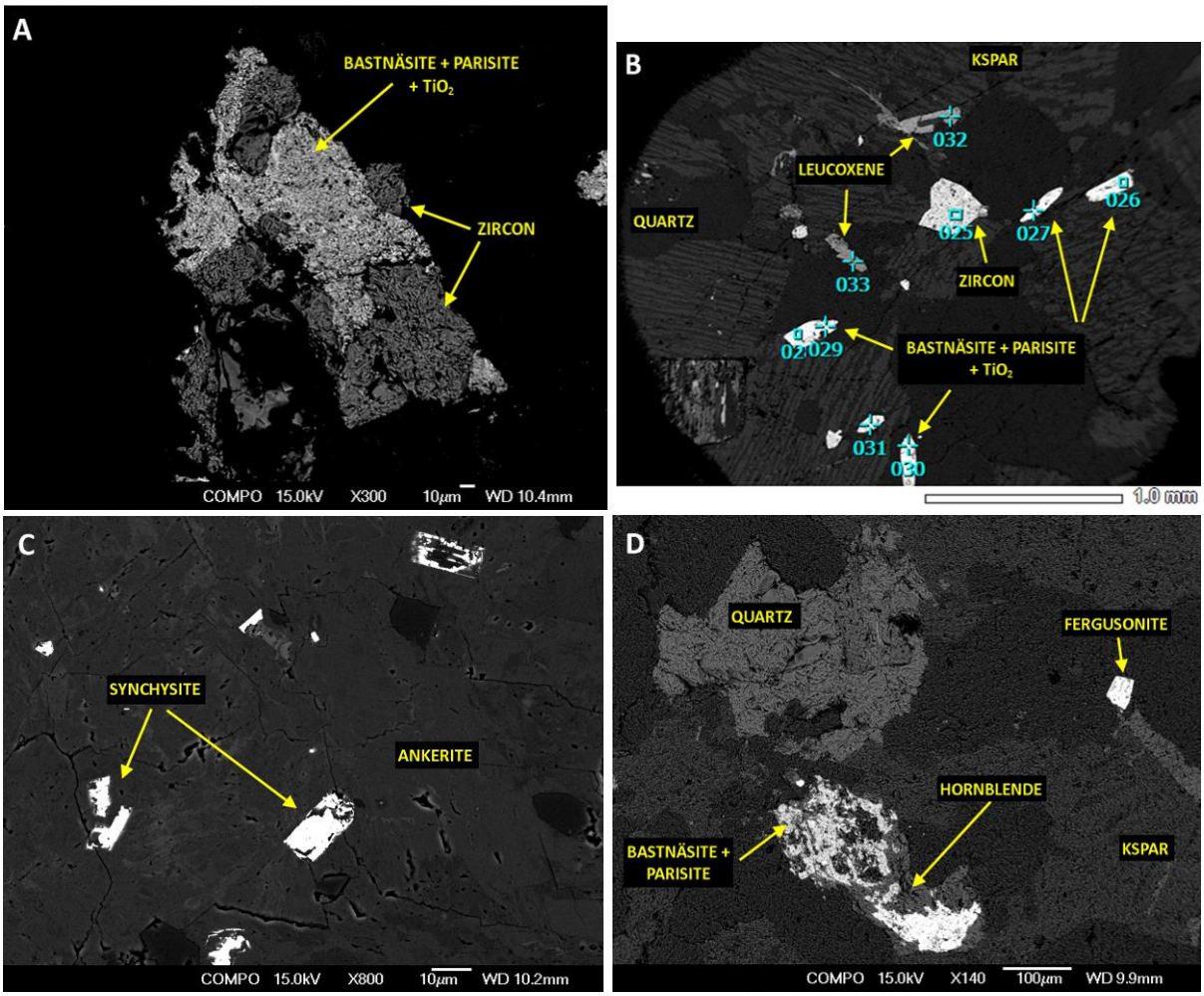

Figure 37. SEM images of (A) EHR81H, complexly intergrown zircon with bastnäsite-parisite + TiO_2; (B) EHR81H, pseudomorphs of bastnäsite-parisite + TiO_2, leucoxene and zircon set in K-feldspar and quartz; (C) LHR25, euhedral synchysite scattered within an ankerite vein; and (D) LHR28, hornblende altering to bastnäsite-parisite, surrounded by quartz and perthitic K-feldspar, a euhedral crystal of fergusonite is also present.

Florencite-(Ce)

Florencite was only found in sample LHR25, a brecciated ankerite vein containing anomalous HREEs, where it forms small subhedral to euhedral zoned rosettes within feathery sericite alteration of a granitic clast (Fig. 38a). Of the seven grains analysed, florencite contains 20 wt. % REOs on average. The most abundant is Ce (13 ox. %), with La (6 ox. %) and Nd (1 ox. %) substituting into the crystal lattice too. Aluminium (36 ox. %) and P (30 ox. %) form the bulk of this mineral, while Sr (6 ox. %), Si (5 ox. %), S (2 ox. %), Ca (1 ox. %) and K (1 ox. %) form minor impurities. Thorium is also present. A representative analysis of florencite is given in Appx. G4.

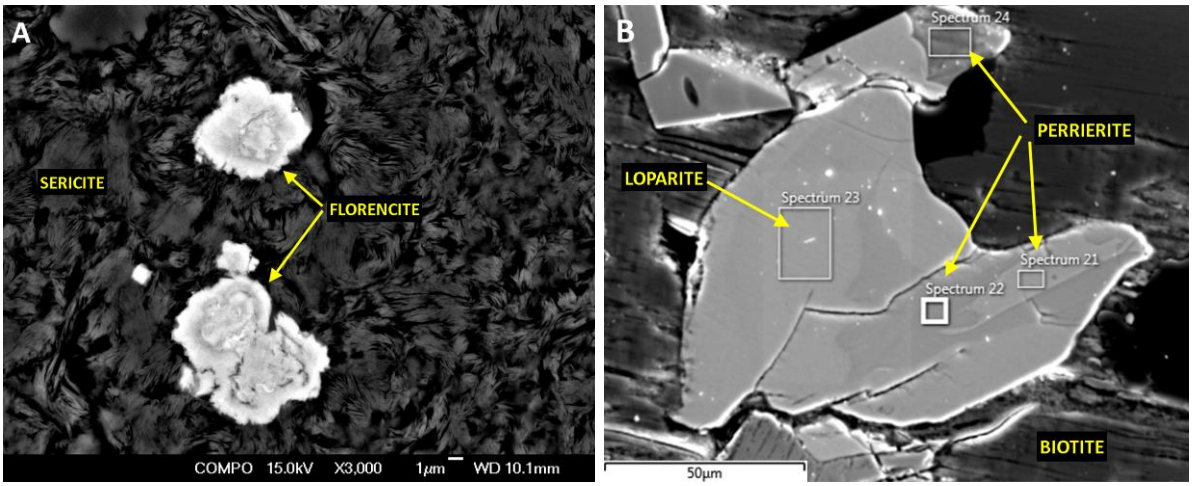

Figure 38. SEM images of (A) LHR25, zoned rosettes of florencite amongst feathery sericite; and (B) GR03, a crystal containing a mix of loparite and perrierite set amongst biotite plates.

Loparite-(Ce)

There was only one sample (GR03 – a mafic-rich variety of the FCG) that contained this mineral which best fits with loparite, part of the perovskite mineral group. However, perovskite usually only occurs in undersaturated alkaline rocks (Mitchell 1996). Alternatively, it may be a Ti-rich, Si-poor alteration product of perrierite. Fourteen different analyses were made, yielding a result of 57 wt. % total REOs on average. Of these, Ce constitutes 31 ox. %, La 16 ox. % and Nd 10 ox. %. Titanium constitutes 31 ox. %, while Ca and Th (4 ox. % each), Nb (2 ox. %) and Fe and Si (1 ox. % each) form minor constituents. Texturally, it forms both individual subhedral crystals, some rounded (Appx. G5), as well as complex intergrowths with perrierite (Fig. 38b), which might reflect changes in silica content, oxygen fugacity and/or fluorine activity (Mitchell 1996). A representative analysis of loparite is given in Appx. G5.

Monazite-(Ce)

Analysis of 13 grains of monazite in samples LHR28, LHR65 and EHR81c, indicated an average total REO content of 68 wt. %. This was dominated by Ce (37 ox. %) with lesser La (19 ox. %) and Nd (12 ox. %). Phosphorous constitutes 28 ox. %, while minor Si (2 ox. %), Th and rare Ca were also present and are principle constituents of the mineral (Wall 2014). Minor Pr and Sm substitution has also occurred. It generally occurs as a subhedral to anhedral primary mineral (Fig. 39a),

and is commonly associated with Fe-oxides and/or zircon (Fig. 20f). A representative analysis of monazite is given in Appx. G6.

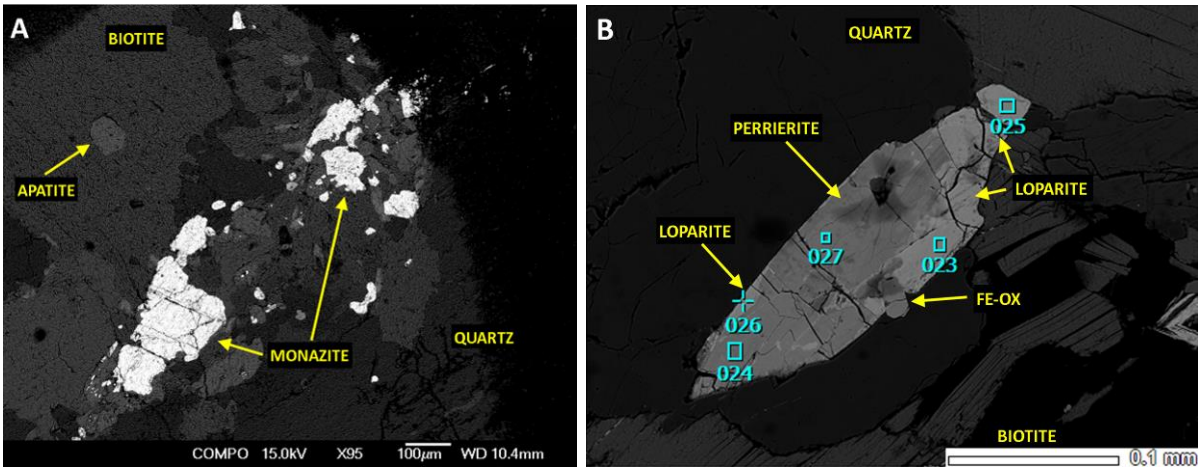

Figure 39. SEM images of (A) LHR65, monazite occurring with biotite, quartz and apatite; and (B) GR03, intergrown perrierite and loparite occurring alongside quartz, biotite and Fe-oxides.

Perrierite-(Ce)

Perrierite is generally the best fit for the 12 analyses taken of this mineral; however, some crystals contain excess fluorine and low silica. Other possibilities include chevkinite or maonuipingite (Townend & Townend 2016b). Alteration of this mineral results in Ti-oxide and quartz, and a reduction in total REEs (Townend & Townend 2016b). Perrierite was observed in the same sample that loparite occurs in (GR03), in which it forms a primary mineral that occurs both individually and intergrown with loparite (Fig. 38b & 39b). It frequently has apatite inclusions and has commonly crystallised alongside biotite-chlorite and quartz, or forms inclusions within them. On average, it contains 42 wt. % total REOs, which are dominated by Ce (22 ox. %) with some La (12 ox. %), Nd (7 ox. %), Pr (1.4 ox. %) and Sm (0.2 ox. %) substitution. It contains relatively low quantities of other cations such as Fe (5 ox. %) Th (4 ox. %), Ca (3 ox. %) and Nb (1 ox. %), but abundant Ti (23 ox. %). Silica is also relatively abundant (19 ox. %) and some Al (3 ox. %) and rare F (up to 3 wt. %) is present. A representative analysis of perrierite is given in Appx. G7.

Xenotime-(Y)

This mineral most frequently forms alteration rims, or inclusions, within zircon crystals (Fig. 40a) in the zone of hydrothermal alteration in the EHR (samples

EHR81a–d). Out of 18 analyses, the average total REO content is 59 wt. %. Of that, Y is the dominant REE at 40 ox. %, with substitution by Dy (8 ox. %), Gd (5 ox. %), Er (3 ox. %), Yb (2 ox. %), Sm (1 ox. %), Ho (0.5 ox. %) and some Tb present. Phosphorous forms the other major constituent of xenotime (38 ox. %), and minor Th and Si, and rare Fe, are also present. A representative analysis of xenotime is given in Appx. G8.

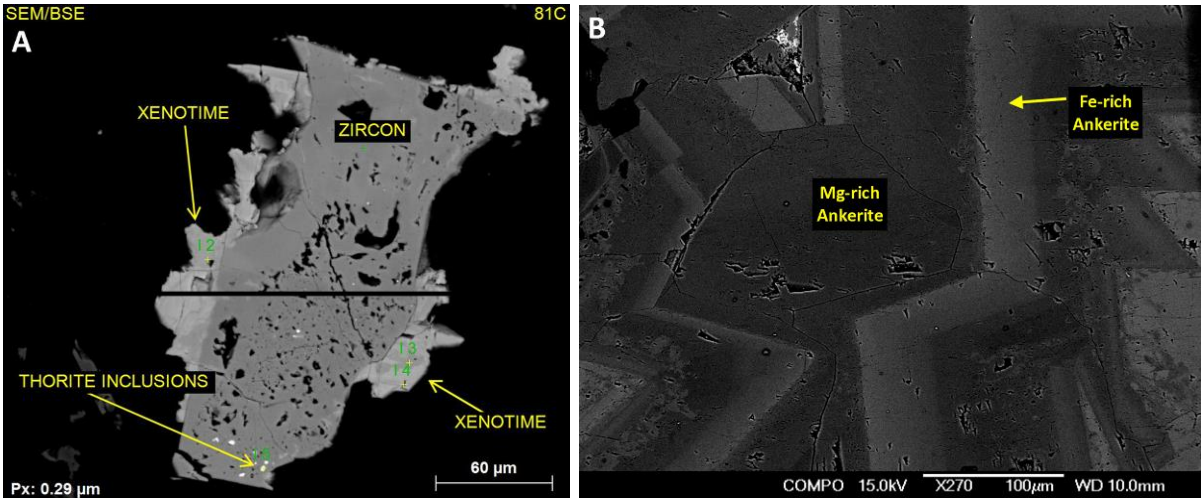

Figure 40. SEM images of (A) EHR81C, a porous zircon with xenotime rims and thorite inclusions [image from Townend & Townend (2016b)]; and (B) EHR80C, compositional zoning within ankerite defined by Fe-rich (lighter) and Mg-rich (darker) zones.

Carbonates

Ankerite was the most common carbonate mineral within the samples that were analysed, and 35 measurements were used to determine an average composition of 56 ox. % Ca, 25 ox. % Mg, 18 ox. % Fe and 1 ox. % Mn (Table G2). Compositional zoning was occasionally present, defined by small variations in the Fe and Mg content (Fig. 40b). Thirteen analyses of siderite indicate 93 ox. % Fe, 3 ox. % Mn, and 2 ox. % each of Ca and Mg is present in this phase on average, while calcite contains 94 ox. % Ca, 3 ox. % Fe, and 1 ox. % each of Mg and Mn. Some calcite crystals in a veinlet cross-cutting a tephrite contained very minor Y.

High-field-strength elements in other minerals

Minor substitution of REEs into zircon (Section 4.6) and apatite has occurred, although it was difficult to quantify these using the SEM alone. Apatite and fluorapatite in the mafic-rich sample GR03 also had some F and Cl present, while the

biotite contained some Cl too. Substitution into these minor rock-forming phases, as well as titanite is common (see Section 2.1.1), and may explain why some samples with relatively abundant zircon and/or apatite contained elevated REE content even when no obvious rare earth minerals were located (e.g., samples LHR63 and LHR65). Apatite in alkaline rocks is well-known to reach REE contents of 1 wt. % or more (Wall 2014). Pyrochlore also contains minor Ce, Nd, Sm, U and Th.

Niobium occurs within pyrochlore in the zone of hydrothermal alteration in the EHR, and is present in minor concentrations within rutile, ilmenorutile, leucoxene and ilmenite (up to 9 ox. %). Titanite in sample LHR65 also contains up to 2 ox. % of both Nb and Y. Thorium is present as a minor constituent in zircon (sometimes occurring separately as thorite) and within almost all rare earth minerals.

4.9 Stable Isotopes

The thirty samples of carbonate minerals, taken from nine different rock specimens that were analysed for $\delta^{13}C$ and $\delta^{18}O$ stable isotopes in order to compare their compositions and determine their source, are plotted in Figure 41. Although isotopic values are all in the ranges of magmatic/mantle fluids rather than meteoric fluids (Fig. 42), they show a considerable spread in the data. Firstly, the two yellow samples are from siderite (EHR81c) and ankerite (EHR81d) veinlets in the inner zone of hydrothermal alteration in the EHR, and cluster relatively well together. The three red samples (EHR80c, LHR25 and LHR77) are from ankerite veinlets that cross-cut the FCG, as well as the HDS in the case of EHR80c, and these show some variability in their $\delta^{18}O$ values in particular. Note ankerite is the likely carbonate in LHR77; however, this was not confirmed with the microscope for this sample. The blue samples (LHR59) cluster reasonably well too and are taken from small calcite veinlets that cut an altered tephrite dyke. The three green samples are from carbonates within the mafic HDS, not the FCG. They show the most variability and generally have an outlier with more negative $\delta^{13}C$ values and more positive $\delta^{18}O$ values. They are samples of igneous carbonates, presumably calcite, found within dykes by Quentin van der Meer – sample QH12 is a 88–86 Ma lamprophyre from Mt Te Kinga (see Fig. 6b), QH20 represents a primitive mantle composition and dates to ~71 Ma,

and QH25 is from Lake Kaniere (Fig. 6b) and is 70 Ma in age. The full isotopic results are given in Appx. H.

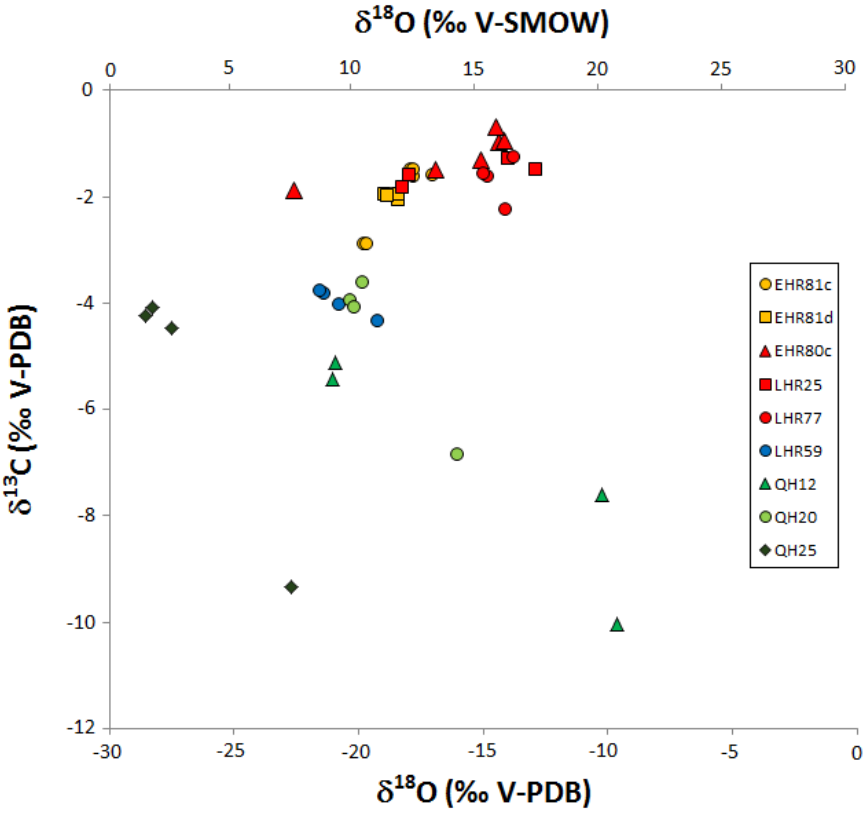

Figure 41. Plot showing the $\delta^{13}C$ (‰ V-PDB) vs. $\delta^{18}O$ (‰ V-SMOW, top) and $\delta^{18}O$ (‰ V-PDB, bottom) isotopic compositions of carbonate minerals in a subset of samples.

From the scatter in the isotopic data, it is apparent that the carbonate veins in the FCG (yellow and red) are separate from the carbonates in the mafic dykes (blue and green), which could be due to a number of factors discussed later. When plotting only the ankerite/siderite veinlets in the FCG (yellow and red) on top of equilibrium calcite stable isotope composition curves for different fluids with different temperatures obtained from fixed/known/assumed initial water isotope compositions, the data give a much clearer trend (Fig. 42). They show a very well constrained magmatic-hydrothermal temperature of ca. 175–250°C (~250°C for the zone of hydrothermal alteration in the EHR), and potentially some slight mixing with meteoric water.

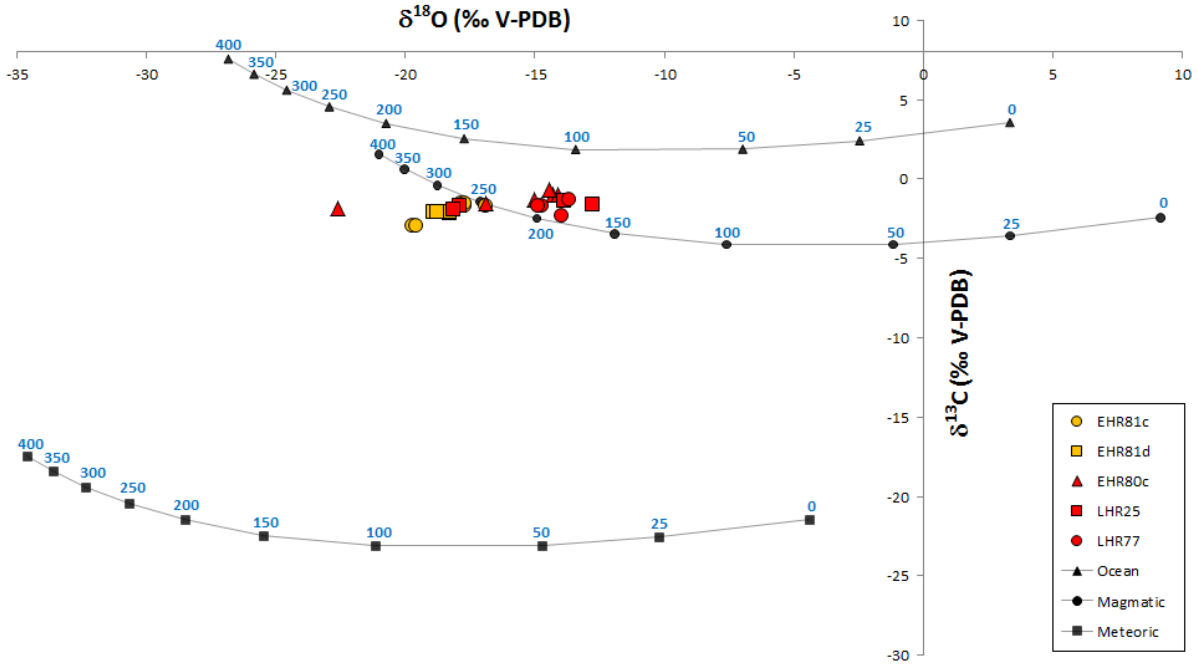

Figure 42. The isotopic composition of secondary carbonates in veinlets cross-cutting the altered French Creek Granite (yellow and red), overlying curves of equilibrium calcite stable isotope compositions formed at different temperatures (blue) from fixed/known/assumed initial water isotope compositions in different fluids (black). Fractionation equations from Bottinga (1968) and O'Neil et al. (1969).

Chapter 5: Discussion

5.1 Magmatic processes and primary REE enrichment

A variety of magmatic processes are responsible for primary REE enrichment in the FCG, which include: small-fraction partial melting of an enriched mantle reservoir; minor crustal assimilation; extensive fractional crystallisation; and late-stage water saturation. Additionally, multiple magma batches are present, which have implications on the REE content. Petrogenesis of rare earth accessory minerals and the shallow, syn-tectonic setting of FCG emplacement will also be discussed.

Source and origin of the A-type FCG and the REEs

The FCG was classified as an A-type granite by Waight (1995) after displaying many physical and geochemical characteristics typical of within-plate, anorogenic, alkaline magmatism. The FCG has low CaO and compatible trace element concentrations, has $K_2O > Na_2O$, and is enriched in SiO_2 (up to 76.7 wt. % in unaltered samples), Al_2O_3 and HFSEs, such as REEs, Nb, Th, Y and Zr. Although the FCG is generally weakly peraluminous, in numerous samples these HFSEs occur in concentrations more typical of peralkaline magmas (Bowden 1985). Maximum values of 716 ppm LREEs; 69 ppm HREEs; 1130 ppm Zr; 109 ppm Y; 155 ppm Nb; 1001 ppm Zn; and 79 ppm Th were measured. Additionally, the FCG has high Rb/Sr, Ga/Al and Fe/Mg, high F content (838 ppm, Tulloch & Robinson 1987) and Fe-rich mafic mineralogy, all typical characteristics of A-type granitoids (Bonin 2007; Frost et al. 2001; Whalen et al. 1987). The combination of high F content (Bowden 1985; Collins et al. 1982) and high heat flow allowed REE-rich minerals (e.g., apatite, zircon and monazite) to partition into the melt. The REEs, Zr and P were then concentrated through differentiation and fluids released during cooling of the pluton (Christie et al. 1998).

On the basis of geochemistry, the source of the FCG magma is inferred to be an enriched mantle reservoir (A_1 subtype; Bonin 2007), which subsequently underwent extensive crystal fractionation and slight contamination by assimilation of the Greenland Group metasedimentary basement (Fig. 43; Waight 1995). This A-type magma was generated by decompression and mantle-upwelling, during regional

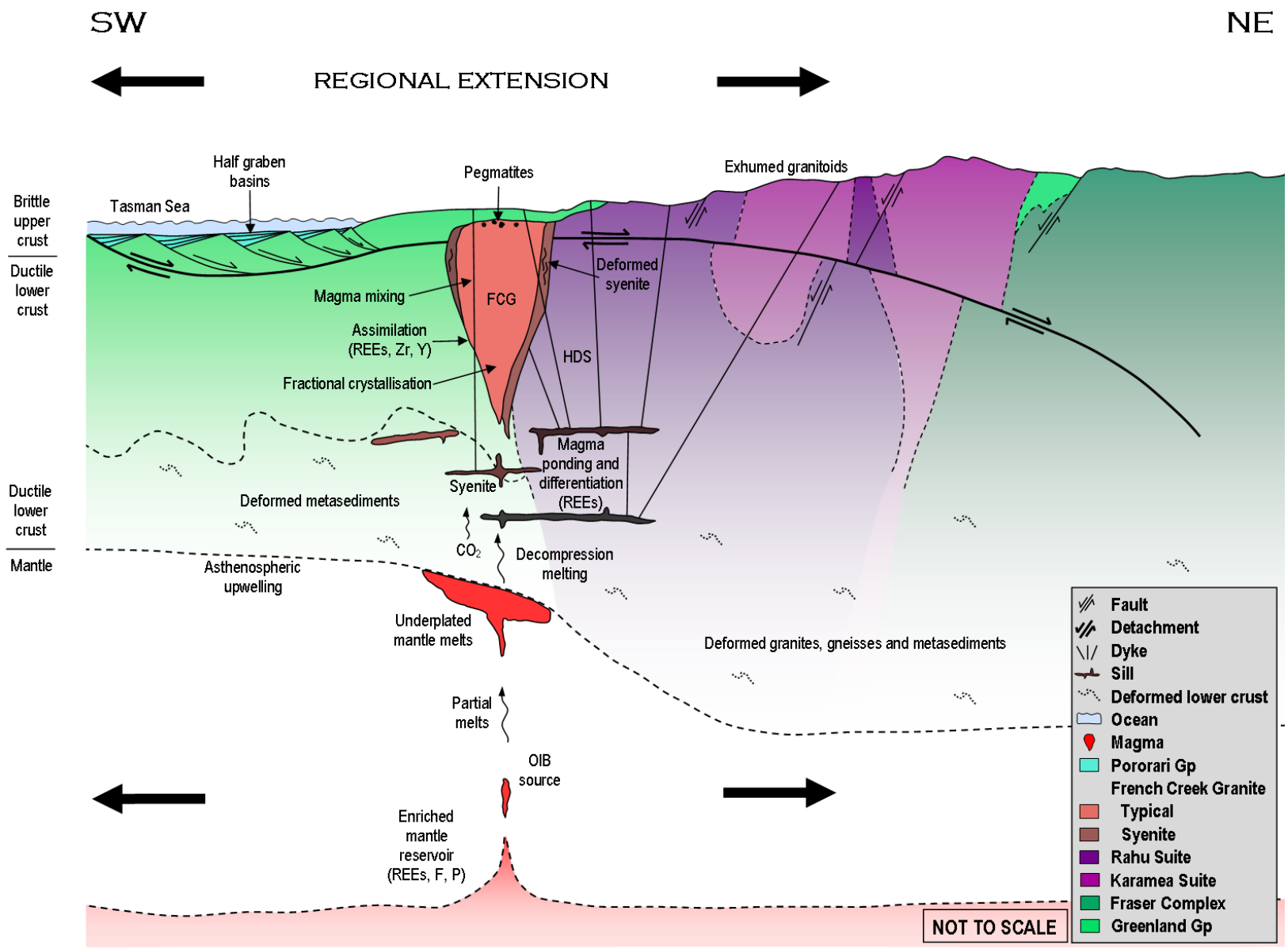

Figure 43. Schematic cross-section of the New Zealand palaeo-Pacific margin 84-82 Ma, showing the anorogenic setting the French Creek Granite (FCG) and Hohonu Dyke Swarm (HDS) were emplaced into. Note the large-scale detachment fault, half-graben basins, normal faults and upwelling asthenosphere in this extensional tectonic setting. Late Cretaceous geology and fundamental concepts from Lister et al. (1986), Nathan et al. (2002), Waight (1995), and Winter (2011).

extension (Fig. 43) that was concomitant with the initial opening of the Tasman Sea 84–82 Ma (Waight 1995). This rifting is speculated to be a consequence of a mantle plume located beneath Gondwana during the Late Cretaceous, which ultimately led to its fragmentation (Storey et al. 1999; Weaver et al. 1994). This model, proposed by Waight (1995), is further supported by analytical results from the current study, which show affiliation with tholeiitic, ferroan, early-anorogenic magmatism at 82.55 ± 0.85 Ma with negative Ba, Sr, P, Eu and Ti anomalies (Fig. 28, and Appx. F1c).

Crystallisation and cooling history of the FCG

Further features characteristic of A-type granitoids are perthitic and granophyric K-feldspar, late-stage crystallisation of the mafic phases, and the relative anhydrous nature of the magma (Bonin 1990; Eby 1990; Whalen et al. 1987). Large, perthitic to mesoperthitic K-feldspar with abundant graphic and granophyric intergrowths typify the FCG. Individual K-feldspar, plagioclase and quartz, some with graphic intergrowths, indicate an early subsolvus system with high H_2O pressure, while extensive granophyric intergrowths and exsolution denote a later change to higher-level, hypersolvus, eutectic crystallisation. This change was likely brought about by decompression during ascent of the crystallising magma as crustal extension during the Late Cretaceous progressed. Sharp boundaries between the pre-eutectic crystals and the granophyric intergrowths (Appx. D1a) suggest this change happened relatively rapidly and was accompanied by higher undercooling rates (Waight 1995). Small interstitial quartz grains are indicative of the last remaining melt fraction, and the high silica content probably meant the viscous FCG crystallised at relatively low temperatures. The interstitial, clustered nature of the mafic minerals, which are dominated by Fe-rich biotite and occasionally by hornblende, indicate that these hydrous phases were prevented from forming early within the anhydrous magma, and could only form once the residual melt fraction had reached water saturation.

A conspicuous association between these late-stage mafic minerals and the occurrence of primary accessory phases such as magnetite, apatite, zircon, allanite, monazite, fergusonite and ilmenite, strongly implies that REEs, Zr, Ti, Nb, Y, P and F were abundant in the magma and concentrated in the residual melt during fractional crystallisation. This is common in F-rich magmas (Creaser et al. 1991), and is a

typical feature of A-type granites. Furthermore, Bea (1996) demonstrated that biotite indirectly controls the distribution of trace elements such as REEs, because it has the greatest tendency to include REE-rich accessory minerals, which are typically too small to settle-out of the magma on their own (Bea 1996; Bonin & Giret 1985).

The accessory rare earth minerals that control the primary abundance and distribution of REEs in the FCG are allanite, monazite, fergusonite, perrierite and loparite. Although most samples enriched in REEs contain the aforementioned minerals, some samples contain elevated REEs even when these rare earth phases are absent. This can be explained through the presence of apatite, fluorapatite and zircon, especially the large zircon, which have likely accommodated significant quantities of REEs within their lattice. These phases also explain the elevated Zr content of the FCG, and are evidence for the involvement of primary F^- and PO_4^{2-} in the magma. Niobium has substituted into Ti-rich phases such as ilmenite, rutile and titanite, and these minerals, as well as rare fergusonite and pyrochlore, control the primary Nb enrichment in the FCG. Equally, it is determined that xenotime, fergusonite, zircon and titanite control the distribution of Y in the FCG.

Aside from the interstitial hydrous mineralogy, the presence of miarolitic cavities, microgranite, sporadic pegmatite pods and patchy graphic and granophyric intergrowths provide evidence for localised segregation of solid, liquid and gas phases within the FCG during the late-magmatic stage (Whalen et al. 1987). These textures also signify high variability in undercooling rates, which is expected in such a shallow (~3 km depth; Waight 1995) pluton (Candela 1997). Miarolitic cavities are evidence for magmatic volatile exsolution (Shelley 1993), and shallow degassing is also one way to produce peraluminous granites (Martin 2006) such as the FCG. This can occur through effervescence or boiling during decompression, ascent and/or cooling of the magma (Bowden & Kinnaird 1984; Candela 1997). Graphic and granophyric intergrowths are evidence for zones of fluid accumulation vs. removal, respectively, and indicate an increase in undercooling rate (Shelley 1993). Three samples of microgranite from the lower southern tributary of the Little Hohonu River (LHR) further indicate a sudden increase in undercooling rates in response to magma ascent. Microgranites are common on the margins of intrusive bodies and, along with

the pegmatite pods in the northern tributary of the LHR, might infer the apical region of the pluton. Although pegmatites are typically associated with crystallisation from a hydrous melt, they can also be produced from a dry felsic melt through undercooling (London 1990), and from a dry alkaline melt at low temperatures and pressures (Raymond 1995). These may explain why the pegmatite pods are predominantly composed of quartz and K-feldspar and deprived of REEs, which are expected to favour the liquid phase (Bowden 1985), instead of forming pegmatite-hosted REE-deposits like those at Strange Lake (Salvi & Williams-Jones 1990) or other alkaline complexes (e.g., Chakhmouradian & Mitchell 1999).

Late-stage internal heterogeneity of the FCG

Both water and elements have a heterogeneous distribution within the FCG, which have implications for the primary mineralogy of the rock. Not all samples containing biotite clusters, which occur throughout the FCG, contain REE-bearing accessory minerals, despite the apparent association between the mafic phases and REE-bearing accessory minerals. Similarly, the mafic-rich variety of the FCG has variable aluminosity, ΣREE content and distinct occurrences of primary monazite, titanite, allanite, loparite and perrierite, although all contain abundant mafic phases. For example, one of these samples (GR03) contains the highest concentration of ΣREEs recorded in the FCG (~800 ppm), while another (LHR44) only contains REE values that typify the background concentrations of the pluton. The mineralogy suggests that at least some of these mafic-rich samples crystallised in areas where residual fluids were particularly rich in water and trace elements, such as Zr, REEs, Nb, Ti, Y, P and F, leading to the crystallisation of zircon, apatite, fluorapatite, allanite, fergusonite, monazite, titanite and Ti- ± Fe-oxides. These water-rich zones are supported by textural evidence that also hint at rapid growth and/or magma chilling, such as granophyric intergrowths, aplitic groundmass and acicular apatite (David Shelley pers. Comm.). Rare biotite-rich lenses indicate the late-stage hydrous melt experienced a component of shearing while it crystallised, and resorbed biotite and amphibole indicate late disequilibrium within the crystallising pluton.

The occurrence of loparite in the mafic-rich sample containing the highest ΣREE content (GR03), might be further evidence for disequilibrium, considering

loparite is an accessory mineral typical of undersaturated rocks only (Bea 1996). *Metaloparite*, a metamict intermediate product between loparite and TiO_2 plus bastnäsite, is a common alteration product of loparite in alkaline rocks, and might better represent the loparite identified in this sample. The *metaloparite* found in peralkaline pegmatites at Bearpaw Mountains, Montana, was found in association with perrierite/chevkinite and fluorapatite, as a product of acidic late-stage deuteric alteration by F-rich fluids (Chakhmouradian & Mitchell 1999); a mineralogical association shared also by this FCG sample. The broken, and sometimes rounded, nature of the loparite in this hydrous sample might indicate its transportation and corrosion in the residual melt, and possibly its alteration to perrierite plus TiO_2 as it reacted with the changing chemistry of the surrounding F-rich fluids.

Diverse magmatism related to the FCG

In addition to the mafic-rich variety, the FCG is compositionally diverse, and Tulloch et al. (1994) and Waight (1995) have previously postulated that this alkaline suite crystallised from several magma batches, pulses and/or fractionates. The marginal QAF syenite more closely represents the parental melt composition (Waight et al. 1998a), and the low K/Rb in the typical FCG (0.01–0.04) is consistent with differentiation from a syenitic parental magma (Fig. 43) through feldspar fractionation (Collins et al. 1982). The syenite occurs along the NE contact between the FCG and Deutgam Granodiorite in at least two locations, one of which has not previously been identified (i.e. on the Mt French Track). Distinct grain boundary deformation unobserved in the typical FCG, implies the syenite formed perthites and underwent solid-state deformation after it had fully solidified, as a result of FCG emplacement (Fig. 43). This makes it chronologically older than the FCG, although the interval between these two pulses was likely relatively short-lived, because temperatures must still have been high enough (i.e. amphibolite facies) to form this type of grain boundary migration. The syenites are geochemically different from the typical FCG too: they have slightly different major element trends, particularly Na_2O (Fig. 27), one sample is metaluminous, and they do not contain anomalous REEs, even though zircon is present. Zircon saturation temperatures are also higher in the syenite (897°C) when compared to typical FCG (822°C; Quiten van der Meer pers.

Comm.; Waight et al. 1998a). This might suggest that the earlier pulse of syenitic magmatism tapped a hotter, less-evolved part of the magma chamber, which had not yet ponded to incorporate more HFSEs through assimilation of the crust.

Similarities of the FCG with an alkaline ring complex model

The presence of the syenite shell and biotite granite also raises the question of whether the intrusive suite was once part of an alkaline ring complex, which has previously been postulated by Geoff Price (pers. Comm.). It has other similarities with the ring complex model presented in Section 2.2, such as the shallow level of intrusion, and the presence of hydrothermal alteration and felsic dykes. Even a section containing minor peralkaline arfvedsonite granite was located between the typical FCG and QAF syenite in the Eastern Hohonu River (EHR) by Waight (1995), although this was not observed in the current study. The absence of fayalite granite, another common feature of an alkaline ring complex, might mean that more field mapping in the hard-to-reach upper catchments is required, or that fayalite has been destabilised by residual fluids, leading to replacement by amphiboles (Bowden 1985), biotite, Fe-oxides and limonite. Similarly, the absence of volcanic rocks might simply mean the erosion level is presently at, or below, level three (Fig. 4) as a result of Cenozoic uplift and Pleistocene glaciations. Another feature the FCG has in common with alkaline ring complexes is the presence of dykes, although the strong WNW-ESE trend of the HDS is related to crustal weaknesses paralleling the opening direction of the Tasman Sea (Waight et al. 1998a), rather than features controlled by a caldera.

Intrusive dykes and their relationship to REE enrichment

Waight (1995) determined a cogenetic and contemporaneous relationship between the HDS and FCG, and the gradational character and coarse devitrification of some of the dykes in this study support this relationship, indicating the dykes were emplaced while the granitic body was still warm. Smooth major element trends between the FCG and HDS also support a genetic relationship, while evidence of magma mixing between a mafic and a more viscous silicate melt is evident, both texturally and geochemically. Dykes of intermediate composition contain skeletal plagioclase phenocrysts which have glassy inclusions that are more felsic than the surrounding

groundmass. Dykes containing resorbed, rounded, rimmed and/or skeletal phenocrysts and xenocrysts hint at both magma mixing and rapid undercooling during magma ascent.

The fact that 1) felsic dykes are red and exhibit similar alumina saturation, mineralogy and ΣREE content as typical FCG; 2) mafic dykes are grey and have lower ΣREE content and metaluminous geochemistry; and 3) the intermediate dykes are geochemically somewhere in between the two, also suggests mixing between two magmas with distinctly different histories of differentiation and crustal contamination. The felsic dykes have therefore likely undergone similar REE enrichment processes as those that occurred in the unaltered FCG. The REE depletion in felsic dykes observed by Waight (1995) was absent in this study, except in two aplitic rhyolite float samples that were chemically and texturally different to the FCG and other felsic dykes found cross-cutting the FCG, which were red and contained similar REE enrichment as the unaltered FCG. These two float samples sound similar to the blue to cream-grey rhyolitic dykes Waight (1995) found throughout the Hohonu Ranges (except for cross-cutting the FCG) that had distinctly lower Ce, La, Nd and Y content, implying they preceded FCG emplacement (Waight 1995), and were therefore probably unrelated to the later REE mineralisation. Cross-cutting dykes and veins are common as pressure builds up in a cooling felsic pluton (Raymond 1995) due to increasing viscosity, resurgent boiling or from high late-stage fluid pressures (Raymond 1995), which result in periodic fracturing of the pluton.

Syn-tectonic deformation within the FCG pluton

More general deformation is evident throughout the FCG, which appears to span the majority of its cooling history. Evidence for minor high-temperature strain during initial crystallisation is indicated by the presence of irregular twins, and curved and deformed perthites, within both K-feldspar and plagioclase. Bent and offset biotite, and elongate semi-igneous–metamorphic biotite growing perpendicular to extensional shear planes, signifies deformation during the late-magmatic stage. This was followed by muscovite and chlorite pressure shadows, chloritic shear planes, grain boundary recrystallisation, and low-temperature cataclastic shearing, which indicate that deformation continued post-crystallisation of the granite, some of which

may be related to reactivation adjacent to the current plate boundary. This moderate to low temperature syn-tectonic deformation can be achieved relatively easily with such a high-level, rapidly cooled granite such as the FCG. The cataclastic shearing is restricted to metre-scale zones in which granulated clasts of quartz and feldspar are surrounded by a pulverised matrix. The quartz is only slightly deformed and has undergone no recrystallisation, implying this activity took place at temperatures <300°C. In other areas, deformation is only expressed by offset minerals along discrete cracks, some of which have also undergone a component of dilatation. The resulting cavities are important aspects to consider as permeable, potentially mineralised zones, and are discussed in more detail in the next section.

5.2 Hydrothermal processes and secondary REE enrichment

The FCG has undergone hydrothermal alteration, which has affected its REE content. Hydrothermal facies, geochemical reactions, remobilisation of elements, and the source of the hydrothermal fluids will be discussed, and how these relate to geological structures and secondary REE mineralisation.

Hydrothermal alteration – with particular emphasis on carbonate minerals

Hydrothermal alteration of the FCG has resulted in variable sericitisation, chloritisation, silicification, hematisation, kaolinisation and carbonate alteration. Of these, ubiquitous sericitisation of feldspar is the most common, ranging from minor plagioclase alteration to complete replacement of feldspars, where only relict pseudomorphs of perthites and grain boundaries remain. Carbonate alteration is a common theme throughout the FCG, where carbonate minerals fill cavities and cracks, and replace mafic minerals and feldspars. This carbonate alteration coincided with precipitation of the fluorcarbonate bastnäsite group minerals – the most common rare earth minerals in the FCG – particularly in the zone of hydrothermal alteration in the EHR. This implies a strong relationship between carbonate alteration and secondary REE mineralisation. The replacement carbonates are most commonly ankerite and siderite, while calcite is generally restricted to cavity fill. The occurrence of ankerite and siderite is a function of the Fe-rich nature of the FCG host, as well as the availability of Fe, Ca and Mg during alteration of plagioclase and mafic

components, which are typically the first to be affected by fluids. Syntaxial bastnäsite-parisite contain the REEs Ce, La, Nd, Gd, Pr, Sm and Y, and commonly replace mafic components such as calcic amphibole, allanite and oxides, a common feature in low-temperature F-, CO_2- and/or H_2O-rich fluids (Berger et al. 2008). The extensive nature of the carbonate alteration indicates the involvement of a large CO_2 reservoir that interacted with this hydrothermal system (Fig. 44). Where multiple overprinting episodes have occurred, carbonates normally represent the product of the last alteration event, suggesting the involvement of this CO_2 reservoir occurred during the later stages of the evolving hydrothermal system.

Stable isotopes from carbonate minerals

The $\delta^{13}C$ [-10.0‰ to -0.7‰ (V-PDB)] and $\delta^{18}O$ [1.5‰ to 21.1‰ (V-SMOW)] isotopic values are consistent with a magmatic origin, and also fit within accepted ranges for carbonatites, the mantle ($\delta^{13}C$ -6 to -5‰) and marbles (Sharp 2007). A marble source is considered unlikely here, since the closest marble, the Ordovician Arthur Marble, is located further north near Springs Junction (at Marble Hill) and in Nelson, and is part of the Takaka Terrane (Fig. 5). The local basement surrounding the Hohonu Ranges is the Greenland Group of the Buller Terrane, and no local limestones are known to outcrop in the area, at least none that have been preserved. Alkaline magmas can contain substantial CO_2 (Robb 2005), and since: 1) A-type granites represent partial melting of carbonated mantle (Lowenstern 2001); 2) the FCG was emplaced into a high-level extensional tectonic setting; and 3) the mantle is known to degas in regions of crustal extension (Martin 2006), a mantle carbon reservoir is considered a strong possibility for the source of the CO_2 (Fig. 44) that complexed the REEs and led to the extensive carbonates and bastnäsite in the FCG. The involvement of this mantle carbon reservoir is inferred to have occurred during the late development of the FCG, rather than during more recent hydrothermal or metamorphic activity associated with the current New Zealand plate boundary, because Late Oligocene–Early Miocene carbonatites in the Haast-Otago region are characterised by more negative $\delta^{13}C$ values (Turner 2015).

The scatter in the isotopic data (Fig. 41) suggests that carbonates found in the mafic HDS came from a compositionally different source to those found in the

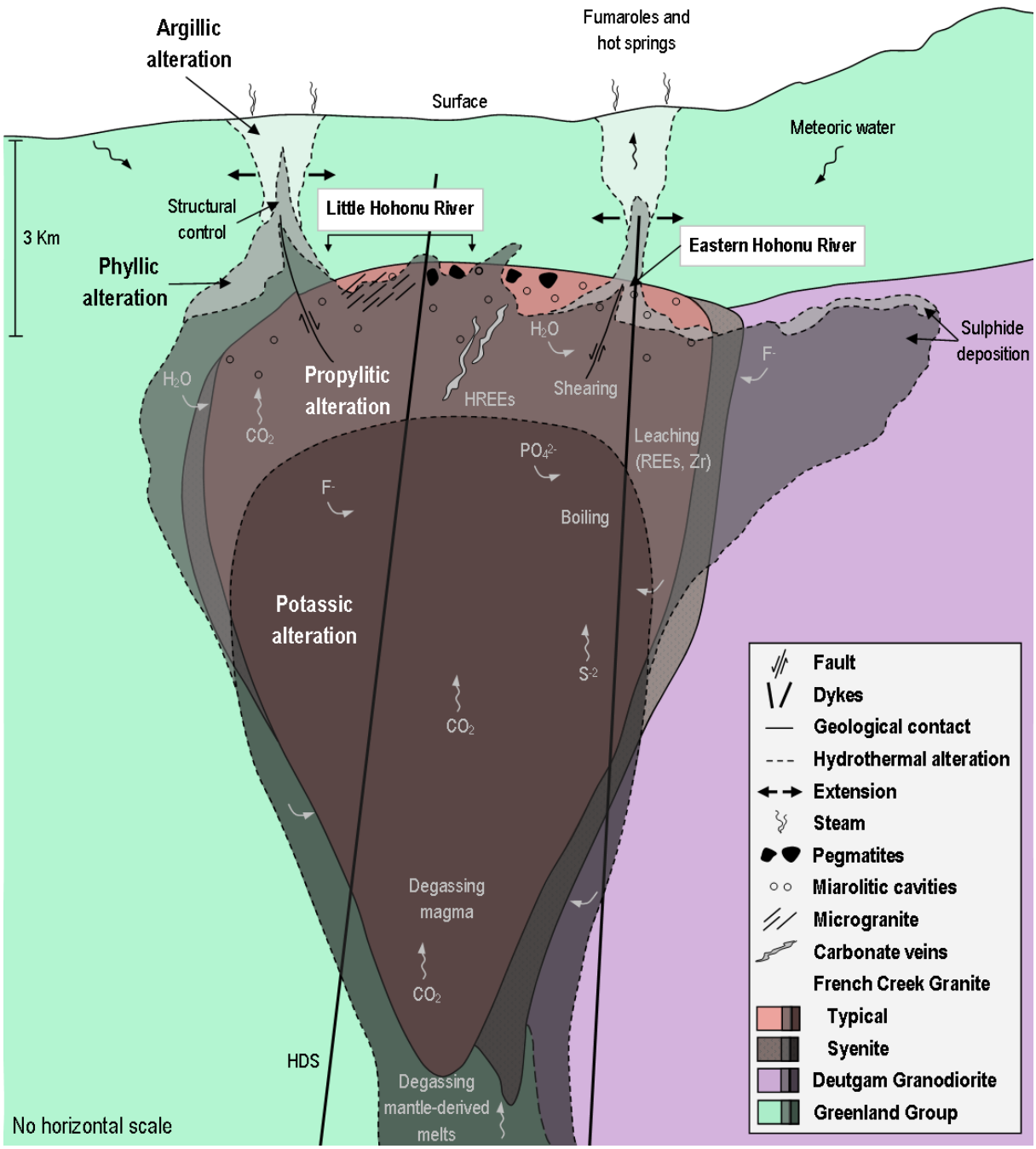

Figure 44. Schematic conceptual model of the late-stage hydrothermal system that operated within the French Creek Granite ~81 Ma, which is composed of alkali-feldspar granite (typical) and a marginal syenite. Different shading indicates zones of potassic, propylitic, phyllic and argillic alteration, of which the phyllic and argillic assemblages are controlled by structural weaknesses. The location of the phyllic alteration assemblage and patchy propylitic alteration in the Eastern Hohonu River and Little Hohonu River, respectively, are also indicated, as are processes, volatiles, structures and textures. Geological concepts are from Ridley (2013).

hydrothermally altered FCG – and hence associated with REE mineralisation – which cluster together much better. This scatter might be due to a variety of factors, including the analysis of different carbonate phases (i.e. ankerite/siderite vs. calcite); the percent of carbonates analysed; out-of-equilibrium crystallisation conditions; or that the fluids from which the carbonates crystallised were at different temperatures or were affected differently by near-surface processes. Fluid inclusions or He isotopes might better constrain the formation conditions of these carbonates in the future, but the role of shallow hydrothermal processes is evident in the secondary carbonates in the FCG, which show affiliation with well-constrained 175-250°C magmatic-hydrothermal fluids (Fig. 42). Mixing with a minor component of meteoric water (Fig. 44) appears likely, is expected in such shallow environments, and can also lead to the high $\delta^{18}O$ values observed in the FCG (Sharp 2007).

The source of the hydrothermal fluids

The fluids responsible for the alteration of the FCG can be derived directly from the granite as a product of cooling and crystallisation, and are a common late-stage feature in intrusive bodies. For example, crystallisation of granophyric intergrowths is an anhydrous process that would generate residual aqueous fluids (Waight 1995); these could lead to pervasive alteration if a convective hydrothermal system established itself above the pluton (Fig. 44). Statistical analyses of Ce, La, Nb, Y and Zr (Section 4.2) suggest that elemental recycling and secondary REE enrichment occurred in the FCG, indicated by a small upper population and/or a long upper tail, which can be attributed to a secondary process such as hydrothermal circulation. A common feature in mineralised A-type granites is late low-temperature sodic metasomatism, characterised by propylitic alteration (Bowden 1985; Kinnaird 1985), that results in leaching of REEs (Fig. 44) by F and/or Cl complexes (Bowden & Kinnaird 1984), REE enrichment in zircon, and precipitation of monazite, xenotime and thorite. This sodic alteration commonly occurs in the apical region of a granite cupola (Kinnaird 1985), consistent with the presence of propylitic alteration, sporadic pegmatite pods and microgranite in the lower LHR (Fig. 44). This assemblage becomes superimposed by late-stage acid metasomatism as fluids are diluted and temperatures decrease, which commonly leads to: greisenisation; precipitation of

quartz, monazite, rutile, zircon, siderite, pyrite, chalcopyrite, sphalerite and galena; late-stage kaolinisation; and deposition of REEs in localised cavities (Bowden 1985; Bowden & Kinnaird 1984; Collins et al. 1982; Kinnaird 1985). All of these features are found in the alteration zone in the EHR.

Hydrothermal facies in the FCG

Different hydrothermal facies have now been found in the FCG, which reflect the changes in temperature, pressure, composition and/or fluid/rock ratios (Robb 2005) of a developing porphyry-type hydrothermal system (Fig. 44), that may, or may not, have been part of an alkaline ring complex. Patchy propylitic alteration, characterised by chlorite + illite ± calcite ± pyrite (Brathwaite 2013) occurs in the FCG in the lower LHR (Fig. 44). This type of alteration is characteristic of low fluid/rock ratios, temperatures between 250–400°C, the addition of H_2O and CO_2, and is common at the margins of porphyry-type and epithermal systems (Ridley 2013; Robb 2005).

The bleached and textureless assemblage in the alteration zone in the EHR (Fig. 44) is dominated by sericite + quartz + pyrite, with rutile/brookite + leucoxene + halloysite + ankerite/siderite + sphalerite + chalcopyrite + galena also present. It is consistently enriched in REEs, and the carbonates formed from ca. 250°C magmatic-hydrothermal fluids (Fig. 42). These are all features characteristic of phyllic alteration, which is acid metasomatism that develops relatively late in a porphyry-type system (Ridley 2013), and often results in localised vein greisens (Bowden 1985). Despite the abundant sericite and quartz, this alteration is not a typical greisen assemblage though, due to the lack of fluorine, topaz and tourmaline. However, F may have preferentially partitioned into fluorcarbonates, in which rare B-rich alteration products also occur, and might indicate the higher stability of the bastnäsite group minerals in these REE-rich fluids, when compared with fluorine, topaz or tourmaline. Although other halloysite occurrences in New Zealand are generally related to rapid low-temperate (<80°C) alteration of rhyolites (Joussein et al. 2005), its presence in this alteration zone likely characterises low temperature (100–300°C), acid (pH 4–6) argillic alteration (Fig. 44; Alderton et al. 1980; Ridley 2013) as a result of sulphide oxidation.

Geochemical reactions during hydrothermal alteration

Acid metasomatism commonly leaches elements from the host and redistributes them, which leads to the precipitation of new minerals. In the alteration zone in the EHR, a progressive replacement of amphibole, biotite, magnetite, ilmenite and apatite by bastnäsite group minerals, rutile/brookite, leucoxene, siderite, ankerite, sulphides, pyrochlore, monazite and xenotime is observed. This suggests the remobilisation of Fe, Ca, Mg, Ti, REEs, Y, Nb, Zn, Pb, Cu, P, F and Cl, and might represent mixing between two fluids: a neutralising fluid containing CO_3^{2-} (± F and H_2O) and ore-forming elements (Pb, Zn, Fe and Cu) – from which the carbonates and fluorcarbonates precipitated – and a reducing acidic fluid containing H_2S (± HF), which led to pyrite, chalcopyrite, sphalerite and galena precipitation. Both of these fluids are capable of transporting significant REEs (Lowenstern 2001; Michard 1989), and mixing an acidic fluid with a cooler, neutral one is a key process for promoting REE metallogenesis in hydrothermal systems (Williams-Jones 2012). A very similar assemblage of Nb (pyrochlore), REEs (monazite, xenotime and fergusonite), Th (thorite), Zn (sphalerite) and Pb (galena) within mineralised alkaline ring complexes in Africa also indicates redistribution of elements during such acid and/or potassic metasomatism following initial sodic alteration (Bowden 1985).

Reducing conditions are inferred by the presence of reduced sulphur species, and a lack of a Ce anomaly in bastnäsite, whose oxidation state is affected under oxidising conditions (Berger et al. 2008). The euhedral, yet resorbed nature of pyrite suggests that an increase in pH occurred, likely a result of: 1) volatile loss – from boiling (Fig. 44), effervescence (Lowenstern 2001), and/or a pressure decrease during rapid ascent or as fluids entered open cavities; and 2) feldspar hydrolysis (Ridley 2013). These processes lowered the stability of pyrite, and led to the precipitation of carbonates and fluorcarbonates, which are only stable under near-neutral to alkaline conditions (Smith et al. 2000).

Hydrothermal alteration typically introduces new elements, many of which can be sourced internally and are redistributed by the fluids. Recycling and secondary REE enrichment in the FCG is evident in strongly altered samples that are consistently more enriched in REEs than unaltered FCG samples. This is similar to the

economic Nb-Zr-REE deposit in the Mongolian Altai, where alkaline rocks were strongly altered by carbonate- and fluorine-rich hydrothermal fluids, concentrating ΣREEs (up to 2406 ppm) and producing a negative Eu anomaly (Kempe et al. 1999). Europium is highly mobile in hydrothermal systems, especially in the presence of F^-, Cl^- or CO_3^{2-} (Bowden 1985; Bowden & Kinnaird 1984), and the breakdown of feldspar to sericite explains the more negative Eu anomaly in altered samples when compared to unaltered FCG (Fig. 29b). Fluorine may also have been sourced internally: the breakdown of biotite and amphibole releases F, and the dissolution of apatite releases F, Ca, P, Th and substantial REEs. Additionally, the replacement of feldspar by sericite and halloysite, as well as the alteration of the mafic silicates, liberates silica, which reprecipitates as quartz. This process also releases Na^+ and K^+ cations, which are readily mobile in aqueous solutions (Bowden 1985), and explains the depletion of alkali components in this alteration zone (Fig. 27). The dissolution of arfvedsonite and aegirine in the peralkaline FCG that Waight (1995) located nearby, can also release substantial F, Zr and minor REEs into solution (Rubin et al. 1993). Therefore, redistribution of elements by hydrothermal fluids likely played a significant role in the formation of bastnäsite, parisite, synchysite, monazite and xenotime in the EHR alteration zone.

The significance of the giant zircon in the Eastern Hohonu River

The giant zircon in the alteration zone in the EHR provide evidence that the REE mineralisation here was not only a product of leaching, recycling and reprecipitation, but also that this was a location where the last residual melt was anomalously enriched in REEs through extensive fractionation. Zirconium is highly soluble in alkalic, F-rich systems, which leads to its progressive enrichment, along with REEs, Y, Nb, Ti, U and Th, during magmatic differentiation (Alderton et al. 1980; Rubin et al. 1993). Fluoride in residual melts can also lower the solidus, enabling crystallisation at lower temperatures (Bowden & Kinnaird 1984). The anhedral, interstitial shapes, the minor compositional zoning, the quartz inclusions (Fig. 23a), and a mean Ti-in-zircon temperature of ~805°C, signify that these giant zircon, and the substantial REEs they contain (Fig. 31), have a late-magmatic origin, where little change in composition occurred, rather than a hydrothermal origin.

Although zircon are generally resistant to alteration (Hanchar & van Westrenen 2007), these giant zircon have undergone considerable metamictisation and modification by the hydrothermal fluids, which increased their solubility (Rubin et al. 1993). This is indicated in the zircon by the: dirty coating (Fig. 33c-d); porous nature (Fig. 40a); inclusions; relative loss of Zr and Hf (Fig. 32d-e); and alteration to xenotime, which has taken in HREEs (Y, Gd, Tb, Dy, Ho, Er and Yb). Therefore, REE content in these giant zircon likely represents a continuum of processes that occurred between the crystallisation of the residual melt and the establishment of the hydrothermal system. During metamictisation, loss of Pb, Th and U can occur (Berger et al. 2008; Geisler et al. 2007; Sinha et al. 1992), especially in the presence of F (Rubin et al. 1993), and is the result of coupled dissolution-reprecipitation reactions in an aqueous fluid or melt at the eutectic point (Berger et al. 2008; Geisler et al. 2007). Evidence for this can be increased porosity of the zircon – as a result of α-particle recoil – in which secondary minerals precipitate, leading to thorite, galena, xenotime and/or monazite inclusions. All of these are present in the giant zircon, and the remobilisation of these radioactive elements during re-equilibration reactions undoubtedly explains why U-Pb dating proved problematic.

Extensional structures and their relationship to hydrothermal alteration

Another conspicuous feature in the zone of hydrothermal alteration in the EHR is the apparent extension preserved in the structures and textures at the locality. Non-systematic vein arrays (Fig. 23f) and en echelon-type veining suggest a component of fragmentation as well as shearing (Ramsay & Lisle 2000; van der Pluijm & Marshak 2004), likely associated with fluid pressure or a degassing episode. Discrete fractures with transtensive offsets are seen in thin section (Fig. 23d) and contain quartz crystals that both continued to crystallise and recrystallise after becoming offset. This indicates the structures were active once the rock had become brittle enough to fracture, but was still hot enough for igneous quartz to continue to grow (i.e. >300°C). Similarly, quartz displays elongate undulose extinction, and the directional protuberances on the quartz (Fig. 22e) indicate that they continued to grow into cavities formed as the rocks were progressively pulled apart during the same late-stage dynamic environment that spans the FCG's cooling history.

Hydrothermal fluids are common features of shallow extensional settings, utilising structural weaknesses to help break-apart the rock, and such areas of localised extension (Fig. 44) are known for their potential to host mineralisation (Murphy 2014). The REE mineralisation within this zone is therefore likely a product of hydrothermal REE-bearing fluids entering these cavities, and, the resulting pressure decrease and volatile loss, along with dilution and a decrease in temperature and ligand activity, forced the precipitation of new minerals. Waight (1995) reported the occurrence of a highly altered mafic dyke within this zone of hydrothermal alteration in the EHR, and the sharp boundaries of this structure probably acted as a conduit for the hydrothermal fluids (Fig. 44). The presence of both the dyke and the cavities indicate that this locality underwent considerable localised extension. Although this dyke was not observed during the current study, the zone of alteration has the same WNW-ESE structural trend as the HDS, and thus supports this theory well. The most important aspect when considering REE mineralisation within the FCG is, therefore, locating where the late-magmatic stage overlaps with the hydrothermal system and a structurally-controlled zone of weakness (Fig. 44). Fortunately, pre-existing weaknesses are often areas exploited by hydrothermal ore-bearing fluids.

Quartz and ankerite veins were observed to intrude sub-parallel to a dyke ~120 m downstream of the alteration zone in the EHR (Fig. 13d). Proximal to these veins, the dyke and FCG have undergone intense alteration and slight brecciation, and numerous generations of silica- and carbonate-rich fluids are recognised from cross-cutting relationships. This indicates different hydrothermal fluids utilising the same structural weakness during multiple tectonic events. Unfortunately samples were not orientated in the field, but further work with a structural focus is recommended and was outside the scope of this project. The exact relationship of the stress directions needed for the quartz protuberances, fractures and shear planes within the FCG, to the orientation of the Cenozoic NE-SW Hohonu Fault and similarly, the elongate dome inferred by Price (2008), the N-S and NE-SW variogram patterns, the WNW-ESE dyke swarm, the Paparoa Metamorphic Core Complex, and the opening direction of the Tasman Sea, remains unclear.

Cross-cutting veins within the FCG

In general, cross-cutting quartz and carbonate veins throughout the FCG displaying sharp contacts contain only very low REE content (Fig. 29a). This indicates that: 1) they occurred after the FCG had completely solidified; 2) negligible fluid-wall rock reactions occurred; and 3) these fluids were likely unrelated to the late-stage, REE-bearing hydrothermal system. Many of the quartz, and even ankerite, crystals in these veins display oriented prismatic growth in a mesh-like texture, indicative of simultaneous crystallisation. These likely occurred as fluids filled open cavities during sudden fracturing events, rather than progressive opening of a cavity, and were not part of the same mineralising event, nor necessarily even part of the same magmatic-tectonic episode that formed the FCG. Other quartz and carbonate veins are brecciated, strained, and display evidence for rapid growth rates, changing fluid composition, and dynamic recrystallisation over multiple deformation events that are also inferred to be unrelated to the main episode of hydrothermal REE enrichment.

One brecciated ankerite vein (LHR25) enclosing clasts of highly altered FCG, contains anomalous HREEs (48% of ΣREEs) with HREE:LREE of almost 1:1. Fine grained ankerite masses replace larger ankerite crystals, indicative of multiple generations of carbonate-rich fluids. The REEs have partitioned into synchysite, known for its HREE content (Chakhmouradian & Wall 2012), and florencite, which occur in the fine grained ankerite and the sericitisation of the altered granite. Quartz overgrowths, florencite rosettes and partial replacement of synchysite, might suggest fluids evolved from SiO_2-rich, to fluids rich in CO_3^{2-} and F^-, and then towards Al^{3+}, OH^-, PO_4^{3-} and sulphur, as they passed through and reacted with the aluminium-rich, apatite-bearing FCG. This HREE-rich vein (Fig. 29c) might represent a small amount of immiscible carbonate fluid that separated from the FCG (Fig. 44), a common process in a granite-H_2O-CO_2 system (Bowden & Kinnaird 1984), and a similar process that occurs with a carbonatite melt. However, these carbonate veins are interpreted as hydrothermal veins and not carbonatites, on the basis that they lack typical carbonatite or fenite textures and mineralogy (e.g., apatite, monazite and amphibole). Although carbonate veins are expected to display textures consistent with crystallisation from cavity walls, rather than equidimensional crystals, the silica

veins also display similar textures, which is therefore also not evidence in favour of a carbonatite source. This vein corresponds with the first order Y anomalies found in the area (note Y is comparable to HREEs), and it probably also represents the HREE mineralisation that led to the unusually high proportions of HREEs (30% of ΣREEs) found in panned stream concentrates in the LHR by Geoff Price.

5.3 Prospectivity and implications for REE mineralisation in the French Creek Granite

The zone of hydrothermal alteration in the Eastern Hohonu River

This phyllic alteration zone displays consistent REE anomalies in rock chip samples (La+Ce+Y up to 527 ppm); however, it is only ca. 30 m wide, and a comprehensive economic assessment of it now needs to be made in order to determine if it has the potential to be a REE deposit. This alteration zone was not observed on the other side of the river, due to dense vegetation and burial beneath rock fall. Furthermore, the zone is located close to the upper contact with the Deutgam Granodiorite, and tracking its strike towards the southeast to determine its extent would prove difficult, because of the southeast dip of the structure, steeple-gorged terrain, and dense vegetation cover with little to no rock exposure. Intrusions, veining and alteration during hydrothermal activity can extend into the country rock, and if it involves the basement, extensive chloritisation can lead to sulphide deposits (Fig. 44; Kinnaird 1985). The period of late-stage hydrothermal activity recognised in the FCG might, therefore, be the source of the sulphides found throughout the Hohonu Batholith by White & Price (2006).

Results from this study show that the most intensely altered samples of the FCG have the most consistent REE anomalies, and are thus most prospective for economic REE mineralisation. It is recommended for future REE exploration efforts to target the upper Mt French Track and adjacent small tributary of the EHR, as well as the upper catchment of the northern tributary of the LHR, in order to search for similar hydrothermal alteration as that found in the EHR. It is suggested that the HREE and first order Y anomalies in the LHR are related to the brecciated ankerite vein (LHR25), therefore attempting to locate the source(s) of this vein is also

recommended. This study indicates that localities displaying evidence for a specific combination of processes, such as the presence of F-rich late-magmatic residual fluid, hydrothermal activity and localised extension, are the most prospective for consistent REE mineralisation in the FCG. Features to look for during further exploration are bleached rocks, clay alteration, landslides and crumbling river banks, embayments in streams indicative of veins, and mafic-rich zones within the FCG.

REE mobilisation during weathering of granitic rocks

Weathering profiles or clays, such as the halloysite in the EHR, can lead to REE laterite or ion-adsorption deposits (Kanazawa & Kamitani 2006) if conditions are right, because fluorcarbonates tend to weather out of their host relatively easily, adsorbing onto clay minerals (Chakhmouradian & Wall 2012; Henderson 1996; Wall 2014). Mature weathering profiles can become effective REE storage reservoirs if weathering rates are high enough and erosion rates low enough (Nesbitt & Markovics 1997), such as the laterites in southern China, which contain up to 700 ppm ΣREEs (Imai et al. 2013). However, REEs are relatively mobile during supracrustal weathering processes, especially in areas with high rainfall and dynamic tectonics, such as on the West Coast of New Zealand. In a study conducted on REE mobility during weathering of a granitic catchment, Aubert et al. (2001) found that REEs were enriched in the dissolved and suspended stream loads (i.e. the 0-20 µm fraction) relative to the soil. This was ascribed to the dissolution of apatite and feldspar in slightly acidic rainwater during weathering processes. Primary apatite, allanite, titanite and epidote are replaced by LREE-bearing secondary minerals – which are mostly relatively soluble phosphates or clays – and REEs are released and subsequently washed away downstream (Aubert et al. 2001; Boulangé & Colin 1994; Braun et al. 1993). Zircon, xenotime and monazite are much more resistant to these weathering processes, and are therefore likely to form secondary placer deposits.

Secondary REE placer deposits

Because panned stream concentrates had a much higher concentration of REEs (La+Ce+Y up to 4633 ppm; Strategic Elements Ltd 2011) than the FCG body itself, secondary deposits might prove to be more prospective. Monazite, xenotime, zircon,

rutile, ilmenite, thorite and uranothorite are important REE-Ti-Nb-Zr-Y-Th-bearing minerals that are resistant and durable during weathering and transportation processes (Wall 2014). They have a specific gravity of 4.0 to 6.7 (Hutton 1950; Mindat and Webmineral databases), and are commonly concentrated in placer deposits as heavy mineral sands. Analysing the panned concentrate samples from Price (2013), Price & Ryland (2011) and White & Price (2006) to determine which minerals host the REEs was outside the scope of this project; however, this would be beneficial in order to understand how the REEs partition during secondary processes, and to determine how economic they might be. Additionally, comparing the panned concentrate samples from the FCG with the large REE placer deposits at Barrytown (James Pope pers. Comm.), and other nearby alluvial and beach heavy mineral sands, would determine if the FCG is at least a partial source to these, since the LHR flows into the Taramakau River and sediments would be transported northwards toward Barrytown by longshore drift. The EHR flows into Lake Brunner on its western margin, at Hohonu Spit, and this might be another location to analyse stream sediments for REE content, bearing in mind that the sediments on the plains have been affected by fluvioglacial processes (White & Price 2006).

Chapter 6: Conclusions

The FCG is a peraluminous, ferroan, A-type granitoid with elevated REEs and other HFSEs, typical of early-anorogenic extensional settings. It was generated 82.55 ± 0.85 Ma during decompression, mantle upwelling and the initial opening of the Tasman Sea. Primary REE enrichment is a function of: 1) derivation from an enriched mantle reservoir; 2) high magmatic F content; 3) high heat flow; 4) assimilation of the Greenland Group crust; and 5) extensive fractionation. Textural evidence indicates the FCG had a subsolvus history, before high-level, hypersolvus, eutectic crystallisation occurred during decompression, undercooling and magma ascent, as Late Cretaceous regional extension progressed. Multiple pulses of magmatism are associated with the compositionally diverse FCG, which underwent dynamic syn-tectonic crystallisation that spans its relatively short cooling history. The cogenetic and contemporaneous mafic HDS displays textural and geochemical evidence for magma mixing; mafic dykes are generally low in ΣREE content, while REE-enrichment is similar between the felsic dykes and the unaltered FCG.

Extensive fractionation and late-stage water saturation of the residual F-rich melt directly controlled the crystallisation of hydrous mafic minerals and REE-bearing accessory phases. This is apparent in the interstitial mafic clusters, and in the mafic-rich FCG variety that contains the highest ΣREE+Y recorded (847 ppm). The REEs, Nb, Ti, Zr, Y, P and F concentrated in the residual melt and partitioned into primary allanite, monazite, fergusonite, perrierite, loparite, titanite, rutile and ilmenite. Significant REE substitution into zircon and apatite has also occurred.

The FCG has undergone sericitisation, chloritisation, silicification, kaolinisation, hematisation and carbonate alteration. Extensive secondary ankerite and siderite coincide with the economically important bastnäsite group minerals throughout the FCG. Syntaxial bastnäsite-parisite replace amphibole, allanite and/or Ti-oxides, and are the most common secondary rare earth minerals in the FCG ahead of synchysite, xenotime, monazite and florencite. Stable isotopic analysis indicates that CO_2, likely sourced from the degassing mantle, was incorporated into magmatic-hydrothermal fluids, and subsequently involved in the extensive carbonate alteration, REE remobilisation, and secondary REE enrichment in the FCG. An immiscible carbonate-

rich fluid also appears responsible for the HREE anomalies in the LHR, although more exploration is recommended to track this brecciated vein float back to its source.

The fluids responsible for the hydrothermal alteration were derived directly from the crystallising pluton, as part of a late-stage porphyry-type system. However, sharply cross-cutting veins of quartz and carbonate are likely younger and unrelated to the secondary hydrothermal REE enrichment. Low-temperature sodic metasomatism led to propylitic alteration in the LHR, and along with the pegmatite pods and microgranite, might denote the apical zone of the pluton. Later, acidic metasomatism by ca. 250°C fluids resulted in the phyllic alteration assemblage in the EHR, characterised by sericite + quartz + pyrite, and in which bastnäsite group minerals, halloysite, rutile, leucoxene, zircon, xenotime, monazite, pyrochlore, sphalerite, galena, chalcopyrite, siderite and ankerite also occur. This assemblage likely indicates mixing between two fluids that had previously leached HFSEs, P and F from the host. Giant, late-magmatic, metamict zircon are evidence that the residual melt was already anomalously enriched in these elements, and that modification and secondary REE enrichment occurred during coupled dissolution-reprecipitation reactions in the hydrothermal solution. The mineralogy and extensional structures at the location indicate boiling, degassing and deformation during the late-magmatic to early-hydrothermal stages, where fluids utilised pre-existing weaknesses to intrude and deposit REEs. A key consideration for further REE exploration in the FCG is, therefore, locating where the late-magmatic stage, with its residual F-rich melt, overlaps permeable zones that the hydrothermal system exploited, leading to structurally-controlled secondary REE mineralisation.

The zone of hydrothermal alteration in the EHR displays consistent REE anomalies (607 ppm ΣREE+Y on average), and now requires a comprehensive economic assessment to determine its potential as New Zealand's first granite-hosted REE deposit. Further investigation around the upper Mt French Track, adjacent EHR tributary, and in the upper northern tributary of the LHR is recommended, in order to explore for similar magmatic-hydrothermal REE mineralisation. In the absence of these – and because of the high rainfall and tectonic activity on the West Coast – secondary REE placer deposits, where REE-bearing zircon, monazite and xenotime are expected to accumulate, might prove more economic.

Table 6. Brief answers to the questions that were posed in the introduction, Section 1.3.

1. Determine the field relationships	
Question:	**Answer:**
What are the field relationships between the FCG, HDS and the alteration?	The mafic HDS cross-cuts the FCG; rare gradational contacts imply concurrent activity. Diffuse alteration affects the FCG; veins with sharp contacts occurred later. Hydrothermal fluids occasionally utilised permeable contacts between the FCG and HDS.
2. Analyse the mineralogy	
Questions:	**Answers:**
What is the primary and secondary mineralogy of the FCG and HDS? Which primary and secondary minerals have the REEs partitioned into?	The FCG is composed of K-feldspar and quartz, with minor plagioclase, biotite and/or amphibole, and accessory zircon, apatite, magnetite, ilmenite and titanite. Mafic–felsic dykes contain variable plagioclase, K-feldspar, quartz, biotite, amphibole, augite, olivine and/or nepheline. Both are affected by alteration; the mafic component by chlorite, limonite, rutile, leucoxene, muscovite, sulphides and carbonates, and the feldspars by sericite, clay and quartz. The REEs are in primary allanite, fergusonite, monazite, loparite and perrierite, and in secondary bastnäsite group minerals, xenotime and florencite.
3. Analyse the geochemistry and evaluate REE enrichment	
Questions:	**Answers:**
What is the geochemistry of the rare earth minerals? What other minerals have the REEs partitioned into? Which REEs are present and what differences in REE content are observed between the FCG, its hydrothermal alteration and the HDS?	Light RE minerals dominate; bastnäsite-parisite are the most common. Allanite, perrierite, loparite, bastnäsite group minerals, monazite and florencite contain Ce, La and Nd, sometimes with minor Y, Gd, Pr and Sm. Fergusonite and xenotime contain HREEs (Y, Dy, Gd, Er, Yb, Sm, Ho and Tb). Substantial REEs occur also in zircon and apatite, and minor Y in titanite and calcite. Fluorine is present in bastnäsite group minerals (up to 8 wt. %), perrierite and fluorapatite, while Th is present within most RE minerals. Unaltered FCG contains 418 ppm average ΣREEs (521 ppm max), while the hydrothermal alteration in the EHR is consistently enriched at 607 ppm average ΣREEs (740 ppm max). Mafic dykes generally have <200 ppm ΣREEs, while felsic dykes contain similar ΣREE content to the unaltered FCG.

Table 6. continued.

4. Determine petrogenetic processes involved in the REE mineralisation	
Questions:	**Answers:**
What primary and secondary petrogenetic processes were involved in the REE mineralisation? What was the source of the hydrothermal fluids, and were they important for the remobilisation of REEs? Were F and Cl important components of the fluid?	Primary REE enrichment in the FCG is a function of partial melting, extensive differentiation and derivation from an enriched mantle reservoir. High magmatic F increased the solubility of REE-Zr, promoting REE enrichment in the residual melt. Hydrothermal circulation remobilised REEs and other HFSEs, and was a crucial process for secondary REE enrichment within the phyllic alteration assemblage. The fluids were sourced from the cooling FCG (e.g., formation of granophyric intergrowths), and developed into a late-stage hydrothermal porphyry-type system. The importance of F in these fluids is evident in the presence of the economically important fluorcarbonate bastnäsite group minerals in the zone of hydrothermal alteration in the EHR. These minerals show evidence for only minor Cl involvement.
5. Identify zones of REE enrichment	
Questions:	**Answers:**
Where has the REE mineralisation occurred? Are there localities with consistent REE anomalies?	Background primary REE enrichment has occurred throughout the FCG. Primary REE-bearing phases are associated with mafic clusters; samples with higher mafic content might thus contain more primary REE enrichment, such as in sample GR03 with ~800 ppm ΣREEs. The zone of hydrothermal alteration in the EHR has the most consistent REE enrichment, and this phyllic alteration assemblage displays evidence of REE mineralisation. This locality is currently the most prospective as a potential REE deposit.

References

Adams CJD, Harper CT, Laird MG 1975. K-Ar ages of low grade metasediments of the Greenland and Waiuta groups in Westland and Buller, New Zealand. New Zealand Journal of Geology and Geophysics 18: 39–48.

Alderton DHM, Pearce JA, Potts PJ 1980. Rare earth element mobility during granite alteration: evidence from southwest England. Earth and Planetary Science Letters 49: 149–165.

Alonso E, Sherman AM, Wallington TJ, Everson MP, Field FR, Roth R, Kirchain RE 2012. Evaluating rare earth element availability: a case with revolutionary demand from clean technologies. Environmental Science and Technology 46: 3406–3414.

ALS Global 2016. Geochemical procedure ME-MS81 ultra-trace level methods. www.alsglobal.com/~/media/Files/Divisions/Minerals/Geochemistry/Geochemistry Resources/Short Method Descriptions/ME-MS81 Lithium Metaborate fusion-ICP-MS Multi-element Method.pdf

Anderson JL & Thomas WM 1985. Proterozoic anorogenic two-mica granites: Silver Plume and St. Vrain batholiths of Colorado. Geology 13: 177–180.

Aubert D, Stille P, Probst A 2001. REE fractionation during granite weathering and removal by waters and suspended loads: Sr and Nd isotopic evidence. Geochimica et Cosmochimica Acta 65: 387–406.

Baker IA, Gamble JA, Graham IJ 1994. The age, geology, and geochemistry of the Tapuaenuku Igneous Complex, Marlborough, New Zealand. New Zealand Journal of Geology and Geophysics 37: 249–268.

Bau M 1991. Rare-earth element mobility during hydrothermal and metamorphic fluid-rock interaction and the significance of the oxidation state of europium. Chemical Geology 93: 219–230.

Bayliss P & Levinson AA 1988. A system of nomenclature for rare earth mineral species: revision and extension. American Mineralogist 73: 422–423.

Bea F 1996. Residence of REE, Y, Th and U in granites and crustal protoliths; implications for the chemistry of crustal melts. Journal of petrology 37: 521–552.

Bell JM & Fraser C 1906. The geology of the Hokitika Sheet, north Westland quadrangle. New Zealand Geological Survey Bulletin 1.

Berger A, Gnos E, Janots E, Fernandez A, Giese J 2008. Formation and composition of rhabdophane, bastnäsite and hydrated thorium minerals during alteration: implications for geochronology and low-temperature processes. Chemical Geology 254: 238–248.

Bishop DJ 1992. Extensional tectonism and magmatism during the middle Cretaceous to Paleocene, North Westland, New Zealand. New Zealand Journal of Geology and Geophysics 35: 81–91.

Black LP, Kamo SL, Allen CM, Davis DW, Aleinikoff JN, Valley JW, Mundil R, Campbell IH, Korsch RJ, Williams IS, Foudoulis C 2004. Improved $^{206}Pb/^{238}U$ microprobe geochronology by the monitoring of a trace-element-related matrix effect; SHRIMP, ID–TIMS, ELA–ICP–MS and oxygen isotope documentation for a series of zircon standards. Chemical Geology 205: 115–14.

Black LP, Kamo SL, Williams IS, Mundil R, Davis DW, Korsch RJ, Foudoulis C 2003. The application of SHRIMP to Phanerozoic geochronology; a critical appraisal of four zircon standards. Chemical Geology 200:171–188.

Black R, Lameyre J, Bonin B 1985. The structural setting of alkaline complexes. Journal of African Earth Sciences 3: 5–16.

Bonin B 1990. From orogenic to anorogenic settings: evolution of granitoid suites after a major orogenesis. Geological Journal 25: 261–270.

Bonin B 2007. A-type granites and related rocks: evolution of a concept, problems and prospects. Lithos 97: 1–29.

Bonin B & Giret A 1985. Contrasting roles of rock-forming minerals in alkaline ring complexes. Journal of African Earth Sciences 3: 41–49.

Bonin B & Giret A 1990. Plutonic alkaline series: Daly gap and intermediate compositions for liquids filling up crustal magma chambers. Schweizerische Mineralogisch und Petrographische Mitteilungen 70:175–187.

Bottinga Y 1968. Calculation of fractionation factors for carbon and oxygen isotopic exchange in the system calcite-carbon dioxide-water. Journal of Physical Chemistry 72: 800–808.

Boulangé B & Colin F 1994. Rare earth element mobility during conversion of nepheline syenite into lateritic bauxite at Passa Quatro, Minais Gerais, Brazil. Applied Geochemistry 9: 701–711.

Bowden P 1985. The geochemistry and mineralization of alkaline ring complexes in Africa (a review). Journal of African Earth Sciences 3: 17–39.

Bowden P & Kinnaird JA 1984. The petrology and geochemistry of alkaline granites from Nigeria. Physics of the Earth and Planetary Interiors 35: 199–211.

Bradley JP 1977. A study of the detrital heavy minerals of Westland. Unpublished thesis, University of Canterbury, Christchurch, New Zealand.

Bradley JP, Wilkins CJ, Oldershaw W, Smale D 1979. A study of detrital heavy minerals in the Taramakau catchment. Journal of the Royal Society of New Zealand 9: 233–251.

Bradshaw JD 1989. Cretaceous geotectonic patterns in the New Zealand region. Tectonics 8: 803–820.

Bradshaw JD 1993. A review of the Median Tectonic Zone: terrane boundaries and terrane amalgamation near the Median Tectonic Line. New Zealand Journal of Geology and Geophysics 36: 117–125.

Brathwaite RL 2013. Petrographic examination and report on five French Creek Granite samples from the Hohonu Ranges, north Westland. GNS Science Consultancy Report 2013/102. 16 p.

Braun JJ, Pagel M, Herbilln A, Rosin C 1993. Mobilization and redistribution of REEs and thorium in a syenitic lateritic profile: a mass balance study. Geochimica et Cosmochimica Acta 57: 4419–4434.

Cande SC & Stock JM 2004. Cenozoic reconstructions of the Australia-New Zealand-South Pacific sector of Antarctica. In: Exon NF, Kennett JP, Malone MJ ed. The Cenozoic Southern Ocean: tectonics, sedimentation, and climate change between Australia and Antarctica. American Geophysical Union 151: 5–17.

Candela PA 1997. A review of shallow, ore-related granites: textures, volatiles, and ore metals. Journal of petrology 38: 1619–1633.

Castor SB & Hedrick JB 2006. Rare earth elements. Industrial minerals volume, 7th ed. Society for mining, metallurgy and exploration: 769–792.

Chakhmouradian AR & Mitchell RH 1999. Primary, agpaitic and deuteric stages in the evolution of accessory Sr, REE, Ba and Nb-mineralization in nepheline-syenite pegmatites at Pegmatite Peak, Bearpaw Mts, Montana. Mineralogy and Petrology 67: 85–110.

Chakhmouradian AR, Mitchell RH, Pankov AV, Chukanov NV 1999. Loparite and ‘metaloparite' from the Burpala alkaline complex, Baikal Alkaline Province (Russia). Mineralogical Magazine 63: 519–519.

Chakhmouradian AR & Wall F 2012. Rare earth elements: minerals, mines, magnets (and more). Elements 8: 333–340.

Chakhmouradian AR & Zaitsev AN 2012. Rare earth mineralization in igneous rocks: sources and processes. Elements 8: 347–353.

Christie AB, Barker RG, Brathwaite RL 2010. Mineral resource assessment of the West Coast region, New Zealand. Institute of Geological and Nuclear Sciences science report 2010/61. 238 p.

Christie T, Brathwaite B, Tulloch A 1998. Rare earths and related elements. GNS Science Mineral Commodity Report 17. 13 p.

Christie AB, Cox SC, Rattenbury MS, Brathwaite RL, Whetter N 2006. Orogenic (mesothermal) gold deposits of the Reefton Goldfield, West Coast - review of exploration and geology. Australasian Institute of Mining and Metallurgy Monograph 25: 255–262.

Coates G, Cox GJ 2002. The rise and fall of the Southern Alps. Christchurch, Canterbury University Press. 80 p.

Collins WJ, Beams SD, White AJR, Chappell BW 1982. Nature and origin of A-type granites with particular reference to southeastern Australia. Contributions to Mineralogy and Petrology 80: 189–200.

Cooper AF 1971. Carbonatites and fenitization associated with a lamprophyric dike-swarm intrusive into schists of the New Zealand geosyncline. Geological Society of America Bulletin 82: 1327–1340.

Cooper RA 1989. Early Paleozoic terranes of New Zealand. Journal of the Royal Society of New Zealand 19: 73–112.

Cooper AF & Paterson LA 2008. Carbonatites from a lamprophyric dyke-swarm, South Westland, New Zealand. The Canadian Mineralogist 46: 753–777.

Cooper RA & Tulloch AJ 1992. Early Palaeozoic terranes in New Zealand and their relationship to the Lachlan Fold Belt. Tectonophysics 214: 129–144.

Creaser RA, Price RC, Wormald RJ 1991. A-type granites revisited: assessment of a residual-source model. Geology 19: 163–166.

Eby GN 1990. The A-type granitoids: a review of their occurrence and chemical characteristics and speculations on their petrogenesis. Lithos 26: 115–134.

Eby GN 1992. Chemical subdivision of the A-type granitoids: petrogenetic and tectonic implications. Geology 20: 641–644.

Ferry JM & Watson EB 2007. New thermodynamic models and revised calibrations for the Ti-in-zircon and Zr-in-rutile thermometers. Contributions to Mineralogy and Petrology 154: 429–437.

Frost BR, Barnes CG, Collins WJ, Arculus RJ, Ellis DJ, Frost CD 2001. A geochemical classification for granitic rocks. Journal of Petrology 42: 2033–2048.

Frost CD & Frost BR 1997. Reduced rapakivi-type granites: the tholeiite connection. Geology 25: 647–650.

Geisler T, Schaltegger U, Tomaschek F 2007. Re-equilibration of zircon in aqueous fluids and melts. Elements 3: 43–50.

Gieré R 1990. Hydrothermal mobility of Ti, Zr and REE: examples from the Bergell and Adamello contact aureoles (Italy). Terra Nova 2: 60–67.

Gieré R 1993. Transport and deposition of REE in H2S-rich fluids: evidence from accessory mineral assemblages. Chemical Geology 110: 251–268.

Gieré R 1996. Formation of rare earth minerals in hydrothermal systems. In: Jones AP, Wall F, Williams CT ed. Rare earth minerals. Chemistry, origin and ore deposits. London, UK, Chapman & Hall 7: 105–150.

GNS Science 2016. Petlab database. http://pet.gns.cri.nz/#/.

Grapes RH 1975. Petrology of the Blue Mountain Complex, Marlborough, New Zealand. Journal of Petrology 16: 371–428.

Hamill LJ 1972. Geology of the western Hohonu Range, north Westland. Unpublished thesis, University of Otago, Dunedin, New Zealand.

Hanchar JM & Van Westrenen W 2007. Rare earth element behaviour in zircon-melt systems. Elements 3: 37–42.

Hatch GP 2012. Dynamics in the global market for rare earths. Elements 8: 341–346.

Henderson P 1996. The rare earth elements: introduction and review. In: Jones AP, Wall F, Williams CT ed. Rare earth minerals. Chemistry, origin and ore deposits. London, UK, Chapman & Hall 7: 1–19.

Howarth RJ 1998. Improved estimators of uncertainty in proportions, point-counting, and pass-fail test results. American Journal of Science 298: 594–607.

Hutton CO 1950. Studies of heavy detrital minerals. Geological Society of America Bulletin 61: 635–710.

Imai A, Yonezu K, Sanematsu K, Ikuno T, Ishida S, Watanabe K, Pisutha-Arnold V, Nakapadungrat S, Boosayasak J 2013. Rare earth elements in hydrothermally altered granitic rocks in the Ranong and Takua Pa Tin-Field, Southern Thailand. Resource Geology 63: 84–98.

Irvine TN & Baragar WRA 1971. A guide to the chemical classification of the common volcanic rocks. Canadian Journal of Earth Sciences 8: 523–548.

Joussein E, Petit S, Churchman J, Theng B, Righi D, Delvaux B 2005. Halloysite clay minerals–a review. Clay Minerals 40: 383–426.

Kanazawa Y & Kamitani M 2006. Rare earth minerals and resources in the world. Journal of Alloys and Compounds 408: 1339–1343.

Kempe U, Götze J, Dandar S, Habermann D 1999. Magmatic and metasomatic processes during formation of the Nb-Zr-REE deposits Khaldzan Buregte and Tsakhir (Mongolian Altai): indications from a combined CL-SEM study. Mineralogical Magazine 63: 165–165.

Kimbrough DL, Tulloch AJ, Rattenbury MS 1994. Late Jurassic-Early Cretaceous metamorphic age of Fraser Complex migmatite, Westland, New Zealand. New Zealand Journal of Geology and Geophysics 37: 137–142.

Kinnaird JA 1985. Hydrothermal alteration and mineralization of the alkaline anorogenic ring complexes of Nigeria. Journal of African Earth Sciences 3: 229–251.

Kovalenko VI, Tsaryeva GM, Goreglyad AV, Yarmolyuk VV, Troitsky VA, Hervig RL, Farmer G 1995. The peralkaline granite-related Khaldzan-Buregtey rare metal (Zr, Nb, REE) deposit, western Mongolia. Economic Geology 90: 530–547.

Laird MG 1993. Cretaceous continental rifts: New Zealand region. South Pacific sedimentary basins. Sedimentary basins of the world 2: 37–49.

Laird MG 1994. Geological aspects of the opening of the Tasman Sea. In: van der Lingen GJ, Swanson KM, Muir RJ ed. Evolution of the Tasman Sea basin. Netherlands, AA Balkema: 1–17.

Laird MG & Bradshaw JD 2004. The break-up of a long-term relationship: the Cretaceous separation of New Zealand from Gondwana. Gondwana Research 7: 273–286.

Land Information New Zealand 2015. Coordinate conversion. http://apps.linz.govt.nz/coordinate-conversion/index.aspx.

Land Information New Zealand 2016. NZ Topo50 Map Sheets. http://data.linz.govt.nz/search/?q=topo.

Larter RD, Cunningham AP, Barker PF, Gohl K, Nitsche FO 2002. Tectonic evolution of the Pacific margin of Antarctica 1. Late Cretaceous tectonic reconstructions. Journal of Geophysical Research, Solid Earth 107: 5/1–19.

Lawver LA, Gahagan LM, Coffin MF 1992. The development of paleoseaways around Antarctica. In: Kennett JP & Warnke DA ed. The Antarctic paleoenvironment: a perspective on global change. Washington DC, American Geophysical Union: 7–30.

Le Bas MJ, Le Maitre RW, Streckeisen AL, Zanettin B 1986. A chemical classification of volcanic rocks based on the total alkali-silica diagram. Journal of Petrology 27: 745–750.

Lee RF 1976. Procedures for chemical analysis, Department of Geology, University of Western Australia.

Levinson AA 1966. A system of nomenclature for rare earth minerals. American Mineralogist 51: 152–158.

Lewis DW & McConchie D 1994. Analytical sedimentology. New York, Chapman & Hall. 197p.

Lister GS, Etheridge MA, Symonds PA 1986. Detachment faulting and the evolution of passive continental margins. Geology 14: 246–250.

London D 1990. Internal differentiation of rare-element pegmatites; a synthesis of recent research. Geological Society of America Special Papers 246: 35–50.

Lottermoser BG 1992. Rare earth elements and hydrothermal ore formation processes. Ore Geology Reviews 7: 25–41.

Lowenstern JB 2001. Carbon dioxide in magmas and implications for hydrothermal systems. Mineralium Deposita 36: 490–502.

Ludwig K 2003. Isoplot 3.00. Berkeley Geochronology Centre Special Publication 4. Berkley, CA.

Luyendyk BP 1995. Hypothesis for Cretaceous rifting of east Gondwana caused by subducted slab capture. Geology 23: 373–376.

Martin RF 2006. A-type granites of crustal origin ultimately result from open-system fenitization-type reactions in an extensional environment. Lithos 91: 125–136.

Massachusetts Institute of Technology 2012. Rare earth elements supply and demand. http://web.mit.edu/12.000/www/m2016/finalwebsite/problems/ree.html.

Massari S & Ruberti M 2013. Rare earth elements as critical raw materials: focus on international markets and future strategies. Resources Policy 38: 36–43.

Mauriohooho K, Barker SL, Rae A 2016. Mapping lithology and hydrothermal alteration in geothermal systems using portable x-ray fluorescence (pXRF): a case study from the Tauhara geothermal system, Taupo Volcanic Zone. Geothermics 64: 125–134.

McConnell JW & Batterson MJ 1987. The strange lake Zr-Y-Nb-Be-REE deposit, Labrador: a geochemical profile in till, lake and stream sediment, and water. Journal of Geochemical Exploration 29: 105–127.

McLennan SM & Taylor SR 1979. Rare earth element mobility associated with uranium mineralisation. Nature 282: 247–250.

Michard A 1989. Rare earth element systematics in hydrothermal fluids. Geochimica et Cosmochimica Acta 53: 745–750.

Mitchell RH 1996. Perovskite: a revised classification scheme for an important rare earth element host in alkaline rocks. In: Jones AP, Wall F, Williams CT ed. Rare earth minerals. Chemistry, origin and ore deposits. London, UK, Chapman & Hall 7: 41–76.

Miyawaki R & Nakai I 1996. Crystal chemical aspects of rare earth elements. In: Jones AP, Wall F, Williams CT ed. Rare earth minerals. Chemistry, origin and ore deposits. London, UK, Chapman & Hall 7: 21–40.

Mortimer N 2004. New Zealand's geological foundations. Gondwana Research 7: 261–272.

Mortimer N, Rattenbury MS, King PR, Bland KJ, Barrell DJA, Bache F, Begg JG, Campbell HJ, Cox SC, Crampton JS, Edbrooke SW, Forsyth PJ, Johnston MR, Jongens R, Lee JM, Leonard GS, Raine JI, Skinner DNB, Timm C, Townsend DB, Tulloch AJ, Turnbull IM, Turnbull RE 2014. High-level

stratigraphic scheme for New Zealand rocks. New Zealand Journal of Geology and Geophysics 57: 402–419.

Mortimer N, Tulloch AJ, Spark RN, Walker NW, Ladley E, Allibone A, Kimbrough DL 1999. Overview of the Median Batholith, New Zealand: a new interpretation of the geology of the Median Tectonic Zone and adjacent rocks. Journal of African Earth Sciences 29: 257–268.

Muir RJ, Ireland TR, Weaver SD, Bradshaw JD 1994. Ion microprobe U-Pb zircon geochronology of granitic magmatism in the Western Province of the South Island, New Zealand. Chemical Geology 113: 171–189.

Muir RJ, Ireland TR, Weaver SD, Bradshaw JD, Waight TE, Jongens R, Eby GN 1997. SHRIMP U-Pb geochronology of Cretaceous magmatism in northwest Nelson-Westland, South Island, New Zealand. New Zealand Journal of Geology and Geophysics 40: 453–463.

Murphy C 2014. PP52704 Hohonu relinquishment report, Strategic Materials Pty Ltd. NZ Petroleum & Minerals, Ministry of Business, Innovation and Employment, Wellington, unpublished open-file mineral report MR5124.

Nathan S, Anderson HJ, Cook RA, Herzer RH, Hoskins RH, Raine JI, Smale D 1986. Cretaceous and Cenozoic sedimentary basins of the West Coast region, South Island, New Zealand. New Zealand Geological Survey Basin Studies 1. Wellington, New Zealand, Department of Scientific and Industrial Research. 90 p.

Nathan S, Rattenbury MS, Suggate RP 2002. Geology of the Greymouth area. Institute of Geological & Nuclear Sciences 1:250 000 geological map 12. Lower Hutt, New Zealand, Institute of Geological & Nuclear Sciences Limited. 1 sheet + 58 p.

Nesbitt HW & Markovics G 1997. Weathering of granodioritic crust, long-term storage of elements in weathering profiles, and petrogenesis of siliciclastic sediments. Geochimica et Cosmochimica Acta 61: 1653–1670.

Norrish K, Chappell BW 1977. X-ray fluorescence spectrography. In: Zussman J ed. Physical methods in determinative mineralogy. New York, Academic Press: 201–272.

Norrish K & Hutton JT 1969. An accurate x-ray spectrographic method for the analysis of a wide range of geological samples. Geochimica et Cosmochimica Acta 33: 431–453.

O'Neil JR, Clayton RN, Mayeda TK 1969. Oxygen isotope fractionation in divalent metal carbonates. Journal of Physical Chemistry 51: 5547–5558.

O'Sullivan PB, Kohn BP, Foster DA, Gleadow AJW 1995. Fission track data from the Bathurst Batholith: evidence for rapid mid-Cretaceous uplift and erosion within the Eastern Highlands of Australia. Australian Journal of Earth Sciences 42: 597–607.

Painter JAC 1972. Final report on Hohonu MPW areas, Lake Brunner, Carpentaria Exploration Co Pty Ltd. NZ Petroleum & Minerals, Ministry of Business, Innovation and Employment, Wellington, unpublished open-file mineral report MR1303.

Paton C, Hellstrom J, Paul B, Woodhead J, Hergt J 2011. Iolite: Freeware for the visualisation and processing of mass spectrometric data. Journal of Analytical Atomic Spectrometry 26: 2508–2518.

Pearce JA, Harris NB, Tindle AG 1984. Trace element discrimination diagrams for the tectonic interpretation of granitic rocks. Journal of Petrology 25: 956–983.

Pearce NJG, Perkins WT, Westgate JA, Gorton MP, Jackson SE, Neal CR, Chenery SP 1997: A compilation of new and published major and trace element data for NIST SRM 610 and NIST SRM 612 glass reference materials. Geostandards Newsletter 21: 115–144.

Pecora W 1956. Carbonatites: a review. Geological Society of America Bulletin 67: 1537–1556.

Pirajno F 2009. Hydrothermal processes and mineral systems. Netherlands, Springer. 1278 p.

Price GD 2008. Final Report for Hohonu Project, West Coast, NZ, Golden Fern Resources Ltd. NZ Petroleum & Minerals, Ministry of Business, Innovation and Employment, Wellington, unpublished open-file mineral report MR4581.

Price GD 2013. PP52704 Hohonu Project Report for Year 2 to 15 Dec 2012, Strategic Materials Pty Ltd. NZ Petroleum & Minerals, Ministry of Business, Innovation and Employment, Wellington, unpublished open-file mineral report MR4955.

Price GD, Ryland CB 2011. Annual report for PP52704 - Hohonu Project, Strategic Materials Pty Ltd. NZ Petroleum & Minerals, Ministry of Business, Innovation and Employment, Wellington, unpublished open-file mineral report MR4886.

Ramsay JG & Lisle RJ 2000. The techniques of modern structural geology: applications of continuum mechanics in structural geology. Vol. 3. California, Academic Press. 360 p.

Raymond LA 1995. Petrology: the study of igneous, sedimentary, and metamorphic rocks. Dubuque, Wm. C. Brown Communications Inc. 742 p.

Ridley J 2013. Ore deposit geology. Cambridge, Cambridge University Press. 398 p.

Robb LJ 2005. Introduction to ore-forming processes. Oxford, Blackwell Publishing. 373 p.

Rocklabs 2016. Range of heads and composition of materials. www.rocklabs.com/parts-and-consumables/downloads/rocklabs-range-of-heads.pdf.

Roser BP & Nathan S 1997. An evaluation of elemental mobility during metamorphism of a turbidite sequence (Greenland Group, New Zealand). Geological Magazine 134: 219–234.

Rubin JN, Henry CD, Price JG 1993. The mobility of zirconium and other “immobile” elements during hydrothermal alteration. Chemical Geology 110: 29–47.

Salvi S & Williams-Jones AE 1990. The role of hydrothermal processes in the granite-hosted Zr, Y, REE deposit at Strange Lake, Quebec/Labrador: evidence from fluid inclusions. Geochimica et Cosmochimica Acta 54: 2403–2418.

Salvi S & Williams-Jones AE 2006. Alteration, HFSE mineralisation and hydrocarbon formation in peralkaline igneous systems: insights from the Strange Lake Pluton, Canada. Lithos 91: 19–34.

Shand SJ 1927. On the relations between silica, alumina, and the bases in eruptive rocks, considered as a means of classification. Geological Magazine 64: 446–449.

Sharp Z 2007. Principles of stable isotope geochemistry. Upper Saddle River, NJ, Pearson Education. 344 p.

Shelley D 1993. Igneous and metamorphic rocks under the microscope: classification, textures, microstructures and mineral preferred-orientations. Cambridge, University Press. 445 p.

Sinha AK, Wayne DM, Hewitt DA 1992. The hydrothermal stability of zircon: preliminary experimental and isotopic studies. Geochimica et Cosmochimica Acta 56: 3551–3560.

Smith MP, Henderson P, Campbell LS 2000. Fractionation of the REE during hydrothermal processes: constraints from the Bayan Obo Fe-REE-Nb deposit, Inner Mongolia, China. Geochimica et Cosmochimica Acta 64: 3141–3160.

Spell TL, McDougall I, Tulloch AJ 2000. Thermochronologic constraints on the breakup of the Pacific Gondwana margin: The Paparoa Metamorphic Core Complex, South Island, New Zealand. Tectonics 19: 433–451.

Storey BC, Leat PT, Weaver SD, Pankhurst RJ, Bradshaw JD, Kelley S 1999. Mantle plumes and Antarctica-New Zealand rifting: evidence from mid-Cretaceous mafic dykes. Journal of the Geological Society 156: 659–671.

Strategic Elements Ltd 2011. Rare earths: prospectus. 58 p.

Suggate RP 1985. The glacial/interglacial sequence of north Westland, New Zealand. New Zealand Geological Survey record 7. Lower Hutt, New Zealand, New Zealand Geological Survey. 22 p.

Suggate P & Waight TE 1999. Geology of the Kumara-Moana area, scale 1: 50 000. Institute of Geological and Nuclear Sciences geological map 24. Lower Hutt, New Zealand, Institute of Geological and Nuclear Sciences Limited. 1 Sheet + 124 p.

Sun SS & McDonough WS 1989. Chemical and isotopic systematics of oceanic basalts: implications for mantle composition and processes. Geological Society Special Publications 42: 313–345.

Tappenden VE 2003. Magmatic response to the evolving New Zealand margin of Gondwana during the mid-Late Cretaceous. Unpublished thesis, University of Canterbury, Christchurch, New Zealand.

Taylor R 2009. Ore textures: recognition and interpretation. Heidelberg, Springer Science & Business Media. 288 p.

Taylor SR & McLennan SM 1985. The continental crust: its composition and evolution. Oxford, Blackwell Scientific. 312 p.

The West Coast Regional Council 2011. Site: Arnold River at Moana. http://data.wcrc.govt.nz/cgi-bin/HydWebServer.cgi/sites/details?site=104&treecatchment=2.

Thompson AJB, Thompson JFH, Allen RL 1996. Atlas of alteration: a field and petrographic guide to hydrothermal alteration minerals. Newfoundland, Canada, Geological Association of Canada - Mineral Deposits Division. 119 p.

Tosolini AMP & Pole M 2010. Insect and clitellate annelid traces in mesofossil assemblages from the Cretaceous of Australasia. Alcheringa: An Australasian Journal of Palaeontology 34: 397–419.

Townend R & Townend D 2016a. Reflected light microscopy analyses of four polished thin sections in regards to opaque minerals. Townend Mineralogy Laboratory, unpublished consultancy report 24058.

Townend R & Townend D 2016b. SEM/EDS analyses of four polished thin sections in regards to rare earth minerals. Townend Mineralogy Laboratory, unpublished consultancy report 24058.

Tulloch AJ 1983. Granitoid rocks of New Zealand—a brief review. Geological Society of America Memoirs 159: 5–20.

Tulloch AJ 1988. Batholiths, plutons, and suites: nomenclature for granitoid rocks of Westland—Nelson, New Zealand. New Zealand Journal of Geology and Geophysics 31: 505–509.

Tulloch AJ 1991. Alkaline plutonic and volcanic rocks of the Late Cretaceous Mandamus Igneous Complex, North Canterbury. New Zealand Geological Survey Record 43: 15–23.

Tulloch AJ & Challis GA 2000. Emplacement depths of Paleozoic-Mesozoic plutons from western New Zealand estimated by hornblende-Al geobarometry. New Zealand Journal of Geology and Geophysics 43: 555–567.

Tulloch AJ & Kimbrough DL 1989. The Paparoa metamorphic core complex, New Zealand: Cretaceous extension associated with fragmentation of the pacific margin of Gondwana. Tectonics 8: 1217–1234.

Tulloch AJ, Kimbrough DL, Waight TE 1994. The French Creek Granite, north Westland, New Zealand–Late Cretaceous A-type plutonism on the Tasman Passive Margin. In: van der Lingen GJ, Swanson KM & Muir RJ ed. Evolution of the Tasman Sea Basin. Rotterdam, AA Balkema: 65–66.

Tulloch AJ, Ramezani J, Mortimer N, Mortensen J, van den Bogaard P, Maas R 2009. Cretaceous felsic volcanism in New Zealand and Lord Howe Rise (Zealandia) as a precursor to final Gondwana break-up. Geological Society, London, Special Publications 321: 89–118.

Tulloch AJ & Robertson S 1987. Fluorine contents of Westland-Nelson granitoid and associated metasedimentary country rocks. New Zealand Geological Survey Record 20: 89–94.

Turnbull RE, Tulloch AJ, Ramezani J, Jongens R 2016. Extension-facilitated pulsed S-I-A-type "flare-up" magmatism at 370 Ma along the southeast Gondwana margin in New Zealand: Insights from U-Pb geochronology and geochemistry. GSA Bulletin 128: 1500–1520.

Turner PD 2015. Carbonatite veins in lamprophyre dykes, Mt Tapuaenuku, New Zealand. Unpublished thesis, University of Canterbury, Christchurch, New Zealand. 146 p.

Turner SP, Foden JD, Morrison RS 1992. Derivation of some A-type magmas by fractionation of basaltic magma: an example from the Pathway Ridge, South Australia. Lithos 28: 151–179.

U.S. Department of Energy 2011. Investigating rare earth element mine development in EPA region 8 and potential environmental impacts. United States Environmental Protection Agency Document 908R11003. 35 p.

van der Meer QHA, Scott JM, Waight TE, Sudo M, Scherstén A, Cooper AF, Spell TL 2013. Magmatism during Gondwana break-up: new geochronological data from Westland, New Zealand. New Zealand Journal of Geology and Geophysics 56: 229–242.

van der Meer QHA, Storey M, Scott JM, Waight TE 2016. Abrupt spatial and geochemical changes in lamprophyre magmatism related to Gondwana fragmentation prior, during and after opening of the Tasman Sea. Gondwana Research 36: 129–143.

Van der Pluijm BA & Marshak S 2004. Earth structure. 2nd ed. New York, WW Norton. 656 p.

Vidanovich P & Thomson Aviation Pty Ltd 2013. Summary report on the government acquired West Coast airborne survey - 2013. NZ Petroleum & Minerals, Ministry of Business, Innovation and Employment, Wellington, unpublished open-file mineral report MR5000.

Waight TE 1995. The geology and geochemistry of the Hohonu Batholith and adjacent rocks, North Westland, New Zealand. Unpublished thesis, University of Canterbury, Christchurch, New Zealand.

Waight TE, Weaver SD, Ireland TR, Maas R, Muir RJ, Shelley D 1997. Field characteristics, petrography and geochronology of the Hohonu Batholith and the adjacent Granite Hill Complex, north Westland, New Zealand. New Zealand Journal of Geology and Geophysics 40: 1–17.

Waight TE, Weaver SD, Maas R, Eby GN 1998a. French Creek Granite and Hohonu Dyke Swarm, South Island, New Zealand: Late Cretaceous alkaline magmatism and the opening of the Tasman Sea. Australian Journal of Earth Sciences 45: 823–835.

Waight TE, Weaver SD, Muir RJ 1998b. Mid-Cretaceous granitic magmatism during the transition from subduction to extension in southern New Zealand: a chemical and tectonic synthesis. Lithos 45: 469–482.

Waight TE, Weaver SD, Muir RJ, Maas R, Eby GN 1998c. The Hohonu Batholith of north Westland, New Zealand: granitoid compositions controlled by source H_2O contents and generated during tectonic transition. Contributions to Mineralogy and Petrology 130: 225–239.

Wall F 2014. Rare earth elements. In: Gunn G ed. Critical metals handbook, John Wiley & Sons Ltd.

Weaver SD & Pankhurst RJ 1991. A precise Rb-Sr age for the Mandamus Igneous Complex, North Canterbury, and regional tectonic implications. New Zealand Journal of Geology and Geophysics 34: 341–345.

Weaver SD, Storey BC, Pankhurst RJ, Mukasa SB, DiVenere VJ, Bradshaw JD 1994. Antarctica-New Zealand rifting and Marie Byrd Land lithospheric magmatism linked to ridge subduction and mantle plume activity. Geology 22: 811–814.

Weissel JK & Hayes DE 1977. Evolution of the Tasman Sea reappraised. Earth and Planetary Science Letters 36: 77–84.

Wellman P & Cooper A 1971. Potassium-argon age of some New Zealand lamprophyre dikes near the Alpine Fault. New Zealand Journal of Geology and Geophysics 14: 341–350.

Whalen JB, Currie KL, Chappell BW 1987. A-type granites: geochemical characteristics, discrimination and petrogenesis. Contributions to Mineralogy and Petrology 95: 407–419.

White PD & Price GD 2006. Technical report Hohonu project for 2 year period ending 13 April 2006, CanAlaska Ventures. NZ Petroleum & Minerals, Ministry of Business, Innovation and Employment, Wellington, unpublished open-file mineral report MR4376.

Williams-Jones AE, Migdisov AA, Samson IM 2012. Hydrothermal mobilisation of the rare earth elements–a tale of “ceria” and “yttria”. Elements 8: 355–360.

Winter JD 2011. Principles of igneous and metamorphic petrology. 2nd ed. New York, Prentice Hall. 702p.

Wood SA 1990a. The aqueous geochemistry of the rare-earth elements and yttrium: 1. review of available low-temperature data for inorganic complexes and the inorganic REE speciation of natural waters. Chemical Geology 82: 159–186.

Wood SA 1990b. The aqueous geochemistry of the rare-earth elements and yttrium: 2. theoretical predictions of speciation in hydrothermal solutions to 350°C at saturation water vapour pressure. Chemical Geology 88: 99–125.

Wyllie PJ, Jones AP, Deng J 1996. Rare earth elements in carbonate-rich melts from mantle to crust. In: Jones AP, Wall F, Williams CT ed. Rare earth minerals. Chemistry, origin and ore deposits. London, UK, Chapman & Hall 7: 77–103.

Appendices

A Detailed Methods and Procedures

1. XRF and ICP-MS/AES Sample Preparation

Geochemistry samples were prepared by trimming any altered material off, and cutting and pulverising the rock into powder at the University of Canterbury. A representative section of each sample was laid onto a tray lined with tin foil and oven dried for 24 hours at 65°C. Samples were then coarsely crushed using a Rocklabs hydraulic ram and transferred to a Rocklabs tungsten carbide ring mill using a clean plastic zip-lock bag. Each sample was pulverised for 1.5 minutes. An extra 0.5 minute was added if the powder still felt slightly gritty. The powder was emptied onto a clean sheet of paper; ~20 g was transferred into a plastic vial and the remainder into a sample bag. Each piece of hardware (i.e. the hydraulic press, ring mill and lab spatula) was thoroughly cleaned with ethanol and paper towels in between each sample, and the ring mill was additionally cleaned with hot water prior to ethanol in order to prevent cross-contamination of samples. Occasionally, the ring mill was cleaned by pulverising silica sand for 1.5 minutes, especially after clay- and carbonate-rich samples were pulverised, which adhered to the inside of the mill and were not easily washed off with water and ethanol.

Table A1. Maximum values of contamination introduced from the tungsten carbide ring mill, from Rocklabs (2016).

Symbol	Element	Max value (ppm)
Al	Aluminium	30
As	Arsenic	<10
B	Boron	<10
Ba	Barium	<10
C	Carbon	5.50%
Ca	Calcium	50
Co	Cobalt	10%
Cr	Chromium	50
Cu	Copper	30
Fe	Iron	100
K	Potassium	30
Mn	Manganese	50
Mo	Molybdenum	50
N	Nitrogen	100
Na	Sodium	30
Nb	Niobium	100
Ni	Nickel	50
P	Phosphorus	30
Pb	Lead	30
S	Sulphur	50
Sb	Antimony	10
Si	Silicon	50
Ta	Tantalum	30
Ti	Titanium	30
V	Vanadium	30
W	Tungsten	84.50%
Zn	Zinc	30
Zr	Zirconium	<10

2. XRD Instrument Specifications and Procedures

X-ray diffraction (XRD) was conducted using a Philips diffractometer with the following specifications:

PW1729 X-ray generator (50kV/40mA)

PW2273/20 Long fine focus 2.2kW Cu anode x-ray tube

PW1820/00 Goniometer

PW1752/00 Monochromator

PW1711/10 Sealed Gas (Xe) filled proportional detector

PW 1710 Diffractometer control (connected to PC)

The sample was milled using an agate mortar and pestle, and ethanol was

added to form a slurry. The slurry was then transferred to half a microscope slide as a thin layer on an orientated mount using a disposable pipette, and allowed to dry at room temperature. The glycolated slide was placed into a muffle furnace for one hour at 550˚C. Once the slide had cooled to room temperature it was scanned from 3–30° two theta, with a step size of 0.02° two theta and scan speed of 0.02° two theta per second. The programs used were the Visual XRD controller software and Traces (V4) search-match software using the Hanawalt search-match algorithm.

3. Detailed LA-ICP-MS Specifications and Procedures

The instrument used was a Resonetics RESOlution M-50-LR laser ablation system incorporating a Coherent CompexPro 102 193 nm ArF excimer laser and Laurin Technic two-volume sample cell. The laser was operated at 100 mJ and 12.5% transmission giving a typical fluence value of 4 J/cm^2. Zircon were analysed in situ from polished thin sections using a spot diameter of 10 μm and a 5 Hz repetition rate. Ablated material was carried by He gas (650–750 ml/min) from a two-volume sample cell, mixed with Ar (650–750 ml/min) and N_2 (2–6 ml/min) and input to an Agilent 7500cs quadrupole ICP-MS. Background data were acquired for 20 seconds followed by 30 seconds with the laser on, giving about 75 mass scans and a penetration depth of ~15 μm. A minimum purge time of 10 seconds was allowed between each spot analysis to permit a return to background signal levels.

Correction factors were applied to each spot analysis to simultaneously correct for instrument mass bias and depth-related elemental fractionation. After laser triggering, several seconds are needed for a steady signal to be obtained, so the first 10 scans were routinely excluded from subsequent calculations. Depth related inter-element fractionation of Pb, Th and U were corrected by reference to the TEMORA-2 zircon standard (Black et al. 2004). TEMORA-2 and R33 zircon standards and silicate glass standard NIST 610 were measured at the beginning and end of each analytical session, and then once every 10 unknown analyses. Measured $^{207}Pb/^{206}Pb$, $^{206}Pb/^{238}U$ and $^{208}Pb/^{232}Th$ in the TEMORA-2 zircon standard and $^{232}Th/^{238}U$ in the NIST610 silicate glass were averaged and used to calculate correction factors based on accepted published values (Black et al. 2003; Pearce et al. 1997). Data reduction was performed using Iolite software (Paton et al. 2011).

B Site Catalogue of Samples

Sample	NZTM Easting	NZTM Northing
14EHR01	E1465125	N5276707
14EHR02	E1465105	N5276692
14GR03	E1461027	N5273707
14EC04	E1466777	N5277730
14MFT05	E1464314	N5276127
14MFT06	E1464454	N5275321
14MFT07	E1464263	N5275493
14MFT08	E1464264	N5275988
14LHR09	E1462328	N5276052
14LHR10	E1462453	N5275757
14LHR11	E1462453	N5275726
14LHR12	E1462466	N5275635
14LHR13	E1462451	N5275851
14EHR14A	E1465197	N5276556
14EHR14B	E1465197	N5276556
14EHR15	E1465375	N5276457
15LHR16	E1462485	N5276575
15LHR17	E1462527	N5276521
15LHR18	E1462845	N5276037
15LHR19	E1462856	N5276005
15LHR20	E1462867	N5275968
15LHR21	E1462929	N5275912
15LHR22	E1462929	N5275912
15LHR23	E1462929	N5275912
15LHR24	E1462929	N5275912
15LHR25A	E1462923	N5275933
15LHR25B	E1462923	N5275933
15LHR26	E1462774	N5276113
15LHR27	E1462455	N5275824
15LHR28	E1462454	N5275752
15LHR29	E1462460	N5275757
15LHR30	E1462452	N5275743
15LHR31	E1462445	N5275704
15LHR32	E1462427	N5275704
15LHR33	E1462448	N5275671
15LHR34	E1462457	N5275662
15LHR35	E1462477	N5275646
15LHR36	E1462497	N5275632
15LHR37	E1462505	N5275603
15LHR38	E1462515	N5275594
15LHR39	E1462531	N5275577
15LHR40	E1462580	N5275531
15LHR41	E1462592	N5275523
15LHR42	E1462597	N5275517
15LHR43	E1462606	N5275499
15LHR44	E1462336	N5276073
15LHR45	E1462525	N5275585
15LHR46	E1462605	N5275503
15LHR47	E1462608	N5275489

Sample	NZTM Easting	NZTM Northing
15LHR48	E1462614	N5275478
15LHR49	E1462596	N5275447
15LHR50	E1462580	N5275421
15LHR51	E1462582	N5275408
15LHR52	E1462583	N5275402
15LHR53	E1462592	N5275396
15LHR54	E1462602	N5275374
15LHR55	E1462602	N5275353
15LHR56	E1462608	N5275329
15LHR57	E1462598	N5275301
15LHR58A	E1462596	N5275292
15LHR58B	E1462596	N5275292
15LHR59	E1462594	N5275288
15LHR60	E1462592	N5275272
15LHR61	E1462587	N5275243
15LHR62	E1462588	N5275213
15LHR63	E1462616	N5275194
15LHR64	E1462662	N5275174
15LHR65	E1462943	N5276609
15LHR66A	E1463027	N5276498
15LHR66B	E1463027	N5276498
15LHR67	E1463051	N5276299
15LHR68	E1463178	N5276197
15LHR69	E1463260	N5276194
15LHR70	E1463306	N5276179
15LHR71A	E1463330	N5276181
15LHR71B	E1463319	N5276170
15LHR72	E1463359	N5276146
15LHR73	E1463368	N5276138
15LHR74	E1463363	N5276116
15LHR75	E1463375	N5276118
15LHR76	E1463378	N5276086
15LHR77	E1463356	N5276073
15LHR78	E1463388	N5276032
15EHR79	E1465191	N5276581
15EHR80A	E1465424	N5276414
15EHR80B	E1465424	N5276414
15EHR80C	E1465424	N5276414
15EHR81A	E1465544	N5276331
15EHR81B	E1465544	N5276331
15EHR81C	E1465522	N5276339
15EHR81D	E1465522	N5276339
15EHR81E	E1465522	N5276339
15EHR81F	E1465522	N5276339
15EHR81G	E1465522	N5276339
15EHR81H	E1465522	N5276339
15EHR81I	E1465522	N5276339
15EHR82	E1465615	N5276232

C Optical Petrology Descriptions

Sample: 14EHR01 **Name: muscovite syeno-microgranite**	**Mineral**	**%**	**Description**
 **Rock textures:** Leucocratic, aplitic, medium grained, phaneritic, microcline common, contact to Deutgam Granodiorite	K-feldspar	50	Rare core sericite + muscovite alteration, microcline common, pericline, simple twins, some embayed by sericite, perthites, some deformed, sub-anhedral, few occur as micro-phenocrysts, some poikiolitic
	Quartz	37	Undulose extinction, commonly cracked, anhedral interstitial, few micro-phenocrysts, some poikiolitic
	Plagioclase	5	Euhedral, some deformed, polysynthetic twinning
	Muscovite	3	Small clusters, anhedral, elongate, product of secondary alteration in feldspar too
	Chlorite	2	Interstitial, anhedral, small clusters
	Apatite	<<1	
	Zircon	<<1	
	Magnetite	<<1	Pretty much none

Sample: 14EHR02 **Name: chlorite-amphibole syenogranite**	**Mineral**	**%**	**Description**
 **Rock textures:** Large k-feldspars, low mafic minerals(<5%), some chloritisation, coarse grained, granitic	K-feldspar	54	Rare simple twins, euhedral, cracked, perthites to mesoperthites, large crystals
	Quartz	30	Undulose extinction, anhedral, anhedral inclusions in kspar, embayed, interstitial around kspar boundaries, graphic intergrowths
	Plagioclase	8	Rare sericite, polysynthetic twins, relatively small
	Biotite-Chlorite	2	Altered almost completely chlorite and opaques, yellow-brown to green, embayed, sub-euhedral, large, some corrosion, some protuberances
	Amphibole	2	Greenish-brown, altered to biotite + limonite + opaques
	Zircon	1	Associated with biotite + opaques, poikiolitic, clustered
	Apatite	1	Small clusters
	Opaques	1	Magnetite, mostly square
	Limonite	2	Fe staining of mafics

Sample: 14GR03 Name: biotite alkali-feldspar granite	Mineral	%	Description
 **Rock textures:** Segregated mafic layers with granophyric vein-like contact, medium grained, mafic-rich (~25%), phaneritic, granitic, equigranular, slight foliation of biotite on hand sample	K-feldspar	35	Rare sericite and perthites, cracked, intense granophyric intergrowths in central zone
	Quarts	27	Undulose extinction, intense granophyric intergrowths in central zone, some skeletal growth
	Plagioclase	2	Slight sericitisation, polysynthetic twins
	Biotite	17	Confined growth, forms thick books, euhedral basal sections, scattered, corrosion, deformed, some alteration to chlorite + opaques + limonite, yellow-green to brown, sieve texture and embayed
	Hornblende	6	Very altered and replaced by biotite, rounded
	Zircon	2	Poikiolitic, abundant in mafic-rich zones (associated with biotite + opaques), large
	Fluorapatite	3-4	Clusters, abundant in mafic-rich zones, prismatic to hexagonal
	Limonite	<1	Especially in cracks, of mafics
	Opaques	5	Dominantly fresh magnetite and altered ilmenite (to titaniferous hematite and high-Ti oxide phase), occasional goethite alteration – possibly ex sulphides, embayed, associated with biotite. Rare pyrite, one partially replaced by marcasite + goethite + flakes of molybdenite, rare leucoxene
	Loparite	1-2	Non-isotropic, reddish-brown, anhedral, heavy cracks + relief, some rounded (xenocrysts), some have apatite inclusions, some intergrown with perrierite
	Perrierite	1-2	Reddish-brown, pleochroic, some intergrown with loparite, alteration to titanium oxide + quartz, inclusions in biotite + quartz or separate, apatite inclusions
	Allanite	<1	Strong reddish-brown pleochroism, sub-anhedral, broken

Sample: 14EC04 Name: kspar-phyric rhyolite	Mineral	%	Description
 **Rock textures:** Porphyritic, clustered phenocrysts, fine grained, no fabric or vesicles, mild sericitisation, feldspars have complex history (including eutectic crystallisation)	K-feldspar	11	Perthites common, some sericite, rare simple + pericline twins, cumulophyric, some xenocrystic, some poikiolitic in quartz, some granophyric intergrowths
	Quartz	8	Euhedral, some cracks, undulose extinction, inclusions common, cumulophyric, some skeletal
	Plagioclase	2	Anhedral, polysynthetic twins, cumulophyric, some xenocrystic
	Biotite	5	Some kinked, commonly anhedral, some xenocrystic, small, cumulophyric, altered, tiny zircon inclusions
	Chlorite	2	Subhedral plates
	Allanite	<1	Associated with mafics commonly
	Groundmass	70	Kspar (40%), quartz (22%) plag (4%), biotite (1%), chlorite (2%), magnetite + ilmenite (1%), amph? (1-2%)

Sample: 14MFT06 Name: amphibole QAF syenite	Mineral	%	Description
 **Rock textures:** Mesoperthitic, coarse grained, granitic, altered, oxidised, relatively high mafics (~10%), cracked, hypersolvus	K-feldspar	73	Mesoperthites, many cracks with limonite, simple twins, large, generally euhedral, crystal boundaries commonly have myrmekite-type growths along perthites into adjacent feldspar (boundary deformed)
	Quartz	10	Undulose extinction, interstitial
	Plagioclase	1	Rare, polysynthetic twins
	Amphibole	10	Interstitial, yellow-green, some altered to limonite + biotite + opaques + chlorite, some euhedral, rare simple twins
	Opaques	3	Magnetite + ilmenite + pyrite, corroded, embayed, limonite alteration, square to hexagonal

Sample: 14MFT08 Name: biotite syenogranite	Mineral	%	Description
 **Rock textures:** Perthitic, coarse grained, granitic, slightly inequigranular	K-feldspar	55	Perthites to mesoperthites esp. in larger population, some simple twinning, cracked, larger ones more euhedral
	Quartz	25	Smaller, cracked, generally euhedral, some undulose extinction, also interstitial grains
	Plagioclase	10	Some sericitisation, clustered, polysynthetic twins, sub-euhedral
	Biotite-chlorite	5	Corroded + embayed, poikiolitic lensoidal quartz parallel to cleavage, yellow-brown to green, clustered
	Opaques	2-3	magnetite
	Zircon	1	Commonly associated with opaques + biotite
	Apatite	<1	
	Amphibole	<1	If at all, very altered pseudomorphs now biotite + opaques + limonite mostly

Sample: 14LHR09 Name: spherulitic rhyolite	Mineral	%	Description
 **Rock textures:** Porphyritic, devitrified, spherulitic, fine-medium grained, carbonate alteration, sericitised, skeletal quartz, vugs	K-feldspar	60	Spherulitic, altered to sericite along granophyric fronds, relict perthites
	Quartz	25	Large euhedral skeletal phenocrysts with embayments, some rounded edges, also anhedral masses with spherulitic kspar
	Carbonate	6	Untwinned, siderite or calcite, one large rhomb, replacing feldspar, small vein
	Muscovite	3	Small spherulitic clusters
	Zircon	1	Clustered around opaques
	Amphibole?	1	Completely altered
	Opaques	1	Magnetite, some corroded, limonite staining

Sample: 14LHR11 Name: highly altered alkali-feldspar granite	Mineral	%	Description
 **Rock textures:** Cracked, highly altered, corroded mafics, medium grained, pervasive sericitisation, relict graphic intergrowths	Feldspar	45	Completely altered to sericite, relict graphic intergrowths
	Quartz	35	Both euhedral and anhedral, relict graphic intergrowths, some protuberances, undulose extinction, poikiolitic biotite
	Siderite	6	Untwinned, alteration of feldspar, limonite staining, small rhombs and aggregates
	Muscovite (secondary)	2	Where sericite is coarser, contains opaques along cleavage
	Biotite	<1	Rare inclusions in quartz
	Apatite	<1	
	Zircon	<1	Clustered with opaques
	Opaques	2	Magnetite?, altered to limonite commonly
	Limonite	8	Alteration of opaques + feldspar + siderite

Sample: 14LHR12 Name: altered syenogranite	Mineral	%	Description
 **Rock textures:** Granitic, coarse grained, sericitised plagioclase, chloritised biotite, low mafic portion	K-feldspar	50	Perthites, many have plag inclusions, simple twins, large
	Quartz	26	Graphic intergrowths, undulose extinction, cracked, interstitial to anhedral
	Plagioclase	15	Sericite common, sub-euhedral, polysynthetic and pericline twins
	Biotite-chlorite	2	Mostly fully altered to chlorite + opaques, small clusters, brownish-green, some embayments
	Apatite	<1	Some quite large, acicular to hexagonal
	Opaques	1	Magnetite?, commonly associated with biotite-chlorite, commonly square
	Zircon	<1	Clustered with biotite-chlorite
	Limonite	<1	In cracks

Sample: 14EHR14A Name: altered potassic trachybasalt	Mineral	%	Description
 **Rock textures:** Porphyritic, fine grained, slightly trachytic groundmass, mod deuteric alteration (chlorite, sericite, calcite, iddingsite), xenocrystic quartz + some feldspar	Plagioclase	12	Highly altered to sericite, some (likely kspar) contain quartz inclusions, polysynthetic and pericline twins, euhedral, tabular to equant, cracked, cumulophyric
	Quartz	1	Rounded, rimmed, cracked
	Augite	5	Very altered, cracked, tabular to stubby, were euhedral, cumulophyric, rare simple + lamellar twins, small + large
	Olivine	1	Altered (iddingsite?) esp. around rims, euhedral, cracked,
	Groundmass	81	Secondary chlorite (15%), apatite (1%), secondary calcite (2%), anhedral augite (4%), feldspar lathes (22%), magnetite + ilmenite (5%), altered mafics (20%)

Sample: 14EHR14B Name: plag-phyric trachydacite	Mineral	%	Description
 **Rock textures:** Porphyritic, fine-medium grained, phaneritic, xenocrystic plagioclase, no flow alignment	Plagioclase	20	Large, tabular, polysynthetic twins, different degrees of sericitisation, euhedral, few cracks, cumulophyric, embayed
	K-feldspar	2	Some quartz inclusions, sericitisation
	Quartz	8	Very rounded, embayed, anhedral, some spherulitic growth
	Groundmass	70	Secondary chlorite (25%), secondary calcite (3%), feldspar 24%), quartz (13%), apatite (1%), zircon (<1%), magnetite + ilmenite (2%), vesicles (<1%)

Sample: 14EHR15 Name: altered alkali-feldspar granite	Mineral	%	Description
 **Rock textures:** Mesoperthites, cracked with shear planes and calcite alteration, coarse grained, granitic, graphic intergrowths	K-feldspar	60	Mesoperthites, cracked, large, simple twins, euhedral,
	Quartz	26	Graphic intergrowths, small interstitial grains, undulose extinction, cracked, euhedral to anhedral
	Plagioclase	1	Tiny, rare, poikiolitic inclusions in kspar
	Altered mafics	4	Amphibole? pseudomorphs, embayed + corroded, altered to limonite + opaques, brown and green
	Calcite	2	Fills matrix of small shear planes and alters along feldspar perthites, untwinned
	Apatite	1	
	Zircon	1	Associates with altered mafics
	Opaques	3	Magnetite + ilmenite, semi-euhedral but sieve textures and embayed, commonly associated with altered mafics

Sample: 15LHR18 Name: biotite alkali-feldspar granite	Mineral	%	Description
 **Rock textures:** Granitic, coarse grained, strong graphic texture, cracked, alteration of mafic component, mesoperthites	K-feldspar	54	Some mesoperthites, graphic + granophyric intergrowths, large + relatively euhedral, some sericite, small plag inclusions in some larger crystals
	Quartz	32	Euhedral inclusions + anhedral masses, graphic + granophyric intergrowths very common, some undulose extinction
	Plagioclase	2-3	Some very large with glassy quartz inclusions, sericite alteration, polysynthetic + pericline twins, tabular common
	Biotite	2	Alteration to muscovite + carbonate + opaques + chlorite, commonly clustered, brownish-green, some embayments
	Amphibole	1	Pseudomorphs, strong green pleochroism, altered to chlorite + opaques + carbonates
	Opaques	2	Magnetite + ilmenite, euhedral square/polygonal, tabular to anhedral, clusters commonly associated to altered biotite + amphibole
	Zircon	1	Associated to mafic clusters
	Apatite	1	Inclusions in kspar + clusters associated with biotite
	Limonite	<1	Associated to mafic minerals and in

			cracks
	Carbonate	1	Alteration of biotite + infilling miarolitic cavities

Sample: 15LHR23 **Name: altered tephrite**	**Mineral**	**%**	**Description**
 **Rock textures:** Porphyritic, fine grained, phenocryst-rich, altered, slightly vesicular (deuteric?) with amygdales (zeolites or carbonates – too fine to tell)	Plagioclase	1-2	Lathes, sub-anhedral, polysynthetic twins, some swallow tails
	Nepheline	15	Polymorphs, completely replaced by carbonates, long tabular to equant, euhedral to anhedral, clustered
	Augite	10	Tabular, sub-anhedral, generally cracked and broken, large and small populations, relatively unaltered
	Amphibole	8	Juvenile, pleochroic brown, subhedral, squashed hexagonal habit common, relatively unaltered
	Groundmass	61	Plagioclase, magnetite + ilmenite (4%), biotite, augite, amphibole, nepheline
	vesicles	3-4	Rounded, small + large, some infilled by very fine material (carbonate or zeolite) + plagioclase lathes + small amphibole/augite

Sample: 15LHR24 **Name: cataclasite**	**Mineral**	**%**	**Description**
 **Rock textures:** Fault breccia, strong brittle deformation and shearing, oxidation, coarse grained, relict granitic texture, shear fabric in at least two orientations, unsorted	K-feldspar	40	Cracked, some large, some perthites + mesoperthites, rare sericite, mostly granulated angular clasts, some very irregular twinning
	Quartz	45	Granulated, angular to sub-rounded, cracked, some embayed, mild undulose extinction, no recrystallisation, rare euhedral igneous quartz
	Plagioclase	1	Polysynthetic twins, rare, some sericite
	Biotite (secondary)	2	Smeared out/secondary in shear planes, oxidised, reddish-brown, clusters, associated with opaques + altered mafics commonly
	Limonite	10	Oxidation of biotite + any altered mafic components, filling late cracks, also form fine veinlets in shears
	Opaques	1	Magnetite ± ilmenite, only occur in shear zones with biotite + limonite, subhedral commonly, square to hexagonal
	Zircon	1	Inclusions in biotite, only in shears with opaques

Sample: 15LHR25A/B Name: quartz-sericite-ankerite breccia	Mineral	%	Description
 **Rock textures:** Clasts of altered granite (quartz-sericite) in ankerite matrix, deformed + strained, columnar vein quartz growths on granite fragments into cavity, interrupted by fine-grained quartz filing gaps between prisms, then fine masses of ankerite (chilled?) changing suddenly to coarse ankerite	Ankerite	40	Coarse equidimensional and very fine mases, some oxidised cracks, very rare twins, forms matrix of brecciated quartz-sericite clasts, some strained grain boundaries, rare calcite
	Quartz	38	Form large breccia clasts in the ankerite matrix, large anhedral crystals, also euhedral hexagonal crystals common and finer masses and columnar vein textures surrounding clasts of sericite (altered feldspar) and euhedral quartz, elongate undulose extinction common, strong deformation some even with subgrains
	Sericite	20	Feathery masses, replacement of feldspar in granite xenoliths
	Altered mafics	2	Within granite, was likely biotite, now leucoxene/TiO_2 + muscovite
	Synchysite	1-2	Tiny euhedral tabular crystals mostly scattered within sericite/ altered FCG and fine grained ankerite, some replaced by ankerite, colourless
	Florencite	<1	Small zoned rosette shaped crystals scattered within sericite of altered FCG
	Zircon	<1	Clusters within altered granite and secondary muscovite

Sample: 15LHR26 Name: calcitic shoshonite	Mineral	%	Description
 **Rock textures:** Fine grained, porphyritic, anastomosing calcite veinlets, non-vesicular, very slightly trachytic, rimmed + altered phenocrysts, chloritisation + carbonate alteration	Plagioclase	2-3	Altered, some rimmed by brown material, very cracked, individual and cumulophyric, some alteration to calcite, sub-anhedral, embayed
	K-feldspar	1	Relict simple twin, cracked, rimmed by brown material, cross-cut by carbonate veinlets, euhedral, xenocrysts
	Quartz	1-2	Rounded + very corroded xenocrysts, embayed, cracked, broken, some undulose extinction, generally individual crystals, rimmed by brown material, euhedral + hexagonal to anhedral habit, some offset
	Calcite veinlet	4-5	Generally twinned, rare albite phenocryst inclusion, anastomosing + discontinuous

	Opaques	1	Magnetite mostly, oxidised, embayed + sieve texture, square to hexagonal, anhedral masses in small solution seams too
	Zircon	<1	Associated to opaques
	Altered mafics	<1	Completely altered to opaques + chlorite + limonite, were possibly amphibole
	Groundmass	90	Feldspar lathes (30-35%), carbonate (5-10%), chlorite (20%), opaques (20%), limonite (5%), quartz (1%)

Sample: 15LHR28 **Name: porphyritic alkali-feldspar microgranite**	**Mineral**	**%**	**Description**
 **Rock textures:** Aplitic, porphyritic, granophyre, medium grained, phaneritic, oxidised cracks	Quartz	50	Both granular phenocrysts (~2%) and smaller populations, phenocrysts embayed and cracked. Smaller ones granophyric and graphic intergrowths (some very intensely), rare slight undulose extinction
	K-feldspar	42	Rare large mesoperthite phenocryst cluster with embayments and simple twins, aplitic in groundmass, granophyric and graphic intergrowths, rare sericite, some inclusions of plagioclase
	Plagioclase	2-3	Small crystals and inclusions in aplitic groundmass, euhedral, polysynthetic twins, mild sericite
	Biotite	1-2	Yellow-brown to green, generally altered to chlorite, muscovite, limonite, carbonates and/or opaques
	Opaques	1	Ilmenite + magnetite, large and anhedral, also small square ones, commonly alteration product of hornblende
	Limonite	1	Oxidation of biotite + opaques + hornblende
	Zircon	<1	Associated with biotite clusters
	Apatite	<<1	Hexagonal, rare
	Bastnäsite-parisite	1-2	Alt. product of hornblende, massive, fine grained, syntaxial as well as individual bastnäsite and parisite, colourless to tan brown, high birefringence
	Monazite - (Ce)	<1	Associated to zircon and magnetite
	Fergusonite - (Y)	<<1	Euhedral, light to dark brown, opaque, square, mod relief

Sample: 15LHR36 **Name: biotite syenogranite**	**Mineral**	**%**	**Description**
 **Rock textures:** Granitic, coarse grained, mesoperthites, altered mafic clusters	K-feldspar	40	Mesoperthites, simple twins, cracked, large, sub-euhedral, rare undulose extinction, rare mild sericite
	Quartz	37	Graphic intergrowths, large anhedral, + small euhedral hexagonal inclusions within kspar, cracked, mild undulose extinction, some small crystals around boundaries of larger crystals
	Plagioclase	10	Sub-anhedral, larger ones tabular euhedral, polysynthetic twins, rare semi-antiperthites
	Biotite	3-4	Dark brown, an-subhedral, limonite alteration, some lensoidal quartz inclusions
	Opaques	1-2	Magnetite + minor ilmenite, commonly euhedral + square, few anhedral, larger ones associated with altered mafics, some contain apatite inclusions
	Amphibole	1-2	Corroded + altered to biotite + limonite + opaques + allanite + bastnäsite, brown-yellow, subhedral, embayed, mild sericite alteration of feldspar around some of the larger mafic clusters common
	Zircon	1-2	Associated with opaques + altered mafics, rare haloes
	Limonite	2	In cracks and around amphibole
	Apatite	<1	More abundant in association with opaques + biotite
	Bastnäsite	<1	Fine grained alteration product of amphibole, colourless
	Allanite	<1	Pleochroic brown, altering to bastnäsite + Fe-oxide mix, possibly alteration product of amphibole originally

Sample: 15LHR38 Name: spherulitic rhyolite	Mineral	%	Description
 **Rock textures:** Porphyritic, completely devitrified and spherulitic groundmass, medium grained, euhedral + skeletal phenocrysts, cracked, highly altered + oxidised	K-feldspar	60	Very large euhedral phenocryst pseudomorphs strongly altered to sericite + limonite, rounded edges. Also as large spherulites radiating off phenocrysts, some fronds segmented/radial/ acicular/bladed, one xenolith containing feldspar cluster
	Quartz	25	Large euhedral skeletal phenocrysts, embayed, cracked, clustered or individuals
	Muscovite (secondary)	2-3	Radiating spherulitic bunches, appear to be infilling miarolitic cavities/vesicles, also associated with opaques + limonite
	Opaques	1-2	Magnetite mostly, euhedral + square commonly, some oxidised
	Limonite	5	Pervasive, alteration of kspar phenocrysts + around some spherulites + of any mafic components that were there + opaques
	Zircon	<1	Associated with opaques
	Carbonate	1-5	No twins, siderite?, small clusters, one coarse grained

Sample: 15LHR41 Name: sheared alkali-feldspar granite (left)	Mineral	%	Description
 **Rock textures:** Sheared, cracked, calcite veinlet intruded prior to latest activity on main shear zone (cataclasite), granulated, granitic, mesoperthites, coarse grained	K-feldspar	43	Mesoperthites, cracked, granulated in shear planes, some deformed, granophyric intergrowths, large, rare simple twins, deformation twinning, cuspate structures
	Quartz	37	Euhedral to interstitial, granophyric and rare graphic intergrowths, some undulose extinction, cracked, granulated in shears, no recrystallisation
	Plagioclase	3	Sericitisation, polysynthetic twins, subhedral, cracked, generally small, tabular
	Biotite	3-4	Altered to chlorite + opaques + muscovite, interstitial pressure shadows, one bent crystal
	Carbonate	10	Likely ankerite, anhedral aggregates + veinlets, occurs within sheared matrix + replacing feldspar, also a calcite veinlet with rare fine twin lamella

	Opaques	2	Mostly ilmenite, commonly anhedral, embayed + sieve texture, commonly associated with altered biotite, clustered, also poikiolitic within kspar
	Zircon	<<1	Associated with biotite commonly

Sample: 15LHR42 **Name: altered alkali-feldspar granite**	**Mineral**	**%**	**Description**
 **Rock textures:** Granitic, coarse grained, mesoperthites, cracked, granophyric and graphic intergrowths, siderite alteration, oxidation, corrosion of mafics	K-feldspar	46	Mesoperthites, large, graphic + granophyric intergrowths, some alteration to sericite + siderite (oxidised), cracked, simple twins
	Quartz	40	Undulose extinction, graphic + granophyric intergrowths, subhedral, cracked, also small interstitial around large crystal boundaries
	Plagioclase	1-2	Polysynthetic twins, tabular, generally small, alteration to sericite + siderite
	Muscovite (secondary)	2-3	Mostly from alteration of biotite, associated to limonite + opaques, some lensoidal quartz + limonite inclusions
	Opaques	1	Magnetite, some embayed, rare, euhedral, usually associated with altered mafics
	Limonite	5	Within kspar, of siderite + altered mafics + opaques
	Zircon	<1	Associated to altered mafics + opaques
	Carbonate	2-3	Siderite likely, sometimes oxidised, small anhedral aggregates filling miarolitic cavities + cracks, also partial replacement of feldspar + altered biotite

Sample: 15LHR44 **Name: amphibole alkali-feldspar microgranite**	**Mineral**	**%**	**Description**
 **Rock textures:** Medium grained, aplitic k-feldspar-rich zone and coarser area, small biotite-rich schlieren, mafic-rich	K-feldspar	35	Perthites to mesoperthites, coarse grained at one end grading into aplitic euhedral to anhedral crystals, highly cracked in coarse end
	Quartz	30	Interstitial and graphic intergrowths at coarse end, undulose extinction, also interstitial amongst aplitic kspar, semi-euhedral
	Plagioclase	1	Polysynthetic twins
	Hornblende	10-15	Pale brown, euhedral, embayed, inclusions of opaques + biotite + qtz, disequilibrium, oval to tabular habit, limonite
	Biotite	8-10	Small lenses where more abundant, yellow-brown, commonly small + stubby, rare chlorite, also near-isotropic stubby basal plates
	Ilmenite	3-4	Elongate prisms to square + hexagonal, euhedral often, small but abundant, some rounded
	Zircon	1	Commonly small + associated with biotite
	Apatite	<1	Small inclusions in quartz + kspar, hexagonal, some rounded
	Titanite	1-2	High relief, discrete crystals, tan, reddish-brown pleochroism, some elongate but often broken + sub-anhedral, very high birefringence, within both coarse and aplitic areas

Sample: 15LHR46A Name: brecciated quartz vein (centre)	Mineral	%	Description
 **Rock textures:** Prismatic quartz vein with cross-cutting comb quartz veinlet, later brecciated and some of the matrix infilled by fine grained carbonates, some dynamic recrystallisation, prismatic growth dominated texture	Quartz	85-90	Vein of massive elongate prismatic crystals, some undulose extinction, cracks filled with carbonates, cross-cut by coarser comb quartz veinlet, both brecciated towards one end, matrix of finely granulated quartz, some recrystallised, angular clasts, matrix further away from massive end becomes finer + more granulated + infilled by ankerite
	Ankerite	10-15	Infills cracks and also some breccia matrix, some oxidation to limonite
	Apatite	<<1	Prismatic, rare
	Opaques	<<1	Single crystal in brecciated matrix

Sample: 15LHR46B Name: sheared alkali-feldspar granite (left)	Mineral	%	Description
 **Rock textures:** Granitic, cataclastic shear zones, smeared-out chlorite, coarse grained, very cracked, mm offsets on crystals, mesoperthite, metamorphic biotite, chlorite + muscovite	Quartz	41	Very cracked + offset, undulose extinction, anhedral + embayed, also semi-euhedral, some feldspar inclusions, granulated in shear zones
	K-feldspar	50	Mesoperthites, some have plag inclusions, cracked + some offset, simple twins, some sericite + carbonate alteration, some quite large, granulated in cataclastic shear zones, some perthites are curved + deformed, grain boundary deformation
	Plagioclase	1-2	Polysynthetic twins, some sericite, cracked, smaller than larger kspar, small inclusions within kspar too, some twins don't align
	Zircon	<1	Associated to biotite
	Opaques	1	Associated with altered biotite
	Biotite	2	Some convoluted + highly altered to metamorphic chlorite + muscovite esp. in shear zones, dark brown, deformed, commonly growing elongate (semi-igneous + metamorphosed) + parallel to shears, commonly contain lensoidal quartz inclusions, also altering to opaques, some pressure shadows of chlorite
	Carbonate	2-3	Infills cracks, alteration of feldspar

Sample: 15LHR50 Name: altered trachyte	Mineral	%	Description
 **Rock textures:** Porphyritic, fine grained, altered, devitrified groundmass, sericitised + carbonate + clay alteration, quartz veinlets are cross-cut by carbonate veinlets, one carbonate veinlet has comb quartz envelopes, non-vesicular or trachytic	Plagioclase	30	Highly altered to sericite + carbonate + clay, anhedral, felsic glassy inclusions, relict polysynthetic twins, tabular to equant, embayed, cross-cut by quartz + carbonate veinlets
	Opaques	3	Magnetite + ilmenite, square to hexagonal, also anhedral
	Groundmass	67	Quartz (8%), feldspar (kspar? altered to sericite + carbonate, 55%), zircon (1%), opaques (1%), spherulitic muscovite (1%), limonite
	Quartz veinlets		Cross-cut rock, some offset along cracks, anastomosing veinlets, some cross-cut by later carbonate veinlets
	Carbonate veinlets		Ankerite or calcite?, one has comb quartz envelopes, untwinned

Sample: 15LHR57 Name: ankerite vein (right)	Mineral	%	Description
 **Rock textures:** Mix of coarse ankerite crystals and fine grained masses of ankerite, edges of vein contains brecciated quartz / altered granite, cracked but not deformed	Ankerite	95	Lamella twinning sometimes present esp. on larger euhedral equidimensional crystals, also masses and small veinlets of fine carbonate mixed with very minor sericite, some larger crystals are slightly replaced by fine aggregates of ankerite, some zoning of larger crystals, lots of streaky inclusions
	Quartz	2	Clasts of small + anhedral masses and brecciated larger cracked crystals on the outsides of the ankerite vein, undulose extinction
	Muscovite	1	Small platy inclusions in granitic clasts on edges of vein
	Zircon	<<1	Associated to muscovite + quartz
	Limonite	1	In cracks

Sample: 15LHR59 Name: altered tephrite (right)	Mineral	%	Description
 **Rock textures:** Fine grained, trachytic, aphyric, two different calcite vein habits (fibrous and equant), both contain opaque envelopes, sub-parallel stylolitic dissolution seams containing Fe-oxides (with minor Ti), veins and solution seams also sub-parallel to trachytic texture	Plagioclase	50	Large microlites, lathes, some altered to calcite + sericite, subhedral, polysynthetic twins, trachytic, some bent
	Nepheline	2	Difficult to differentiate from the plag, minority
	Calcite	20	Large anhedral masses, some twins, some pseudomorphing plag, also infilling vein with columnar/fibrous calcite and older veins with equant twinned calcite
	Opaques	10	Magnetite + ilmenite, square to spindly, Fe-oxides filling vein envelopes and solution seams, some oxidised
	Groundmass	18	Devitrified almost completely to feldspars/feldspathoids, amphibole altered to chlorite (20%), opaques, hematite, prismatic apatite

Sample: 15LHR63 Name: biotite alkali-feldspar granite	Mineral	%	Description
 **Rock textures:** Coarse grained, miarolitic cavities, granitic, cracked	K-feldspar	45	Large, minor perthites, plag inclusions, simple twins, some cracked
	Quartz	42	Mostly anhedral, rare undulose extinction, small interstitial crystals around boundaries of large crystals, some cracked, some graphic intergrowths
	Plagioclase	4-5	Polysynthetic twins, generally smaller than kspar but also large ones, minor sericite + muscovite alteration, euhedral
	Biotite	2-3	Small clusters with amphibole + opaques, some oxidation, light-brown to foxy-red, some quartz + embayments, some chlorite
	Opaques	1-2	Magnetite + ilmenite, euhedral-anhedral, associated with biotite + amphibole
	Zircon	1-2	Associated with opaques + biotite + amphibole, small clusters
	Amphibole	1	Pseudomorphs, very altered to biotite + opaques + limonite + cavities, euhedral
	Apatite	1	Associated with biotite clusters

Sample: 15LHR65 Name: biotite granodiorite	Mineral	%	Description
 **Rock textures:** Coarse grained, granitic, monzonitic texture, feldspar has labradorescence, biotite-rich, inequigranular, apatite-rich	K-feldspar	5-10	Equant and euhedral, cracked, simple twins, minor sericite, some very large interstitial perthitic crystals enclose plag
	Quartz	30	Smaller than feldspar, cracked, undulose extinction, commonly anhedral, commonly occurs in clusters, some embayed
	Plagioclase	40-45	Some poikiolitic/enclosed in very large kspar, polysynthetic twins, large, minor sericite, euhedral but embayed, cracked
	Biotite	20	Brown, platy clusters common, anastomosing around qtz + feldspar crystals, embayed, contain inclusions of apatite + zircon + qtz + other biotite + opaques, rare chlorite alt., some isotropic basal plates
	Ilmenite	1	Anhedral to euhedral and square + hexagonal, embayed, commonly associated to biotite, some quite large, commonly contain apatite + zircon inclusions
	Apatite	4-5	Euhedral, inclusions mostly within biotite, commonly hexagonal, some quite large, few rounded
	Zircon	2-3	Commonly associated to biotite, acicular, some metamict
	Monazite	1	Commonly anhedral, appear primary

Sample: 15LHR66A/B Name: trachyandesite to trachyte	Mineral	%	Description
 **Rock textures:** Porphyritic, fine grained, cracks contain carbonate veinlets, composite dyke from intermediate mafic (left) to intermediate felsic (right). Mafic end contains abundant opaques in groundmass and less phenocrysts. Felsic end contains more + larger kspar, more quartz and opaques are almost all oxidised	K-feldspar	2-10	Euhedral, altered brown rims very common, cracked, some glomeroporphyritic
	Quartz	2-3	Some skeletal, some rimmed by fine calcite, embayed, rare undulose extinction
	Plagioclase	1	Euhedral, polysynthetic twins, cracked, sericite, some broken then rounded, rare zoning
	Amphibole	<1	Green, pseudomorphs mostly altered to chlorite + later carbonate + opaques, anhedral
	Limonite	2-8	All through cracks, also of opaques esp. on red end
	Carbonate veinlets		Infills cracks
	Groundmass	78-94	Feldspar lathes (30-60%), carbonate (2-30%), devitrified volcanic glass (2-20%), opaques (2-5%), zircon (<1%), prismatic apatite (<1%), rare vesicles

Sample: 15LHR69 Name: altered trachyandesite (left)	Mineral	%	Description
 **Rock textures:** Porphyritic, fine grained, devitrified groundmass	Plagioclase	20	Probably andesine/oligoclase, sericitised, large skeletal phenocrysts with glassy quartz inclusions, relict polysynthetic twins, eu-subhedral, smaller non-skeletal phenocrysts too, tabular, some broken, cumulophyric and individuals, zircon trails in xenocrysts
	Chlorite	8	Altered mafics (amphibole and/or pyroxene pseudomorphs) to chlorite + opaques + calcite, an-subhedral, cumulophyric, embayed
	Opaques	5-6	Magnetite + ilmenite ± pyrite, euhedral, anhedral, square, hexagonal, some embayed + sieve textures, larger ones commonly associated with altered mafics, some oxidised
	Apatite	1	Prismatic to hexagonal, euhedral, some quite large that are poikiolitic in the smaller phenocrysts and groundmass (not in the larger phenocrysts)
	Groundmass	65	Feldspar, quartz, opaques, chlorite, calcite, recrystallised vesicles, apatite

Sample: 15LHR70 Name: altered rhyolite (left)	Mineral	%	Description
 **Rock textures:** Porphyritic, fine grained, non-vesicular, devitrified groundmass, sericitisation	K-feldspar	12	Large, euhedral pseudomorphs almost completely sericitised + minor limonite, relict perthites + simple twins, equant, some skeletal, individuals and glomeroporphyritic
	Quartz	6	Skeletal, later rounding, embayed, some cracked, commonly rimmed by feathery feldspar crystals
	Plagioclase	1	Rare, enclosed in phenocrysts
	Ilmenite	2	Mostly tiny and anhedral, also larger ones associated with altered mafics
	Altered mafics	5	Mostly limonite + opaques now, patchy
	Groundmass	75	Feldspar (some spherulitic), quartz, opaques, zircon

Sample: 15LHR72 Name: altered trachyte (left)	Mineral	%	Description
 **Rock textures:** Porphyritic, fine-medium grained, devitrified groundmass, sericitised, chloritised	Plagioclase	25	Mostly pseudomorphs, heavy sericitisation, also altered to chlorite + carbonates, semi-euhedral, tabular, polysynthetic twins, brown alteration rims, embayed, individual and cumulophyric, larger skeletal ones with glassy quartz inclusions
	K-feldspar	2	Sericitised, possibly originally sanidine, brown alteration rims, simple twins, embayed
	Chlorite	5-6	Originally biotite or pyroxene, now chlorite + opaque clusters + spherulitic calcite, yellow-green
	Opaques	2	Magnetite + ilmenite, square euhedral, anhedral, tabular, hexagonal, commonly associated with alter mafics, also poikiolitic in phenocrysts
	Groundmass	65	Quartz (10%), kspar (46%), chlorite (4%), opaques (2%), calcite (2%), apatite (1%), zircon (<<1%)

Sample: 15LHR78 **Name: biotite alkali-feldspar granite**	**Mineral**	**%**	**Description**
 **Rock textures:** Coarse grained, granitic, mesoperthites, graphic intergrowths, clusters of mafic minerals	K-feldspar	47	Mesoperthites, graphic intergrowths, cracked, large + euhedral crystals, rare sericite, simple twins
	Quartz	40	Graphic intergrowths, some finer crystals at boundaries of large ones, undulose extinction, large + anhedral and smaller hexagonal euhedral crystals, cracked
	Plagioclase	4	Some sericite (esp. in cores), polysynthetic twins, tabular, euhedral, cracked
	Biotite	3	Altering to chlorite, euhedral but commonly embayed, clusters common, opaque + apatite + zircon inclusions, yellow-brown
	Amphibole	1	Green, some chlorite alteration, subhedral
	Magnetite	1	Ti-rich magnetite to titanomagnetite, square to hexagonal, some anhedral + embayed, clustered with biotite commonly
	Zircon	1-2	Abundant, some quite large, associated + clustered with opaques + biotite, rare haloes
	Rutile	<1	Cracked, associated with biotite + magnetite clusters
	Bastnäsite-parisite	1	Associated with biotite + magnetite clusters, large, subhedral, altered, light tan, amphibole shapes – possibly replacing hornblende
	Fergusonite	<1	Small sub-euhedral, individual crystals, brown, mod-high relief, mod birefringence, associated with biotite + magnetite clusters
	Apatite	1	Inclusions, especially in magnetite + biotite, hexagonal

Sample: 15EHR79 **Name: biotite syenogranite**	**Mineral**	**%**	**Description**
 **Rock textures:** Granitic, coarse grained, altered amphibole, mafic clusters, mesoperthites, graphic intergrowths	K-feldspar	45-50	Mesoperthites, graphic intergrowths, simple twins, large + euhedral, cracked, rare sericite, some plag inclusions
	Quartz	30-35	Commonly sub-anhedral but also small hexagonal euhedral ones, interstitial small crystals too, some cracked, undulose extinction
	Plagioclase	5-6	Polysynthetic + pericline twins, some sericite alteration, tabular, cracked, subhedral, smaller than kspar
	Biotite	2-3	Brown, sub-anhedral, associated to clusters of opaques + altered amphibole, some oxidised, opaque + zircon + apatite inclusions common
	Opaques	3-4	Ilmenite + magnetite, anhedral, quite large commonly, oxidised, some zircon + apatite inclusions
	Zircon	2-3	Associated to biotite + opaques, some quite large
	Amphibole	2	Altered to biotite + limonite + opaques + cavities + bastnäsite-TiO_2
	Apatite	2	Hexagonal to acicular, poikiolitic in biotite + opaques commonly
	Bastnäsite-parisite	1	Euhedral discrete crystals, colourless to brownish-opaque, also fine grained mass, also parisite on its own, some prisms, one encloses small allanite cluster
	Allanite	1	Euhedral-subhedral, discrete crystals, prismatic to equant habit, clusters, strong brown pleochroism, also anhedral fine grained mass

Sample: 15EHR80A Name: altered alkali-feldspar granite	Mineral	%	Description
 **Rock textures:** Coarse grained, granitic, highly altered, sericitised, intruded by quartz and carbonate veins (samples 15EHR80c below), cracked	K-feldspar	57	Pseudomorphs completely sericitised (some coarser muscovite too) ± illite + siderite (oxidised), relict boundaries + perthites + simple twins
	Quartz	40	Anhedral, cracked, some protuberances, undulose extinction, also microcrystalline in feldspar perthites
	Zircon	1	In clusters or trails associated with opaques, some quite large, radiation halos
	Opaques	1	Ilmenite + magnetite, possibly some pyrite, some also associated with muscovite cleavage, some oxidised, sieve textures
	Limonite	1	Part of siderite alteration and around opaques/completely altered mafics

Sample: 15EHR80B Name: altered olivine basalt	Mineral	%	Description
 **Rock textures:** Mafic dyke with ankerite vein containing brecciated clasts of the dyke, fine grained, highly altered by carbonates, porphyritic	Olivine	5	Highly altered to carbonates
	Groundmass	95	Feldspar lathes (50%), pyroxene (~5%), altered magnetite (15-20%), carbonate (20%)
	Ankerite veins		Rare twins, comb structures around edges, zoning common, rhombs

Sample: 15EHR80C Name: ankerite-quartz vein	Mineral	%	Description
 **Rock textures:** At least silica-carbonate-silica-carbonate cross-cutting relationships, contains chunks of altered granite, some earlier veins have become brecciated	Quartz	35	Elongate medium grained semi-euhedral prismatic vein quartz/ crystal mesh, also microcrystalline zones + comb quartz, undulose extinction, sometimes cut by carbonate veinlets
	Ankerite	65	Outer veins have microcrystalline ankerite grading into euhedral rhombs and then to comb structures towards inner vein before quartz took over, untwinned, compositional zoning common, contains some clasts of earlier microcrystalline quartz, sometimes cut by quartz veinlets

Sample: 15EHR81A **Name: altered alkali-feldspar granite**	**Mineral**	**%**	**Description**
 **Rock textures:** Granitic, coarse grained, mesoperthitic, limonite + sericite + siderite alteration esp. proximal to cracks, chloritic cracks, dendritic/spherulitic muscovite, offset fractures	K-feldspar	44	Mesoperthite, simple twins, sericitisation, esp. of exsolved albite proximal to fractures, large crystals, cracked, alteration to siderite along perthites
	Quartz	34	Finer crystals around boundaries of large crystals, some undulose extinction, embayments, sub-anhedral, some discontinuous cross-cutting anastomosing quartz veinlets, some (re)crystallising in parallel fractures
	Altered mafics	8	Completely altered to limonite + siderite + opaques + minor chlorite + parisite-synchysite + ilmenorutile + leucoxene + muscovite
	Chlorite	2	As small veinlets in cracks
	Zircon	1-2	Commonly clusters associated with altered mafics + opaques, some quite large, rare alteration to thorite + xenotime
	Opaques	1	Ilmenite + magnetite + galena, commonly anhedral, also euhedral hexagonal, associated with altered mafic components + zircons. Rare pyrite veinlets and galena
	Muscovite	1	Occurs in dendritic/spherulitic habit with ilmenorutile + Fe-oxides, sometimes in-fills miarolitic cavities
	Apatite	<1	rounded
	Siderite	4-5	In cracks and alteration of kspar, oxidised, appears secondary to sericite sometimes
	Sphalerite	<1	Associated with altered mafics + limonite
	Parisite-synchysite	2-3	Colourless to tan brown, also opaque dark-brown (where altered to TiO_2), associated with zircon + ilmenorutile
	Pyrochlore	<1	Semi-euhedral amongst quartz and feldspar, but altering to Fe-oxides, some tend towards the plumbopyrochlore endmember
	Leucoxene	1-3	Occurs with limonite + parisite-synchysite, common alteration product of mafic minerals

Sample: 15EHR81C Name: granitic palimpsest	Mineral	%	Description
 **Rock textures:** Medium grained, highly altered, textural destruction, disseminated sulphides, siderite veinlets, oxidation, partial remnant granophyric texture	Quartz	40	Some euhedral igneous quartz, also vein quartz and finer + anastomosing crystals, irregular occurrence, strong elongate to radial undulatory extinction, some crystals have protuberances
	Sericite	35-40	Complete and pervasive replacement of feldspar to sericite + fine grained quartz masses, relict perthites and vague crystal boundaries defined by sericite + quartz
	Siderite	5-6	Fine clusters commonly associated with quartz, some iron staining
	Pyrite	3-4	Euhedral but some sieve texture and embayments esp. in larger crystals, individuals and clusters, commonly occurs with quartz + bastnäsite
	Chalcopyrite	<1	Rare, separate grains and composite with pyrite, also as narrow veinlets cross-cutting rare earth mineral
	Sphalerite	1	Occurs in association with pyrite, anhedral
	Galena	<<1	Present in some pyrite
	Zircon	1-2	Giant crystals, eu-anhedral but commonly broken and odd shapes, small ones commonly associated with altered mafics, large ones to quartz, some partially altered to xenotime + thorite, also parisite + ilmenorutile-ferrocolumbite + rare galena inclusions
	Brookite/ rutile	1	Acicular, aligned, appears to be alteration product of mafic components, associated to pyrite + carbonates + limonite, dark brown
	Xenotime	<1	Rare alteration rims around zircon
	Monazite	<<1	
	Bastnäsite-synchysite-parisite	2	Associated to altered mafic material + zircon commonly, anhedral masses, lower birefringence than sericite, fine grained
	Altered mafics	2-4	Completely corroded and altered to TiO_2 + limonite + carbonates + pyrite

Sample: 15EHR81D **Name: granitic palimpsest**	**Mineral**	**%**	**Description**
 **Rock textures:** Medium grained, highly altered, textural destruction, disseminated sulphides, small comb quartz veinlet cross-cut by later carbonate veinlet, en echelon ankerite veins, small solution seams with sericite and granulated quartz that tend to be orientated perpendicular to quartz protuberances + ankerite veins	Quartz	50	Undulose extinction, mostly vein quartz but also igneous, euhedral prisms + hexagons common inside larger quartz, protuberances common, also fine anastomosing crystals, irregular, one comb quartz veinlet with zoned crystals cross-cut by carbonate veinlet
	Sericite	25-30	Pervasive replacement of feldspar, defines remnant perthites + boundaries with fine quartz, also in small solution seams with granulated quartz
	Ankerite	10-15	Untwinned, small anhedral clusters, small veinlet cross-cutting quartz veinlet, discontinuous en echelon-style veinlets, alteration of mafics
	Zircon	2	Small clusters associated with quartz + altered mafics + brookite/rutile, few giant crystals, inclusions of galena + xenotime
	Altered mafics	5-6	Completely altered to brookite/ rutile + carbonates, interstitial clusters
	Leucoxene/ rutile	2-3	Extensive secondary Ti oxides, both prismatic-tabular- acicular pseudomorphs of former ?ilmenite and also as dispersed equivocal material, alteration product of mafic component, commonly aligned, commonly “covers” quartz, opaque dark brown to black, some skeletal, few embayments
	Hematite	<<1	Rare
	Pyrite	<1	Euhedral, few embayments, usually associated with quartz + altered mafic clusters
	Chalcopyrite	<1	Up to 300 µm, rare
	Galena	1	Anhedral, associated with rutile/brookite + parisite-synchysite, some up to 500 µm veining pyrite
	Sphalerite	<1	Similar to galena
	Parisite with subordinate synchysite	2	Associated with altered mafics and zircon, tan to brown, near-opaque + subhedral where altered to TiO_2, normally fine grained masses with birefringence where alone

Sample: 15EHR81H **Name: alkali-feldspar granite**	**Mineral**	**%**	**Description**
 **Rock textures:** Coarse grained, granitic, corroded mafics, graphic intergrowths, mesoperthites, dendritic muscovite-opaques, cracked	K-feldspar	50-55	Mesoperthites, some plag inclusions, rare kinking, graphic + granophyric intergrowths, simple twins, large + euhedral, minor interstitial crystals
	Quartz	30-35	Graphic intergrowths, undulose extinction, anhedral but also euhedral, anhedral interstitial crystals
	Plagioclase	<1	Inclusions in larger kspar, polysynthetic twins
	Altered mafics	5	More abundant, but very corroded, pseudomorphs of amphibole + biotite, altered to opaques + chlorite + hematite + limonite + siderite + bastnäsite-TiO_2
	Opaques	2-3	Magnetite + ilmenite, euhedral + anhedral, some tabular prisms, commonly as alteration product of mafic minerals, some spherulitic Fe-oxide + siderite + ilmenite clusters
	Zircon	2-3	Clusters, commonly associated with opaques + altered mafics, also as inclusions in kspar, some quite large
	Muscovite	<1	Dendritic/spherulitic, intergrown with Fe-Ti oxides, very fine
	Bastnäsite group	1-2	Elongate prismatic commonly, discrete euhedral-subhedral crystals, also massive fine grained, altering to/from TiO_2, dark brown, some closely associated with zircon

Sample: 15EHR81I **Name: altered alkali-feldspar granite**	**Mineral**	**%**	**Description**
 **Rock textures:** Granitic, pervasive ankerite alteration, mesoperthites, cracked, coarse grained, corroded mafic minerals, graphic intergrowths	K-feldspar	40-45	Mesoperthite, pervasive carbonate alteration, simple twins, graphic intergrowths, cracked, large and euhedral
	Quartz	30-35	Undulose extinction, graphic intergrowths, commonly anhedral, some embayed, minor cracking
	Ankerite	20-30	Replacing kspar in irregular patches along perthites, fine grained
	Altered mafics	2	Pseudomorph biotite and/or amphibole, corroded and altered to opaques + limonite + carbonate + chlorite
	Ilmenite	1-2	Some going to leucoxene, square + hexagonal, euhedral to anhedral, some embayed + sieve texture, commonly associated with altered mafics, some zircon inclusions
	Zircon	2	Commonly associated with altered mafics + opaques, also as inclusions in kspar, some halos, some metamict + have qtz inclusions, some quite large
	Limonite	1	Around altered mafic components
	Bastnäsite group	1-2	Opaque brown to colourless, commonly dark blurry edges, eu-subhedral, elongate and prismatic, clustered commonly with each other + ilmenite + zircon + in altered mafic clusters, altering to/from TiO_2

Sample: 15EHR82 **Name: altered QAF syenite**	**Mineral**	**%**	**Description**
 **Rock textures:** Granitic, coarse grained, some sericite, cracked, completely corroded mafic minerals, carbonate alteration, small veinlets of quartz and carbonates, coarse felsitic texture	K-feldspar	~70	Perthites, sericite alteration (some replaced by carbonates), some quite large, mosaic and commonly 'messy' looking with very irregular boundaries, small interstitial crystals at some crystal boundaries
	Quartz	15	Undulose extinction, smaller, sub-anhedral, small interstitial crystals at crystal boundaries
	Plagioclase	1	Polysynthetic twins, sericite alteration
	Altered mafics	2-3	Messy alteration to muscovite + opaques + rutile + limonite + clay + carbonates (some carbonate replacing muscovite)
	Opaques	2	Magnetite + ilmenite, euhedral to anhedral, commonly associated with altered mafics
	Zircon	2	Associated with altered mafics + opaques, also as inclusions in kspar, some quite large, haloes common
	Carbonate	4-5	Interstitial, small aggregates, also replacing sericite, muscovite + feldspar
	Apatite	1	Rounded inclusions, equant, commonly associated with mafic clusters
	Small veinlets		Of quartz, also calcite + opaques

D Supplemental Photomicrographs

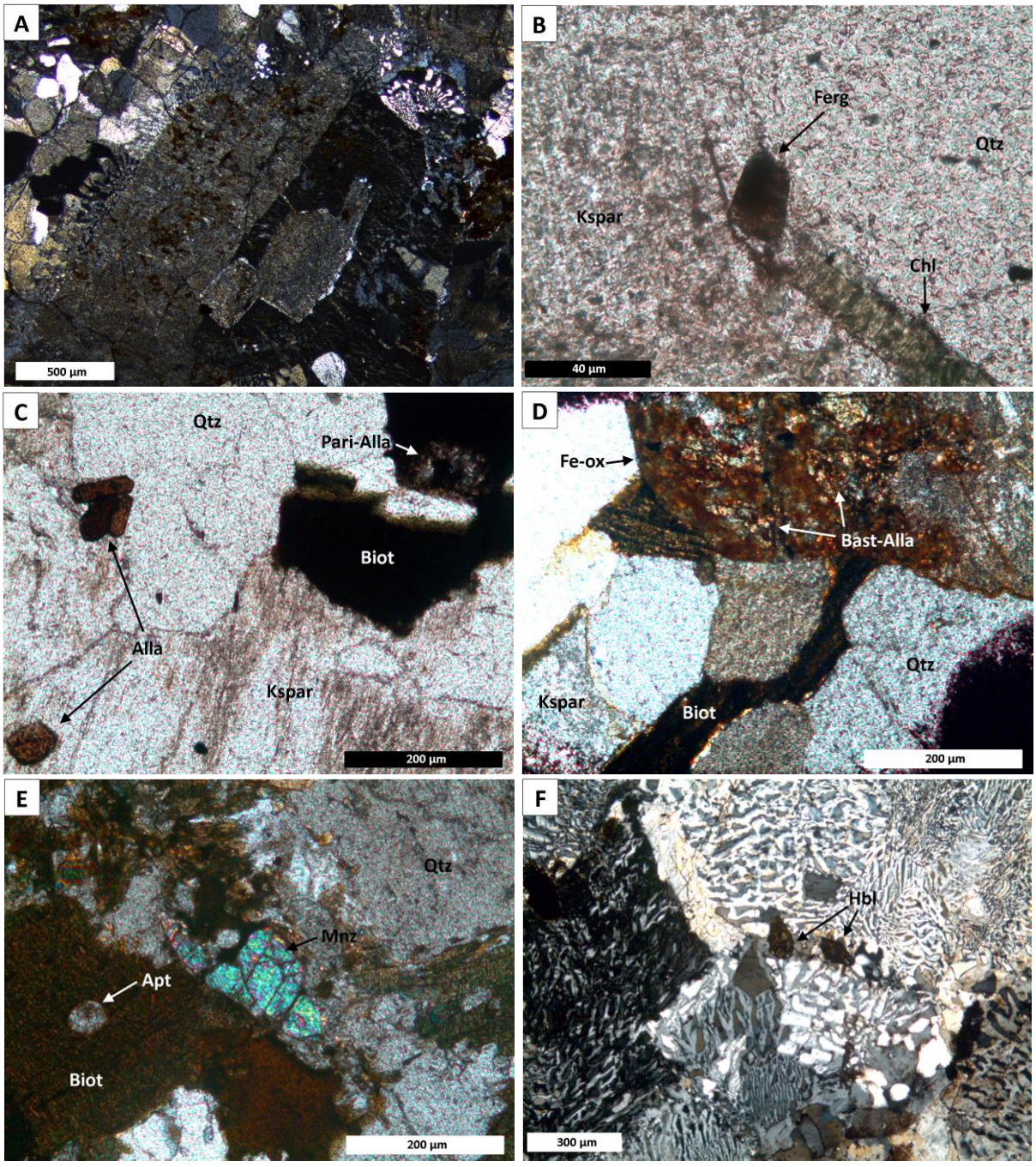

Photo D1. Photomicrographs of (A) LHR42, a large euhedral perthitic K-feldspar phenocryst with granophyric intergrowths around its boundaries (in CPL); (B) LHR28, a euhedral fergusonite inclusion within interstitial quartz at the boundary between quartz and K-feldspar, interstitial chlorite is also present (in PPL); (C) EHR79, primary allanite inclusions within quartz and K-feldspar, also present are altered biotite as well as parisite altering and pseudomorphing allanite (in PPL); (D) LHR36, bastnäsite + allanite + Fe-oxides replacing hornblende, with quartz, K-feldspar and interstitial biotite also present (in CPL); (E) LHR65, monazite, biotite, apatite and quartz (in CPL); and (F) GR03, intense granophyric intergrowths between quartz and K-feldspar (in CPL).

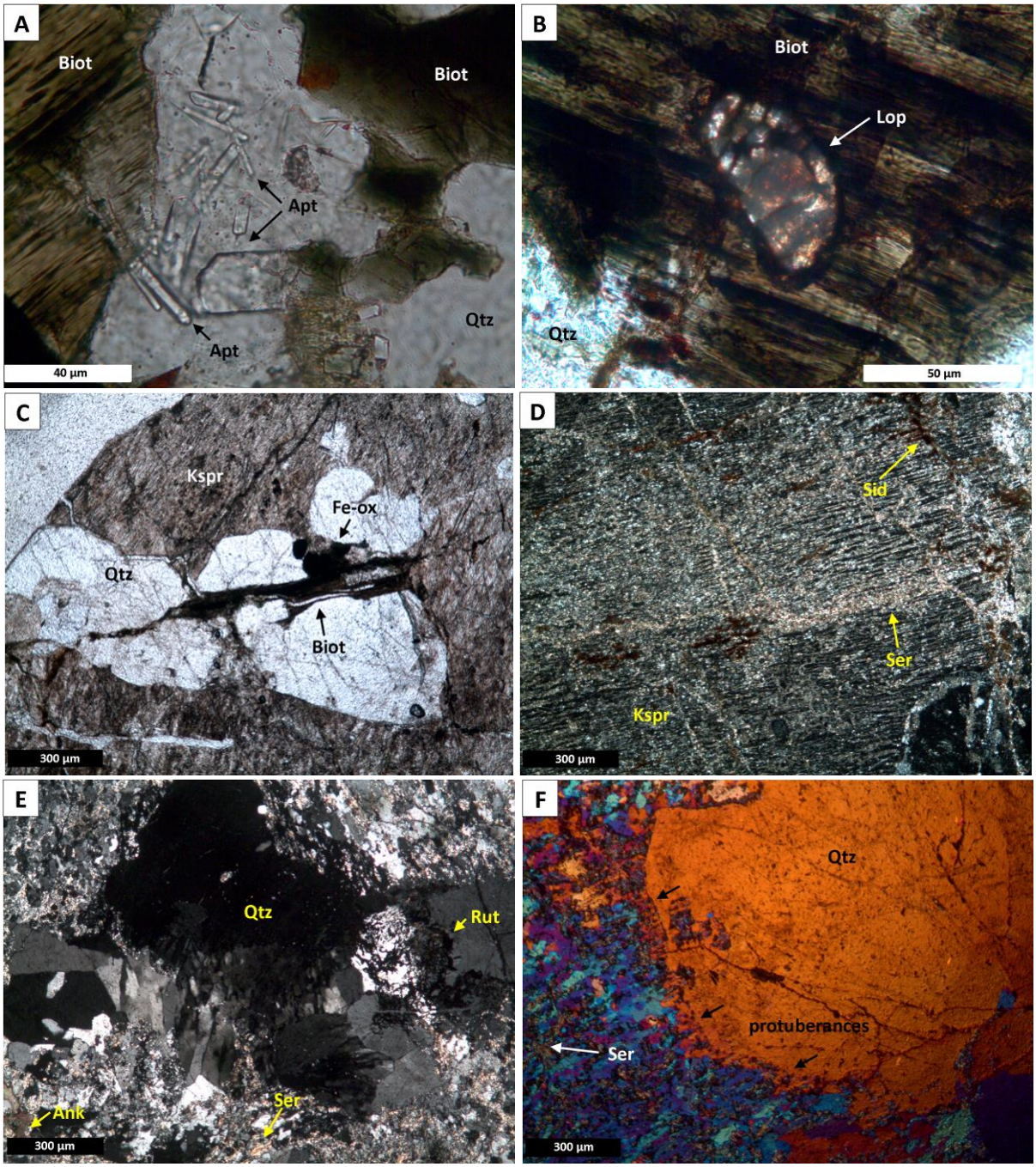

Photo D2. Photomicrographs of (A) GR03, clusters of acicular apatite inclusions within biotite and quartz (in PPL); (B) GR03, rounded loparite inclusion within biotite (in PPL); (C) LHR46, an elongate crystal of biotite with a lensoidal quartz inclusion grown along a shear plane within quartz and K-feldspar (in); (D) EHR81A, extensive sericitisation and slight siderite alteration along perthites in K-feldspar (in CPL); (E) EHR81D, quartz displaying elongated undulose extinction in the inner zone of hydrothermal alteration in the Eastern Hohonu River, also present are rutile needles, ankerite, sericite and fine grained quartz (in CPL); and (F) EHR81D, protuberances on the edge of a quartz crystal surrounded by a mix of sericite and fine grained quartz (in CPL with the sensitive tint plate in).

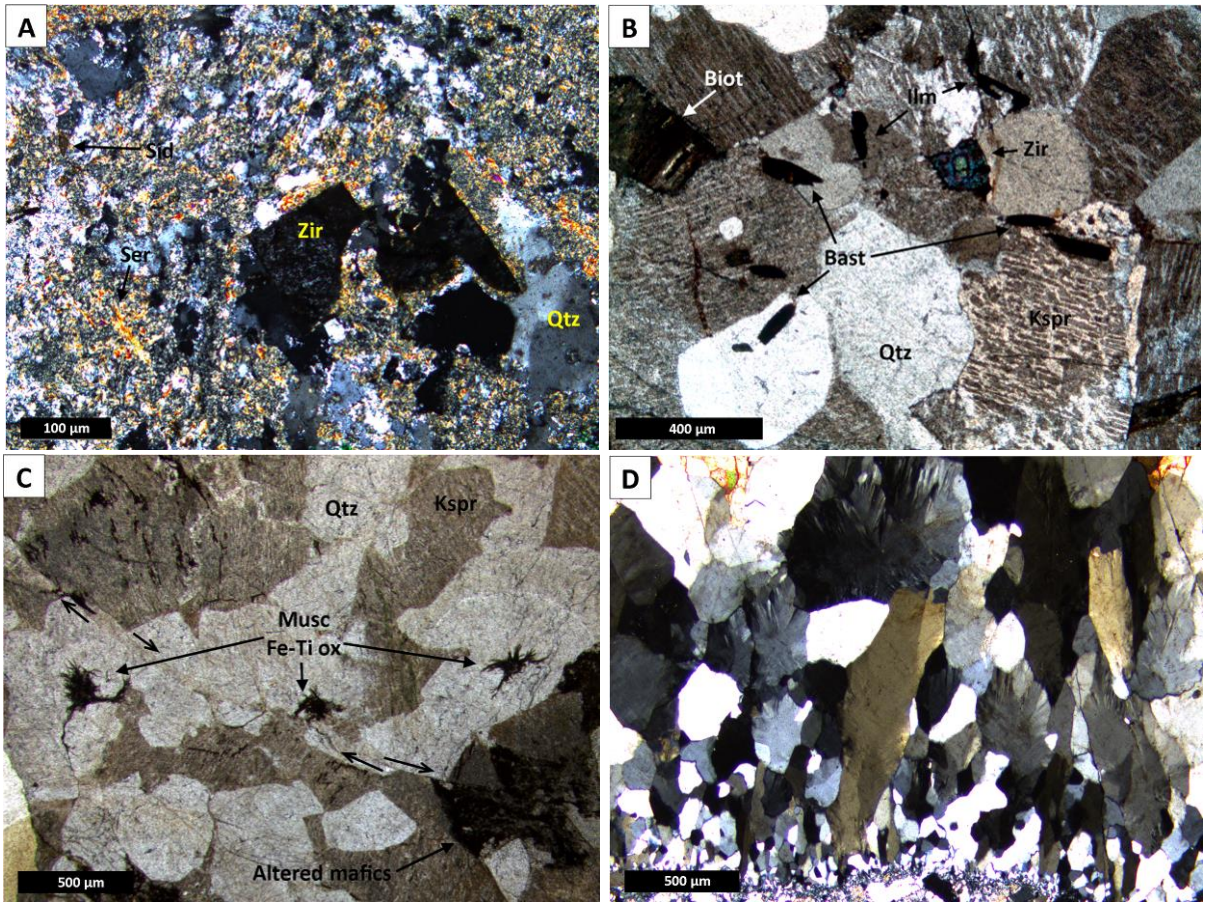

Photo D3. Photomicrographs of (A) EHR81C, large metamict zircon surrounded by sericite, quartz and siderite (in CPL); (B) EHR81H, scattered bastnäsite-TiO_2 , zircon, ilmenite, leucoxene and altered biotite, set amongst K-feldspar and quartz (in CPL); (C) EHR81A, intergrown muscovite and Fe-Ti oxides occurring with quartz and K-feldspar, note offset fracture (in PPL); and (D) LHR25, undulose extinction in columnar vein quartz (in CPL).

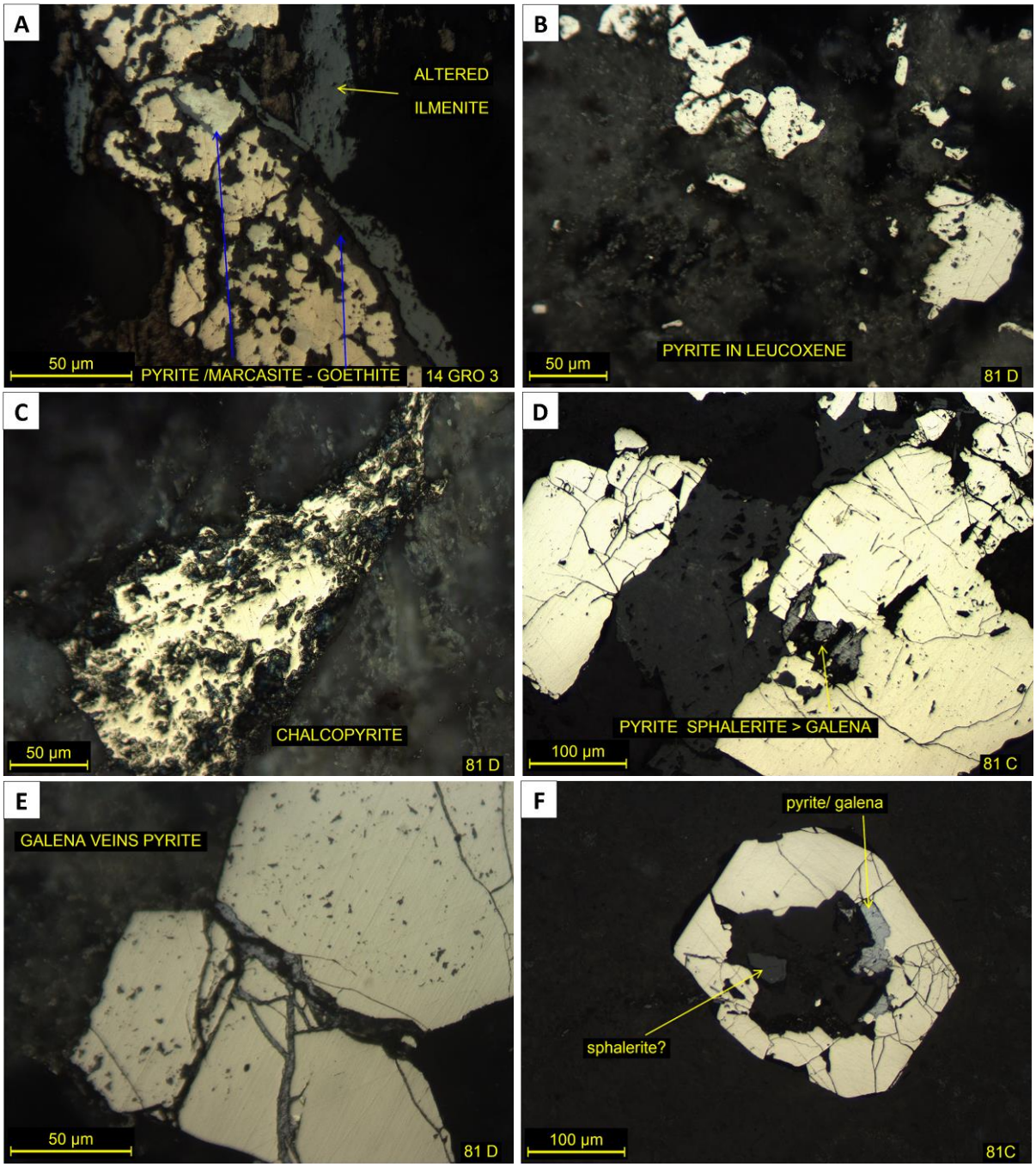

Photo D4. SEM images taken in reflected light of (A) GR03, pyrite with partial marcasite and goethite alteration; (B) EHR81D, pyrite grains in leucoxene; (C) EHR81D, a grain of chalcopyrite in leucoxene; (D) EHR81C, pyrite, sphalerite and galena; (E) EHR81D, galena veining pyrite; and (F) EHR81C, galena and sphalerite in pyrite. Images from Townend & Townend (2016a).

E Full Whole Rock Geochemistry

1 Full XRF Results

Oxide (%)	EHR01	EHR02	GR03	EC04	MFT06	MFT07	MFT08	LHR09	LHR11	LHR12	EHR14A	EHR14B	EHR15	LHR18	LHR23	LHR24	LHR25A	LHR25B
SiO_2	72.87	73.76	69.53	75.62	65.87	74.35	73.51	73.46	75.55	74.93	51.84	65.95	75.68	73.80	44.53	73.11	85.82	7.71
TiO_2	0.03	0.18	1.04	0.11	0.52	0.19	0.22	0.17	0.17	0.20	1.84	0.79	0.17	0.19	2.60	0.21	0.06	<0.01
Al_2O_3	15.11	13.58	12.08	13.39	15.16	13.14	13.40	13.92	13.54	13.22	15.33	14.75	12.20	13.35	18.73	13.05	5.72	0.49
Fe_2O_3	0.36	1.93	7.08	1.27	5.93	2.01	2.27	1.71	1.41	1.59	10.15	5.07	2.07	1.65	12.20	1.95	0.83	7.61
MnO	0.01	0.03	0.05	0.03	0.22	0.02	0.01	0.02	0.03	0.01	0.17	0.09	0.05	0.03	0.24	0.03	0.03	0.42
MgO	0.08	0.09	0.89	0.07	0.06	0.12	0.08	0.35	0.52	0.13	5.32	1.38	0.18	0.14	5.62	0.17	0.98	13.41
CaO	0.67	0.39	0.86	0.44	0.66	0.17	0.13	0.34	1.06	0.48	6.40	1.28	0.24	0.57	4.80	0.24	1.62	29.06
Na_2O	4.46	4.03	2.92	4.45	5.47	3.31	2.99	1.64	<0.1	3.93	3.35	3.47	3.80	3.51	1.96	3.19	<0.1	<0.1
K_2O	5.74	5.46	4.69	4.53	5.62	5.74	6.29	5.83	4.25	5.07	2.02	4.74	4.71	5.46	2.97	4.79	1.58	0.12
P_2O_5	0.10	0.03	0.22	0.02	0.02	0.02	0.01	0.02	0.03	0.03	0.30	0.28	<0.01	0.04	0.81	0.03	<0.01	<0.01
LOI	0.42	0.40	0.52	0.04	0.42	0.88	1.06	2.47	3.24	0.30	3.19	2.16	0.79	1.10	5.50	3.15	3.18	41.10
Total	99.85	99.88	99.89	99.96	99.95	99.96	99.96	99.94	99.79	99.90	99.89	99.95	99.88	99.84	99.95	99.93	99.83	99.92
Element (ppm)																		
V	11	7	47	8	8	8	11	10	9	15	224	76	8	13	302	12	13	8
Cr	3	4	5	3	3	3	<3	5	4	4	175	22	3	4	412	<3	<3	4
Ni	<3	4	5	<3	<3	<3	3	4	3	4	80	11	3	4	201	<3	3	4
Zn	8	54	123	17	118	45	42	30	34	30	116	102	63	35	120	36	23	150
Zr	26	315	842	116	133	271	298	259	180	203	210	294	389	189	235	227	68	12
Nb	4	86	132	64	88	77	89	82	60	64	42	45	102	48	128	63	16	<2
Ba	188	210	202	109	52	202	255	132	110	172	507	685	71	216	898	182	21	33
La	10	102	175	25	57	50	34	87	86	98	28	56	98	70	84	97	24	8
Ce	10	199	337	36	98	117	54	161	158	161	71	104	166	155	154	167	60	36
Nd	<10	99	189	17	67	46	23	70	66	83	38	49	91	57	64	78	23	38
Ga	17	24	22	19	30	24	26	23	21	21	22	20	26	21	20	21	11	3
Pb	50	22	30	15	10	17	19	13	26	20	11	21	17	22	6	16	6	33
Rb	209	222	209	300	128	207	229	282	207	224	117	213	183	234	196	203	98	6
Sr	130	29	68	50	6	29	28	46	61	42	414	237	16	53	532	43	18	168
Th	2	26	41	39	10	29	16	37	35	32	9	16	20	29	11	33	10	8
Y	10	55	81	19	34	42	28	50	41	49	31	39	55	44	61	46	19	114

Oxide (%)	LHR26	LHR28	LHR36	LHR38	LHR41	LHR42	LHR44	LHR46	LHR50	LHR56	LHR57	LHR59	LHR63	LHR65	LHR66A	LHR66B	LHR69	LHR70
SiO_2	53.01	75.37	74.68	73.32	73.13	73.99	67.79	96.18	62.71	75.26	3.15	43.30	73.13	55.49	58.99	66.97	60.83	75.24
TiO_2	2.53	0.10	0.19	0.18	0.19	0.20	0.61	<0.01	0.69	0.21	<0.01	1.68	0.22	1.71	1.49	0.67	1.21	0.19
Al_2O_3	13.96	12.64	13.31	13.42	12.99	12.82	12.24	0.84	14.54	12.87	0.46	16.55	13.57	16.69	15.54	14.09	15.80	13.46
Fe_2O_3	9.80	1.32	1.72	2.00	2.78	1.94	5.58	0.35	4.38	1.64	9.92	9.92	2.07	8.08	6.96	3.87	6.54	1.74
MnO	0.15	0.02	0.02	0.04	0.05	0.03	0.12	0.04	0.12	0.02	0.85	0.18	0.03	0.10	0.14	0.09	0.11	0.02
MgO	2.86	<0.05	0.13	0.67	0.45	0.27	2.17	0.25	1.34	0.14	13.44	3.90	0.15	4.34	2.68	0.96	1.77	0.22
CaO	4.81	0.44	0.42	0.88	1.19	0.37	1.87	0.80	2.41	0.56	29.35	8.32	0.42	3.30	3.01	1.89	1.55	0.07
Na_2O	4.21	3.97	3.95	0.43	3.04	3.02	4.13	<0.1	3.20	3.75	<0.1	4.04	4.01	3.15	4.43	4.05	4.27	2.09
K_2O	2.98	4.79	5.11	5.59	4.83	5.37	4.59	0.10	4.83	5.02	0.10	2.34	5.38	4.71	3.60	4.48	4.25	5.43
P_2O_5	0.46	0.01	0.03	0.03	0.03	0.04	0.17	<0.01	0.20	0.03	<0.01	0.59	0.03	1.01	0.29	0.13	0.44	0.03
LOI	5.14	1.25	0.37	3.37	1.22	1.86	0.65	1.29	5.52	0.43	42.59	9.10	0.85	1.29	2.63	2.73	3.16	1.45
Total	99.91	99.89	99.92	99.93	99.89	99.91	99.91	99.85	99.93	99.93	99.87	99.92	99.86	99.87	99.75	99.93	99.93	99.93
Element (ppm)																		
V	252	8	12	10	13	10	76	9	42	13	15	209	12	260	145	63	83	11
Cr	<3	3	4	<3	<3	<3	74	4	8	4	4	43	<3	111	38	15	8	<3
Ni	13	<3	<3	5	<3	4	31	<3	5	<3	8	44	<3	50	33	16	6	3
Zn	107	16	27	40	54	33	148	6	75	30	151	209	27	120	116	72	109	42
Zr	253	205	188	265	196	211	220	9	426	232	11	169	252	586	308	294	404	321
Nb	64	71	68	83	78	69	85	<2	66	62	3	38	83	46	75	81	70	91
Ba	360	45	181	138	154	156	176	50	401	145	28	285	177	381	362	315	493	95
La	40	72	98	91	81	70	54	<5	58	92	<5	31	76	73	58	76	57	85
Ce	105	138	173	158	145	126	98	<5	121	163	19	75	149	166	120	139	124	174
Nd	51	56	61	57	65	50	68	<10	52	64	19	34	67	79	54	50	52	63
Ga	21	21	22	23	22	19	25	<2	22	20	<2	20	22	28	25	23	24	22
Pb	12	21	19	15	16	14	13	3	19	21	20	25	17	30	31	24	22	15
Rb	122	280	223	262	205	234	122	6	204	226	4	159	263	407	170	206	186	267
Sr	385	13	42	37	39	59	32	16	206	34	124	357	42	248	249	139	216	69
Th	15	43	39	39	32	29	13	<1	20	32	1	3	51	75	19	28	17	37
Y	38	52	50	53	49	44	82	4	40	45	42	23	58	78	42	46	44	54

Oxide (%)	LHR71A	LHR72	LHR73	LHR76	LHR77	LHR78	EHR79	EHR80A	EHR80B	EHR80C	EHR81A	EHR81B	EHR81C	EHR81D	EHR81F	EHR81H	EHR81I	EHR82
SiO_2	63.53	63.94	74.55	87.19	88.78	73.68	71.29	76.60	45.80	31.20	75.77	76.21	73.34	78.05	77.91	73.08	71.63	62.33
TiO_2	0.87	0.86	0.18	0.01	0.04	0.26	0.28	0.18	2.17	0.03	0.19	0.20	0.21	0.15	0.20	0.17	0.19	0.39
Al_2O_3	15.28	15.51	12.92	6.71	5.53	13.54	14.15	11.03	15.87	1.29	12.40	13.31	15.75	9.47	13.23	12.53	11.94	18.53
Fe_2O_3	5.30	5.25	1.95	0.24	0.67	2.21	2.83	1.22	11.76	7.80	2.26	3.02	3.00	1.68	2.33	2.45	1.99	3.46
MnO	0.10	0.10	0.04	<0.01	0.02	0.03	0.06	0.04	0.15	0.34	0.05	0.07	0.07	0.11	0.07	0.08	0.08	0.09
MgO	1.31	1.46	0.35	<0.05	0.56	0.21	0.15	1.24	3.46	9.63	0.05	0.26	0.32	1.16	0.27	<0.05	1.16	0.43
CaO	2.07	1.76	0.67	0.14	0.91	0.64	0.64	1.92	4.71	19.59	0.05	0.11	0.12	2.66	0.10	0.07	2.32	0.73
Na_2O	4.31	4.37	2.30	1.69	<0.1	3.97	3.91	<0.1	0.12	<0.1	3.11	<0.1	0.11	<0.1	<0.1	4.43	0.18	6.71
K_2O	4.37	4.41	5.12	3.33	1.56	5.14	5.69	3.00	2.10	0.34	4.90	3.67	4.26	2.54	3.62	4.77	4.79	4.98
P_2O_5	0.30	0.31	0.03	<0.01	0.03	0.05	0.04	0.04	0.28	<0.01	<0.01	<0.01	<0.01	<0.01	<0.01	<0.01	<0.01	0.09
LOI	2.43	1.92	1.80	0.57	1.68	0.17	0.76	4.59	12.76	29.67	1.18	3.03	2.63	3.40	2.11	2.26	5.60	2.21
Total	99.87	99.89	99.90	99.89	99.78	99.90	99.79	99.86	99.16	99.89	99.96	99.87	99.81	99.22	99.84	99.85	99.87	99.94
Element (ppm)																		
V	55	55	11	6	12	11	12	14	312	23	9	10	14	10	10	7	9	16
Cr	9	11	4	4	<3	<3	4	5	331	<3	<3	3	<3	5	<3	<3	<3	<3
Ni	7	7	3	4	<3	4	<3	9	89	24	3	3	5	<3	4	<3	4	3
Zn	93	86	39	4	17	39	75	46	126	227	128	101	1001	102	91	93	80	44
Zr	418	424	297	57	51	300	457	360	131	57	581	560	589	420	579	531	460	469
Nb	62	61	84	9	15	72	102	71	29	11	148	164	165	117	155	133	114	106
Ba	598	592	121	44	33	172	192	44	264	29	45	35	56	35	38	29	62	471
La	57	51	77	13	37	108	101	106	6	13	113	89	93	82	98	84	91	36
Ce	125	126	154	27	59	196	196	197	40	32	211	179	206	169	189	160	172	77
Nd	52	52	60	37	40	70	88	74	21	23	89	57	72	59	81	53	74	34
Ga	20	22	22	11	11	22	27	28	20	4	31	33	36	20	32	29	24	21
Pb	23	17	17	9	7	16	21	8	8	11	14	11	231	415	38	12	12	16
Rb	153	162	243	169	99	215	237	165	187	17	220	188	224	136	184	221	197	182
Sr	193	207	93	5	100	44	33	88	103	93	9	8	10	32	11	17	16	143
Th	18	19	34	26	11	35	25	16	<1	2	28	24	32	26	32	27	23	22
Y	40	39	51	43	12	52	75	39	23	21	73	78	104	59	83	71	53	26

2 Full ICP-MS/AES Results

Oxide (%)	EHR02	GR03	MFT07	LHR09	EHR14A	LHR18	LHR23	LHR24	LHR25A	LHR25B	LHR26
SiO_2	75.8	69.2	75.6	-	-	75.1	-	-	-	-	-
Al_2O_3	13.15	11.35	12.8	-	-	13	-	-	-	-	-
Fe_2O_3	1.84	6.95	1.98	-	-	1.62	-	-	-	-	-
CaO	0.36	0.83	0.16	-	-	0.56	-	-	-	-	-
MgO	0.11	0.85	0.13	-	-	0.16	-	-	-	-	-
Na_2O	3.78	2.67	3.21	-	-	3.32	-	-	-	-	-
K_2O	5.46	4.62	5.67	-	-	5.52	-	-	-	-	-
Cr_2O_3	<0.01	<0.01	<0.01	-	-	<0.01	-	-	-	-	-
TiO_2	0.18	1.02	0.18	-	-	0.18	-	-	-	-	-
MnO	0.03	0.05	0.01	-	-	0.02	-	-	-	-	-
P_2O_5	0.02	0.23	0.02	-	-	0.05	-	-	-	-	-
SrO	0.01	0.01	<0.01	-	-	0.01	-	-	-	-	-
BaO	0.02	0.02	0.02	-	-	0.03	-	-	-	-	-
LOI	0.54	0.89	0.67	-	-	1.14	-	-	-	-	-
Total	101.3	98.69	100.45	-	-	100.71	-	-	-	-	-
Elements (ppm)											
Ba	209	192	210	121.5	513	234	781	161	26.7	18.1	346
Ce	180.5	352	118	157	63	165.5	150	153	43.3	27.8	105.5
Cr	<10	10	10	<10	190	10	410	10	10	<10	10
Cs	5.22	7.58	3.13	8.59	7.8	7.14	22.8	4.44	9.03	0.7	2.2
Dy	8.87	14.8	7.24	8.04	5.51	7.63	9.74	7.38	3.12	18.8	6.84
Er	5.23	7.7	4.62	4.73	3.04	4.3	5.54	4.31	1.67	10.5	3.54
Eu	0.76	1.18	0.58	0.46	1.75	0.74	2.58	0.51	0.23	2.11	2.06
Ga	26	23.4	25.2	21.6	20.7	21.6	18.4	20.6	11.2	1.3	20.4
Gd	9.64	19.4	6.14	8.33	6.09	8.66	11.2	8.45	3.11	15.55	8.45
Hf	11.5	28.4	8.3	8.7	5.1	7.3	5	7.9	2.2	0.2	6.5
Ho	1.71	2.81	1.51	1.58	1.02	1.49	1.9	1.47	0.61	3.63	1.32
La	89.5	173.5	54.2	85.1	32.5	86.9	94.8	90.1	22.7	10.4	53.6
Lu	0.7	0.95	0.66	0.65	0.38	0.59	0.73	0.6	0.26	1.72	0.43
Nb	78.2	130	75.2	71.9	39.4	45.4	115	56.6	15.1	0.9	58.3
Nd	60.7	129	35.1	51.5	27.4	55.7	62.8	56.5	15.9	20.7	45.2
Pr	18.1	36.5	10.4	15.15	6.72	17	17.2	17.45	4.55	4.02	11.5
Rb	221	199	206	267	113.5	233	186.5	190	89	7.6	116.5
Sm	11.65	24.5	6.8	9.22	5.97	10.7	12.1	10.35	3.37	11.15	8.94
Sn	7	9	6	5	4	6	2	5	2	<1	4
Sr	28.9	64.6	29.7	44.3	421	53.5	527	39.9	18.1	167	385
Ta	5.7	6.7	5.3	5.4	2.3	4.6	6.5	4.4	1.7	0.2	3.8
Tb	1.48	2.76	1.14	1.41	0.99	1.36	1.78	1.38	0.52	3.25	1.29
Th	24	38.4	28.8	33.2	6.26	29.5	9.18	33.7	9.33	6.38	14.35
Tm	0.74	1.06	0.67	0.68	0.38	0.63	0.76	0.61	0.24	1.61	0.47
U	5.91	7.55	5.4	4.57	2.06	7.77	11.25	7.28	1.83	1.03	6.6
V	5	48	7	7	224	9	282	9	14	<5	237
W	188	99	483	123	49	593	39	342	535	54	83
Y	49.5	74.6	40.8	44.5	30.2	43.8	55.2	41	16.8	100	35.4
Yb	4.75	6.61	4.73	4.54	2.52	4.23	4.67	4.04	1.68	11.65	3.12
Zr	427	1130	308	276	213	231	229	252	73	5	257

Oxide (%)	LHR28	LHR36	LHR38	LHR41	LHR42	LHR44	LHR46	LHR50	LHR56	LHR57	LHR59
SiO_2	-	76.6	-	-	76.7	69.7	-	-	-	-	-
Al_2O_3	-	12.8	-	-	12.45	11.8	-	-	-	-	-
Fe_2O_3	-	1.66	-	-	1.89	5.49	-	-	-	-	-
CaO	-	0.41	-	-	0.35	1.83	-	-	-	-	-
MgO	-	0.15	-	-	0.29	2.13	-	-	-	-	-
Na_2O	-	3.68	-	-	2.8	3.86	-	-	-	-	-
K_2O	-	5.04	-	-	5.41	4.61	-	-	-	-	-
Cr_2O_3	-	<0.01	-	-	<0.01	0.01	-	-	-	-	-
TiO_2	-	0.18	-	-	0.19	0.59	-	-	-	-	-
MnO	-	0.02	-	-	0.03	0.12	-	-	-	-	-
P_2O_5	-	0.03	-	-	0.04	0.17	-	-	-	-	-
SrO	-	0.01	-	-	0.01	0.01	-	-	-	-	-
BaO	-	0.02	-	-	0.02	0.02	-	-	-	-	-
LOI	-	0.42	-	-	1.58	0.53	-	-	-	-	-
Total	-	101.02	-	-	101.76	100.87	-	-	-	-	-
Elements (ppm)											
Ba	32.6	172.5	135	149.5	156	177.5	33.1	390	136.5	13.9	262
Ce	149.5	200	174.5	157	136.5	113.5	3	128	170	21.7	75
Cr	10	10	10	10	10	70	10	10	10	10	50
Cs	3.34	3.04	6.76	6.53	4.51	2.12	0.91	7.61	5.14	0.83	27
Dy	8.23	8.34	9.13	8.8	7.28	13.05	0.48	6.88	6.9	5.74	3.82
Er	5.23	4.77	5.39	5	4.15	7.04	0.23	3.74	4.06	2.99	2.08
Eu	0.18	0.59	0.48	0.51	0.53	1.23	<0.03	1.61	0.49	0.39	1.76
Ga	22.7	23.4	24.4	23.8	21.3	26	1.4	21.5	21	1.2	17.4
Gd	7.27	9.22	8.69	9.29	7.54	14.65	0.4	7.73	7.71	4.85	4.96
Hf	8.8	7	10.1	6.4	7.1	8.2	<0.2	11.7	8	0.2	3.9
Ho	1.69	1.65	1.75	1.73	1.43	2.54	0.07	1.35	1.4	1.1	0.72
La	80.9	108.5	95	84	70.4	61.4	1.5	66.8	90.9	9.1	38.2
Lu	0.87	0.63	0.72	0.63	0.6	0.77	0.02	0.54	0.58	0.36	0.29
Nb	70.5	62.4	79.1	73.7	63.1	81.3	1.7	62.2	56.4	2.4	32.7
Nd	47.3	64.4	56.4	53.8	45.7	62.3	1.1	49.3	57.1	10.1	30.9
Pr	14.7	20.3	16.95	15.85	13.7	16	0.31	13.25	16.9	2.48	8.28
Rb	282	226	272	212	233	118.5	7.1	203	221	7.2	149
Sm	8.77	12.2	10.5	10.15	9.12	15.25	0.31	8.81	9.78	3.43	5.67
Sn	7	5	5	6	17	4	1	7	12	2	3
Sr	14.1	42.2	38.9	41.2	59.6	31.8	16	207	33	127.5	345
Ta	7	5.2	6.6	4.2	5.7	6	0.4	3.9	5	0.2	1.8
Tb	1.31	1.46	1.53	1.56	1.2	2.32	0.06	1.18	1.28	0.94	0.72
Th	44	38.2	37.3	31.2	27.6	14.4	0.52	19.6	31.3	1.98	4.43
Tm	0.79	0.69	0.74	0.69	0.65	0.98	0.02	0.54	0.55	0.41	0.28
U	13.55	7.41	10.25	13.3	7.5	4.35	0.6	5.41	7.56	1.28	2.77
V	7	<5	9	13	6	86	<5	40	10	13	184
W	851	526	125	395	439	279	885	150	582	19	28
Y	50.7	47	50	47	41.7	74.6	2.7	36.8	40.2	36.4	20.9
Yb	5.7	4.63	4.93	4.42	4.21	5.74	0.2	3.53	4	2.63	1.91
Zr	224	220	329	232	237	255	4	492	255	7	160

Oxide (%)	LHR63	LHR65	LHR66A	LHR66B	LHR69	LHR70	LHR71A	LHR72	LHR73	LHR76	LHR77	LHR78
SiO_2	-	55.4	-	-	-	-	-	-	-	-	-	73
Al_2O_3	-	16.25	-	-	-	-	-	-	-	-	-	12.9
Fe_2O_3	-	8.09	-	-	-	-	-	-	-	-	-	2.09
CaO	-	3.21	-	-	-	-	-	-	-	-	-	0.6
MgO	-	4.28	-	-	-	-	-	-	-	-	-	0.23
Na_2O	-	2.89	-	-	-	-	-	-	-	-	-	3.6
K_2O	-	4.77	-	-	-	-	-	-	-	-	-	4.95
Cr_2O_3	-	0.02	-	-	-	-	-	-	-	-	-	<0.01
TiO_2	-	1.72	-	-	-	-	-	-	-	-	-	0.25
MnO	-	0.1	-	-	-	-	-	-	-	-	-	0.03
P_2O_5	-	1.03	-	-	-	-	-	-	-	-	-	0.03
SrO	-	0.03	-	-	-	-	-	-	-	-	-	0.01
BaO	-	0.04	-	-	-	-	-	-	-	-	-	0.02
LOI	-	0.95	-	-	-	-	-	-	-	-	-	0.64
Total	-	98.78	-	-	-	-	-	-	-	-	-	98.35
Elements (ppm)												
Ba	161.5	368	343	339	510	106	661	624	124.5	37.8	20.6	168
Ce	168.5	217	117	158	137.5	184.5	130.5	127	150	32.2	63.8	207
Cr	10	110	40	20	20	10	20	20	<10	10	<10	<10
Cs	9.22	35	11.3	11.05	8.4	5.61	6.05	5.25	4.14	1.69	7.93	3.86
Dy	10.4	12.95	7.09	8.55	7.92	9.15	7.55	7.21	8.03	8.93	2.13	7.96
Er	6.24	6.63	3.89	4.83	4.13	5.39	4.16	3.81	4.65	4.78	1.25	4.52
Eu	0.55	1.43	1.68	1.04	2.33	0.51	2.16	2.16	0.42	0.04	0.2	0.64
Ga	22.8	28.6	25.4	25.7	25.6	24.7	23.5	22.7	22.1	11.7	10.1	22.3
Gd	10.25	15.6	7.71	8.77	9.81	9.42	8.78	8.69	8.02	8.46	2.61	9.46
Hf	8.9	21.8	8	9.8	11.3	10.9	10.8	11	9.3	3.5	1.8	10.1
Ho	2.1	2.41	1.37	1.6	1.53	1.87	1.39	1.42	1.58	1.64	0.39	1.6
La	89.4	105	61.4	82.4	69.2	98	66.5	65.9	81.8	6.8	31.8	111
Lu	0.85	0.83	0.47	0.71	0.53	0.76	0.55	0.52	0.65	0.54	0.15	0.62
Nb	87.5	51	68.9	80.5	67.6	90	61.5	60.1	78.3	11.7	13.6	66.5
Nd	58.3	85.2	43.8	55.9	56	60	52.7	51.2	49.3	26.4	23.8	67.2
Pr	16.75	23.2	12	16.1	14.6	18.15	13.8	13.75	14.4	5.52	6.72	20
Rb	263	393	169	221	190.5	289	162	167	245	168.5	96.2	204
Sm	11.55	18.2	8.33	10	11.1	11	9.67	9.95	9.03	9.03	4.12	12
Sn	44	19	5	14	6	4	7	6	3	1	1	5
Sr	42.6	233	252	151.5	227	77	211	218	97	5.4	101	42
Ta	6.2	6	4.5	5.8	4.1	6.9	3.9	3.9	5.8	2	1.2	5.2
Tb	1.8	2.33	1.24	1.51	1.54	1.59	1.34	1.32	1.41	1.54	0.37	1.45
Th	51.5	78.5	17.75	30.1	16.65	38.1	17.6	18.15	32.2	28.1	11	31.5
Tm	0.87	0.91	0.51	0.64	0.5	0.75	0.56	0.52	0.68	0.63	0.15	0.68
U	12.45	16.25	5.27	8.07	5.35	8.75	5.29	5.94	7.09	6.22	6.02	7.5
V	9	257	142	67	83	10	58	59	10	6	8	6
W	610	118	96	265	89	307	165	266	203	1070	554	456
Y	57.7	69.6	38.9	45.1	41.6	53.7	39.2	37.9	47.9	38.5	11.4	45.9
Yb	5.68	5.72	3.25	4.43	3.57	5.11	3.58	3.45	4.49	3.95	1.1	4.28
Zr	297	696	306	344	469	373	471	462	315	55	53	355

Oxide (%)	EHR79	EHR80A	EHR80B	EHR80C	EHR81A	EHR81B	EHR81C	EHR81D	EHR81F	EHR81H	EHR81I	EHR82
SiO_2	72.3	-	44.5	-	-	78	73.1	78.6	-	75.7	-	-
Al_2O_3	13.85	-	15.2	-	-	12.75	14.95	9.01	-	12.1	-	-
Fe_2O_3	2.81	-	11.7	-	-	2.96	2.91	1.62	-	2.34	-	-
CaO	0.62	-	4.57	-	-	0.1	0.11	2.59	-	0.07	-	-
MgO	0.16	-	3.36	-	-	0.27	0.31	1.14	-	0.07	-	-
Na_2O	3.84	-	0.11	-	-	0.02	0.04	0.02	-	4.13	-	-
K_2O	5.64	-	2.08	-	-	3.68	4.22	2.55	-	4.72	-	-
Cr_2O_3	<0.01	-	0.04	-	-	<0.01	<0.01	<0.01	-	<0.01	-	-
TiO_2	0.28	-	2.11	-	-	0.18	0.2	0.14	-	0.16	-	-
MnO	0.06	-	0.14	-	-	0.07	0.07	0.1	-	0.07	-	-
P_2O_5	0.04	-	0.28	-	-	0.01	0.01	0.02	-	<0.01	-	-
SrO	0.01	-	0.01	-	-	<0.01	<0.01	<0.01	-	<0.01	-	-
BaO	0.02	-	0.03	-	-	<0.01	0.01	<0.01	-	<0.01	-	-
LOI	0.66	-	14.73	-	-	2.86	3.51	5.09	-	0.97	-	-
Total	100.29	-	98.86	-	-	100.9	99.44	100.88	-	100.33	-	-
Elements (ppm)												
Ba	199	43.3	238	14.8	34.8	43.2	67	42.1	38.9	27.8	49.5	459
Ce	233	222	37.3	31	237	256	274	199	275	214	220	62.8
Cr	10	10	310	10	<10	<10	10	10	<10	10	<10	<10
Cs	6.78	12.15	98.1	1.46	3.25	10.1	12.4	6.94	9.53	2.32	4.5	2.24
Dy	12.55	7.44	4.53	3.42	11.95	13.55	18.7	9.47	14.05	12.25	8.67	3.52
Er	6.39	3.89	2.42	1.74	6.8	8.14	10.7	5.53	7.83	7.27	5.02	2.25
Eu	0.79	0.38	1.83	0.23	0.35	0.4	0.49	0.3	0.36	0.4	0.3	1.27
Ga	27.8	28.5	19.9	3.2	30.2	37	37.9	21	30.2	32.9	23.1	20.1
Gd	14.1	9.05	5.11	3.05	12.7	14.2	18.4	10.45	14.5	12.9	10.95	3.19
Hf	14.2	9.2	3.4	1.3	15.2	16.1	18.5	13.5	15.9	17.7	11.2	10.8
Ho	2.48	1.36	0.88	0.65	2.26	2.71	3.69	1.89	2.74	2.49	1.7	0.72
La	121.5	120.5	17.7	16.3	126.5	135	144.5	105	144.5	111.5	117.5	34.4
Lu	0.85	0.6	0.26	0.24	0.99	1.12	1.4	0.79	1.06	0.97	0.77	0.39
Nb	91.8	67.4	27.3	9.4	131	149.5	149	108.5	154.5	122	109.5	91.9
Nd	80	75.1	18.6	11.6	84.8	88.5	96.9	66.5	93.7	72.4	76.3	20.9
Pr	24	22	4.58	3.18	23.9	26.2	28.4	19.75	27.3	21.7	21.9	6.06
Rb	230	163	183.5	20.1	210	190	222	136	171	216	188	170
Sm	16.2	12	5.01	2.7	15.2	17.1	19.95	12.9	17.35	14.75	13.7	3.58
Sn	6	5	2	1	10	14	14	7	11	9	5	8
Sr	32.2	89.9	105	101.5	8.7	10	11.3	34	10.3	17	15.3	136.5
Ta	4.9	4	1.8	0.5	8.9	10.2	11.2	7.8	9.4	8.5	6.7	6.8
Tb	2.16	1.35	0.81	0.54	2.02	2.28	3.08	1.67	2.43	2	1.63	0.57
Th	24.1	15.25	2.07	2.4	26.1	27.3	34.9	26.1	32.3	29.8	24	19.75
Tm	0.97	0.52	0.34	0.21	0.94	1.19	1.56	0.84	1.13	1.09	0.71	0.34
U	5.75	8.52	0.86	0.72	9.19	11.9	12.15	6.41	10.4	8.46	4.9	3.64
V	7	7	301	19	<5	7	12	<5	5	<5	5	11
W	477	229	30	146	453	383	193	282	363	585	374	315
Y	65.3	37.6	23.2	18.8	65.8	75.9	108.5	54.4	76.5	70.4	45.7	22.1
Yb	5.84	3.67	1.9	1.61	6.26	7.49	10.1	5.27	7.24	6.67	4.66	2.46
Zr	514	446	128	66	656	665	748	490	641	651	510	551

F Full LA-ICP-MS Result

1 Zircon Analysis

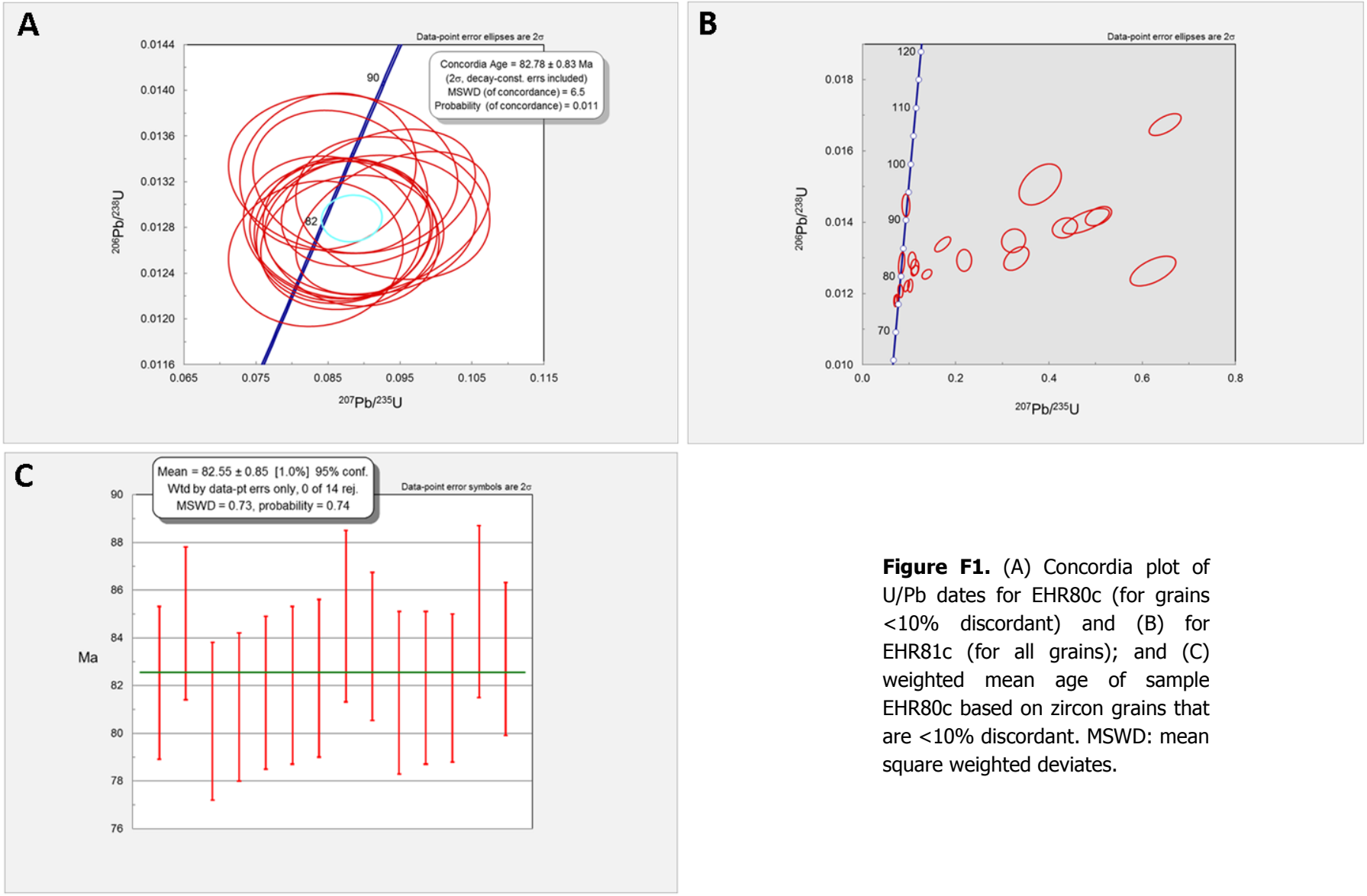

Figure F1. (A) Concordia plot of U/Pb dates for EHR80c (for grains <10% discordant) and (B) for EHR81c (for all grains); and (C) weighted mean age of sample EHR80c based on zircon grains that are <10% discordant. MSWD: mean square weighted deviates.

Sample	EHR80c 1	EHR80c 2	EHR80c 4	EHR80c 5	EHR80c 6	EHR80c 7	EHR80c 9	EHR80c 11	EHR80c 14	EHR80c 15	EHR80c 16	EHR80c 17
Final Age $^{206}Pb/^{238}U$	82.1	84.6	80.5	81.1	81.7	-	-	87.7	82	-	82.3	-
Final Age $^{206}Pb/^{238}U$ (2 SE)	3.2	3.2	3.3	3.1	3.2	-	-	3.7	3.3	-	3.3	-
% Discordant	6.8	-0.4	1.6	5.0	3.7	12.5	19.4	5.7	1.4	20.4	9.6	18.0
Elements (ppm)												
P	730	660	494	1,540	659	520	761	527	412	607	539	336
P (2 SE)	100	39	42	800	40	45	57	37	30	42	36	32
Ti	11.2	7.6	9.8	10.8	9.8	16.6	6.1	10.1	10.5	11.1	7.1	7.1
Ti (2 SE)	2.2	1.8	1.9	2.3	2.1	8.1	2	2	2.4	2.3	1.8	1.9
Y	7,190	7,580	8,660	11,400	11,300	4,260	12,200	6,950	6,370	8,820	9,840	4,410
Y (2 SE)	520	390	360	1,400	470	490	1,500	670	250	320	260	290
Zr	1,239,000	1,289,000	1,252,000	1,321,000	1,193,000	1,290,000	1,500,000	1,250,000	1,260,000	1,258,000	1,260,000	898,000
Zr (2 SE)	62,000	70,000	55,000	74,000	57,000	140,000	220,000	130,000	36,000	42,000	31,000	31,000
La	0.09	0.0001	0.02	0.32	0.11	0.45	0.78	0.08	0.05	0.06	0.03	0.19
La (2 SE)	0.04	1	0.02	0.21	0.04	0.38	0.15	0.04	0.03	0.03	0.02	0.06
Ce	117.1	138.7	63.3	106.8	83.3	87	88	74.9	84.8	186	87.1	58.8
Ce (2 SE)	7.1	7.2	3.4	7.3	4.6	11	14	8.9	3.8	6.7	4.8	3.7
Sm	36.1	27.6	40.8	64	50.6	19.5	54.3	31.7	28.1	43	41.6	19.1
Sm (2 SE)	4.1	2.2	2.4	21	3.6	2.7	8.6	4.1	1.7	2.6	2	1.7
Eu	1.97	0.85	1.13	3.3	1.78	0.56	1.91	1.04	0.98	1.62	1.22	0.69
Eu (2 SE)	0.39	0.14	0.2	1.9	0.25	0.14	0.38	0.2	0.18	0.26	0.21	0.15
Dy	735	729	865	1,200	1,166	410	1,210	701	617	950	973	436
Dy (2 SE)	58	37	41	220	74	49	140	67	24	35	27	25
Lu	256	269	322	404	429	182	456	284	243	294.9	366	183.2
Lu (2 SE)	17	12	14	28	23	20	51	25	9.9	9.6	11	8.2
Hf	16,570	22,270	22,200	22,900	21,270	21,400	24,700	22,200	18,390	16,560	21,620	14,710
Hf (2 SE)	780	900	890	1,100	990	2,000	2,600	2,000	570	580	560	430
^{206}Pb	63.7	123.2	74.1	113.7	106.3	73.2	105.3	82	62.1	151.6	87.7	47.9
^{206}Pb (2 SE)	2.5	6	2.4	4.2	3.7	6.6	6.1	4.1	2.2	5.8	3.3	3.6
^{207}Pb	3.56	6.46	3.81	6.26	5.56	4.2	6.78	4.61	3.24	10	5.06	2.88
^{207}Pb (2 SE)	0.36	0.46	0.24	0.43	0.3	0.39	0.63	0.41	0.23	1.3	0.38	0.33
^{208}Pb	4.29	8.31	5.25	9.59	8.07	6.53	10.3	5.99	3.79	16.8	6.14	4.02
^{208}Pb (2 SE)	0.36	0.51	0.36	0.6	0.44	0.88	1.4	0.61	0.19	1.4	0.37	0.36
^{232}Th	478	1,004	642	1,279	953	760	1,120	627	481	1,874	732	405
^{232}Th (2 SE)	37	60	32	81	55	110	170	67	14	78	18	29
^{235}U	3,360	6,610	4,050	6,790	5,620	3,950	6,190	4,240	3,360	8,210	4,780	2,780
^{235}U (2 SE)	210	340	200	370	310	460	690	400	110	300	110	170
^{238}U	1,105	2,171	1,347	2,155	1,885	1,250	1,962	1,342	1,114	2,718	1,573	911
^{238}U (2 SE)	52	68	34	63	75	110	85	54	24	69	28	55
Ti temperature (°C)	771	736	759	768	759	809	718	762	765	771	731	731

Sample	EHR80c 18	EHR80c 19	EHR80c 20	EHR80c 21	EHR80c 22	EHR80c 23	EHR80c 24	EHR80c 25	EHR80c 26	EHR80c 27	EHR80c 28	EHR80c 29	EHR80c 30
Final Age $^{206}Pb/^{238}U$	84.9	83.64	-	81.7	81.9	81.9	85.1	93.9	-	-	83.1	-	-
Final Age $^{206}Pb/^{238}U$ (2 SE)	3.6	3.1	-	3.4	3.2	3.1	3.6	4.2	-	-	3.2	-	-
% Discordant	-0.5	6.1	13.1	4.7	3.1	4.7	-3.0	6.6	28.0	28.6	8.7	42.1	23.7
Elements (ppm)													
P	449	396	1,097	451	373	399	526	580	2,130	2,690	533	1,080	654
P (2 SE)	43	30	89	29	34	30	31	57	240	250	27	88	47
Ti	11.5	9.5	7.0	7.8	5	6.4	8.9	10	400	9.7	7.1	10.9	15.7
Ti (2 SE)	2.6	2	1.7	2	1.6	1.4	1.7	2.7	230	2.5	1.4	2.2	2.1
Y	5,400	6,720	11,550	9,510	10,060	11,010	7,050	7,610	17,100	13,800	11,490	9,000	10,020
Y (2 SE)	360	160	350	340	390	530	330	430	1,200	1,400	520	1,100	420
Zr	1,279,000	1,273,000	1,261,000	1,280,000	1,275,000	1,296,000	1,307,000	1,383,000	1,220,000	1,311,000	1,347,000	1,320,000	1,300,000
Zr (2 SE)	91,000	32,000	36,000	57,000	59,000	64,000	64,000	65,000	57,000	68,000	65,000	160,000	64,000
La	0.0001	0.02	0.15	0.07	0.04	0.07	0.19	1.60	3.50	1.32	1.77	0.28	7
La (2 SE)	1.00	0.01	0.05	0.04	0.03	0.03	0.06	2.00	2.10	0.28	0.24	0.08	4.1
Ce	86.6	94.7	137	110.6	60.5	82.3	70.8	72.5	88.3	106.7	72.3	133	150
Ce (2 SE)	6.7	3.3	5	8.4	3.5	4.7	4.6	8.9	6.2	7.9	3.6	19	15
Sm	23	30.4	46.9	52.2	54.3	58.6	29.7	42.7	134	153	39.2	52.2	58.60
Sm (2 SE)	2.4	1.8	2.8	3.5	3.8	4.2	2.4	5	16	24	3.1	7.1	3.60
Eu	0.77	1.26	2.16	2.09	2.3	1.84	1.18	1.55	10.6	14.1	1.38	2.62	2.94
Eu (2 SE)	0.2	0.17	0.34	0.21	0.22	0.24	0.2	0.39	1.80	2.60	0.18	0.4	0.31
Dy	537	668	1,140	1,024	1,108	1,173	694	780	2,000	1,640	1,146	1,020	1,084
Dy (2 SE)	36	21	35	49	64	64	37	52	180	190	59	120	48
Lu	214	244.6	412	334	360	387	285	307	477	379	428	340	370
Lu (2 SE)	14	7.6	12	14	19	19	13	21	22	23	20	34	13
Hf	19,300	17,610	22,270	16,820	16,500	17,040	21,250	22,100	21,480	22,800	23,400	21,900	16,360
Hf (2 SE)	1,200	520	600	740	790	880	980	1,000	800	1,100	1,000	1,900	580
^{206}Pb	62.2	67.9	145.6	82.7	72.5	77	78.1	79.2	124	101.7	99	113	90.8
^{206}Pb (2 SE)	3	1.6	4.3	3.4	2.50	2.60	3	5.8	3.80	3.30	3.00	10	2.50
^{207}Pb	3.11	3.81	8.54	4.34	3.63	4.04	3.72	4.2	8.34	7.05	5.48	11	6.17
^{207}Pb (2 SE)	0.32	0.3	0.35	0.28	0.25	0.34	0.27	0.43	0.68	0.51	0.35	1.3	0.33
^{208}Pb	4.26	4.40	10.95	6.08	4.54	5.54	5.22	5.39	12.00	8.71	6.7	15.1	8.23
^{208}Pb (2 SE)	0.33	0.21	0.45	0.41	0.26	0.31	0.34	0.49	0.89	0.57	0.34	2.30	0.44
^{232}Th	486	527	1,099	738	566	650	567	595	1,226	852	745	1,190	1,053
^{232}Th (2 SE)	35	22	41	54	30	36	35	58	70	61	40	180	59
^{235}U	3,140	3,600	7,680	4,430	3,820	4,190	4,000	3,710	6,970	5,390	5,270	6,150	6,120
^{235}U (2 SE)	230	130	240	270	200	200	220	310	290	330	320	690	260
^{238}U	1,017	1,186	2,527	1,418	1,240	1,352	1,293	1,171	2,217	1,757	1,678	1,950	1,959
^{238}U (2 SE)	40	31	65	67	38	31	34	67	51	92	63	160	51
Ti temperature (°C)	774	756	729	739	701	722	750	761	1,261	758	731	769	804

Samples	EHR81c 1	EHR81c 2	EHR81c 4	EHR81c 5	EHR81c 6	EHR81c 8	EHR81c 11	EHR81c 12	EHR81c 13	EHR81c 17
Final Age $^{206}Pb/^{238}U$	-	-	-	-	76	76	-	-	-	-
Final Age $^{206}Pb/^{238}U$ (2 SE)	-	-	-	-	1	1	-	-	-	-
% Discordant	-141	-229	-360	-24	6	8	-248	-87	-506	-63
Elements (ppm)										
P	706	6,560	705	395	777	5,560	12,860	1,740	3,930	2,517
P (2 SE)	30	600	32	18	21	130	670	79	190	67
Ti	14.1	46.4	21.8	7.7	12.5	4.1	18.6	43	30	26.2
Ti (2 SE)	2.2	6.2	2.2	1.3	1.5	1.2	5.3	10	3.7	2.8
Y	7,980	25,100	7,370	9,620	16,050	66,800	50,600	18,600	25,700	37,500
Y (2 SE)	620	2,000	180	400	420	2,100	3,200	380	1,000	1,300
Zr	1,187,000	1,175,000	1,029,000	1,224,000	1,192,000	1,131,000	1,196,000	1,107,000	1,031,000	1,087,000
Zr (2 SE)	71,000	50,000	27,000	31,000	25,000	35,000	33,000	24,000	29,000	30,000
La	11	1.93	3.42	0.201	0.039	0.138	35	5.13	222	101
La (2 SE)	12	0.61	0.22	0.053	0.019	0.041	12	0.29	91	35
Ce	134	103.7	116.7	69.4	416	588	180	97.9	580	1003
Ce (2 SE)	10	5.8	3.7	3.2	10	20	23	2.6	220	79
Sm	40.3	230	37	43	75.7	346	378	17.9	134	213
Sm (2 SE)	3.7	16	1.9	3	2.8	15	36	1.4	34	13
Eu	1.91	14.7	1.86	1.78	3.06	14.51	33.8	1.36	6.4	8.8
Eu (2 SE)	0.27	1.1	0.22	0.19	0.25	0.77	2.5	0.21	1.2	0.68
Dy	856	2,940	789	1,004	1,706	9,160	5,410	1,167	1,990	4,490
Dy (2 SE)	70	200	20	51	45	360	540	31	100	180
Lu	306	461	326.6	336	439.4	1,248	772	371.9	459	779
Lu (2 SE)	25	30	8.6	15	9.6	46	39	7.9	14	26
Hf	17,110	17,230	13,880	15,720	16,130	15,500	25,990	25,210	29,410	15,230
Hf (2 SE)	920	790	380	430	350	490	670	430	870	410
^{206}Pb	110.1	98.7	120.6	69.2	327.9	722	372.7	367.8	102.5	828
^{206}Pb (2 SE)	3.3	3.6	2.3	1.9	5.4	13	8.9	5.5	3	15
^{207}Pb	15.02	19.65	36.8	4.93	17.67	38.2	73.7	37.1	40.2	67.7
^{207}Pb (2 SE)	0.74	0.94	1.2	0.28	0.55	1	5.5	2.8	2.8	3.3
^{208}Pb	20.66	26	40.1	5.54	43.58	62.8	137.2	70.5	124.6	124.3
^{208}Pb (2 SE)	0.99	1.4	1.2	0.23	0.79	1.6	9.6	4.3	8.5	4.3
^{232}Th	1,336	1,392	1,010	586	5,970	8,620	13,600	6,760	14,400	14,700
^{232}Th (2 SE)	71	70	27	23	110	290	1,400	240	2,200	680
^{235}U	6,180	5,320	6,230	4,000	19,080	41,600	19,670	19,150	6,030	46,000
^{235}U (2 SE)	310	280	190	160	400	1,200	590	350	250	1,600
^{238}U	2,049	1,787	2,085	1,326	6,860	14,890	7,200	6,750	1,971	16,310
^{238}U (2 SE)	75	54	51	44	110	360	210	140	49	460
Ti temperature (°C)	793	923	837	738	782	685	821	914	872	857

Samples	EHR81c 20	EHR81c 21	EHR81c 22	EHR81c 23	EHR81c 24	EHR81c 25	EHR81c 26	EHR81c 27	EHR81c 29
Final Age $^{206}Pb/^{238}U$	-	-	93	-	77	82	-	-	-
Final Age $^{206}Pb/^{238}U$ (2 SE)	-	-	2	-	1	2	-	-	-
% Discordant	-33	-33	3	-26	-3	1	-377	-348	-17
Elements (ppm)									
P	1,780	1,234	488	896	1,220	401	1,136	1,807	2,816
P (2 SE)	190	99	35	37	170	23	32	85	54
Ti	11.3	18.5	8.3	8.2	6.6	7.8	18.2	34	19.1
Ti (2 SE)	2.1	2.5	1.8	1.7	1.7	1.6	2.9	8.9	2.2
Y	8,430	18,570	9,350	22,580	21,200	8,510	20,430	15,570	41,500
Y (2 SE)	850	460	230	560	1,200	430	500	270	1,200
Zr	1,217,000	1,196,000	1,146,000	1,180,000	1,223,000	1,238,000	1,236,000	1,088,000	1,137,000
Zr (2 SE)	22,000	23,000	18,000	28,000	39,000	35,000	23,000	23,000	32,000
La	0.98	58	1.54	0.893	0.82	50	7.87	25.1	1.91
La (2 SE)	0.16	28	0.42	0.099	0.25	18	0.5	9.6	0.75
Ce	104	331	85.7	297.3	245.2	250	506	87	618
Ce (2 SE)	2	73	2.3	9.4	9.8	49	13	23	19
Sm	68	118	50.8	114.9	96.4	66.3	97.4	24.6	205.8
Sm (2 SE)	12	15	2.4	3.7	7.8	9.4	4.8	3.4	8.1
Eu	4.32	4.34	1.95	4.49	4.6	1.85	3.89	1.19	8.59
Eu (2 SE)	0.97	0.55	0.27	0.33	0.64	0.27	0.32	0.27	0.47
Dy	1,040	2,149	974	2,451	2,300	888	2,237	844	4,920
Dy (2 SE)	140	71	23	70	150	48	54	32	150
Lu	224.2	532	315.9	707	625	283	609	393	747
Lu (2 SE)	9.1	14	6.6	17	27	12	16	11	23
Hf	16,030	15,410	14,540	16,010	16,330	16,240	16,390	45,320	16,850
Hf (2 SE)	340	280	250	390	420	520	450	770	470
^{206}Pb	70.3	222.2	77.1	210.1	206.9	71.8	454	94.6	766
^{206}Pb (2 SE)	1.4	6.1	3.6	3.1	5	1.9	10	4.2	13
^{207}Pb	4.59	16.08	4.22	14.51	11.73	3.98	154	28.3	51.2
^{207}Pb (2 SE)	0.24	0.84	0.34	0.36	0.53	0.25	5	2.8	2.5
^{208}Pb	6.23	21.36	5.93	23.28	15.2	6.17	176.2	60.8	115.9
^{208}Pb (2 SE)	0.25	0.76	0.43	0.55	0.51	0.32	6.2	3.5	4.5
^{232}Th	787	2,290	602	2,669	1,883	772	5,650	6,030	14,820
^{232}Th (2 SE)	25	130	30	93	58	37	270	480	430
^{235}U	4,260	12,170	3,890	11,970	11,850	4,390	19,650	4,990	44,300
^{235}U (2 SE)	140	460	190	320	450	210	770	200	1,100
^{238}U	1,394	4,280	1,285	4,260	4,190	1,422	7,020	1,636	15,460
^{238}U (2 SE)	26	160	62	110	120	51	260	55	310
Ti temperature (°C)	772	820	744	743	724	739	819	886	824

2 Bastnäsite Analysis

Oxide (wt%)	Spot-1	Spot-2	Spot-3	Spot-4	Spot-5	Spot-6	Spot-7	Spot-8	Spot-9	Spot-10
Ce_2O_3	32.09	31.66	31.39	31.77	26.58	31.26	32.03	31.86	30.32	30.58
La_2O_3	17.33	20.40	20.37	18.21	15.49	15.67	16.81	17.91	17.03	16.55
Nd_2O_3	10.44	9.79	9.78	10.18	8.14	11.44	11.14	10.82	10.14	11.14
Pr_2O_3	3.27	3.24	3.09	3.29	2.58	3.37	3.33	3.28	3.04	3.23
CaO	2.10	1.71	1.75	2.04	1.34	1.94	1.91	2.13	2.62	2.15
Sm_2O_3	1.51	1.24	1.24	1.50	0.95	2.10	1.91	1.60	1.46	2.09
Gd_2O_3	0.98	0.67	0.72	0.87	0.58	1.36	1.24	0.89	0.84	1.16
Y_2O_3	0.84	0.59	0.60	0.66	0.44	1.74	1.08	0.57	0.80	0.80
ThO_2	1.47	0.93	1.03	1.17	0.96	1.18	0.99	1.16	2.19	2.31
FeO	0.45	0.50	0.66	0.80	11.25	0.44	0.15	0.45	1.82	0.54
SrO	0.13	0.06	0.08	0.10	0.07	0.11	0.11	0.09	0.18	0.21
MgO	0.09	0.06	0.10	0.13	0.70	0.03	0.02	0.03	0.20	0.19
LOI	29.30	29.14	29.18	29.28	30.93	29.36	29.26	29.20	29.35	29.04
Total	100	100	100	100	100.00	100	100	100	100	100
Element (ppm)										
Ce	273,937.38	270,268.52	268,012.40	271,267.79	226,940.97	266,907.40	273,444.41	271,966.03	258,874.89	261,053.40
La	147,762.69	173,968.74	173,705.23	155,237.63	132,120.63	133,575.40	143,347.74	152,705.22	145,183.71	141,127.27
Nd	89,535.86	83,931.37	83,835.67	87,296.09	69,807.28	98,102.68	95,536.55	92,801.87	86,973.59	95,528.14
Pr	27,963.58	27,693.78	26,437.56	28,112.26	22,059.05	28,790.48	28,422.23	28,035.63	25,976.77	27,633.01
Sm	13,026.45	10,725.76	10,668.62	12,957.62	8,157.62	18,088.68	16,495.31	13,791.89	12,602.91	18,048.34
Gd	8,471.00	5,824.60	6,234.40	7,560.62	5,027.29	11,831.18	10,790.54	7,714.04	7,295.35	10,106.49
Th	12,931.07	8,161.18	9,026.94	10,260.97	8,393.02	10,353.10	8,737.25	10,190.72	19,215.57	20,277.37
Y	6,584.43	4,658.37	4,756.38	5,206.09	3,436.03	13,718.80	8,505.01	4,519.40	6,307.52	6,296.43
Dy	2,145.57	1,432.76	1,432.29	1,603.36	1,076.54	3,929.96	2,941.40	1,623.75	1,874.10	2,240.01
K	15,145.18	11,119.67	17,324.07	26,087.12	187,681.31	3,995.32	2,371.29	6,851.54	36,142.66	31,608.40
Ga	1,390.54	1,474.66	1,229.15	1,215.31	1,275.08	1,679.61	1,969.50	1,580.90	1,176.19	1,381.82
Sr	1,112.93	519.37	657.23	859.41	560.60	962.85	958.28	780.52	1,550.42	1,797.07
Tb	667.41	429.65	446.71	535.54	351.47	1,088.83	898.31	578.66	575.54	766.25
Er	331.81	258.98	249.82	260.91	206.95	879.28	364.65	227.31	279.44	277.43
Nb	654.45	432.49	588.89	729.75	1,400.28	301.00	362.90	216.37	265.28	219.01
Ti	3,905.72	2,771.83	3,651.13	4,539.05	8,732.54	1,526.28	337.60	1,061.11	1,107.05	705.30
Eu	217.79	148.94	157.95	214.16	133.78	325.04	289.07	213.10	207.67	293.17
Ho	217.44	153.15	156.99	166.32	121.32	466.05	271.46	150.43	197.31	205.79
U	191.02	142.01	158.33	187.27	229.25	421.09	199.82	182.76	99.44	712.62
Pb	321.45	196.59	238.74	310.86	724.05	213.48	159.74	169.45	469.38	2,049.31
P	242.41	145.74	109.68	391.54	782.33	1,283.55	113.00	84.91	507.94	8,886.69
Yb	153.01	167.83	149.09	178.46	181.98	826.85	88.12	124.48	104.64	101.63
Mn	130.64	162.33	203.08	80.98	162.13	31.93	35.63	75.84	154.27	37.55
Tm	29.20	25.90	24.64	25.65	29.20	104.47	23.31	20.48	21.94	20.11
Ba	44.25	24.01	34.13	45.66	197.35	24.26	18.64	30.74	135.35	67.61
Zn	53.40	39.00	46.11	64.68	528.79	62.67	13.01	28.25	134.44	79.99
Rb	79.51	64.40	102.03	145.71	1,143.59	22.93	12.88	33.49	177.42	154.09
Ta	53.24	35.32	51.84	61.12	122.90	33.97	10.91	15.76	17.08	12.45
Lu	19.94	25.58	22.97	29.84	31.95	138.86	7.79	19.69	11.68	10.76
Zr	2,324.69	3,568.22	3,149.02	3,734.97	3,823.09	16,122.72	3.15	1,765.78	355.89	139.75
Cs	4.31	2.66	6.01	5.94	42.42	2.00	0.81	2.37	12.90	7.74
Cu	1.99	1.40	2.05	2.40	21.66	0.49	0.79	0.49	4.02	4.70
V	12.18	14.52	17.09	24.75	187.93	2.84	0.74	3.33	4.16	4.31
Hf	90.51	133.85	101.56	144.26	207.05	722.43	0.74	68.51	14.75	5.38
Co	bdl	bdl	0.08	0.05	0.18	0.06	0.04	bdl	1.21	0.42
Sc	2.36	4.19	3.72	4.85	9.28	14.41	bdl	1.94	0.49	0.58
Ni	bdl	bdl	0.50	bdl	bdl	0.39	bdl	bdl	0.79	0.79

G Representative SEM-EDS Analytical Results

Table G1. The average, maximum and minimum concentrations of each element present (as oxide %) within the different rare earth minerals.

	Bastnäsite-(Ce)			**Bastnäsite-Parisite**			**Bastnäsite-TiO_2**			**Loparite-(Ce)**			**Synchysite-(Ce)**			**Florencite-(Ce)**		
	Wt% oxides			Wt% oxides			Wt% oxides			Wt% oxides			Wt% oxides			Wt% oxides		
	Average	Maximum	Minimum	Average	Maximum	Minimum	Average	Maximum	Minimum	Average	Maximum	Minimum	Average	Maximum	Minimum	Average	Maximum	Minimum
Ce_2O_3	53.3	54.5	52.5	42.7	53.8	32.2	33.9	48.4	20.2	30.9	37.0	16.2	22.1	28.1	14.4	12.8	15.1	10.8
La_2O_3	27.1	29.2	25.0	21.5	29.1	13.0	18.8	27.5	11.0	16.2	20.1	7.8	9.1	11.4	4.6	6.0	6.5	5.3
Nd_2O_3	13.3	15.3	10.3	13.2	20.2	8.4	9.9	15.0	4.7	9.7	11.1	5.4	12.4	16.8	7.8	0.9	3.7	0.0
Pr_2O_3	-	-	-	0.3	5.0	0.0	-	-	-	-	-	-	-	-	-	-	-	-
Sm_2O_3	-	-	-	0.1	2.3	0.0	-	-	-	-	-	-	-	-	-	-	-	-
Gd_2O_3	-	-	-	0.0	1.6	0.0	-	-	-	-	-	-	4.9	6.6	3.1	-	-	-
Tb_2O_3	-	-	-	0.0	0.5	0.0	-	-	-	-	-	-	-	-	-	-	-	-
Y_2O_3	-	-	-	1.3	3.5	0.0	0.1	4.7	0.0	-	-	-	13.4	17.0	7.6	-	-	-
ThO_2	-	-	-	present			present			4.1	5.8	2.6	present			present		
Nb_2O_5	-	-	-	-	-	-	1.7	4.2	0.0	1.6	2.8	1.0	-	-	-	-	-	-
TiO_2	-	-	-	-	-	-	19.1	37.9	3.2	30.8	60.1	19.4	-	-	-	-	-	-
CaO	-	-	-	13.9	28.7	0.8	3.9	14.9	0.8	4.2	5.5	1.9	30.4	40.3	26.8	1.0	1.4	0.5
Na_2O	-	-	-	-	-	-	0.1	2.7	0.0	-	-	-	-	-	-	-	-	-
K_2O	-	-	-	-	-	-	0.1	1.4	0.0	-	-	-	-	-	-	0.7	4.0	0.0
FeO	-	-	-	0.4	4.0	0.0	2.1	9.8	0.0	1.1	2.3	0.8	1.6	8.1	0.0	-	-	-
MgO	-	-	-	-	-	-	-	-	-	-	-	-	1.1	6.0	0.0	-	-	-
SrO	-	-	-	-	-	-	-	-	-	-	-	-	-	-	-	6.2	10.0	0.0
SO_3	-	-	-	-	-	-	-	-	-	-	-	-	-	-	-	2.1	2.7	1.0
P_2O_5	-	-	-	-	-	-	-	-	-	-	-	-	-	-	-	29.5	32.6	19.3
SiO_2	1.1	1.5	0.6	1.7	8.0	0.0	5.2	20.4	0.0	1.1	1.5	0.7	-	-	-	4.7	21.4	0.0
Al_2O_3	-	-	-	0.3	4.0	0.0	0.7	5.8	0.0	-	-	-	-	-	-	36.2	37.6	35.3
F	5.1	5.9	3.6	4.6	7.0	0.0	5.0	7.7	0.0	-	-	-	4.9	7.3	1.7	-	-	-
Cl	-	-	-	0.1	0.9	0.0	0.0	1.1	0.0	-	-	-	-	-	-	-	-	-
ΣRE_2O_3	**93.7%**			**79.0%**			**62.7%**			**56.8%**			**61.9%**			**19.7%**		
n	*3*			*1*			*68*			*14*			*13*			*7*		

Table G1. continued.

	Allanite-(Ce)			Perrierite			Fergusonite-(Y)			Monazite-(Ce)			Xenotime-(Y)		
	Wt% oxides			Wt% oxides			Wt% oxides			Wt% oxides			Wt% oxides		
	Average	Maximum	Minimum	Average	Maximum	Minimum	Average	Maximum	Minimum	Average	Maximum	Minimum	Average	Maximum	Minimum
Ce_2O_3	14.8	18.2	7.8	22.1	25.2	17.6	-	-	-	36.8	45.4	35.4	-	-	-
La_2O_3	8.9	18.5	7.4	11.9	13.9	8.7	-	-	-	19.0	24.4	15.4	-	-	-
Nd_2O_3	2.4	4.3	0.0	6.5	7.9	5.7	-	-	-	11.8	15.1	9.0	-	-	-
Pr_2O_3	-	-	-	1.4	3.2	0.0	-	-	-	0.5	3.4	0.0	-	-	-
Sm_2O_3	-	-	-	0.2	0.9	0.0	-	-	-	0.2	1.9	0.0	0.9	2.7	0.0
Gd_2O_3	-	-	-	-	-	-	-	-	-	-	-	-	4.7	8.5	2.6
Tb_2O_3	-	-	-	-	-	-	-	-	-	-	-	-	-	1.5	0.0
Dy_2O_3	-	-	-	-	-	-	3.9	6.7	0.0	-	-	-	7.7	10.2	5.5
Ho_2O_3	-	-	-	-	-	-	-	-	-	-	-	-	0.5	1.9	0.0
Er_2O_3	-	-	-	-	-	-	-	-	-	-	-	-	3.2	4.7	0.0
Yb_2O_3	-	-	-	-	-	-	-	-	-	-	-	-	2.3	3.0	0.0
Y_2O_3	-	-	-	-	-	-	28.8	34.2	23.8	-	-	-	40.0	53.4	26.7
ThO_2	-	-	-	4.3	6.5	2.5	present			present			1.0	3.0	0.0
Nb_2O_5	-	-	-	0.6	0.6	0.0	56.5	59.1	54.4	-	-	-	-	-	-
TiO_2	2.4	3.2	0.0	22.6	28.2	16.6	2.1	3.1	1.0	-	-	-	-	-	-
CaO	10.0	10.8	9.1	2.9	3.7	1.5	2.7	5.7	1.3	0.6	1.4	0.0	-	-	-
FeO	19.9	21.5	18.2	5.3	10.3	1.5	1.1	3.9	0.0	-	-	-	-	8.5	0.0
P_2O_5	-	-	-	-	-	-	-	-	-	27.5	32.9	17.0	37.8	51.2	21.4
SiO_2	30.5	32.4	27.9	19.0	25.7	13.7	4.5	7.7	1.5	2.2	6.1	0.0	0.7	2.3	0.0
Al_2O_3	10.9	13.7	9.5	2.5	4.9	1.1	-	-	-	-	-	-	-	-	-
F	-	-	-	-	3.3	0.0	-	-	-	-	-	-	-	-	-
Cl	-	-	-	-	-	-	-	-	-	-	-	-	-	-	-
ΣRE_2O_3	**26.1%**			**42.0%**			**32.7%**			**68.4%**			**59.3%**		
n	*12*			*12*			*5*			*13*			*18*		

Table G2. The average, maximum and minimum concentrations of each element present (as oxide %) within the different carbonate minerals.

	Calcite			**Siderite**			**Ankerite**		
	Wt% oxides			Wt% oxides			Wt% oxides		
	Average	Maximum	Minimum	Average	Maximum	Minimum	Average	Maximum	Minimum
CaO	94.2	97.3	91.0	1.7	2.8	1.2	56.2	59.6	53.1
MgO	1.0	3.5	0.0	1.7	4.0	0.6	24.5	31.4	17.7
FeO	2.7	5.0	0.0	92.9	96.1	89.0	18.4	28.4	11.0
MnO	0.7	2.1	0.0	3.0	6.9	0.6	0.7	2.1	0.0
Y_2O_3	0.2	1.3	0.0	-	-	-	-	-	-
n	*11*			*13*			*35*		

1 Allanite

14GR03

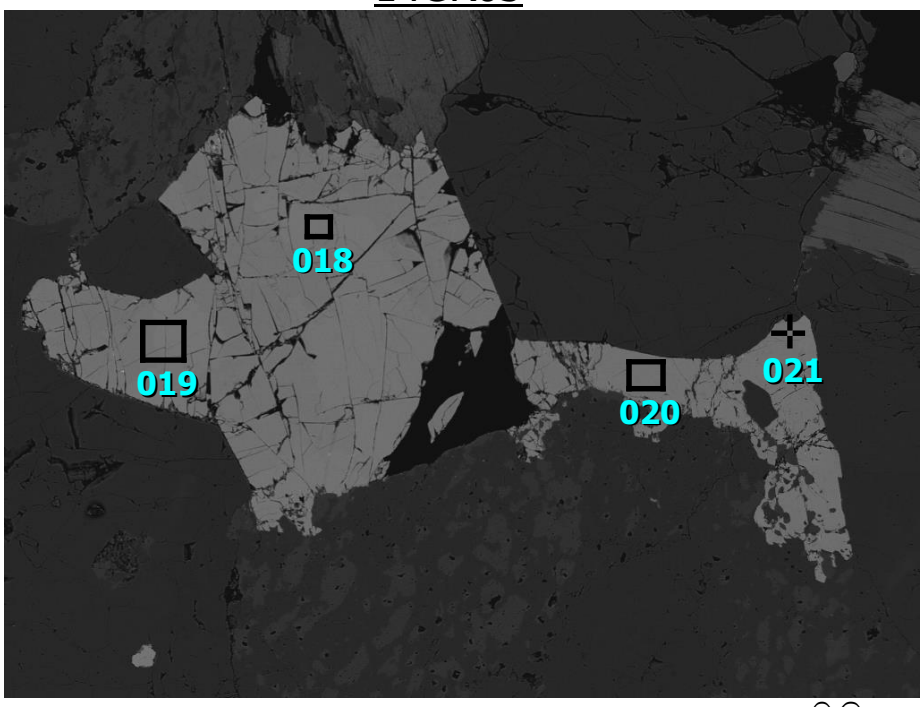


```
Title       : IMG1
------------------------
Instrument  : 7000F
Volt        : 15.00 kV
Mag         : x 140
Date        : 2016/07/19
Pixel       : 1024 x 768

Acquisition Parameter
Instrument    : 7000F
Acc. Voltage  : 15.0 kV
Probe Current: 0.59000 nA
PHA mode      : T3
Real Time     : 95.89 sec
Live Time     : 70.00 sec
Dead Time     : 27 %
Counting Rate: 5739 cps
Energy Range :  0 - 20 keV
```

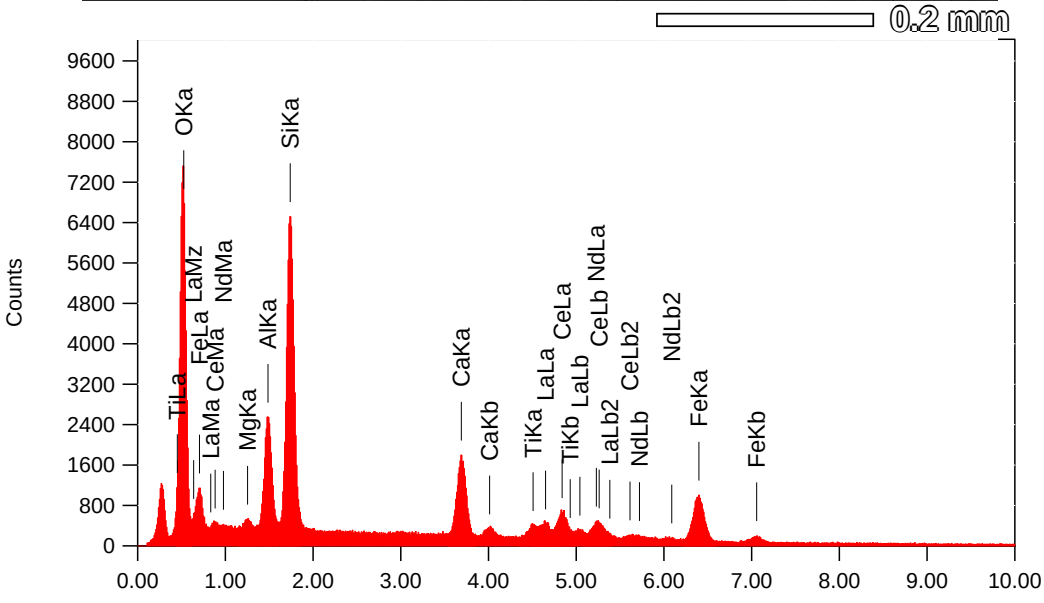

ZAF Method Standardless Quantitative Analysis(Oxide)
Fitting Coefficient : 0.1520
Total Oxide : 24.0

Element	(keV)	mass%	Error%	Mol%	Compound	mass%	Cation	K
O		33.86						
Mg K*	1.253	0.49	0.12	1.66	MgO	0.82	0.23	0.4747
Al K	1.486	5.02	0.14	7.59	Al2O3	9.49	2.11	5.5981
Si K	1.739	14.22	0.16	41.31	SiO2	30.42	5.74	18.5005
Ca K	3.690	6.94	0.17	14.12	CaO	9.70	1.96	13.7035
Ti K*	4.508	1.84	0.33	3.14	TiO2	3.07	0.44	3.0526
Fe K	6.398	15.17	0.47	22.16	FeO	19.51	3.08	24.5910
La L*	4.648	6.77	0.69	1.99	La2O3	7.94	0.55	10.2143
Ce L	4.837	12.00	0.67	6.99	CeO2	14.74	0.97	18.2439
Nd L*	5.227	3.69	0.73	1.04	Nd2O3	4.31	0.29	5.6213
Total		100.00		100.00		100.00	15.37	

2 Bastnäsite Group Minerals

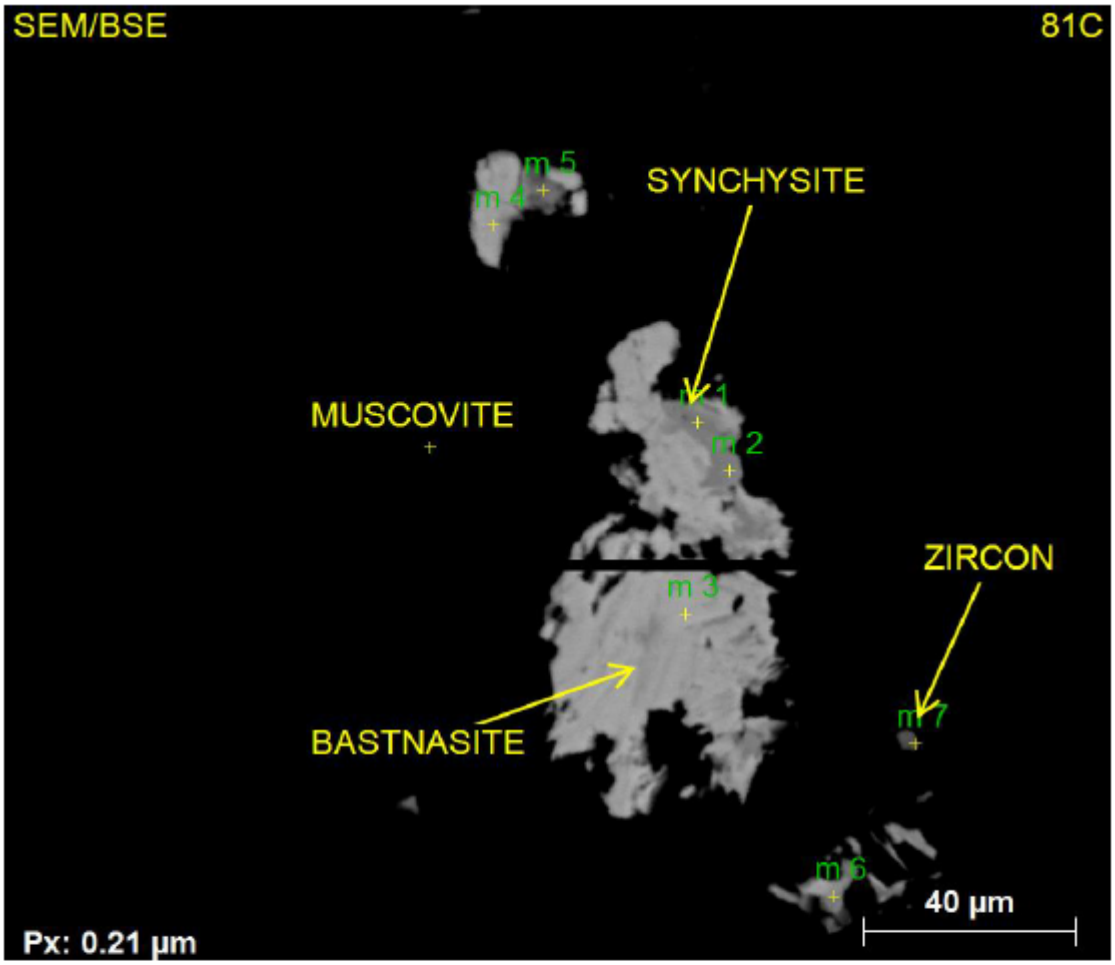

	m 1	m 2	m 3	m 4	m 5	m 6
CaO	16.1	15.2	2.0	2.8	29.8	13.4
FeO	b.d.	b.d.	b.d.	b.d.	1.1	b.d.
F	5.3	5.1	6.8	8.0	4.5	6.9
ThO2	2.6	1.5	1.7	4.1	31.3	3.7
Ce2O3	36.8	38.1	43.0	41.5	14.4	36.5
Nd2O3	12.7	12.1	15.0	14.1	8.2	12.9
La2O3	19.3	21.3	22.2	21.4	5.0	18.5
Pr2O3	4.3	3.8	5.4	4.6	2.2	4.0
Sm2O3	1.6	1.5	2.1	1.9	1.9	2.4
Gd2O3	1.3	1.5	1.7	1.4	1.6	1.8

M1/m2/m6 are parisite, m5 is synchysite, and m3/m4 are most likely analyses of bastnasite.

Report from Townend & Townend (2016b).

3 Fergusonite

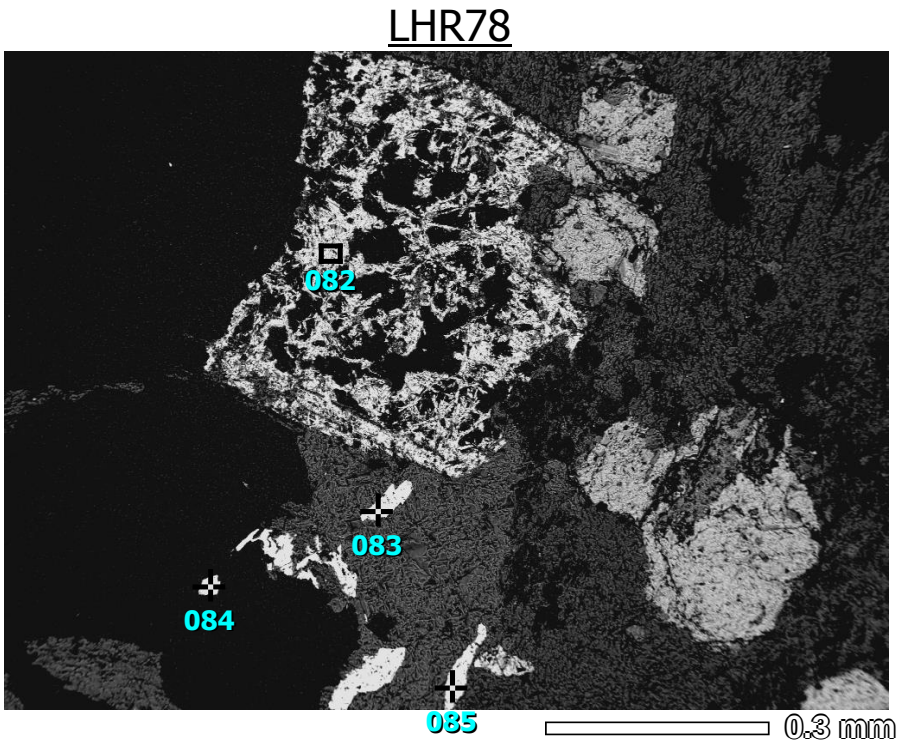


```
Title        : IMG1
-------------------------
Instrument   : 7000F
Volt         : 15.00 kV
Mag          : x 100
Date         : 2016/08/10
Pixel        : 1024 x 768
```

```
Acquisition Parameter
Instrument    : 7000F
Acc. Voltage  : 15.0 kV
Probe Current: 0.59000 nA
PHA mode      : T3
Real Time     : 78.02 sec
Live Time     : 60.92 sec
Dead Time     : 21 %
Counting Rate: 4567 cps
Energy Range :  0 - 20 keV
```

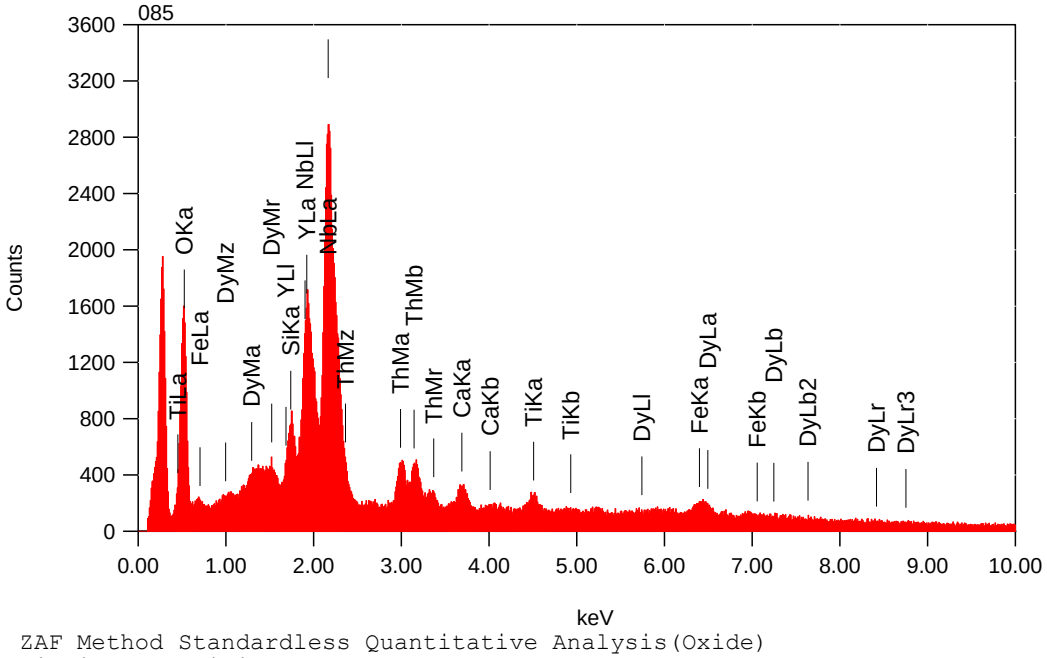

ZAF Method Standardless Quantitative Analysis(Oxide)
Fitting Coefficient : 0.4119
Total Oxide : 24.0

Element	(keV)	mass%	Error%	Mol%	Compound	mass%	Cation	K
O		28.31						
Si K	1.739	1.93	0.40	12.70	SiO2	4.14	0.93	2.7634
Ca K	3.690	1.75	0.60	8.03	CaO	2.44	0.59	2.7306
Ti K	4.508	1.88	0.89	7.23	TiO2	3.13	0.53	2.6303
Fe K*	6.398	2.99	1.52	9.88	FeO	3.85	0.73	4.4369
Y L*	1.922	18.74	1.09	19.43	Y2O3	23.80	2.86	23.6684
Nb L	2.166	41.31	0.93	40.98	Nb2O5	59.09	6.03	47.2599
Dy M*	1.293	3.08	2.79	1.75	Dy2O3	3.54	0.26	3.1135
Th L*	12.952	0.00	0.00	0.00	ThO2	0.00	0.00	13.3970
Total		100.00		100.00		100.00	11.93	

4 Florencite

LHR25

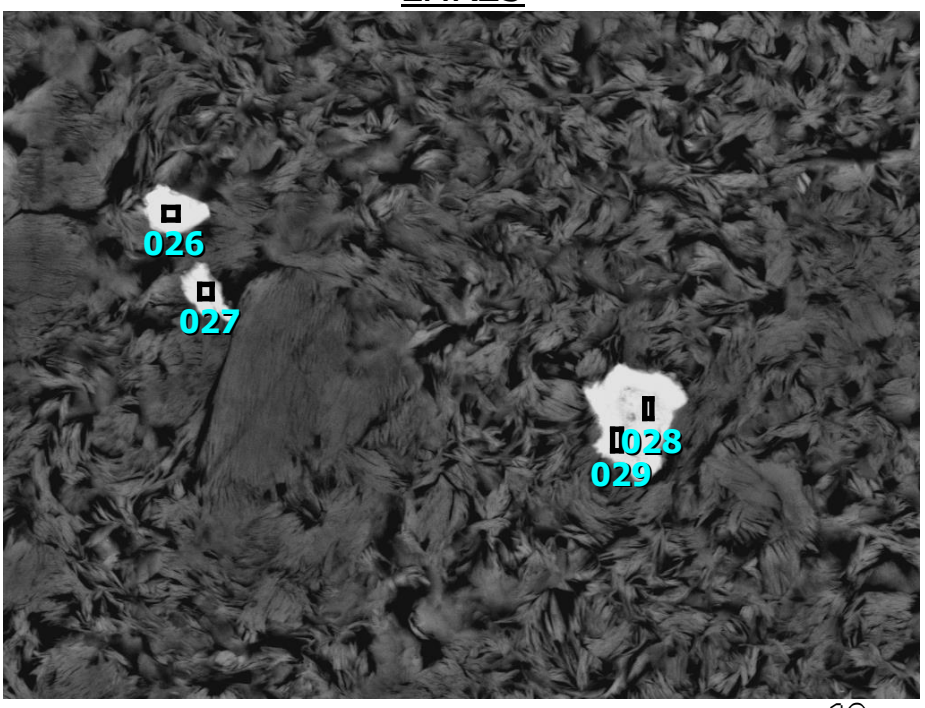


```
Title       : IMG1
----------------------
Instrument  : 7000F
Volt        : 15.00 kV
Mag         : x 3,000
Date        : 2016/08/10
Pixel       : 1024 x 768

Acquisition Parameter
Instrument    : 7000F
Acc. Voltage : 15.0 kV
Probe Current: 0.59000 nA
PHA mode      : T3
Real Time     : 93.19 sec
Live Time     : 62.45 sec
Dead Time     : 32 %
Counting Rate: 7285 cps
Energy Range :  0 - 20 keV
```

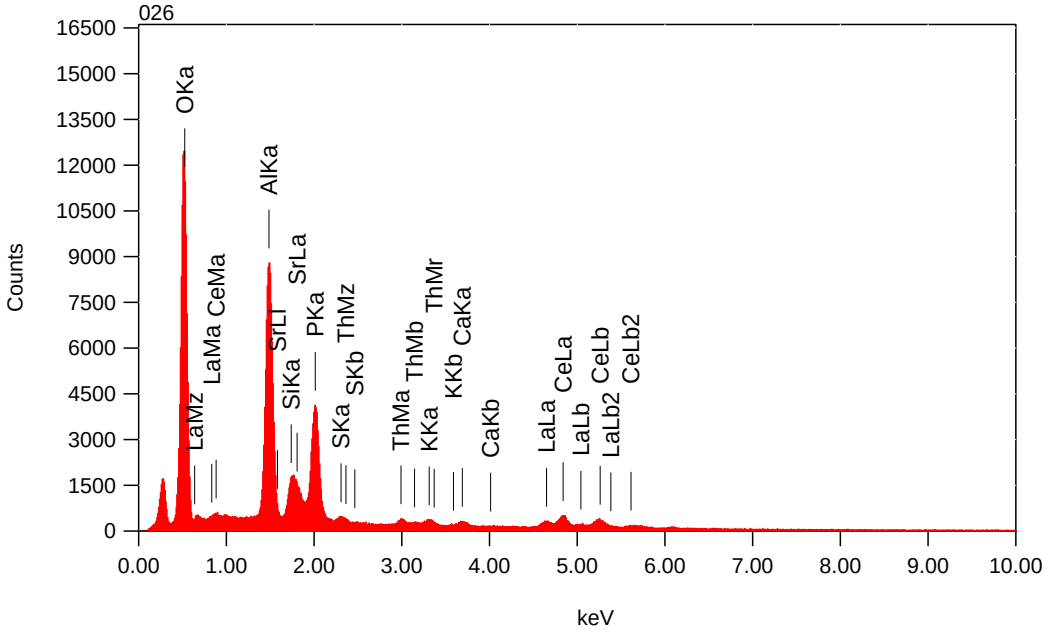

ZAF Method Standardless Quantitative Analysis(Oxide)
Fitting Coefficient : 0.1858
Total Oxide : 24.0

Element	(keV)	mass%	Error%	Mol%	Compound	mass%	Cation	K
O		42.31						
Al K	1.486	18.87	0.21	40.22	Al2O3	35.66	6.35	28.0692
Si K	1.739	3.12	0.36	12.76	SiO2	6.67	1.01	4.6609
P K	2.013	12.57	0.32	23.33	P2O5	28.80	3.68	20.2471
S K	2.307	0.67	0.32	2.40	SO3	1.67	0.19	1.1384
K K	3.312	0.87	0.24	1.28	K2O	1.04	0.20	1.7389
Ca K	3.690	0.80	0.33	2.31	CaO	1.12	0.18	1.7323
Sr L*	1.806	5.24	0.53	6.88	SrO	6.20	0.54	8.3849
La L	4.648	4.76	1.04	1.97	La2O3	5.59	0.31	8.0049
Ce L	4.837	10.79	1.21	8.86	CeO2	13.26	0.70	18.2595
Th L*	12.952	0.00	0.00	0.00	ThO2	0.00	0.00	7.7639
Total		100.00		100.00		100.00	13.16	

5 Loparite

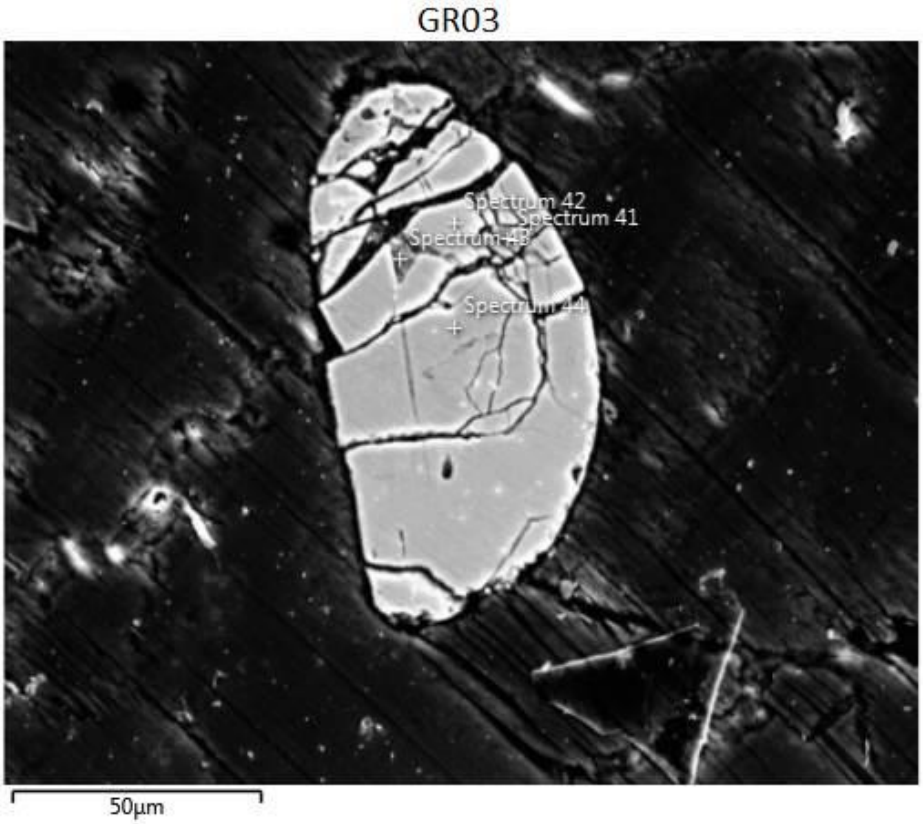
GR03
Spectrum 42
Spectrum 41
Spectrum 43
Spectrum 44
50µm

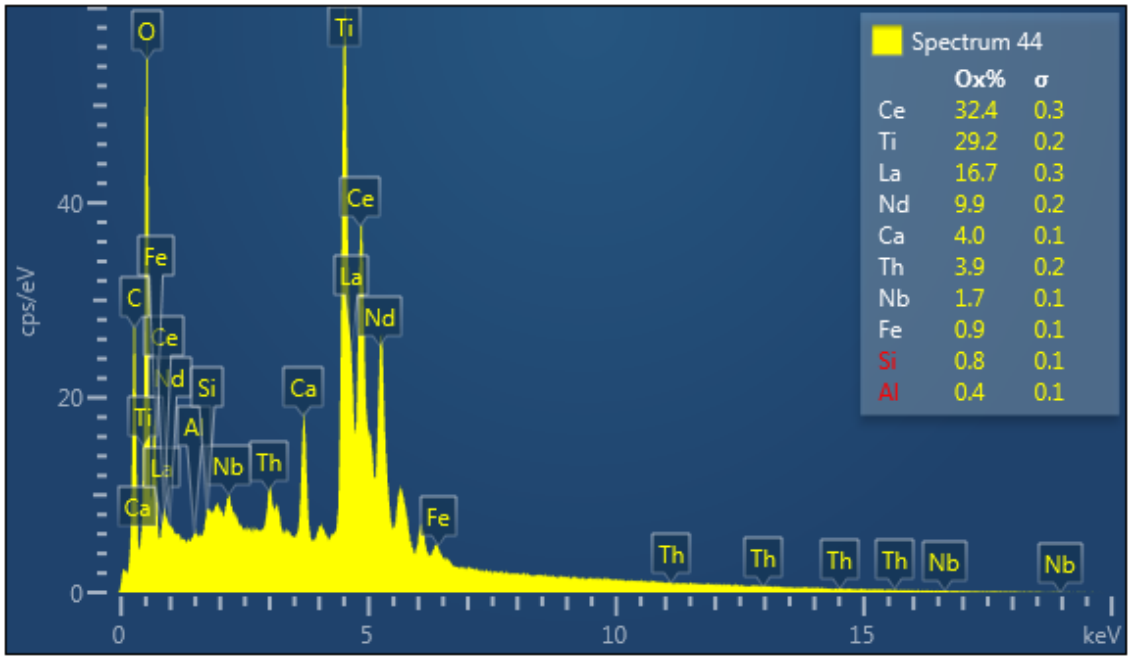
Spectrum 44
Ox% σ
Ce 32.4 0.3
Ti 29.2 0.2
La 16.7 0.3
Nd 9.9 0.2
Ca 4.0 0.1
Th 3.9 0.2
Nb 1.7 0.1
Fe 0.9 0.1
Si 0.8 0.1
Al 0.4 0.1
cps/eV
keV
O
Ti
Ce
La
Nd
Fe
C
Si
Ca
Al
Th
Nb

6 Monazite LHR28

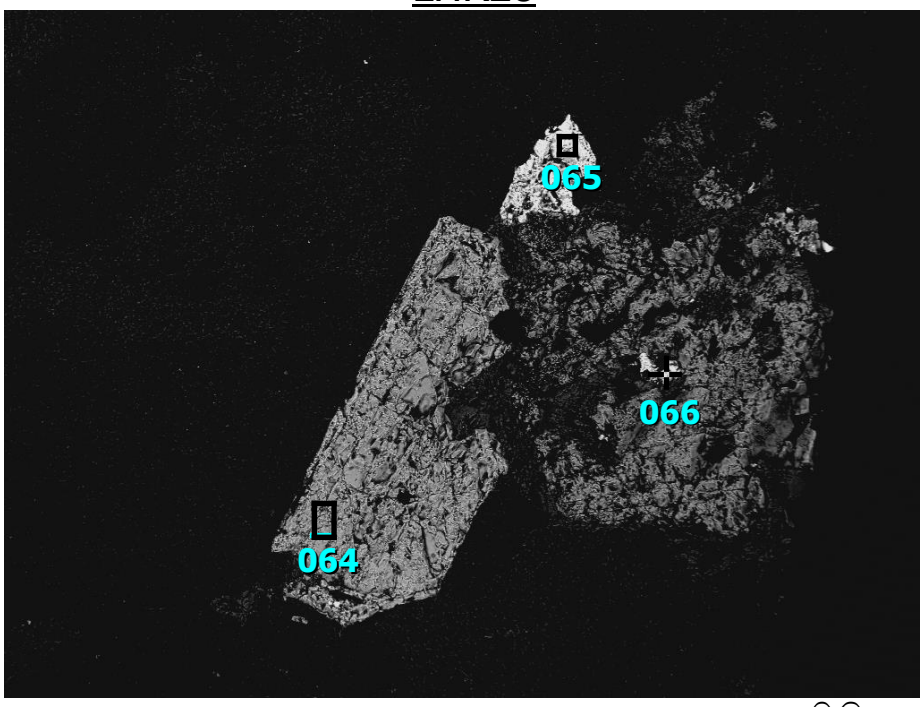


```
Title       : IMG1
-----------------------
Instrument  : 7000F
Volt        : 15.00 kV
Mag         : x 160
Date        : 2016/07/12
Pixel       : 1024 x 768
```

```
Acquisition Parameter
Instrument    : 7000F
Acc. Voltage  : 15.0 kV
Probe Current: 0.59000 nA
PHA mode      : T3
Real Time     : 106.32 sec
Live Time     : 70.00 sec
Dead Time     : 33 %
Counting Rate: 7615 cps
Energy Range :  0 - 20 keV
```

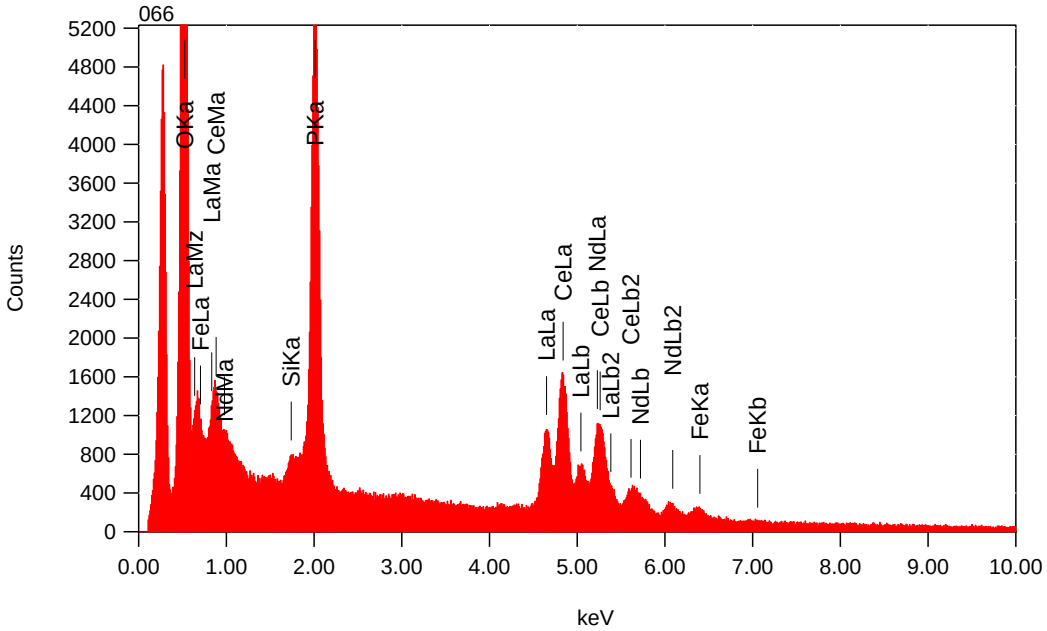

ZAF Method Standardless Quantitative Analysis(Oxide)
Fitting Coefficient : 0.2815
Total Oxide : 24.0

Element	(keV)	mass%	Error%	Mol%	Compound	mass%	Cation	K
O		29.66						
Si K*	1.739	0.32	0.53	2.03	SiO2	0.69	0.15	0.3568
P K	2.013	13.75	0.55	39.38	P2O5	31.51	5.75	17.9048
Fe K	6.398	1.48	1.43	4.69	FeO	1.90	0.34	2.2405
La L	4.648	16.62	1.69	10.62	La2O3	19.50	1.55	23.9638
Ce L	4.837	30.43	1.98	38.52	CeO2	37.37	2.81	44.2193
Nd L*	5.227	7.74	2.17	4.76	Nd2O3	9.03	0.70	11.3149
Total		100.00		100.00		100.00	11.30	

7 Perrierite

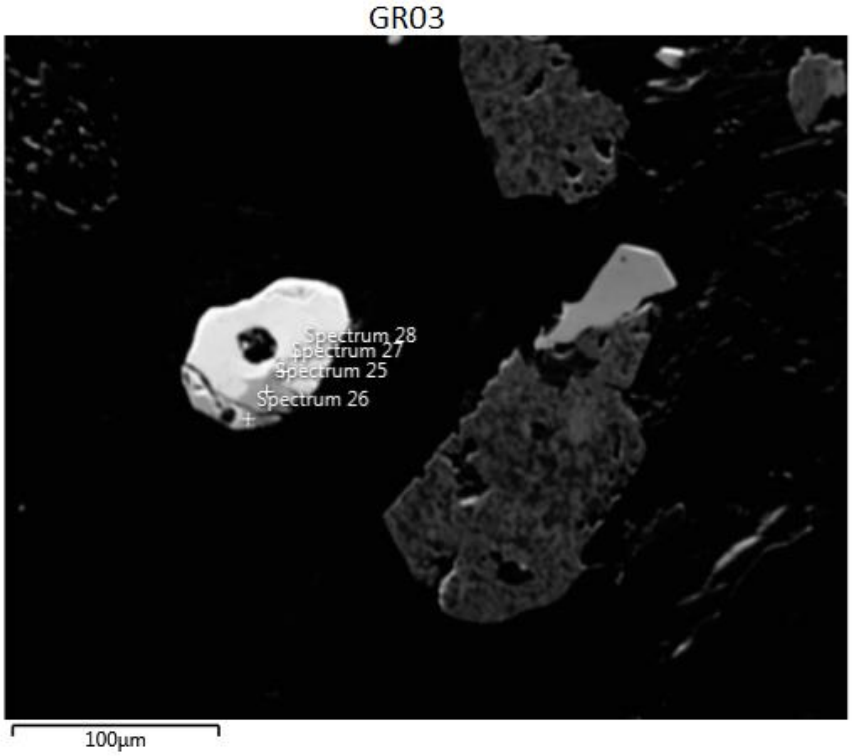

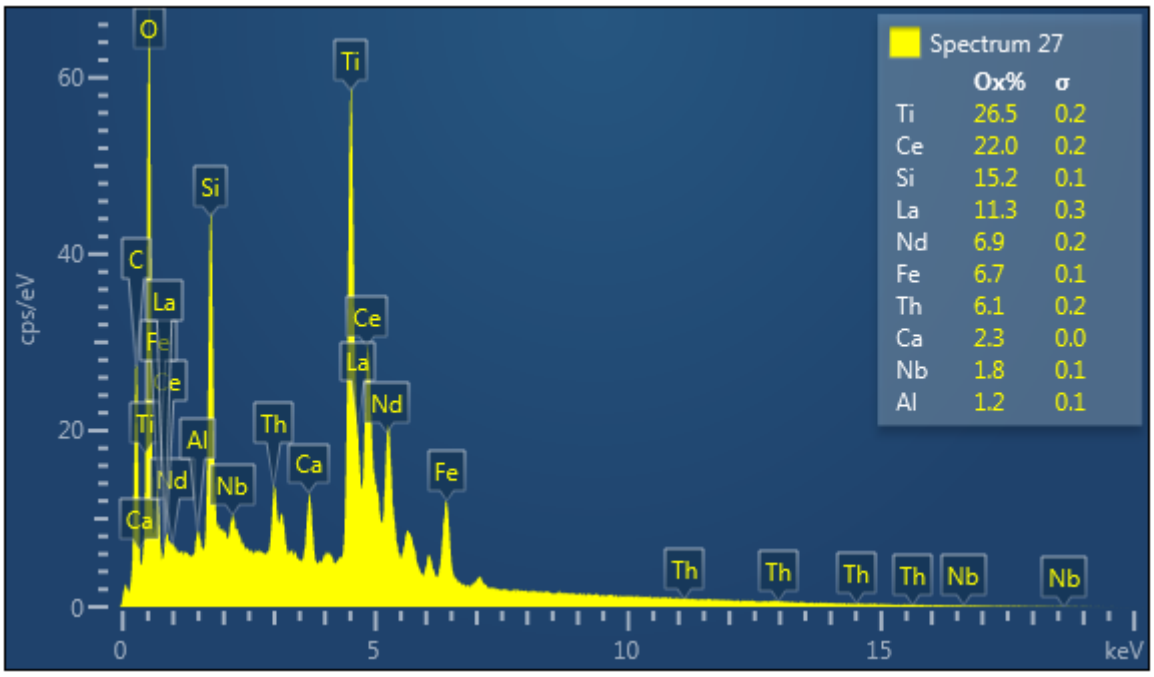

8 Xenotime

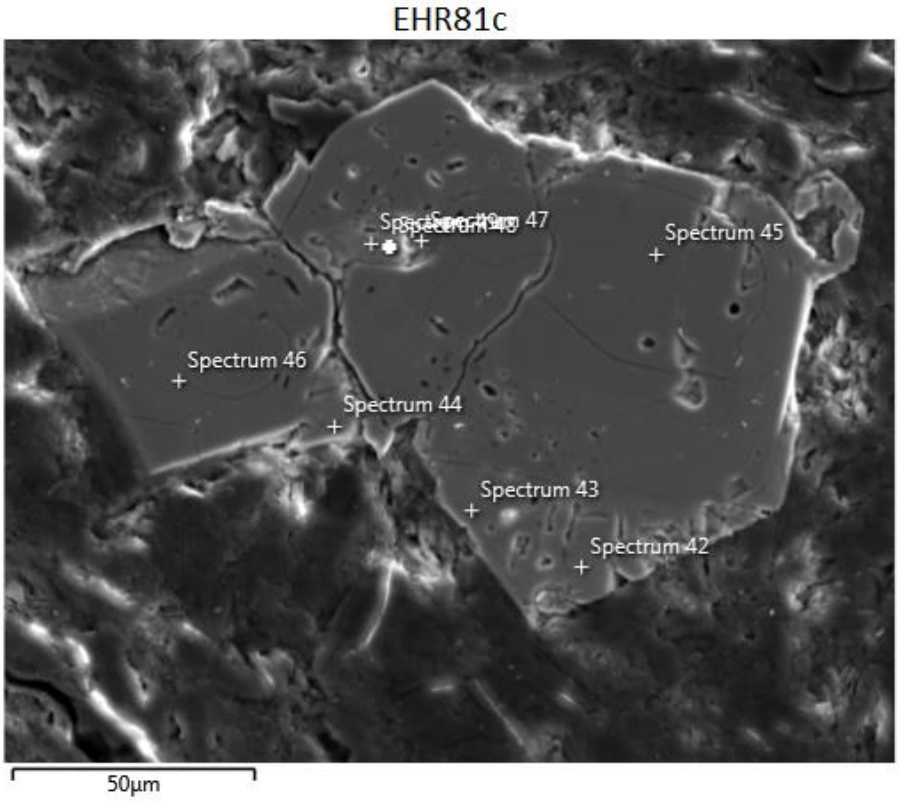
EHR81c
Spectrum 47
Spectrum 45
Spectrum 46
Spectrum 44
Spectrum 43
Spectrum 42
50µm

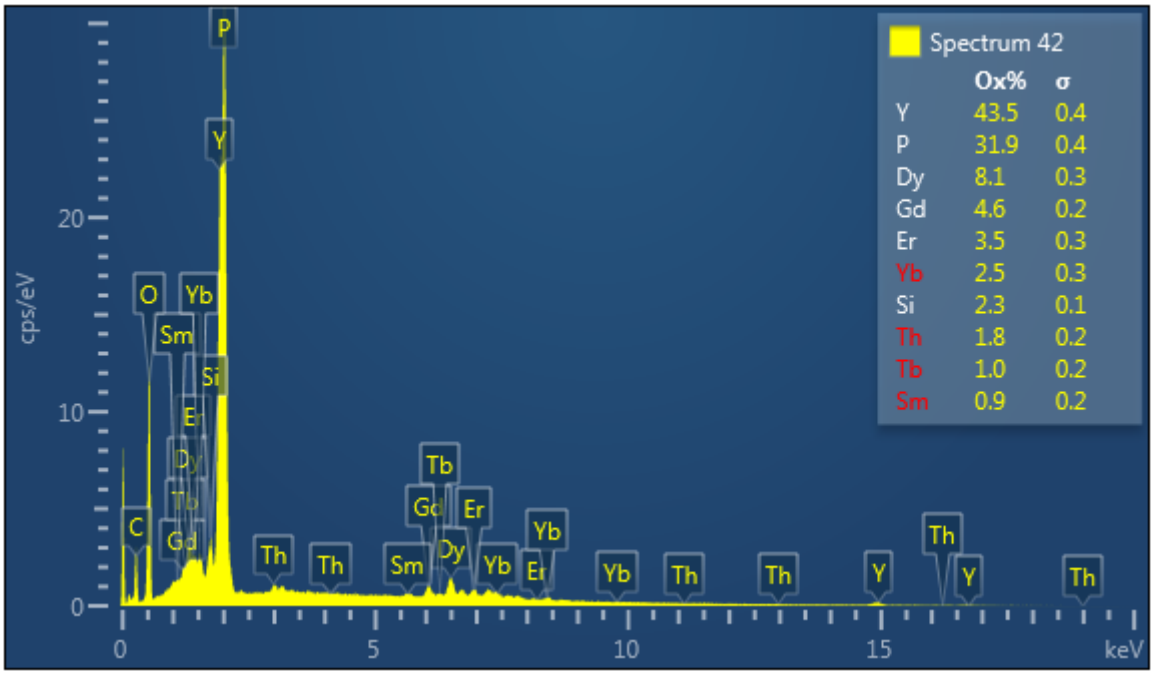
Spectrum 42
Ox% σ
Y 43.5 0.4
P 31.9 0.4
Dy 8.1 0.3
Gd 4.6 0.2
Er 3.5 0.3
Yb 2.5 0.3
Si 2.3 0.1
Th 1.8 0.2
Tb 1.0 0.2
Sm 0.9 0.2
cps/eV
keV

H Full Stable Isotope Results

Sample	$\delta^{18}O$ (‰ V-PDB)	$\delta^{18}O$ (stdev)	$\delta^{13}C$ (‰ V-PDB)	$\delta^{13}C$ (stdev)	$\delta^{18}O$ (‰ V-SMOW)
EHR80C-23	-22.62	0.09	-1.88	0.06	7.60
EHR80C-24	-16.89	0.06	-1.50	0.14	13.49
EHR80C-25	-15.03	0.05	-1.32	0.07	15.42
EHR80C-26	-14.29	0.05	-0.97	0.10	16.17
EHR80C-27	-14.09	0.06	-0.95	0.03	16.38
EHR80C-28	-14.43	0.11	-0.68	0.04	16.04
EHR81C-17	-17.90	0.13	-1.48	0.07	12.46
EHR81C-18	-17.77	0.16	-1.63	0.10	12.60
EHR81C-19	-19.77	0.08	-2.89	0.10	10.53
EHR81C-20	-16.96	0.12	-1.61	0.11	13.42
EHR81C-21	-19.63	0.04	-2.88	0.03	10.67
EHR81C-22	-17.75	0.04	-1.49	0.10	12.61
EHR81D-29	-18.36	0.21	-2.06	0.17	11.98
EHR81D-30	-18.36	0.14	-1.97	0.12	11.99
EHR81D-31	-18.96	0.09	-1.97	0.07	11.37
EHR81D-32	-18.79	0.17	-2.00	0.13	11.54
LHR25-37	-12.82	0.19	-1.50	0.09	17.69
LHR25-38	-13.90	0.15	-1.30	0.12	16.58
LHR25-39	-17.93	0.11	-1.59	0.10	12.43
LHR25-40	-18.20	0.05	-1.84	0.04	12.15
LHR59-13	-20.74	0.04	-4.03	0.04	9.53
LHR59-14	-21.35	0.11	-3.82	0.11	8.90
LHR59-15	-21.53	0.03	-3.77	0.06	8.71
LHR59-16	-19.21	0.03	-4.34	0.05	11.11
LHR77-33	-13.72	0.04	-1.25	0.03	16.77
LHR77-34	-14.94	0.10	-1.58	0.07	15.51
LHR77-35	-14.76	0.22	-1.63	0.17	15.70
LHR77-36	-14.02	0.12	-2.25	0.09	16.46
QH12-9	-20.92	0.09	-5.12	0.05	9.34
QH12-10	-10.14	0.18	-7.61	0.12	20.46
QH12-11	-21.04	0.05	-5.43	0.08	9.22
QH12-12	-9.52	0.08	-10.03	0.06	21.09
QH20-1	-20.32	0.10	-3.96	0.05	9.96
QH20-2	-16.00	0.96	-6.86	0.76	14.41
QH20-3	-20.17	0.02	-4.08	0.01	10.12
QH20-4	-19.80	0.14	-3.61	0.14	10.49
QH25-5	-28.30	0.04	-4.07	0.11	1.74
QH25-6	-28.57	0.10	-4.23	0.07	1.46
QH25-7	-27.52	0.09	-4.47	0.05	2.54
QH25-8	-22.73	0.27	-9.32	0.50	7.48